Measurement of the Tritium pumping properties of a 4.2 K Argon Condensate for the Cryogenic Pumping Section of KATRIN

Zur Erlangung des akademischen Grades eines
DOKTORS DER NATURWISSENSCHAFTEN
von der Fakultät für Physik der Universität (TH)
Karlsruhe

genehmigte

DISSERTATION

von

Dipl. Phys. Frank Eichelhardt
aus Singen (Htwl.)

Tag der mündlichen Prüfung: 16.01.2009

Referent: Prof. Dr. G. Drexlin
Institut für Experimentelle Kernphysik, Universität Karlsruhe (TH)

Korreferent: Prof. Dr. Chr. Weinheimer
Institut für Kernphysik, Westfälische Wilhelms-Universität Münster

Abstract

This work was performed in the framework of the KATRIN (Karlsruhe Tritium Neutrino) experiment, the next generation tritium beta decay experiment which aims to determine the neutrino mass scale with a sensitivity of 0.2 eVc^{-2} (90% CL). In KATRIN, the tritium flow rate has to be suppressed by more than 14 orders of magnitude from the tritium injection point in the middle of the tritium source to the entrance of the spectrometers. The major part ($> 10^7$) has to be provided by the Cryogenic Pumping Section (CPS) that is operated at a baseline temperature of $3 - 4.5$ K with pre-condensed argon or krypton as adsorbent.

In order to evaluate the performance of such a cryo-pump in the tritium partial pressure regime of $\sim 10^{-16}$ mbar as required for KATRIN, the test experiment TRAP (Tritium Argon frost Pump) was built at the Tritium Laboratory Karlsruhe and upgraded for tritium operation during this work. TRAP is a mock-up of the CPS with regard to its cryogenic properties allowing for the measurement of the tritium flow rate suppression factor. The results and also the experiences obtained in this experiment are imperative for the detailed specification of the CPS.

TRAP consists of a bent tube (Cryo-trap) inside a liquid helium bath cryostat. The main experimental sequence is the following: After evacuating the system and cooling with liquid helium, the pre-condensed gas layer - in this work only argon was used - is prepared by gas inlet through a capillary. Tritium is then injected with a known flow rate at the bottom of the Cryo-trap. The small number of tritium molecules which are able to penetrate the Cryo-trap are detected at the upper end in the Detection System. From the ratio of the flow rates (flow in/flow out), the suppression factor is calculated. After a measurement campaign, the Cryo-trap is regenerated by warming up and purging with gaseous helium.

Most challenging in the experiment is the detection of tritium in the Detection System. Since the amount of tritium to be detected is very low, high sensitivity devices such as a residual gas analyzer and a silicon solid state detector were employed. Furthermore, a Monte Carlo electron tracking simulation was necessary for calculating the total amount of tritium in the Detection System.

Three measurements with tritium are presented in this thesis. The upper limit for the tritium flow rate suppression factor F of TRAP was determined to be

$$F = (6.9 \pm 0.5_{\text{stat}} \pm 3.1_{\text{sys}}) \cdot 10^6$$

and the DT partial pressure during injection of tritium was below

$$(8.67 \pm 0.06_{\text{stat}} \pm 2.60_{\text{sys}}) \cdot 10^{-16} \text{ mbar}\,.$$

Both values are barely within the order of magnitude specified for the CPS. Therefore, it was suggested to operate the CPS at 3 K.

During operation of TRAP, decontamination methods were developed, too. These allow for an in-situ decontamination of the CPS and the Pre-spectrometer in case of an unforeseen tritium contamination in these components.

Erklärung

Hiermit versichere ich, dass ich die vorliegende Arbeit selbständig und nur unter Verwendung der angegebenen Hilfsmittel und Quellen verfasst habe.

Frank Eichelhardt
Karlsruhe, den 19.01.2009

Contents

List of Figures

List of Tables

List of Abbreviations

ADC	Analog-to-Digital Converter
AMOR	Anlage zur Molsieb Regenerierung
amu	atomic mass unit
ASTM	American Society for Testing and Materials
CC	Charged Current
CMBR	Cosmic Microwave Background Radiation
CPS	Cryogenic Pumping Section
DIN	Deutsche Industrie Norm
DPS	Differential Pumping Section
ES	Elastic Scattering
EXO	Enriched Xenon Observatory
FT-ICR	Fourier-Transform Ion Cyclotron Resonance
FWHM	Full Width Half Maximum
FZK	Forschungszentrum Karlsruhe (Research Center Karlsruhe)
GALLEX	Gallium Experiment
GERDA	Germanium Detector Array
GHe	Gaseous Helium
HV	High Voltage
IK	Institut für Kernphysik (Institute for Nuclear Physics)
IPE	Institut für Prozessdatenverarbeitung und Elektronik (Institute for Data Processing and Electronics)
ITP	Institut für Technische Physik (Institute for Technical Physics)
JFET	Junction Field Effect Transistor
K2K	KEK to Kamioka
Kamiokande	Kamioka Nucleon Decay Experiment
KamLAND	Kamioka Liquid Scintillator Antineutrino Detector
KATRIN	Karlsruhe Tritium Neutrino (experiment)
LHC	Large Hadron Collider
LHe	Liquid Helium

LN_2	Liquid N_2, liquid nitrogen
LSC	Liquid Scintillation Counting
MAC-E	Magnetic Adiabatic Collimation with Electrostatic (filter)
MARE	Microcalorimeters for a Rhenium Experiment
MC	Monte Carlo
MIBETA	Milano Beta
MSW	Mikheyev Smirnov Wolfenstein (effect)
NEG	Non-Evaporable Getter
NC	Neutral Current
ORCA	Object oriented Realtime Control and Acquisition software system
PID	Process and Instrumentation Diagram
PIN	P-doted - Intrinsic - N-doted
Q_2	H_2, D_2, T_2, HD, HT or DT
RGA	Residual Gas Analyzer
RMS	Root Mean Square
SAGE	Soviet-American Gallium Experiment
SM	Standard Model
SNO	Sudbury Neutrino Observatory
SS	Stainless Steel
TILO	Test of Inner Loop
TLK	Tritiumlabor Karlsruhe (Tritium Laboratory Karlsruhe)
TMP	Turbomolecular Pump
TRAP	Tritium Argon frost Pump
TVO	Translation of "TBO" from Russian: thermally resistant, moisture resistant, pressurized/compacted
UHV	Ultra-High Vacuum
WGTS	Windowless Gaseous Tritium Source
WMAP	Wilkinson Microwave Anisotropy Probe
XHV	Extreme-High Vacuum

Chapter 1

Introduction

The present work is focused on test measurements for the Karlsruhe Tritium Neutrino (KATRIN) Experiment, the next-generation tritium beta decay experiment for the determination of the neutrino mass scale. This chapter gives a short introduction to neutrinos and the measurement of their masses. A detailed overview on this topic is available in [Ott08].

Neutrinos are the lightest elementary particles in the *Standard Model* (SM) of particle physics. The SM reduces the number of fundamental particles, which form all matter, to 12 fermions of spin-1/2. These are grouped into 6 *quarks* (up u, down d, charm c, strange s, top t, bottom b) and 6 *leptons* (electron neutrino ν_e, electron e^-, muon neutrino ν_μ, muon μ^-, tau neutrino ν_τ, tauon τ^-) categorized in three *families* or *generations*. Table 1.1 gives an overview of these 12 fundamental particles, wherein each particle is associated to a corresponding anti-particles of opposite electric charge.

The neutrinos (ν_e, ν_μ, ν_τ) were introduced in the SM as massless and electrically neutral particles [Sch97]. However, several experimental observations during the last decade indicate that neutrinos have mass in contrast to the assumption of the SM. In the following, the importance of neutrino masses will be discussed by grouping the relevant themes into three questions.

Table 1.1: The 12 fundamental fermions. The 12 fundamental fermions and their interactions are summarized in this table. Besides, the corresponding anti-particle with opposite electric charge exists for each particle.

	Generation			Electric	Interaction
	1	2	3	Charge	
Leptons	ν_e	ν_μ	ν_τ	0	weak
	e^-	μ^-	τ^-	$-e$	weak, electromagnetic
Quarks	u	c	t	$+2/3\,e$	weak, electromagnetic, strong
	d	s	b	$-1/3\,e$	weak, electromagnetic, strong

1. Why are neutrino masses so interesting?

Particle Physics: In the SM of particle physics, the fundamental charged fermions acquire mass through Yukawa couplings of the left-handed[1] weak isospin fermion doublets (ν_e^L, e^L), (ν_μ^L, μ^L) or (ν_τ^L, τ^L) to the Higgs doublet (Φ^+, Φ^0) and the right-handed fermion singlets e^R, μ^R or τ^R, respectively[2]. The masses themselves are not predicted by the SM; they are free parameters that need to be determined experimentally. Because of maximum parity violation in weak interactions [Gol58], no right-handed neutrinos and no left-handed anti-neutrinos exist in the SM, which yields zero neutrino masses.

Non-vanishing neutrino masses are a clear indication for physics beyond the SM. There is a large quantity of theoretical models to explain how neutrinos acquire mass. Some particularly attractive models use the *See-Saw* mechanism, for example, to generate light neutrino masses from a heavy sterile neutrino that does not participate in weak interactions. Others require a *Higgs triplet* that couples directly to the neutrinos and produces slightly heavier neutrino masses. Depending on the experimental results on the neutrino mass scale and the hierarchy of the masses as well as their mixings, some models will be preferred, others refuted. The knowledge of the neutrino masses is crucial for the understanding of the generation of fermion masses in general due to the fact that neutrinos are lighter than all other elementary fermions by a factor of 10^5.

Cosmology: Neutrinos play a fundamental role in astrophysical and cosmological processes, too, for example in supernova explosions. Furthermore, so-called *relic neutrinos*, which decoupled < 1 s after the Big Bang, are $\sim 10^9$ times more abundant than baryons in the universe. These neutrinos are distributed homogeneously over the whole universe with an average particle density of 339 neutrinos per cm^3 and play a significant role in the formation of large scale structures acting as hot dark matter. Figure 1.1 shows how massive neutrinos, even with very low mass, could contribute to the universe's overall mass and energy density on the same scale as all visible matter due to their large number. Because of the Hubble expansion of the universe, the temperature of these neutrinos has decreased to ~ 1.95 K [Rin05] rendering any detection not feasible within the foreseeable future: The cross section for the commonly considered detection reactions of inverse beta decay and elastic scattering is $\sim 10^{-54}$ cm^2 at this energy [Sch97].

2. How do we know that neutrinos have mass?

A vanishing neutrino rest mass was in agreement with experimental data until recently when neutrino oscillations were discovered in solar, atmospheric as well as in

[1] Left- and right-handedness (or *chirality*) are defined by the sign of the eigenvalues of the operator γ^5: $+1$ for right-handed and -1 for left-handed particles. γ^5 can be calculated from the the Dirac Matrices γ^μ: $\gamma^5 = i\gamma^0\gamma^1\gamma^2\gamma^3$ [Gri87]. The left-handed Ψ^L and right-handed Ψ^R components of a Dirac Spinor Ψ are obtained in the following way: $\Psi^L = (1-\gamma^5)\Psi/2$ and $\Psi^R = (1+\gamma^5)\Psi/2$. For massless particles, chirality is equal to *helicity* $H = (\vec{s}\cdot\vec{p})/(|\vec{s}|\cdot|\vec{p}|)$ with spin $\vec{s}$ and momentum $\vec{p}$.

[2] This mechanism postulates the existence of the Higgs particle that has not been discovered yet, but which might be found soon at the Large Hadron Collider (LHC) at CERN [Mai99, LHC].

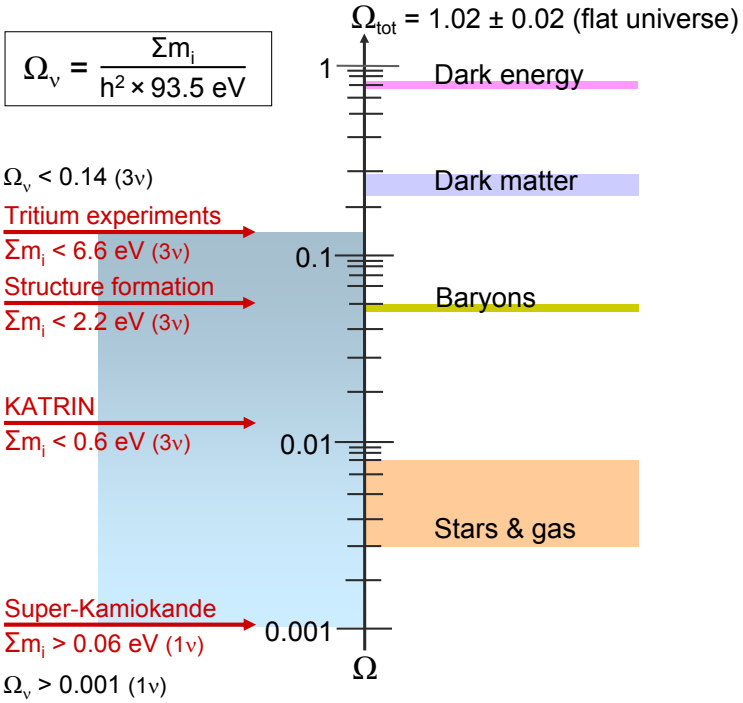

Figure 1.1: Dark matter in the universe. The figure shows the possible contribution of massive neutrinos to the relative density of the universe in comparison to the other contributions. Ω denounces the density in units of the critical density $\Omega_c = 1$ for a flat universe (for an introduction see, for example, [Sch08]). The contribution of massive neutrinos to hot dark matter is not yet clarified: An upper limit is given by tritium decay experiments, a lower limit by data extracted from oscillation experiments of atmospheric neutrinos. The possible parameter space spans ~ 2 orders of magnitude.

reactor and accelerator neutrino experiments. The observation of neutrino oscillations is a strong evidence for massive neutrinos.

The first hint to neutrino oscillations was found in the neutrino flux from the sun. Neutrinos are produced in the sun by several different thermonuclear reactions, the overall reaction in the *pp fusion chain* being [Bah06]

$$4\,p \rightarrow {}^4\mathrm{He} + 2\,e^+ + 2\,\nu_e \qquad (E_{\nu_e} < 20\ \mathrm{MeV})\,. \tag{1.1}$$

The neutrino flux from the sun has been determined by experiments like Homestake [Dav94, Cle95, Dav96], GALLEX [Ans92], SAGE [Abd94], (Super-)Kamiokande [Hos06, Hir89] SNO [SNO00, SNO01, SNO02] and Borexino [Arp08]. It shows a neutrino deficit compared to the neutrino flux expected from the Standard Solar Model [Bah06] if the detection reaction is a charged current (CC) reaction mediated by $W^\pm$ bosons. In this case, the reaction is sensitive to the neutrino flavor as, for example,

$$\nu_e + {}^{37}\mathrm{Cl} \rightarrow {}^{37}\mathrm{Ar}^* + e^- \tag{1.2}$$

in the Homestake experiment [Dav94]. Neutral current (NC) reactions, on the other hand, which are mediated by Z^0 bosons, show no neutrino deficit as, for example,

$$\nu_\alpha + {}^2\mathrm{H} \rightarrow \nu_\alpha + n + p \tag{1.3}$$

with $\alpha = e, \mu, \tau$ in the neutral current induced deuterium breakup observed in SNO [SNO00]. Here, the total flux of all three neutrino flavors is determined[3]. The explanation to this paradigm is the following: Neutrino oscillations transform the neutrino source flavor state, e.g. ν_e in case of solar neutrinos, into a different flavor state, e.g. ν_μ. These oscillations are enhanced by matter effects (MSW-effect) in the sun.

The measurement of the flux of atmospheric neutrinos with energies up to several GeV has been pioneered by Super-Kamiokande [Hos06]. These neutrinos are created in the earth's outer atmosphere mainly through the following reactions:

$$\begin{aligned} \pi^+ \quad &\rightarrow \quad \underbrace{\mu^+} + \nu_\mu \\ &\qquad \mu^+ \rightarrow e^+ + \overline{\nu}_\mu + \nu_e\,, \end{aligned} \tag{1.4}$$

$$\begin{aligned} \pi^- \quad &\rightarrow \quad \underbrace{\mu^-} + \overline{\nu}_\mu \\ &\qquad \mu^- \rightarrow e^- + \nu_\mu + \overline{\nu}_e\,. \end{aligned} \tag{1.5}$$

The ratio of fluxes of muon and electron neutrinos on the earth is therefore ~ 2; it is not exactly 2 since some $\mu^\pm$ reach the ground level without decaying. Atmospheric neutrinos are detected in the Super-Kamiokande detector via their scattering on nuclei N

$$\nu_l + N \quad \rightarrow \quad l + N'\,. \tag{1.6}$$

where the flavor of the resulting lepton l is equal to the flavor of the detected neutrino ν_l. This CC reaction is strongly directional: The velocity vectors of the original neutrino and the lepton are almost parallel. Only the leptons $e^\pm$ and $\mu^\pm$ are detected by the current event reconstruction algorithms which can distinguish between the two lepton flavors by analyzing the shape of Cerenkov signals. It turns out that the ratio of ~ 2 is only valid for neutrinos with short path length, that hit the detector straight from above. Depending from the zenith angle, the muon neutrino flux showed a deficit compared to results from Monte Carlo simulations. A possible explanation are $\nu_\mu \rightarrow \nu_\tau$ oscillations in the atmosphere [Fuk98].

Experiments with reactor neutrinos, for example KamLAND [Ara04], and with neutrinos created in particle accelerators, for example in the K2K experiment [Alu94], support the neutrino oscillation hypothesis and allow for an improved determination of some of the oscillation parameters (see below).

[3] Elastic scattering (ES) reactions between (anti-)neutrinos and electrons are sensitive to all three neutrino flavors, too. However, the cross section for this reaction is higher for ν_e than for $\nu_{\mu,\tau}$ by a factor of ~ 7 since Z^0 and $W^\pm$ bosons are involved in the former case and not only Z^0 bosons. Therefore, a neutrino deficit is also observed.

The fundamental mechanism of neutrino oscillations is the following: Neutrinos are created via a weak interaction in a specific *flavor eigenstate* $|\nu_\alpha\rangle$ with $\alpha = e, \mu, \tau$. The flavor eigenstates themselves are superpositions of *mass eigenstates* $|\nu_j\rangle$ ($j = 1, 2, 3$) of the *mass operator* $\hat{M}$ [Sch97]:

$$\hat{M}\,|\nu_j\rangle = m_j\,|\nu_j\rangle\ . \tag{1.7}$$

Neutrino flavor and mass eigenstates are connected by a mixing matrix[4] U:

$$|\nu_\alpha\rangle = \sum_j U_{\alpha j}\,|\nu_j\rangle \qquad \text{and} \tag{1.8}$$

$$|\nu_j\rangle = \sum_\alpha U^\dagger_{j\alpha}\,|\nu_\alpha\rangle = \sum_\alpha U^*_{\alpha j}\,|\nu_\alpha\rangle\ . \tag{1.9}$$

The time dependence of a mass eigenstate is given by

$$|\nu_j(t)\rangle = e^{-iE_j t/\hbar}\,|\nu_j\rangle \quad \text{with} \quad E_j = \sqrt{p^2c^2 + m_j^2c^4} \approx pc + \frac{m_j^2c^3}{2p} \quad \text{for} \quad p \gg m_j c\,. \tag{1.10}$$

Herein p is the neutrino's momentum and c the speed of light. It follows that the time development of a pure flavor eigenstate $|\nu_\alpha\rangle$ is then

$$|\nu(t)\rangle = \sum_j U_{\alpha j}\,e^{-iE_j t/\hbar}\,|\nu_j\rangle = \sum_{j,\beta} U_{\alpha j}U^*_{\beta j}\,e^{-iE_j t/\hbar}\,|\nu_\beta\rangle\ . \tag{1.11}$$

Thus, the neutrino's flavor composition changes with time. In the simplified case of two flavor mixing, the probability P of finding the original ν_α in the distance L as ν_β is given by

$$P(\nu_\alpha \to \nu_\beta, L) = \sin^2(2\Theta)\cdot\sin^2\left(\frac{\Delta m^2\cdot L}{4E}\right) \tag{1.12}$$

with the neutrino energy E, the mass square difference $\Delta m^2 = |m_1^2 - m_2^2|$ and the so-called mixing angle Θ. Therefore, the observation of neutrino oscillations requires at least one non-zero neutrino mass. In the case of solar and atmospheric neutrinos, $\nu_e \to \nu_\mu$ and $\nu_\mu \to \nu_\tau$ are the dominant oscillation channels, respectively. The free parameters, difference of squared ν-masses Δm^2_{ij} and the mixing angles Θ_{ij}, have to be determined experimentally. The latest results for the squared mass differences obtained from oscillation experiments are [PDG08]

$$\Delta m^2_{12} = \Delta m^2_{\text{solar}} \approx 8.0\cdot 10^{-5}\ \text{eV}^2\text{c}^{-4}\,, \tag{1.13}$$

$$1.9\cdot 10^{-3}\ \text{eV}^2\text{c}^{-4} < \Delta m^2_{23} = \Delta m^2_{\text{atmos}} < 3.0\cdot 10^{-3}\ \text{eV}^2\text{c}^{-4}\,. \tag{1.14}$$

The absolute neutrino mass scale has to be determined in a different type of experiment. Until now, only upper limits for the neutrino mass eigenvalues are available, allowing for two mass scenarios as presented in fig. 1.2:

[4] U is unitarian with $U^\dagger_{j\alpha} = \left(U^*_{j\alpha}\right)^T = U^*_{\alpha j}$, where $U^*_{\alpha j}$ is the complex conjugate of $U_{\alpha j}$

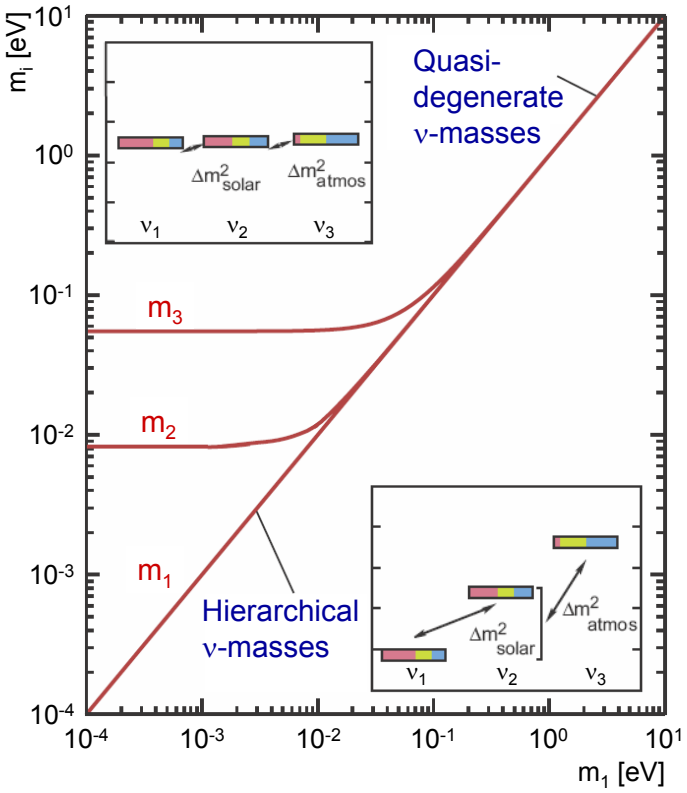

Figure 1.2: Neutrino mass hierarchy. Shown are the mass eigenvalues m_i with $(i = 1, 2, 3)$ as function of m_1. The mass differences are determined by solar ($\Delta m^2_{\text{solar}}$) and atmospheric ($\Delta m^2_{\text{atmos}}$) neutrino oscillation experiments. Two scenarios are possible: *Hierarchical neutrino masses* where the masses are small compared to the mass differences and *quasi-degenerate neutrino masses* where all masses are approximately equal. [KAT04]

- *Hierarchical neutrino masses*: The neutrino masses are small compared to the mass differences. This scheme could be of an *inverted hierarchy* type, too.
- *Quasi-degenerate neutrino masses*: All neutrinos have approximately the same mass; the fundamental mass scale is large compared to the mass differences.

3. How can the absolute mass scale be determined experimentally?

The absolute neutrino mass scale is accessible via various experiments, that can be subdivided into two groups:

- *Indirect methods* are model dependent, but generally feature a very high sensitivity to the neutrino mass.
- *Direct methods*, on the other hand, rely only on the relativistic energy-momentum relation

$$E^2 = m^2c^4 + p^2c^2 \tag{1.15}$$

with total energy E, rest mass m, velocity of light c and momentum p. Furthermore, the conservation of energy and momentum is presumed.

These methods are described in the following. More detailed introductions to neutrino mass searches are available in [Dre05, Ott08].

Indirect methods - $0\nu\beta\beta$: The first indirect method given here is the search for neutrinoless double beta decay ($0\nu\beta\beta$). The double beta decay is a rare process where two beta decays happen simultaneously in one nucleus. It is observed in ~ 30 isotopes for which the simple beta decay is energetically forbidden. In the neutrino afflicted double beta decay ($2\nu\beta\beta$) two neutrinos are emitted, thus no information on the neutrino mass can be extracted. For the neutrinoless double beta decay to happen, the neutrino has to be a *Majorana particle*[5]: An anti-neutrino, which is emitted at the first decay vertex as a right-handed particle, is reabsorbed in the second decay vertex as a left-handed neutrino. The helicity flip involved in this process additionally requires massive neutrinos since the flip is only possible if a reference system exists that moves at a higher velocity than the neutrino. $0\nu\beta\beta$ experiments are sensitive to the so-called *Majorana mass*

$$m_{ee} = \left| \sum_{j=1}^{3} U_{ej}^2 \cdot m_j \right| , \tag{1.16}$$

a coherent sum where annihilations are possible due to the matrix elements U_{ej} which are generally complex numbers [Sch05]. The signature of a $0\nu\beta\beta$ event is the emission of two electrons with a total energy equal to the total decay energy Q. The experimental observable, the half-life $T_{1/2}$ of this process, is connected to the Majorana mass by

$$\frac{1}{T_{1/2}} = G \cdot |M_{had}|^2 \cdot m_{ee}^2 \tag{1.17}$$

with the nuclear matrix element M_{had} and the phase space factor G.

The highest sensitivity on m_{ee} was achieved by the Heidelberg-Moscow-Experiment that investigates the decay of ^{76}Ge. An upper limit for the Majorana mass of

$$m_{ee} < 0.35 \text{ eV/c}^2 \tag{1.18}$$

was determined [Kla01]. Part of this collaboration later published a 4.2σ evidence for the $0\nu\beta\beta$ process and a Majorana neutrino mass of [Kla04]

$$m_{ee} = 0.44 \text{ eV/c}^2 . \tag{1.19}$$

Since this result is discussed in a highly controversial manner in the community, several new $0\nu\beta\beta$ experiments are under development for clarification, for example

[5]The fact that the neutrinos are electrically neutral raises the question whether they are their own anti-particles. In this case they are called *Majorana* neutrinos in contrast to *Dirac* neutrinos where particle and anti-particle are different.

GERDA [Sch05], Majorana [Aal02] and EXO [Dan00].

Indirect methods - Cosmology: Cosmological studies yield upper limits for the neutrino masses, too. As mentioned above, relic neutrinos play a significant role in the development of large scale structures in the universe. The cosmic microwave background radiation (CMBR) can be used to infer the existence of these neutrinos as well as to deduce their mass in cosmological parameter analyses. The CMBR was charted by the WMAP satellite [Hin08]. Its data can be used to extract an upper limit for the sum of the neutrino mass eigenvalues [Fuk06]:

$$\sum_{j=1}^{3} m_j < 2.0 \text{ eV/c}^2 \,. \tag{1.20}$$

When implementing additional model assumptions and information from other sources, for example structure investigations in the universe, more stringent results are possible. A recent investigation published

$$\sum_{j=1}^{3} m_j < 0.62 \text{ eV/c}^2 \,. \tag{1.21}$$

using data from supernovae type Ia and large scale structures disregarding Lyman-α data [Han06]. However, one should not forget that these results are highly model dependent. Results from a direct neutrino mass measurement could furthermore provide additional input data for these models.

Direct methods - Time of flight: The central idea of time of flight measurements is the following: If the neutrino has mass, its velocity is energy dependent. Neutrinos from a distant source, e.g. the supernova explosion SN1987A, will arrive on the earth at distance L at different times depending on the total energy. The neutrino mass can then be calculated according to

$$\Delta t_{obs} = t_{obs}(E_1) - t_{obs}(E_2) = \frac{L}{c} \frac{m_v^2 c^4}{2} \left(\frac{1}{E_1^2} - \frac{1}{E_2^2} \right) + \Delta t_0 \tag{1.22}$$

with the supernova model parameter Δt_0 that describes the energy dependent neutrino starting time difference. Thus, this method is not completely model independent although the time of flight principle itself is. From the 19 detected electron neutrinos from SN1987A an upper limit of

$$m_{\nu_e} < 5.7 \text{ eV/c}^2 \tag{1.23}$$

was derived for the electron neutrino mass [PDG08].

Direct methods - Kinematics of weak decays: The neutrino mass can be derived from the kinematics of weak decays. Most accessible is the so-called *effective neutrino mass*

$$m_{\nu_e} = \sqrt{\sum_{i=1}^{3} |U_{ei}|^2 m_i^2} \tag{1.24}$$

that can be determined from beta decay. The mass eigenstates m_j are then given by

$$m_j^2 = m_{\nu_e}^2 - \sum_{i=1}^{3} |U_{ei}|^2 \Delta m_{ij}^2 \qquad (j = 1, 2, 3) \tag{1.25}$$

using the squared mass differences Δm_{ij}^2 from neutrino oscillation experiments. In order to evaluate m_{ν_e}, the energy spectrum of beta decay electrons is measured near the energy endpoint E_0. As we shall see in sec. 2.1.1 the number of events with energies just slightly below E_0 is proportional to E_0^{-3}. Therefore, elements with low endpoint energies yield a relatively high number of events in the region of interest.

The beta-emitting element ^{187}Re which decays according to

$$^{187}\mathrm{Re} \;\rightarrow\; ^{187}\mathrm{Os} \;+\; \mathrm{e}^- \;+\; \overline{\nu}_\mathrm{e} \tag{1.26}$$

has the lowest endpoint energy of all beta emitters with $E \approx 2.46$ keV. However, the specific decay rate is very low and the nuclear matrix element of the transition from ^{187}Re to ^{187}Os is complicated. The main advantage here is that cryogenic bolometers can be used to detect the decay heat. The rhenium crystal is then beta emitter and detector at the same time. Up to now, the sensitivity of rhenium experiments is ~ 7 times worse than that of tritium decay experiments which are introduced in the next paragraph. The upper limit on the effective neutrino mass provided by the MIBETA experiment is [Sis04]

$$m_{\nu_e} < 15 \text{ eV/c}^2 \quad (90\% \text{ Confidence Level}) \,. \tag{1.27}$$

The future rhenium experiment MARE [Mon06] aims at a sensitivity of ~ 0.2 eV/c^2 on the effective neutrino mass within a time frame of ~ 10 years.

Until now, the highest sensitivity for the effective neutrino mass in a direct measurement was obtained in tritium beta decay experiments. In these experiments the energy spectrum of beta decay electrons of the decay

$$^3\mathrm{H} \;\rightarrow\; ^3\mathrm{He} \;+\; \mathrm{e}^- \;+\; \overline{\nu}_\mathrm{e} \tag{1.28}$$

is analyzed near its endpoint of ~ 18.6 keV. The technique of tritium beta decay experiments is introduced in detail in chapter 2. The limit obtained with this method up to now is [PDG08]

$$m_{\nu_e} < 2.0 \text{ eV/c}^2 \,. \tag{1.29}$$

The next generation tritium beta decay experiment KATRIN will improve this sensitivity by one order of magnitude. KATRIN will employ a very strong gaseous tritium source and a high sensitivity electromagnetic spectrometer for the analysis of beta decay electrons. A cryogenic pump is used in the so-called Cryogenic Pumping Section (CPS) to keep the spectrometer essentially free from tritium. In order to evaluate the pumping properties of such a cryo-pump for tritium, the test experiment TRAP was built.

In the framework of the present work, the TRAP setup was modified and upgraded for tritium operation, and long-term measurements with tritium were conducted. The results and experiences obtained at TRAP turned out to be imperative for the final specification of the CPS. This thesis is structured in the following way: After an introduction to tritium beta decay experiments in general and the KATRIN experiment in particular in chapter 2, the basic principles of cryo-sorption are presented in chapter 3. Chapter 4 describes the experimental setup of TRAP. The measurements conducted at TRAP and the results obtained are discussed chapter 5. During the operation of TRAP, an unforeseen tritium contamination occurred in the system. Several detritiation campaigns followed and a detritiation method for the CPS was developed as described in chapter 6. A summary of the final specification of the CPS focusing on the input from the TRAP experiment concludes this work with chapter 7.

Chapter 2

The Karlsruhe Tritium Neutrino Experiment

This chapter gives an overview of the motivation and experimental techniques of the Karlsruhe Tritium Neutrino (KATRIN) experiment, whose aim is the determination of the absolute neutrino mass scale with sub-eV sensitivity. Section 2.1 explains how the radioactive decay of tritium can be used for the determination of the neutrino mass. Furthermore, the standard setup of tritium beta decay experiments as well as the MAC-E-Filter, a high resolution electrostatic retarding spectrometer, are discussed. After summarizing the requirements for a next generation tritium beta decay experiment, the KATRIN experiment is presented in sec. 2.2.

2.1 Tritium beta decay experiments

The kinematic investigation of the weak decay of tritium

$$^3\mathrm{H} \;\rightarrow\; ^3\mathrm{He} \;+\; \mathrm{e}^- \;+\; \overline{\nu}_\mathrm{e} \tag{2.1}$$

is the most sensitive model independent way to investigate the neutrino mass scale relying only on the conservation of energy and momentum. For about 60 years now, the energy spectrum of tritium beta electrons has been investigated near its endpoint of ~ 18.6 keV to determine the *effective neutrino mass*

$$m_{\nu_e} = \sqrt{\sum_{i=1}^{3} |U_{ei}|^2 m_i^2} \tag{2.2}$$

using the notation introduced in chapter 1. Together with the results from neutrino oscillation experiments for the squared mass differences Δm_{ij}, all mass eigenvalues m_j can be derived according to

$$m_j^2 = m_{\nu_e}^2 - \sum_{i=1}^{3} |U_{ei}|^2 \Delta m_{ij}^2 \qquad (j = 1, 2, 3)\,. \tag{2.3}$$

2.1.1 Tritium beta spectrum and neutrino mass

The energy spectrum of beta electrons can be deduced theoretically from *Fermi's Golden Rule*[1]. Assuming a bare nucleus that decays weakly, one obtains [Wei03]:

$$\frac{d^2N}{dt\,dE} = C \cdot F \cdot p \cdot (E + m_e c^2)(E_0 - E)\sqrt{(E_0 - E)^2 - m_{\nu_e}^2 c^4} \cdot \Theta\,. \tag{2.4}$$

Herein, p, E and m_e are the momentum, the kinetic energy and the mass of the decay electron, respectively. $F = F(E, Z+1)$ is the Fermi function accounting for the Coulomb interaction of the outgoing electron with the daughter nucleus of proton number $Z+1$. It can be approximated by

$$F(E, Z+1) = \frac{2\pi\alpha(Z+1)/\beta}{1 - \exp[-2\pi\alpha(Z+1)/\beta]} \tag{2.5}$$

with the fine structure constant α and the relativistic electron velocity $\beta = v_e/c$. The step function $\Theta = \Theta(E_0 - E - m_{\nu_e}c^2)$ ensures energy conservation and C is given by

$$C = \frac{G_f^2}{2\pi^3\hbar^7 c^5} \cdot \cos^2\theta_C\,|M_{had}|^2 \tag{2.6}$$

with the Fermi constant G_f, the Cabibbo angle θ_C and the nuclear matrix element M_{had}. $E_0 \approx 18.6$ keV marks the endpoint of the β spectrum in case of zero neutrino mass and equals the total decay energy minus the recoil and vibrational energy of the daughter nucleus. Figure 2.1 shows a schematic electron spectrum from tritium beta decay.

When taking excitations of the electron shell into account, eq. 2.4 transfers to a sum of single spectra

$$\frac{d^2N}{dt\,dE} = \sum_i W_i \cdot \frac{d^2N_i}{dt\,dE} \tag{2.7}$$

with endpoint energies $E_{0,i} = E_0 - V_i$, where the associated electron excitation energy V_i is occupied with probability W_i.

Since $|M_{had}|^2$ and $F(E, Z+1)$ are independent of m_{ν_e}, the dependence of the spectral shape from m_{ν_e} is given by the phase space only. Furthermore, eq. 2.4 shows that $m_{\nu_e}^2$ is the experimental observable and that the influence of the neutrino mass is only significant at the very endpoint of the spectrum near E_0. This implies major experimental demands for tritium beta decay experiments with sub-eV sensitivity:

[1] According to Fermi's Golden Rule, the transition rate for a beta decay, where an electron with kinetic energy between E and $E + dE$ is emitted, is given by the transition matrix element M and the density of final states $\rho(E)$ [Wei03]:

$$\frac{d^2N}{dt\,dE} = \frac{2\pi}{\hbar}\,|M^2|\,\rho(E)\,.$$

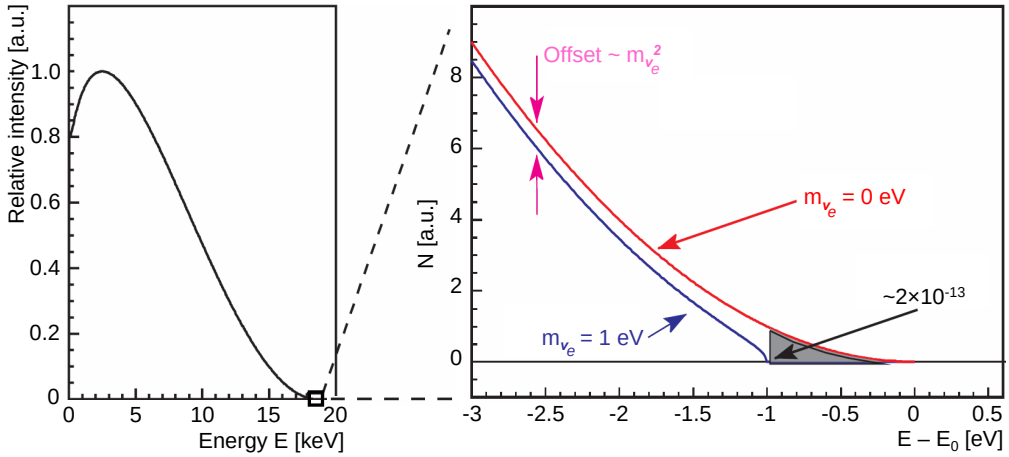

Figure 2.1: Schematic electron spectrum of tritium beta decay. Left: complete spectrum; right: endpoint region enlarged with two different spectra for two different neutrino masses. (based on [LoI01])

- A strong tritium source with high beta decay rate is needed for a sufficient count rate in the region just below the endpoint energy E_0. Only a fraction of $2 \cdot 10^{-13}$ of all tritium beta events are within 1 eV below E_0 (see fig. 2.1).
- The luminosity of the source, that is the product of its cross-section area and the accepted solid angle for decay electrons, must be large.
- A spectrometer with very high resolution and low background is required for the energy analysis of decay electrons.

Tritium has the following advantages over other beta emitters for neutrino mass investigations:

- Tritium has the second lowest total decay energy of all beta emitters. Only ^{187}Re with ~ 2.5 keV has a lower endpoint energy [Arn03]. Since the portion of decay electrons with energies just slightly below the endpoint energy E_0 is proportional to E_0^{-3}, the rate of those electrons is high for tritium compared to other beta emitters.
- Its short half life of 12.3 y corresponds to a high specific decay activity. Therefore, only a relatively small amount of source material is needed and the rate of inelastic scattering in the source is small.
- Tritium beta decay is a *superallowed* nuclear transition, the nuclear matrix element $|M_{had}|^2$ is therefore independent of E and no energy corrections have to be applied [Rob88].
- ^{3}H and its daughter, the ^{3}He$^+$ ion, have a simple electron shell configuration where the excitation energies and probabilities can be calculated precisely (e.g. for molecular tritium decay $T_2 \rightarrow HeT^+ + e^- + \overline{\nu}_e$ in [Sae00]).

- The cross section for inelastic scattering is relatively low for tritium compared to other elements due to the low charge number ($Z = 1$).

A long series of tritium beta decay experiments has been conducted in the past. Figure 2.2 summarizes some of the results obtained during the last two decades. It is striking that the error bars on the experimental observable $m^2_{\nu_e}$ have been decreased by two orders of magnitude from the earlier experiments of this kind to the very latest in Mainz and Troitsk. This was only made possible by turning away from magnetic spectrometers and using a new type of electrostatic retarding spectrometer, the MAC-E-Filter (see sec. 2.1.2). Equally important is the fact that the problem of negative $m^2_{\nu_e}$ could be solved by a better understanding of systematic effects and by improving the experimental setups.

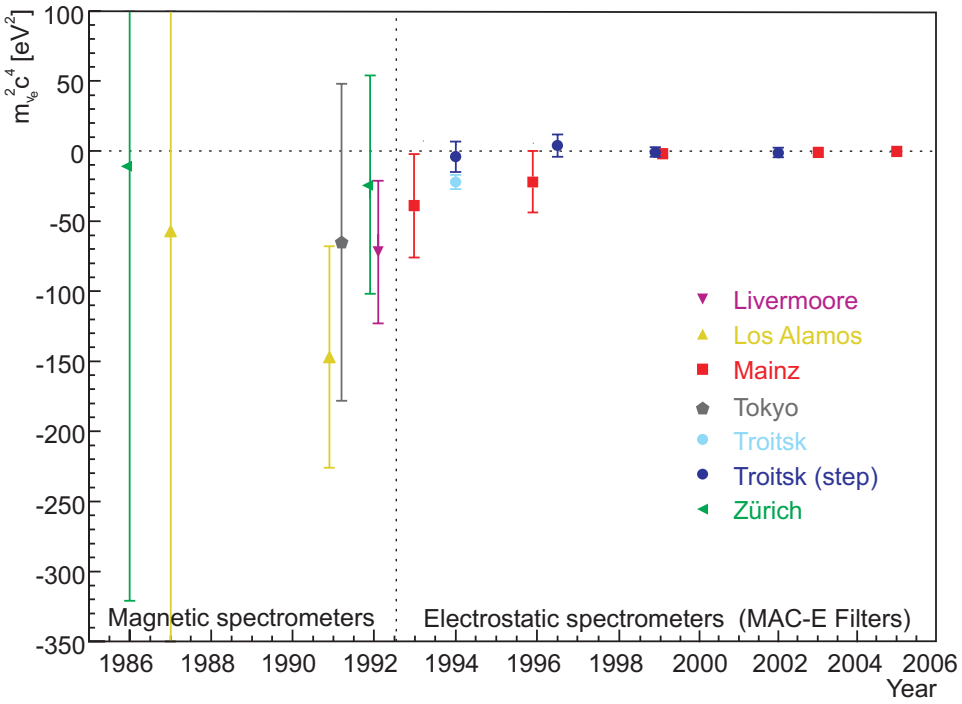

Figure 2.2: History of tritium beta decay experiments. Shown are selected results for the observable $m^2_{\nu_e} c^4$ of past tritium beta decay experiments. The newest two experiments in Mainz and Troitsk used MAC-E-Filters and solved the problem of negative mass-squares by a better understanding of systematic effects.

2.1.2 Standard setup and MAC-E-Filter

Since the end of the 1950s, a standard setup for tritium beta decay experiments has evolved with the following main components:

- **Tritium source:** The tritium source contains tritium and provides the beta decay electrons used in the analysis of the neutrino mass. The main require-

ments are a high luminosity and a very good understanding of systematic effects which might influence the shape of the electron energy spectrum.

- **Transport system:** The transport system guides the decay electrons from the source to the spectrometer without altering their energy. Furthermore, any tritium flow rate from the source to the spectrometer needs to be suppressed in order to keep the spectrometer essentially free from tritium.
- **Spectrometer:** The spectrometer filters the decay electrons from the source according to their energy. The spectrometer features a high energy resolution and low (electron) background.
- **Detector:** The detector counts the electrons that passed the spectrometer.

The high sensitivity of the tritium beta decay experiments in Mainz and Troitsk would not have been reached if not a new type of spectrometer had been introduced: the MAC-E-Filter (Magnetic Adiabatic Collimation combined with an Electrostatic filter). These spectrometers feature a large accepted solid angle, high energy resolution and low background [Lob85, Bac88, Bon99].

Figure 2.3 shows the principle of the MAC-E-Filter. Two superconducting solenoids at each end of the spectrometer create a strong inhomogeneous magnetic guiding field for the decay electrons. The magnetic field strength drops from the bore of the solenoids to the middle plane, called analyzing plane, by many orders of magnitude. Decay electrons starting from the tritium source at the left are guided along the magnetic field lines on cyclotron tracks to the detector on the right with an accepted solid angle of up to 2π. Due to the magnetic gradient force in an inhomogeneous magnetic field, the electrons' cyclotron energy $E_\perp$ is transferred *adiabatically* to longitudinal energy $E_\parallel$. Adiabatic means that the magnetic field changes only slightly during one cyclotron circulation of the electrons, that is the electrons' magnetic moment $\mu = E_\perp / B$ remains constant [Jac99]. As indicated by the momentum vectors in fig. 2.3, the beam of electrons in the analyzing plane will be almost parallel.

A strong electrostatic field is applied inside the spectrometer vessel by means of ring or wire electrodes set on high voltage. The electric field created in that way retards electrons on the left side and repels those with insufficient energy to overcome the potential barrier. On the right side, the electrons are re-accelerated to the original energy before hitting the detector. Thus, the spectrometer works as an integrating high-pass filter, whereas the detector counts the electrons that passed the retarding potential. The relative sharpness $\Delta E/E$ of a MAC-E-Filter is given by the ratio of the minimum magnetic field B_{min} in the analyzing plane and the maximum magnetic field B_{max} in the beamline of the whole experimental setup:

$$\frac{\Delta E}{E} = \frac{B_{min}}{B_{max}} \,. \tag{2.8}$$

The tritium beta spectrum is analyzed by changing the relative electrostatic potential between the tritium source and the MAC-E-Filter stepwise. At each voltage setting, the detector counts the number of electrons reaching the detector.

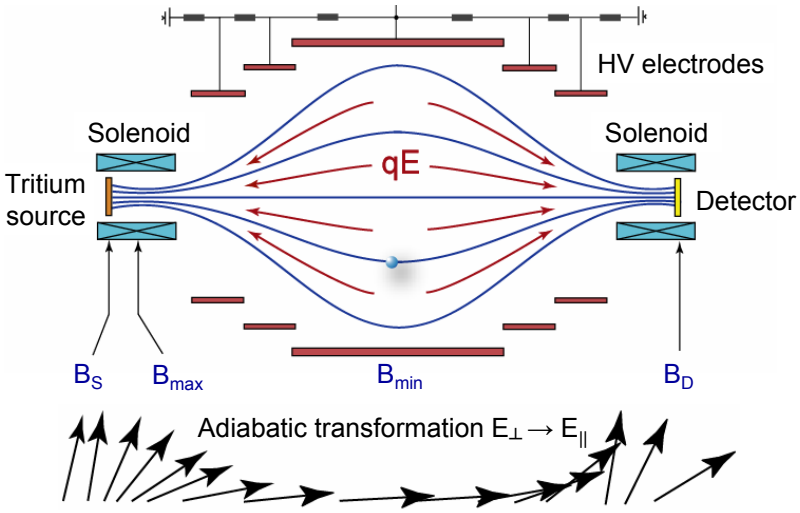

Figure 2.3: Principle of the MAC-E filter. Electrons from the source are guided through the spectrometer on cyclotron tracks along the magnetic field lines. Since the magnetic field drops by several orders of magnitude along the way, cyclotron energy is transferred to energy in longitudinal motion (indicated by momentum vectors). In the central analyzing plane, the electron beam is almost parallel and an electrostatic retarding potential can be used for analyzing the energy of the decay electrons.

2.1.3 Current neutrino mass limits and requirements for a next generation beta decay experiment

The latest tritium beta decay experiments in Mainz [Pic92, Wei93] and Troitsk [Lob85, Bel95] both employ MAC-E-Filters as spectrometers but different tritium sources with different systematic effects. The Mainz experiment, which uses a quench condensed krypton source, published [Kra05]

$$m^2_{\nu_e} = (-0.6 \pm 2.2_{\mathrm{stat}} \pm 2.1_{\mathrm{sys}})\ \mathrm{eV}^2/\mathrm{c}^4 \tag{2.9}$$

corresponding to an upper limit for the effective neutrino mass of

$$m_{\nu_e} < 2.3\ \mathrm{eV}/\mathrm{c}^2 \quad (95\%\ \text{Confidence Level})\,. \tag{2.10}$$

The Troitsk experiment, using a gaseous molecular tritium source, obtained [Lob99]

$$m^2_{\nu_e} = (-1.9 \pm 3.4_{\mathrm{stat}} \pm 2.2_{\mathrm{sys}})\ \mathrm{eV}^2/\mathrm{c}^4 \tag{2.11}$$

under empiric consideration of a step function with two additional fit parameters[2]. They published an upper limit of

$$m_{\nu_e} < 2.5\ \mathrm{eV}/\mathrm{c}^2 \quad (95\%\ \text{Confidence Level})\,. \tag{2.12}$$

[2] New limits for the neutrino mass from the Troitsk experiment were published in 2003 [Lob03]:

$$m^2_{\nu_e} = (-2.3 \pm 2.5_{\mathrm{stat}} \pm 2.0_{\mathrm{sys}})\ \mathrm{eV}^2/\mathrm{c}^4 \ \Rightarrow m_{\nu_e} < 2.05\ \mathrm{eV}/\mathrm{c}^2 \quad (95\%\ \text{Confidence Level})\,.$$

However, this result was not published as a regular journal paper and is not considered by the Particle Data Group [PDG08].

The results from both experiments, eqs. 2.10 and 2.12, were used by the Particle Data Group for a combined analysis which led to an upper limit for the neutrino mass of [PDG08]

$$m_{\nu_e} < 2.0 \text{ eV/c}^2 \,. \tag{2.13}$$

The experiments in Mainz and Troitsk have reached their respective sensitivity limits since the systematic uncertainties cannot be reduced further. A new generation of tritium beta decay experiments is required to reach a sensitivity in the cosmologically relevant sub-eV regime. The aim is to improve the sensitivity for m_{ν_e} by one order of magnitude, which is equivalent to an improvement of the sensitivity on the observable $m^2_{\nu_e}$ by two orders of magnitude. Compared with the current experiments, a next generation tritium beta decay experiment therefore requires:

- **a higher tritium source strength** ($\sim$ factor 80): Since the energy interval of interest below the beta decay endpoint rapidly decreases with smaller neutrino masses, the signal rate has to be increased in order to maintain a sufficient count rate on the detector. This can be accomplished by a larger source cross-section and an increased tritium column density in the source.
- **a larger analyzing plane in the spectrometer** ($\sim$ factor 10): Because of magnetic flux conservation ($\Phi = B \cdot A = const$), any increase in the source cross-section leads to an increase of the analyzing plane area. The same is true for any decrease of $\Delta E/E$ according to eq. 2.8.
- **a better energy resolution** of $\Delta E \approx 1$ eV in the spectrometer ($\sim$ factor 4)
- **a reduction of systematic uncertainties** ($\sim$ factor 100)
- **an increased measurement time** ($\sim$ factor 10) for decreasing statistical errors

2.2 The KATRIN experiment

The Karlsruhe Tritium Neutrino (KATRIN) Experiment is the next generation tritium beta decay experiment whose aim is the determination of the effective neutrino mass with a sensitivity of

$$m_{\nu_e} < 0.2 \text{ eV/c}^2 \quad (90\% \text{ Confidence Level}) \tag{2.14}$$

for a vanishing neutrino mass signal. The discovery potential for a neutrino mass of 0.35 eV/c^2, for example, will be 5σ according to the reference design [KAT04].

2.2.1 General overview

The KATRIN experiment is being built and will be operated on site of the Forschungszentrum Karlsruhe (FZK) by an international collaboration that includes

most of the expertise on tritium beta decay experiments worldwide. The tritium source of KATRIN (see sec. 2.2.2) as well as the transport system (sec. 2.2.4) will be located inside the existing Tritium Laboratory Karlsruhe (TLK), which is licensed to handle the required amount of tritium and has a closed tritium loop for purification of tritium [TLK05, TLK08].

Figure 2.4 shows an overview of the KATRIN beamline, which follows the standard setup of tritium beta decay experiments introduced in sec. 2.1.2. KATRIN consists of a strong gaseous tritium source, the magnetic transport system, a tandem of two spectrometers of MAC-E type and the electron detector at the very end of the 70 m beamline. A detailed description of the KATRIN experiment is available in [KAT04]. In the following, only the most important aspects of the KATRIN setup will be highlighted with emphasis on the necessary tritium flow rate suppression in the transport system.

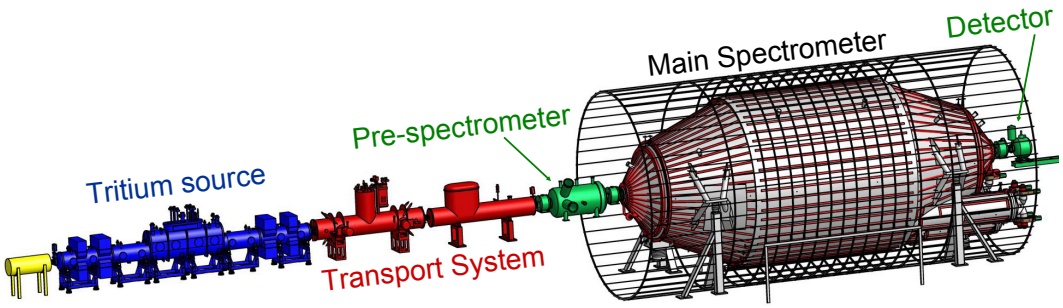

Figure 2.4: Overview of the beamline of the KATRIN experiment. The beta decay electrons from the tritium source are guided adiabatically via superconducting solenoids along the Transport System into the spectrometers. The main energy analysis is being performed in the Main Spectrometer, an electrostatic retarding spectrometer of MAC-E type (see sec. 2.1.2). The detector at the very end of the beamline counts the electrons with energies high enough to pass the spectrometers. (based on [Leu07])

2.2.2 Tritium source

The tritium source of KATRIN is an ultra-luminous Windowless Gaseous Tritium Source (WGTS) that delivers $\sim 10^{10}$ beta electrons per second for analysis in the spectrometers[3]. The WGTS consists of a 10 m long tube of 90 mm diameter filled with gaseous molecular tritium. The tritium is injected in the middle of this tube and pumped out at its ends with turbomolecular pumps providing a source profile as depicted schematically in fig. 2.5. The tube is embedded in a series of superconducting solenoids which create a maximum magnetic field strength of 3.6 T inside the beamline for transportation of the decay electrons.

[3]The total tritium activity in the source is $> 10^{11}$ Bq. However, only electrons which are emitted in the transported magnetic flux tube of 191 Tcm^2 in forward direction with an angle $< 51^\circ$ with respect to the magnetic field lines are analyzed in the spectrometers and may finally reach the detector.

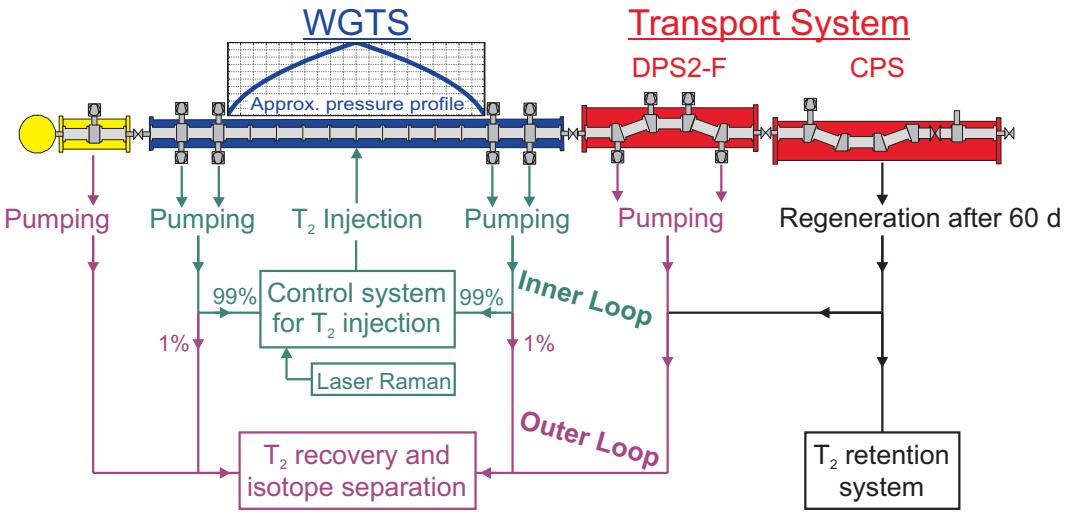

Figure 2.5: The tritium source of KATRIN is operated in closed loops in order to achieve both the stabilized tritium injection rate and the purity. Tritium is injected in the middle of the WGTS tube (Windowless Gaseous Tritium Source) and pumped out at its ends. 99% of the tritium is re-transferred to the control system for T_2 injection (Inner Loop), 1% is redirected into the laboratory's tritium recovery and isotope separation system for purification (Outer Loop). Tritium from the Transport System (see sec 2.2.4) is transferred to the Outer Loop and the laboratory's tritium retention system.

The main task of the WGTS is to provide a stable and energetically undisturbed beta rate. Systematic investigations yield an optimum tritium column density of $\rho d = 5 \cdot 10^{17}$ molecules/cm^2, where the tritium beta decay rate is high, yet the probability for inelastic scattering relatively low. The column density must be kept stable on a 0.1% level during each runtime period of $\sim$ 60 d with $3 - 5$ runs per year. Since ρd is directly connected to the tritium purity in the source, the WGTS temperature and the tritium injection rate, stringent requirements exist on these parameters, too:

- The tritium injection rate of 1.8 mbar l/s or 40 g/d must be stabilized on an 0.1% level. The stabilization is provided in the so-called *Inner Loop* (fig. 2.5), where the tritium gas is injected into the middle of the WGTS from a pressure stabilized buffer vessel via a capillary of stabilized gas conductance [Stu10].

- The tritium purity in the source must be above 95%. The purity is ensured in the so-called *Outer Loop* (fig. 2.5), which consists mainly of infrastructure facilities of the TLK like, for example, the Isotope Separation System. 1% of the gas flow from the Inner Loop is redirected to the Outer Loop for purification. The tritium purity is monitored in real time via Raman spectroscopy [Sch09].

- The source temperature of 27 K must be kept homogeneous along the WGTS tube and stable in time, both on an 0.1% level. The temperature of 27 K lowers

the gas conductance of the WGTS tube, therefore decreasing the necessary tritium injection rate to maintain the column density. Furthermore, Doppler broadening is suppressed. The solution for the stabilized temperature of the source tube is that of forced flow cooling by two-phase neon in two copper tubes which are brazed along the WGTS tube.

In order to test the feasibility of the stabilized tritium injection, the test experiment TILO (Test of Inner Loop) was built by TLK and the Institute for Nuclear Physics (Institut für Kernphysik, IK) of FZK. It was operated with deuterium and helium at 77 and 300 K and confirmed the principle of using a pressure stabilized vessel for injection [Kaz08]. Furthermore, in-line Raman spectroscopy on flowing hydrogen isotopes was examined at TILO [Lew07].

2.2.3 Energy analysis and electron detection

2.2.3.1 Spectrometer tandem

For energy analysis, KATRIN uses two spectrometers, the smaller Pre-spectrometer working as a pre-filter for the larger Main Spectrometer. Both feature the same underlying principles (refer to fig. 2.6):

- Both spectrometers are of MAC-E type (see sec. 2.1.2) sharing one superconducting solenoid.

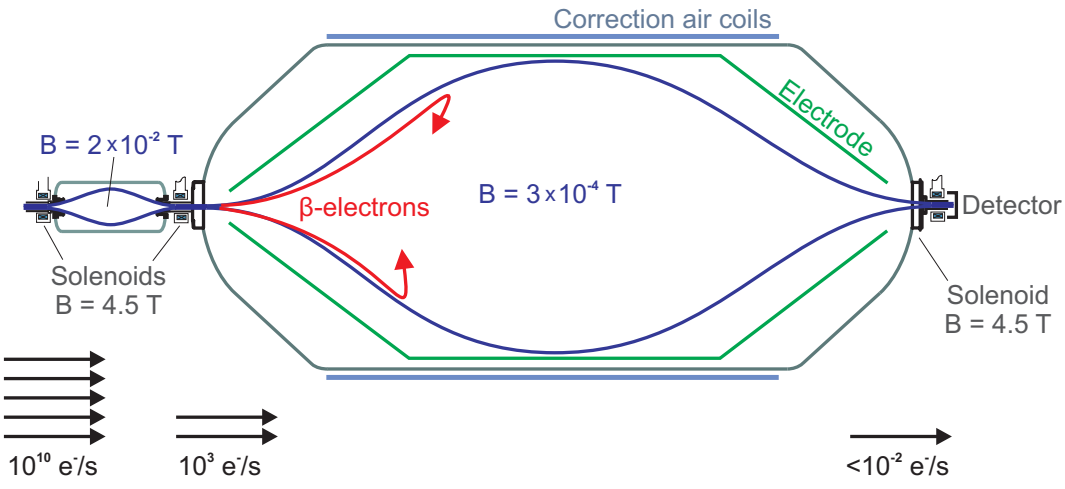

Figure 2.6: Schematic of the spectrometers of KATRIN. The smaller Pre-spectrometer operates as a pre-filter for the larger Main Spectrometer, suppressing the electron rate by 7 orders of magnitude from $\sim 10^{10}$ e^-/s to 10^3 e^-/s. The Main Spectrometer analyzes the electron energy and further reduces the electron rate to $< 10^{-2}$ e^-/s at the detector. Air coils are employed to compensate the terrestrial magnetic field in the analyzing plane, where the magnetic field strength is only $3{\cdot}10^{-4}$ T.

- In order to minimize background events from ionization of the residual gas, both vessels are operated at ultra-high vacuum (UHV) conditions (pressure below 10^{-11} mbar).
- A stable retarding potential relative to the ground potential is applied to wire electrodes inside the spectrometer vessels. The beta spectrum is scanned by varying the electric potential on the WGTS between -20 and -1000 V. Therefore, a ceramic insulator is necessary in the beamline. It will be inserted in the Transport System in-between the DPS2-F and the CPS (see fig. 2.5).
- The outer walls of the spectrometers are also on high (negative) potential for electromagnetic shielding. Furthermore, electrons released from the walls of the spectrometers by cosmic rays are rejected by the slightly higher (negative) potential of the wire electrodes ($100 - 200$ V).

Yet, the two spectrometers strongly differ in dimension and purpose: The Pre-spectrometer works as a pre-filter for the Main Spectrometer at a relative voltage of -18.3 kV to the WGTS. It rejects all decay electrons except those near the endpoint E_0 of the spectrum (electron rate reduction factor $\sim 10^7$). This strongly minimizes background in the Main Spectrometer due to ionization of the residual gas. The Pre-spectrometer itself is a stainless steel UHV recipient of 3.4 m length and 1.7 m diameter [Hab09].

The energy analysis of the electrons is performed in the Main Spectrometer of ~ 24 m length and 10 m diameter (see fig. 2.7). The retarding potential relative to the WGTS can be varied between -18.5 and -18.7 kV for scanning of the spectrum. With a maximum magnetic field of 6 T in the KATRIN beamline and a minimum field of $3 \cdot 10^{-4}$ T in the analyzing plane of the Main Spectrometer, the energy resolution (0% to 100% transmission) is

$$\Delta E = 0.93 \text{ eV} \tag{2.15}$$

at 18.6 kV according to eq. 2.8. Air coils arranged around the main spectrometer vessel allow to compensate the terrestrial magnetic field [Val09].

It is imperative for KATRIN to keep the spectrometers essentially free from tritium. Beta electrons from tritium decaying in the spectrometers can create secondary, low energy electrons by shake off and ionization of the residual gas. If those enter the transported magnetic flux and are guided onto the detector, they increase the background in the energy region of interest below the endpoint E_0. In order to keep the background contribution due to tritium penetration into the spectrometers below 1 mHz, the maximum tritium flow rate into the Pre-spectrometer must be kept below 10^{-14} mbar l/s [KAT04]. With a hydrogen pumping speed of $\sim 10^4$ l/s in the Pre-spectrometer and $\sim 5 \cdot 10^5$ l/s in the Main Spectrometer, the worst case tritium pressures are about 10^{-18} mbar and 10^{-20} mbar, respectively [KAT04]. More details on the tritium flow rate suppression can be found in sec. 2.2.4.

Figure 2.7: The inside of the Main Spectrometer vessel. The photo shows the inside of the Main Spectrometer vessel during construction of the scaffolding that is needed for mounting of the inner wire electrodes.

2.2.3.2 Focal Plane Detector

The Focal Plane Detector at the very end of the beamline should not only detect all electrons, that passed the retarding potentials, but also enable systematic investigations. This leads to the following requirements:

- a high electron detection efficiency ($> 90\%$)
- the ability to process high signal rates ($\sim$ 1 MHz) for calibration measurements with sources like ^{83m}Kr
- a good positional resolution for monitoring the radial source density and the electron transport properties of the spectrometers
- a high background suppression ($<$ 1 mHz), which requires active and passive shielding as well as a good energy resolution ($<$ 600 eV FWHM, Full Width Half Maximum) to suppress background events at different energies
- a good time resolution ($<$ 100 ns) to enable time-of-flight measurements

The Focal Plane Detector is jointly being developed by the Massachusetts Institute of Technology, Massachusetts (USA), the University of Washington, Seattle (USA), and FZK. The detector will be a segmented PIN diode of $\sim$ 90 mm sensitive diameter. The detector segments are arranged in a dartboard design with 12 rings, each ring featuring 12 segments. Adding the 4 segments in the center, this amounts to a total number of 148 pixels, each with a surface area of $\sim$ 42 mm^2. Figure 2.8 shows a prototype of the detector that will be tested in the near future.

Figure 2.8: Prototype of the Focal Plane Detector. [Doe08]

2.2.4 Transport system

The task of the Transport System is twofold:

- At first, decay electrons from the source must be transported adiabatically on cyclotron tracks along the magnetic field lines to the Pre-spectrometer.
- Secondly, the tritium flow rate must be suppressed from $\sim 10^{-3}$ mbar l/s at the exit of the WGTS to $< 10^{-14}$ mbar l/s at the entrance of the Pre-spectrometer as indicated in fig. 2.9.

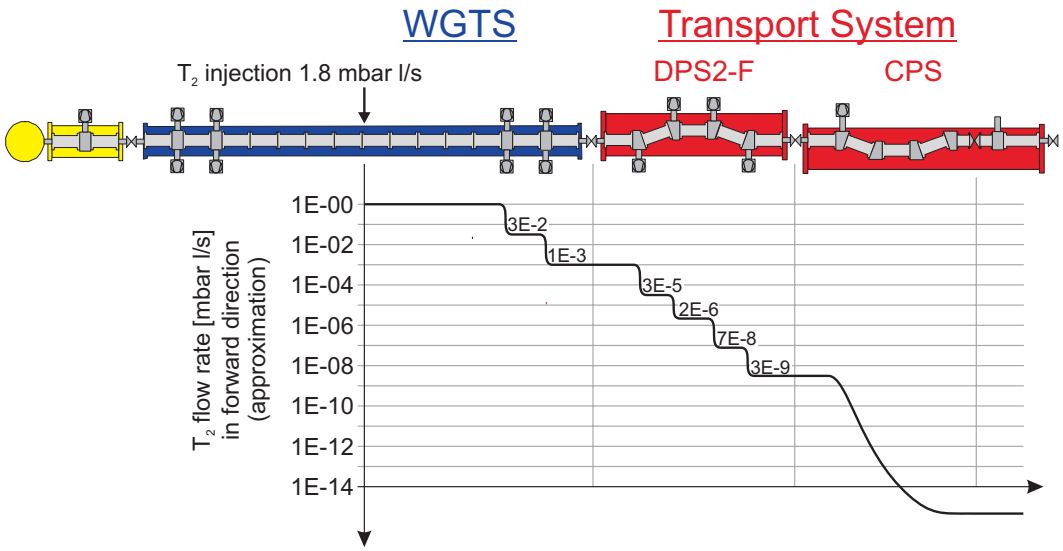

Figure 2.9: Tritium flow rate suppression in KATRIN. Since tritium in the spectrometers will increase the experiment's background, the maximum allowed tritium flow rate into the spectrometers is 10^{-14} mbar l/s. Therefore, the tritium flow rate has to be suppressed by more than 14 orders of magnitude from the injection point in the middle of the WGTS to the entrance of the Pre-spectrometer. A first reduction in the order of $10^7 - 10^8$ is achieved by differential pumping with turbomolecular pumps in the WGTS and DPS2-F. The remaining reduction factor is achieved via cryo-sorption in the CPS. The indicated flow rate values were obtained from Monte Carlo simulations [Luo05, Luo04]; the run of the curve for the flow rate in the CPS is a rough approximation.

The Transport System consists of two main components: the Differential Pumping Section (DPS2-F, refer to sec. 2.2.4.1) and the Cryogenic Pumping Section (CPS, sec. 2.2.4.2). Both feature a maximum magnetic guiding field of 5.6 T generated by superconducting solenoids at liquid helium temperature.

2.2.4.1 Differential Pumping Section (DPS2-F)

The Differential Pumping Section DPS2-F suppresses the tritium flow rate toward the spectrometers by differential pumping with turbomolecular pumps. Figure 2.10 shows a schematic of the DPS2-F. It consists of five tubes of 1 m length and 90 mm diameter which are kept at 77 K in order to reduce their vacuum conductance. They are tiled by 20° with regard to each other in order to prevent beaming effects of molecular flow, and intersected by four pump ports of 2000 l/s conductance each, where turbomolecular pumps are attached. Monte Carlo simulations predict that this configuration will reduce the tritium flow rate toward the spectrometers by approximately 5 orders of magnitude from $\sim 10^{-3}$ mbar l/s to $\sim 3 \cdot 10^{-9}$ mbar l/s [Luo04]. For safety reasons, however, 10^{-7} mbar l/s is considered to be the tritium flow rate which enters the CPS and needs to be suppressed there [KAT04].

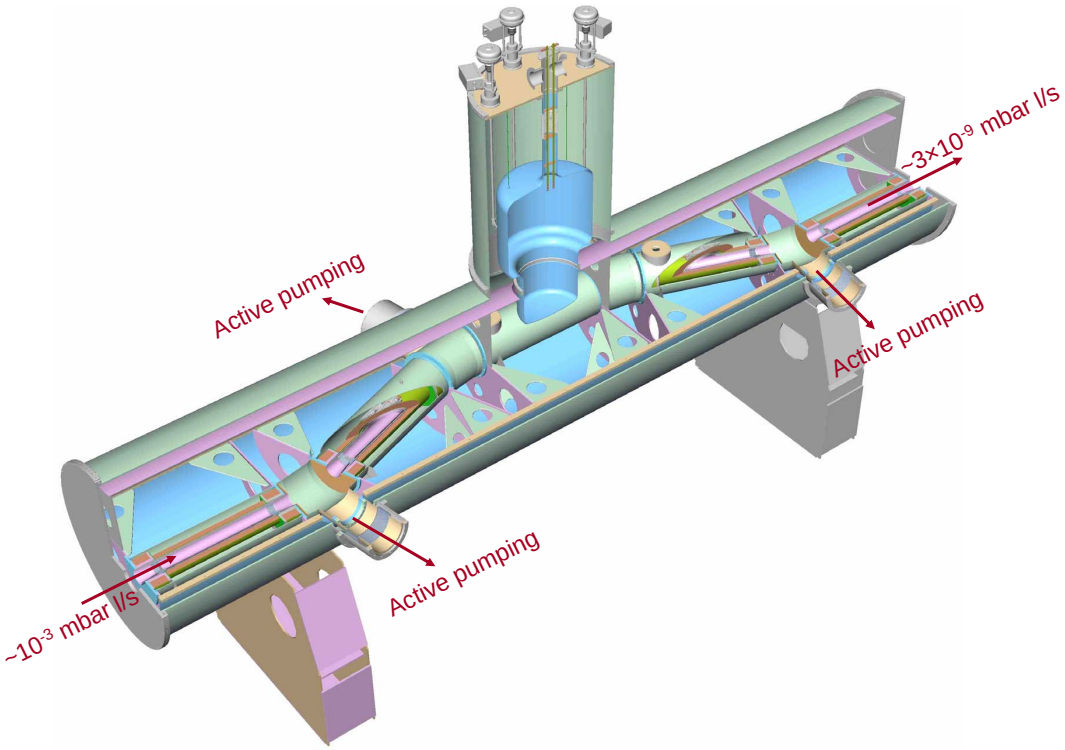

Figure 2.10: Schematic of the Differential Pumping Section DPS2-F. The DPS2-F employs the principle of differential pumping in order to suppress the tritium flow rate in the direction of the beamline. The beamline's vacuum conductance is decreased by keeping the tubes at ~ 77 K, whereas the pumping ports avail a pumping speed of 2000 l/s. Strong superconducting solenoids set up a maximum magnetic field of 5.6 T for guiding the decay electrons. (based on [KAT04])

Ions like T^+, T_3^+, DT_2^+ or $^3He^+$ are continuously produced in the WGTS by tritium decay and ionization processes. As charged particles of low energy, they could be guided along the magnetic field lines into the Pre-spectrometer past the pump ports of the DPS2-F. In order to eliminate this additional tritium flow of charged particles, electric dipoles are foreseen in the DPS2-F which deflect the ions to the walls of the beamline where they will be neutralized. Furthermore, Fourier-Transform Ion Cyclotron Resonance (FT-ICR) can be used to monitor the ion density and composition at the entrance and exit of the DPS2-F [Sta04].

2.2.4.2 Cryogenic Pumping Section (CPS)

A further reduction of the tritium flow rate with mechanical transport pumps is not possible due to the pumps' capture factor and back-diffusion inside the turbomolecular pumps. Since the tritium flow rate from the DPS2-F toward the spectrometers will be $< 10^{-7}$ mbar l/s, the integral amount of tritium leaving the DPS2-F during one measurement campaign of ~ 60 days will only be ~ 0.5 cm^3.

Therefore, a sorption pump integrated into the beam tube is considered as the next pumping unit, which means that the beam tube itself is operated as a cryo-surface for pumping tritium. The main requirements for this pump are a high pumping speed for tritium per surface area and a long term tritium retention at operation conditions resulting in a tritium flow rate suppression of $> 10^7$ [KAT04]. Additionally, it should allow for an easy and complete removal of the tritium at stand-by conditions (regeneration). A cryo-sorption pump with pre-condensed argon as adsorbent at $3 - 4.5$ K (see fig. 2.11) turns out to be the ideal choice for pumping tritium in the CPS as discussed in sec. 3.1.2.

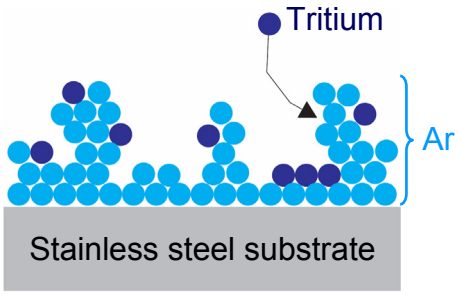

Figure 2.11: Schematic of tritium pumping on pre-condensed argon. The CPS employs cryo-sorption of tritium on pre-condensed argon.

In order to test such a cryo-pump with pre-condensed argon as adsorbent for pumping tritium in the very low pressure and flow rate regime required for the Pre-spectrometer, the test experiment TRAP has been built at TLK. This rig is not only used to measure the tritium retention factor of a CPS-like cryo-pump, but also to obtain input data for the specification of the CPS. In this thesis the mechanism of cryo-sorption of tritium on pre-condensed argon is investigated theoretically and experimentally leading to the specification of the CPS [CPS08a] that is summarized in the following. An explanation for the different design choices is available in sec. 7.2.

According to the specification [CPS08a], the CPS will consist of two parts, the upstream CPS1-F and the downstream CPS2-F (see fig. 2.12). The CPS1-F is a cryo-pump at $3 - 4.5$ K with pre-condensed argon as adsorbent and will pump the major part of tritium during standard operation. It consists of tube sections that are tilted by 15° with respect to each other in order to prevent beaming effects of molecular flow. The different sections of the CPS1-F are:

- **Section 1:** This section at 77 K is 655 mm long and has a diameter of $148 - 152$ mm. A black coated ringlike insert with a high thermal absorption coefficient (> 0.9) shields the following $3 - 4.5$ K sections from thermal irradiation from the DPS2-F. The insert can be exchanged for an alternative solid tritium source (condensed tritium source).

- **Port 1:** This port features a DN160 CF and three DN40 CF flanges for connection of vacuum pumps and sensors.

- **Sections 2-4:** These tube sections of $\sim$ 1100 mm length each are kept at $3 - 4.5$ K coated with pre-condensed argon during standard operation. In order to increase the adsorption surface, these tubes feature fins as depicted in fig. 2.13. The remaining free inner diameter is $\sim$ 75 mm. The argon condensate is prepared by injection of gaseous argon through three perforated capillaries

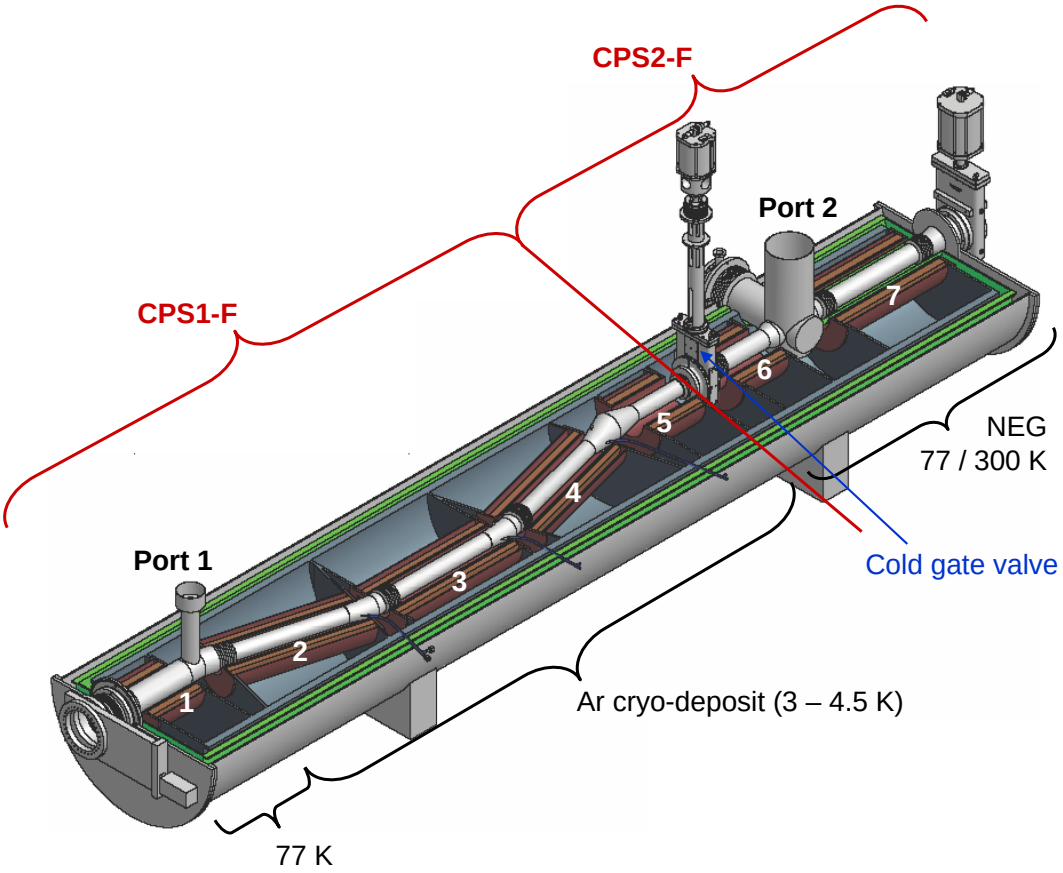

Figure 2.12: Schematic of the Cryogenic Pumping Section. The CPS consist of two parts: the CPS1-F, where the major part of tritium is pumped by cryo-sorption on pre-condensed argon at $3 - 4.5$ K and the CPS2-F where both, residual tritium from the CPS1-F and residual hydrogen from the Pre-spectrometer, are pumped by non-evaporable getter (NEG) strips. The CPS1-F and CPS2-F are separated by a cold gate valve. Strong superconducting solenoids around the beamline set up a maximum magnetic field of 5.6 T for guiding the decay electrons. (based on [CPS08a])

placed along the tubes. The temperature of the walls is kept at 6 K during argon preparation.

- **Section 5:** This shorter section of 688 mm length corresponds to sections 2-4, yet does not feature argon injection capillaries.

In the CPS2-F non-evaporable getter (NEG) strips will be used to pump traces of tritium from the CPS1-F as well as residual hydrogen from the Pre-spectrometer. Furthermore, the CPS2-F will function as a backup pump in case of failures in the cooling system of the CPS1-F to provide enough pumping speed until the gate valve in front of the Pre-spectrometer is closed. The CPS2-F consists of:

- **Section 6:** This section of 734 mm length and $112 - 114$ mm diameter at 77 K houses cartridges with NEG strips.

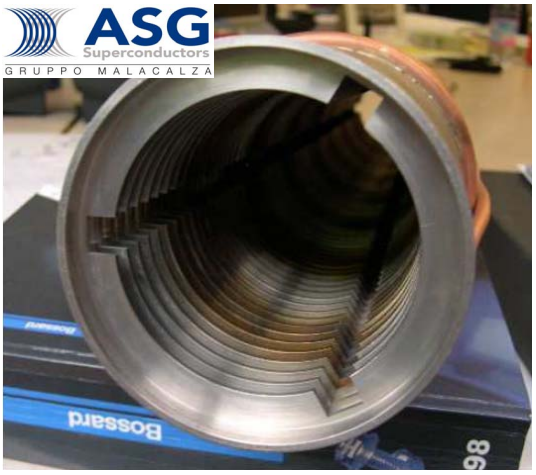

Figure 2.13: Test piece of the CPS1-F beamline. The fins were manufactured by milling and the 3 grooves along the beamline, where the argon injection capillaries will be placed, by spark erosion. [CPS08b]

- **Port 2:** This port features a DN250 CF and a DN200 CF flange for access of a ^{83m}Kr calibration source and a monitor detector for monitoring the source parameters. The large ducts are furthermore needed for access to the NEG cartridges.
- **Section 7:** The last section of ~ 1274 mm length and $112-114$ mm diameter at 300 K houses cartridges with NEG strips. During calibration measurements with the ^{83m}Kr source, this section will be operated at 77 K.

Both parts, the CPS1-F and the CPS2-F, are separated by a cold gate valve of 150 mm inner diameter at ~ 4.5 K that allows for an independent regeneration of the components. In order to facilitate any unforeseen decontamination procedures of the CPS, the complete beamline will be gold plated. A magnetic guiding field of 5.6 T maximum field strength is applied along the beamline for electron transportation.

The tender for the construction of the CPS was won by *ASG Superconductors S.p.A., Malacalza Group*. The technical design report for the CPS [CPS08b] is now finished and construction may start. The delivery of the CPS is expected for 2010.

Chapter 3

Cryo-Sorption on Pre-Condensed Gases

This chapter describes the important aspects of cryo-sorption with regard to the Cryogenic Pumping Section of KATRIN (chapter 2) and the test experiment TRAP (chapter 4). Section 3.1 summarizes the requirements for the CPS and demonstrates why a cryo-sorption pump with pre-condensed argon as *adsorbent*, that is the substrate on which the gas molecules are bound, was chosen for KATRIN. Section 3.2 presents the basic mechanisms of cryo-sorption, whereas the influence of various parameters on the pumping performance is discussed in sec. 3.3. Finally, some relevant data for cryo-sorption of hydrogen on pre-condensed argon is addressed in sec. 3.4.

3.1 The Cryogenic Pumping Section of KATRIN

3.1.1 Requirements for the CPS

The Cryogenic Pumping Section (CPS) is the final pumping stage in front of the spectrometers. Since basically no tritium is allowed in the spectrometers (tritium partial pressure in the Pre-spectrometer $< 10^{-18}$ mbar), special care has to be taken when specifying the CPS. The main requirements are

- a high pumping speed for tritium per unit surface (specific pumping speed),
- a long term tritium retention at operation conditions and
- an easy and complete removal of the tritium at stand-by conditions (regeneration).

The tritium retention efficiency of a sorption pump can be estimated using the so-called *mean sojourn time*, which describes the time period after which a previously

adsorbed gas particle is again desorbed [Hae81]:

$$t_s = t_0 \cdot \exp\left(\frac{E_B}{RT_c}\right), \tag{3.1}$$

where t_0 is the adsorbed particle's period of oscillation perpendicular to the surface ($\sim 10^{-13}$ s), E_B is the binding energy for one mole of adsorbed gas, T_c the operation temperature and $R = 8.314$ J/(K mol). For acceptable performance within KATRIN the sorption pump should have a mean sojourn time which is comparable to the experimental run duration (~ 60 days or about $5.2 \cdot 10^6$ s).

3.1.2 Possible pumping mechanisms for CPS

Two kinds of sorption pumps with different binding energies are known: getter pumps in which gas molecules are chemically bound to the adsorbent (chemisorption) with typical binding energies in the order of 100 kJ/mol and cryo-sorption pumps based on van der Waals forces between gas and adsorbent molecules with binding energies below 10 kJ/mol.

The getter pumps widely used for pumping hydrogen in UHV and XHV[1] systems have a very high specific pumping speed and can provide the required suppression factor with reasonable dimensions (see for example [Ben83]). The characteristic binding energy for hydrogen in getter material is as large as 85 kJ/mol leading to a mean sojourn time of about $8 \cdot 10^8$ s at 200 K operation temperature [Hae81]. On the other hand, the high binding energy demands a high temperature during regeneration. In fact, with technically feasible temperatures, tritium cannot be completely extracted from the getter material. Taking into account the three year integral operation time of KATRIN, a significant accumulation of tritium in the getter is to be expected increasing the probability of tritium migration toward the spectrometers.

Other kinds of pumps often used at UHV conditions are cryo-sorption pumps. The energy of physisorption employed in these pumps is much lower than that in getter materials (e.g. for hydrogen it is lower than 2 kJ/mol). With such a binding energy the mean sojourn time of hydrogen molecule in the adsorbent is about 10^{-12} s at 100 K. Since the strength of the attractive van der Waals forces goes like r^{-7} with distance r between the molecules [Hak06], the effective operation of a physisorption pump requires low temperatures. At liquid helium (LHe) temperature, for example, the mean sojourn time for hydrogen is in the order of 10^{10} s. Due to the lower binding energy, the removal of hydrogen during regeneration can be performed at lower temperatures compared to getter materials. Two adsorbents are most widely used in cryo-sorption pumps: activated charcoal and molecular sieves. Both of them have similar adsorption properties and can provide huge specific pumping speeds [Day03]. The main disadvantages of these are possible dust production and the formation of chemical compounds during the regeneration at elevated temperature.

[1] Ultra-high vacuum: 10^{-12} mbar $< P < 10^{-7}$ mbar; extreme-high vacuum: $P < 10^{-12}$ mbar

Over the last decades (from 1960 on) layers of pre-condensed gases were investigated as adsorbents in UHV conditions [Hae81]. The results obtained show that the adsorption energy is close to that for solid adsorbents but that the sorption capacitance is much lower due to the much smaller condensed gas layer thickness available. Morphology studies of condensed gas layers such as argon, krypton and xenon [Nep05] indicate a high porosity (up to 15%) when prepared at low temperatures (below 20 K). The main advantage of condensed gas layers compared to solid adsorbents is that the layer can easily be removed together with any adsorbed tritium, which minimizes the residual tritium contamination. Furthermore, the use of an inert gas as adsorbent is ideal for operation with tritium due to its chemical inactivity. For the Cryogenic Pumping Section of KATRIN pre-condensed argon or krypton at $3 - 4.5$ K are therefore considered.

3.2 Cryo-sorption on pre-condensed gases

The term *cryo-sorption* describes a process where gas particles are bound at low temperature to a highly porous adsorbent. Latter can be, for example, charcoal but also a gas condensate, in which case the adsorbent is also named *cryo-deposit*. The pumped gas bound onto the adsorbent by van der Waals forces is named *adsorbate*. The *coverage* a is defined as the ratio[2]

$$a = \frac{\text{number of particles in adsorbate}}{\text{number of particles in adsorbent}} \tag{3.2}$$

and should be kept as low as possible (refer to sec. 3.2.3).

As cryo-deposits, gases with higher characteristic temperatures (e.g. melting point) than those of the gases to be pumped are considered. With a well suited adsorbent/adsorbate combination, the intermediate forces between the two species are higher than the forces amongst the adsorbate particles[3]. Therefore, a final pressure below the saturation pressure of the gas in question is possible and gases like neon, helium and hydrogen can be pumped effectively at higher temperatures.

Among others, CO_2, CH_4, NH_3 and Ar are considered as cryo-deposits. Although CO_2 provides the lowest final pressure [Hae81], the question of which gas to use is decided by the application. The chemical inactivity of noble gases like Ar and Kr, for example, makes them ideal cryo-deposits for tritium adsorption in KATRIN.

Common to other solid adsorbents, gas condensates feature high specific (inner) surfaces, yet with some additional advantages:

- Due to the preceding condensation, very clean adsorption surfaces are provided.

[2] The definition given here is taken from [Hae81].

[3] The latter describes pure sublimation which is also called *condensation* in cryogenics

- One of the major issues when using solid adsorbents like charcoal is the mechanical attachment of the adsorbent to the metal cryo-surface with good thermal contact. Since cryo-deposits are adsorbed onto the cryo-surface, the thermal contact is excellent.
- The cryo-deposits themselves have a good thermal conductance; the temperature of the adsorbent surface facing the recipient is therefore cooled effectively by the cryo-surface below.
- The adsorption properties of cryo-deposits can be regulated by the choice of the gas and by the preparation conditions (see to sec. 3.3.1).
- Cryo-deposits allow to completely remove the adsorbed gas. The cryo-deposit is freshly prepared for the next pumping cycle.

The last item is the most important one for KATRIN: By using pre-condensed noble gases as adsorbent in the CPS, no tritium inventories are collected over time. After each measurement period of ~ 60 d the CPS is regenerated by warming up, which releases the adsorbed tritium together with the adsorbent. For the next measurement period, a new adsorbent is prepared without any residual tritium contamination.

3.2.1 Average crystallite size and monolayer capacitance

The major property of any adsorbent is the *average crystallite size* δ, which is strongly connected to the *specific surface* A_0 [$\mathrm{cm}^2\ \mathrm{g}^{-1}$] and hence, to the adsorption capacitance [Hae81]:

$$A_0 = \frac{a_0 F N_A}{M_A} \qquad \text{with} \qquad F = 3.464 \left(\frac{M}{4\sqrt{2}\, N_A \cdot \rho} \right)^{2/3} . \tag{3.3}$$

Herein, F [cm^2/particle] describes the surface area occupied by one adsorbate particle, which can be calculated assuming tightest packing [Emm37]. M_A and M are the molar masses of adsorbent and adsorbate particles, respectively, ρ is the adsorbate density and N_A the Avogadro number. a_0 describes the adsorbent's monolayer capacitance:

$$a_0 = \frac{\text{adsorbate amount forming one monolayer on the adsorbent}}{\text{adsorbent amount}} \tag{3.4}$$

which is practically independent of the adsorbate type [Hae81]. Assuming that the adsorbent consists only of cubicles with edge length δ, the following relation between δ, a_0 and A_0 is valid:

$$\delta = \frac{6}{A_0\, \rho_A} = \frac{6 M_A}{\rho_A\, a_0\, F N_A} \quad \Leftrightarrow \quad a_0 \propto \frac{1}{\delta} \tag{3.5}$$

with the adsorbent's density ρ_A. Thus, the more grained the adsorbent is, the more adsorption spots are available on the inner surface of the adsorbent; a_0 increases.

The particle diameters of He, H_2 and Ne are smaller than the distances between next neighbors in cryo-deposits like CO_2, CH_4 and Ar. Therefore, adsorption on lattice sites can be assumed [Hae81]. All the adsorbents and adsorbates mentioned here form cubic face centered lattice structures. If the interaction to the next neighbors is predominant, the preferred area of growth are the 111 and 100 lattice planes. A particle adsorbed at such a site has three or four next neighbors. A smaller average crystallite size δ promotes the existence of incomplete lattice planes and holes, where adsorbate particles can have five, eight or even nine next neighbors. These adsorption sites are energetically favored due to the higher binding energy and will be occupied first after adsorption of the adsorbate particle by diffusion along the crystallite surfaces (also refer to sec. 3.2.2).

During the pumping process, the coverage a increases. The binding energy per mole E_B decreases at the same time, since unfavored adsorption spots will be increasingly occupied. If the monolayer capacitance a_0 is reached, forces amongst the adsorbate particles become predominant: The cryo-sorption is degenerated towards condensation resulting in a higher equilibrium pressure. Thus, the design of any cryo-sorption pump needs to take this effect into account by providing a cryo-surface large enough for very low coverage a and high monolayer capacitance a_0.

3.2.2 Cryo-sorption mechanics

According to [Hae81], the following steps can be considered as the process involved in physical adsorption:

1. A gas particle hits the adsorbent by chance.
2. The gas particle is thermally accommodated and sticks with probability α to a crystallite surface facing the recipient. The *sticking coefficient* α strongly increases with decreasing temperature.
3. The gas particle, now called adsorbate particle, diffuses along the crystallite surface into deeper layers of the adsorbent.
4. After the mean sojourn time t_s, the gas particle is desorbed from the crystallite requiring the energy E_B per mole.
5. At low temperatures with $\alpha \approx 1$, the adsorption on neighboring adsorbent crystallites is very probable.

With pumping time t, the coverage a increases until the maximum coverage

$$a_{max} = \frac{dn_A/dt \cdot t_{max}}{n_{adsorbent}} \quad \Leftrightarrow \quad t_{max} = \frac{n_{adsorbent}}{dn_A/dt} \cdot a_{max} \tag{3.6}$$

is reached. Herein, $n_{adsorbent}$ is the total number of adsorbent particles and dn_A/dt the constant adsorption rate which is given in eq. 3.7. t_{max} is the pumping time

after which the pumping speed per surface area quickly drops to zero, whereas it is essentially constant for $t < t_{max}$.

The measurement time period of KATRIN, that is the time period before the cryo-surface in the CPS is regenerated, needs to be chosen in a way to ensure a sufficiently high pumping speed. According to eq. 3.6, a large number of adsorbent particles $n_{adsorbent}$ will increase the maximum pumping time t_{max}. Since the adsorbent layer thickness is limited (refer to sec. 3.3.1), an adequately large cryo-surface area needs to be made available. For KATRIN, 60 days are planned for one measurement time period.

3.2.3 Adsorption, desorption and equilibrium pressure

The adsorption rate on the surface area S can be expressed as [Rot90]

$$\frac{dn_A}{dt} = 2.63 \cdot 10^{22} \left[\frac{\sqrt{\text{g/mol K}}}{\text{s mbar cm}^2} \right] \cdot \frac{P \alpha S}{\sqrt{MT}} \tag{3.7}$$

for pure physisorption, where P is the partial pressure of the pumped gas, M the adsorbate molecular mass, T the gas temperature and α the sticking coefficient. The desorption rate, on the other hand, is [Rot90]

$$\frac{dn_D}{dt} = \frac{n}{t_s} = n \cdot 10^{13} \left[\frac{1}{\text{s}} \right] \cdot e^{-E_B/(RT_c)} \tag{3.8}$$

with the number of adsorbed gas particles n and t_s as introduced in eq. 3.1.

In equilibrium the adsorption and desorption rates are equal and the adsorbate pressure is called equilibrium pressure

$$P_{eq} = \frac{n\sqrt{M\,T}}{\alpha\, S} \cdot 3.80 \cdot 10^{-10} \left[\frac{\text{mbar cm}^2}{\sqrt{\text{g/mol K}}} \right] \cdot e^{E_B/(RT_c)} \,. \tag{3.9}$$

A strong dependence of the equilibrium pressure from both, the binding energy E_B and the cryo-surface temperature T_c, is observable. Furthermore, P_{eq} increases with increasing coverage a, since

$$a = \frac{n}{n_{adsorbent}} \,. \tag{3.10}$$

This general behavior is summarized in so-called adsorption *isosteres* and *isotherms*. The former describe the dependence of adsorbate pressure from adsorbent temperature at constant coverage, the latter give the adsorbate pressure vs. coverage at constant temperature. Examples of these characteristics are presented in fig. 3.1 and 3.2. It is obvious that P_{eq} strongly depends on the kind of cryo-deposit in question and its preparation conditions, too. The best results (lowest equilibrium pressure) were achieved for CO_2. Furthermore, fig. 3.1 demonstrates that the equilibrium pressure due to H_2 cryo-sorption on CO_2 is considerably lower than the saturated vapor pressure from H_2 condensation.

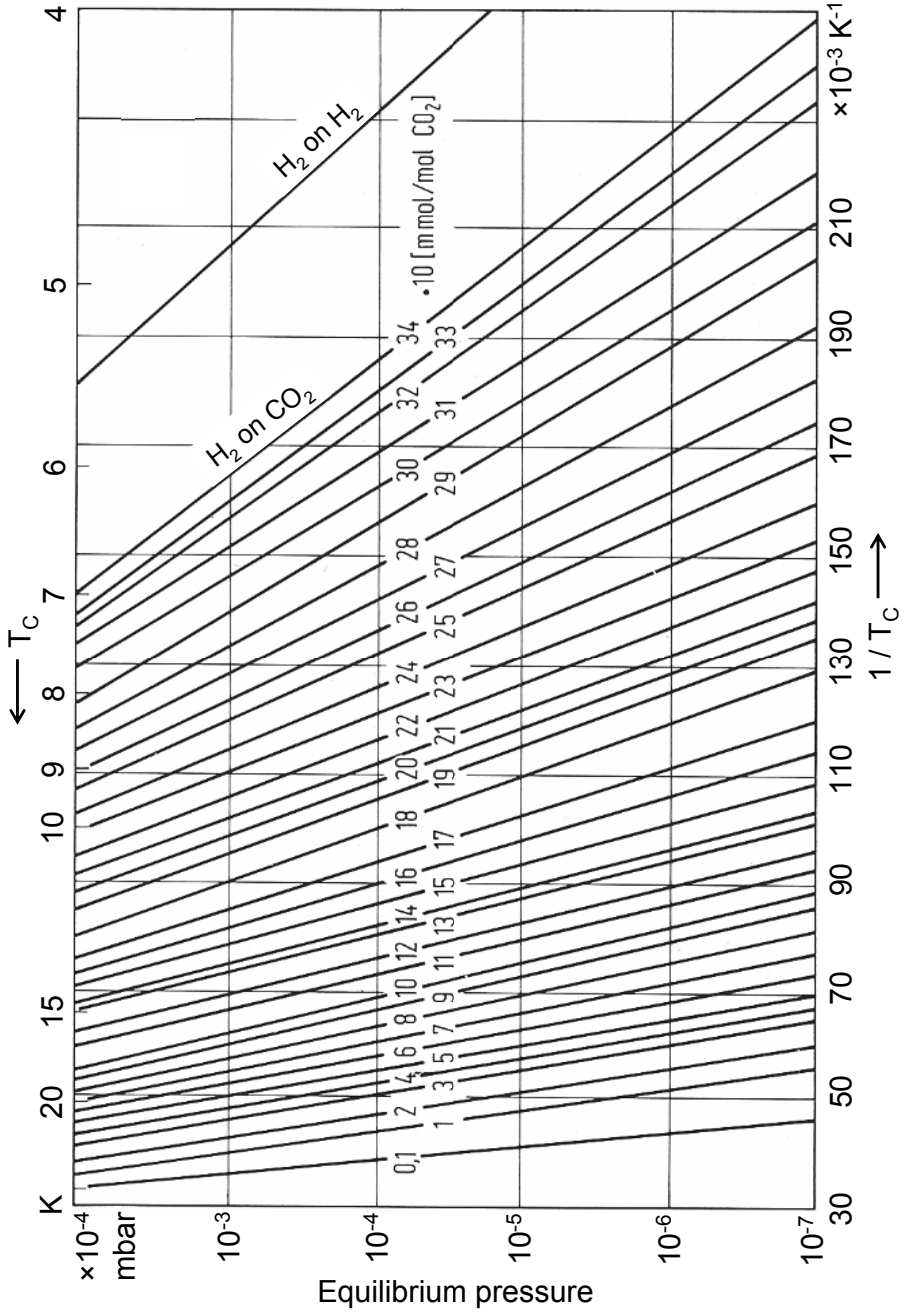

Figure 3.1: Adsorption isosteres of H_2 adsorption on CO_2. Parameters during the preparation of the CO_2 condensate: thickness 28 μm, condensation temperature 11.2 K and condensation pressure $7 \cdot 10^{-5}$ mbar. Additionally, the isostere for H_2 condensation is shown. (based on [Hae81])

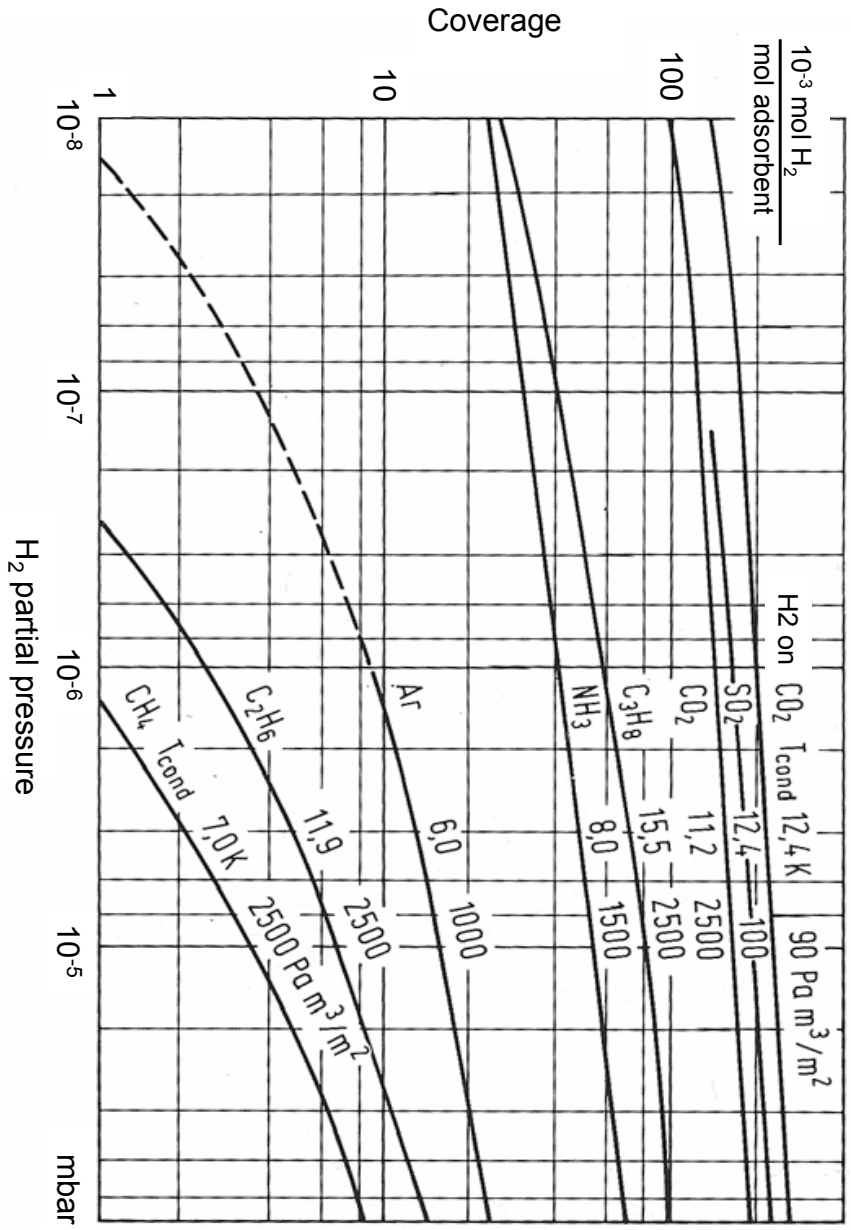

Figure 3.2: Adsorption isotherms of H_2 adsorption on various cryo-deposits. The preparation parameters for each adsorbent are given. (based on [Hae81])

3.3 Parameters of cryo-sorption on pre-condensed gases

Generally, the performance of a cryo-sorption pump is dependent on the cryo-deposit preparation and the operation conditions. The most important parameters to be considered when designing any cryo-pump are discussed in the following.

3.3.1 Preparation parameters

Preparation temperature: Experimental studies predict that an optimal condensation temperature exists for each cryo-deposit which provides a minimal average crystallite size δ and hence a maximum specific (inner) surface A_0 [$cm^2\ g^{-1}$] and a maximum monolayer capacitance a_0 [Hae81]. For argon, 6 K turns out to be the optimal preparation temperature [Nep05], which should be taken into account when specifying the CPS.

Deposition rate: Generally a high deposition rate will lead to small crystallite sizes, as the cryo-deposit buildup is too fast for the re-crystallization, which is favoring large crystallite sizes [Hae81].

Layer thickness: The cryo-deposit surface facing the recipient is subject to heating by irradiation and adsorption. The heat conductance of the residual gas can be neglected in UHV conditions. Since the heat conductance of the cryo-deposit is not infinite, its temperature will be higher than the temperature in the bulk material (see fig. 3.3). This will lead to a higher equilibrium pressure and decrease the capacity as the crystallite size will grow. The thickness d of the cryo-deposit should therefore not exceed $\sim 1\ \mu$m too much [Hae81].

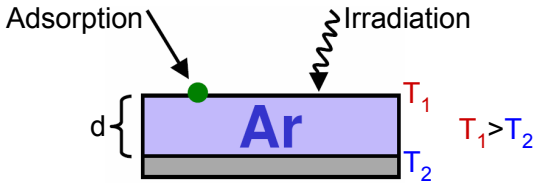

Figure 3.3: Thickness of cryo-deposit layer.

3.3.2 Operating parameters

Operating temperature: The operating temperature of the cryo-surface has a strong impact on the partial pressure as shown in fig. 3.1. The lower the temperature, the lower the equilibrium pressures will be. Furthermore, if the cryo-surface's operating temperature is increased above the temperature at which the cryo-deposit was prepared, an irreversible re-crystallization will occur towards an increasing of the average crystallite size due to the increased mobility of the adsorbent particles

at higher temperatures. The tritium retention performance of the CPS is therefore connected to the operational temperature. If lowering the temperature from ~ 4.5 K to ~ 3 K is technically not too complicated, it would be beneficial for KATRIN as the tritium pressure would be decreased by several orders of magnitude.

Amount of pumped gas, coverage: During the pumping process, the coverage increases with time along with the equilibrium pressure according to fig. 3.2. The KATRIN measurement time period needs to be chosen accordingly.

Heat load on cryo-surface: The adsorption of warm gas on the cryo-deposit will lead to evaporation of the latter. Therefore, measures should be taken for pre-cooling the gas which is being adsorbed. Furthermore, it is known that heat irradiation from other (warm) parts of the recipient can lead to desorption of hydrogen from the cryo-surface [Ben76]. This effect will be weakened by employing a cryo-deposit, but should nonetheless be avoided by shielding the cryo-surface in the CPS from this irradiation (refer to sec. 3.4.3).

Radioactivity of adsorbed gas: The radioactivity of adsorbate particles transfers additional energy to the cryo-deposit which can lead to desorption of both, cryo-deposit and adsorbate particles. This issue will be further addressed in sec. 4.1.

3.4 Data for hydrogen and argon at low temperature

In the CPS-relevant low tritium pressure regime of $< 2.6 \cdot 10^{-16}$ mbar [CPS08a] no literature data are available for cryo-sorption of tritium on argon cryo-deposit at $3 - 4.5$ K. Yet, some data exist that should be taken into account. They are summarized in the following.

3.4.1 Argon cryo-deposit properties

An important aspect of the performance of a cryo-sorption pump with pre-condensed gas as adsorbent are the preparation parameters of the cryo-deposit as described in sec. 3.3.1. For argon, 6 K turns out to be the ideal preparation temperature [Nep05] leading to an average crystallite size of $\delta = 60$ nm. In this case, the monolayer capacitance a_0 and the specific surface A_0 are

$$a_0 = 5.8 \cdot 10^{-2} \text{ mol } H_2/\text{mol Ar} \quad \text{and} \tag{3.11}$$

$$A_0 = 138 \text{ m}^2 \text{ g}^{-1}, \tag{3.12}$$

respectively [Hae81]. Figure 3.4 shows the vapor pressure over temperature for various gas condensates including argon. The lowest temperature in the diagram for argon is ~ 20 K; data for the argon vapor pressure at ~ 4.5 K was not available. However, it shows that the argon pressure at 4.5 K should be well below 10^{-11} mbar. Therefore, the argon gas load from the CPS to the Pre-spectrometer is low enough to maintain a total pressure below 10^{-11} mbar in the Pre-spectrometer as specified in [KAT04] via pumping with turbomolecular pumps.

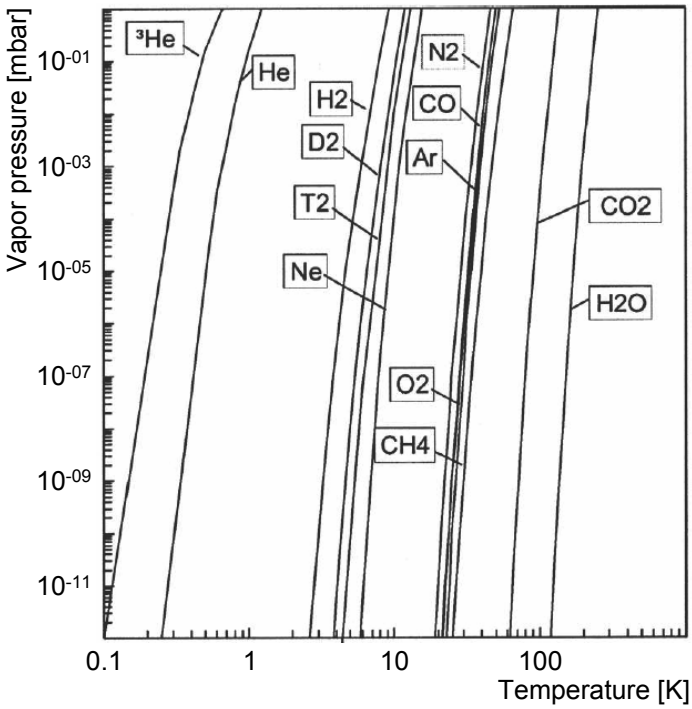

Figure 3.4: Vapor pressure for various gas condensates. Data for the argon vapor pressure could not be found for ~ 4.5 K. For most data sets the lowest temperature is that of the triple point of argon (83 K). (based on [Day04])

3.4.2 Hydrogen vapor pressure

The vapor pressure dependence from temperature for the six hydrogen isotopomers is given in fig. 3.5. This is the pressure in thermal equilibrium one would expect above the condensate if more than one monolayer of hydrogen was adsorbed on the cryo-surface. In this case the forces in-between the hydrogen molecules are dominating over the forces in-between hydrogen molecules and the cryo-surface substrate.

The data allow for some predictions for cryo-sorption of hydrogen on argon at 4.2 K, the temperature of the cryo-surface in the TRAP experiment: The equilibrium pressures in the case of cryo-sorption will follow those of condensation of the pure isotopomer (see table 3.1): It will increase in the sequence T_2, DT, D_2, HT, HD, H_2 [Sou86]. Since the zero point energy of vibration of the molecule against the ad-

Table 3.1: Molar mass and vapor pressure at 4.2 K of hydrogen isotopomers. The masses are calculated using data from [Lid92]; the pressure data are from [Sou86].

	H_2	HD	HT	D_2	DT	T_2
Molar mass [g/mol]:	2.016	3.022	4.024	4.028	5.030	6.032
Pressure at 4.2 K [mbar]:	8E-7	5E-9	5E-10	5E-11	4E-12	2E-13

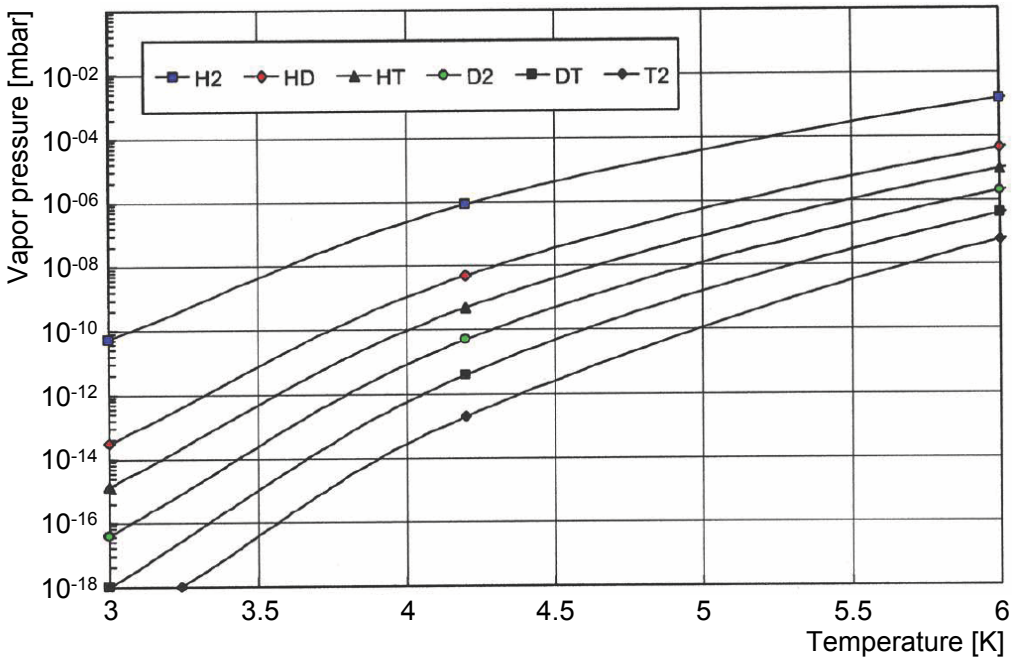

Figure 3.5: Vapor pressure for hydrogen isotopes. (based on [Sou86])

sorption surface goes with $m^{-1/2}$, the vapor pressure follows the sequence of falling molar masses (see table 3.1): The smaller the mass, the higher the zero point energy and the easier to remove the molecule from the surface.

3.4.3 Influence of infrared irradiation

Figure 3.6 shows the vapor pressure dependence at very low temperatures for H_2 and D_2. It was found that the pressure is practically constant at $\sim 10^{-9}$ mbar for temperatures below ~ 3 K [Ben76], a circumstance that questions the possibility of pumping H_2, which is the major component in UHV systems, at low pressure.

Benvenuti et al. [Ben76] found that infrared irradiation from parts inside the vacuum vessel, which are at room temperature, impinges on the condensation surface and creates phonons inside of the material. These phonons travel to the cryo-surface, transmit their energy to the condensate and lead to the desorption of H_2. This increases the equilibrium pressure according to sec. 3.2.3. Furthermore, it was found that a pre-condensed layer of a heavier gas like Ne, Ar or N_2 significantly lowers the H_2 desorption rate: This layer with a much lower Debye temperature[4] than H_2 works just like a low-pass filter preventing the high energy phonons from entering the layer and reaching the H_2 condensate [Hae81].

In order to reach a low H_2 pressure, the cryo-surface should be made of a material

[4]The Debye temperature θ defines the maximum energy of phonons inside a solid state body: $E < \hbar\omega_D = k_B\theta$ with the cut-off frequency ω_D and the Boltzmann constant k_B [Iba99].

with a low absorption coefficient for infrared irradiation and it should be covered with an adsorbate, e.g. a pre-condensed layer of a heavier gas. Furthermore, any infrared irradiation should be either shielded, its temperature lowered or prevented altogether. The influence of the aforementioned measures are shown in fig. 3.6.

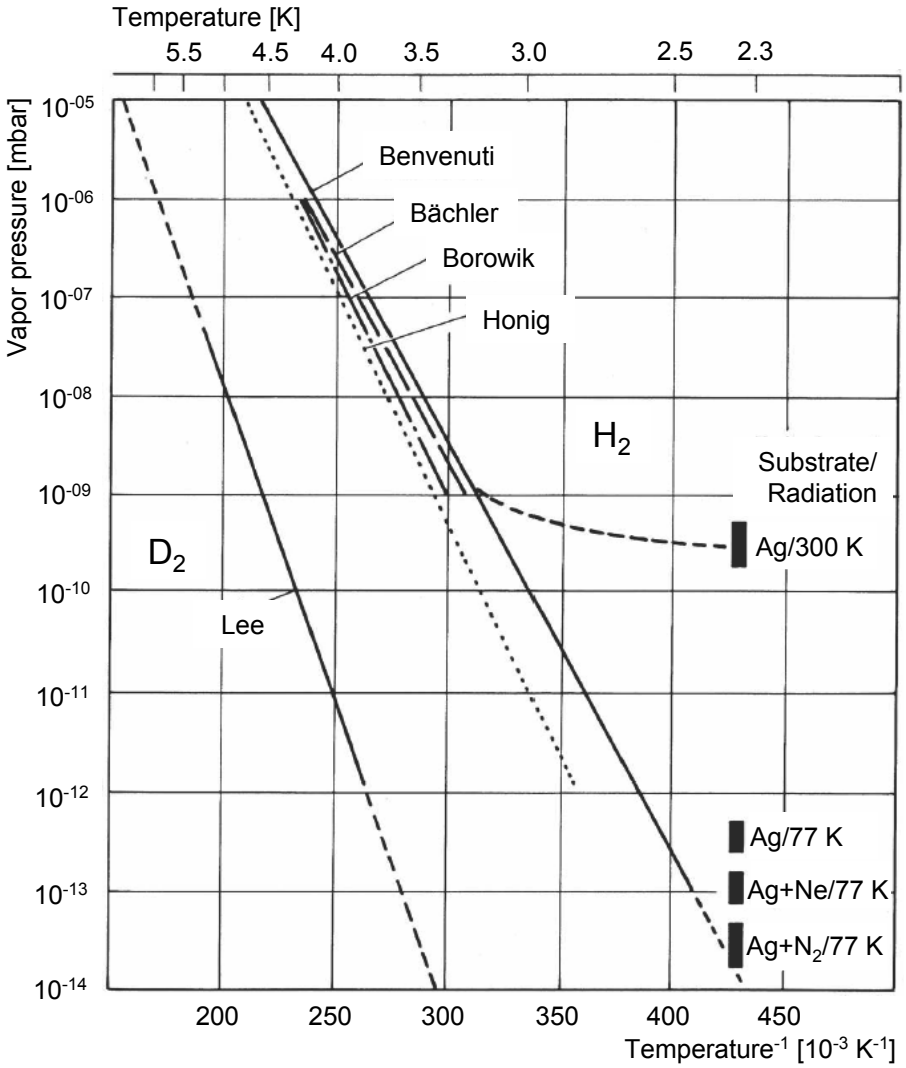

Figure 3.6: H_2 and D_2 vapor pressure at very low temperature. Based on measurements from Benvenuti et al. [Ben76], Bächler et al. [Bae62], Borowik et al. [Bor60], Honig et al. [Hon60] and Lee [Lee72]. The continuous line belonging to the data set of Benvenuti et al. gives the pressure P in dependence of condensate temperature T calculated according to the Clausius-Clapeyron equation $\ln P = -B/T + C$ with constants B and C. The black boxes indicate the hydrogen pressure measured at ~ 2.3 K for different substrate/irradiation combinations. The vapor pressure is higher at very low temperatures than theoretically expected. (based on [Hae81])

3.4.4 Hydrogen cryo-sorption on pre-condensed argon

Table 3.2 shows some data for sticking coefficients α for hydrogen cryo-sorption on various cryo-deposits. Since no isotope effect is visible for the systems H_2/CO_2 and D_2/CO_2, no isotope effect is expected in the system Q_2/Ar (Q=H,D,T), either. Therefore, the sticking coefficient for tritium cryo-sorption on pre-condensed argon at 4.2 K is about 0.7.

Table 3.2: Sticking coefficients for different cryo-deposit/adsorbate systems at low coverage $a \to 0$ and gas temperature $T = 300$ K.

cryo-deposit	adsorbate	T_c [K]	α	reference
Ar	H_2	11	0.1	[Hun63]
		4.2	0.7	[Yuf70]
CO_2	H_2	20	0.42	[Yuf67]
		12.4	0.68	[Tem71]
		11	0.5	[Hun63]
		4.2	0.6	[Yuf70]
CO_2	D_2	20	0.4	[Yuf70]
		14	0.5	[Yuf70]
		4.2	0.6	[Yuf70]
H_2O	H_2	20	0.55	[Yuf67]
		11	0.9	[Hun63]

Chapter 4

The Test Experiment TRAP

This chapter describes the TRAP (Tritium Argon frost Pump) test experiment for the Cryogenic Pumping Section of KATRIN. Section 4.1 gives the motivation for the experiment and in sec. 4.2 the general principle is discussed. A detailed description of the experimental setup can be found in sec. 4.3.

4.1 The Motivation

The Cryogenic Pumping Section (CPS) being operated at $3 - 4.5$ K according to [CPS08a] needs to suppress the tritium flow rate by seven orders of magnitude below 10^{-14} mbar l/s (refer to sec. 2.2.4.2). The maximum allowed T_2 pressure at the outlet of the CPS1-F can be estimated from this by considering CPS2-F as a straight tube of vacuum conductance $C \approx 38$ l/s without any getters. In the molecular flow regime, the gas flow rate Q through a tube of vacuum conductance C and upstream (downstream) pressure P_1 (P_2) is given by [Rot90]

$$Q = C \cdot (P_1 - P_2) \approx C \cdot P_1 \,. \tag{4.1}$$

From this, an upper limit for the T_2 pressure at the outlet of the CPS1-F can be derived [CPS08a]:

$$P_{CPS1-F} < 2.6 \cdot 10^{-16} \text{ mbar} \,. \tag{4.2}$$

However, tritium in the CPS is not only pure T_2: DT is also present, since the isotope separation system of TLK always provides tritium with a small amount of DT. In the worst case of 95% purity, for example, the isotopic mixture contains 90% T_2 and 10% DT. Furthermore, HT will be generated by isotopic exchange reactions with residual H_2 from the beamline walls of the transport system. Only with increased runtime of the experiment, the walls will be thoroughly contaminated with tritium and the generation of HT will abate. All three tritiated hydrogen isotopomers T_2, DT and HT will hence be present in the CPS and all their partial pressures should not exceed the order of 10^{-16} mbar. For comparison, their saturation pressures at

4.2 K are orders of magnitude higher (see table 3.1).

In order to reach significantly lower partial pressures, pre-condensed argon will be employed as adsorbent at $3-4.5$ K in CPS1-F. However, the radioactivity of tritium will transfer additional energy to the adsorbent and lead to desorption of both, adsorbent and adsorbate. With an average beta electron energy of about 6 keV, the range of these is in the order of μm. This means that essentially all energy could be deposited in the adsorbent since the pre-condensed gas layer is similar in thickness. As the sublimation energy for solid argon is 8048 J/mol [Hae81], up to $\sim$ 60 000 atoms of argon could be evaporated by a single average tritium decay. Depending on the coverage of tritium on argon, also tritium will be evaporated and might therefore pass the CPS (*migration*, see fig. 4.1).

Cryo-sorption pumps for pumping tritium were already employed in earlier tritium β decay experiments, in Mainz [Kra05] with graphite coating of the electron transport channel and in Troitsk [Bel95] with argon frost coating. Both experiments published an observed tritium flow rate suppression toward the spectrometers due to these pumps, yet no numerical data on the suppression factors were published.

Since no further data on tritium adsorption on pre-condensed gases at the CPS relevant pressure regime of $\sim 10^{-16}$ mbar are available in literature and because of the immense importance of the CPS as the last tritium retention unit in front of the KATRIN spectrometers, the test experiment TRAP has been built at TLK to investigate the properties of tritium adsorption on pre-condensed noble gases. The main objectives of TRAP are:

- to prove that the concept of tritium retention by a cryo-pump with pre-condensed argon is working and to determine the tritium flow rate suppression factor,
- to provide input data and experience for the specification of the CPS,
- to develop and test the regeneration procedure of the cryo-pump and
- to have the possibility to test different cryo-deposits (e.g. krypton).

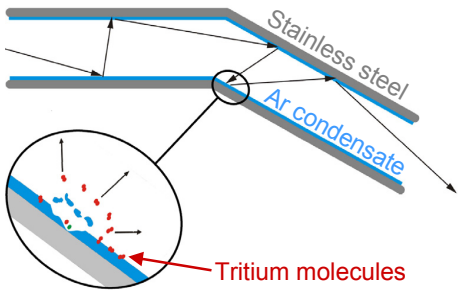

Figure 4.1: Tritium migration. Through successive adsorption-desorption processes, tritium might migrate trough the CPS.

4.2 Principle of TRAP

The main task of the TRAP experiment is to determine the tritium flow rate suppression factor

$$F = \frac{Q_{in}}{Q_{out}} = \frac{\text{incoming tritium flow rate}}{\text{outgoing tritium flow rate}} \tag{4.3}$$

of a cryo-sorption pump at 4.2 K[1] with pre-condensed argon as adsorbent. TRAP can be considered as a mock-up for the Cryogenic Pumping Section of KATRIN with the following general features (see fig. 4.2):

1. TRAP is comparable to the CPS with regard to its cryogenic parts:
   - The cryo-surface consisting of a 20° bent tube (*Cryo-trap*) is cooled in a liquid helium (LHe) bath cryostat to a temperature of $\sim$ 4.2 K.
   - The vacuum conductance of the Cryo-trap is approximately the same which is planned for the CPS.
   - The cryo-surface area is about 1/10 of the CPS. However, with only about 1/10 of injected tritium in TRAP compared to the CPS[2], the tritium surface densities will be similar.
2. Unlike the CPS, TRAP does not include a superconducting magnet system for guiding decay electrons.
3. TRAP is constructed in such a way that it simulates the most important functions of the CPS (refer to fig. 4.2):
   - The argon cryo-deposit is prepared on the cryo-surface via a capillary. The argon gas exits the capillary through tiny holes along its length and is distributed approximately homogeneously over the cryo-surface.
   - Tritium is injected from a calibrated buffer vessel at the bottom of the Cryo-trap. From the pressure drop in the vessel the average injection flow rate Q_{in} can be calculated.
   - Tritium passing through the Cryo-trap can be detected by a residual gas analyzer (RGA) or a silicon solid state detector. The outgoing flow rate Q_{out} needs to be determined in the *Detection System* (sec. 4.3.7).
   - The Cryo-trap is regenerated after each measurement interval by warming up and evaporating any adsorbed tritium together with the argon cryo-deposit. In order to avoid an increase of contamination of the weakly contaminated (upper) parts of the Cryo-trap, purging with gaseous helium (GHe) in the direction from low to high contamination is applied during warm up.
   - The cryo-surface can be baked afterwards at $\sim$ 400 K.

[1] In TRAP, a liquid helium bath cryostat is used. Therefore, the temperature of the cryo-surface is that of the helium boiling point.

[2] Maximum inventory in the CPS: 1 Ci after $\sim$ 60 d

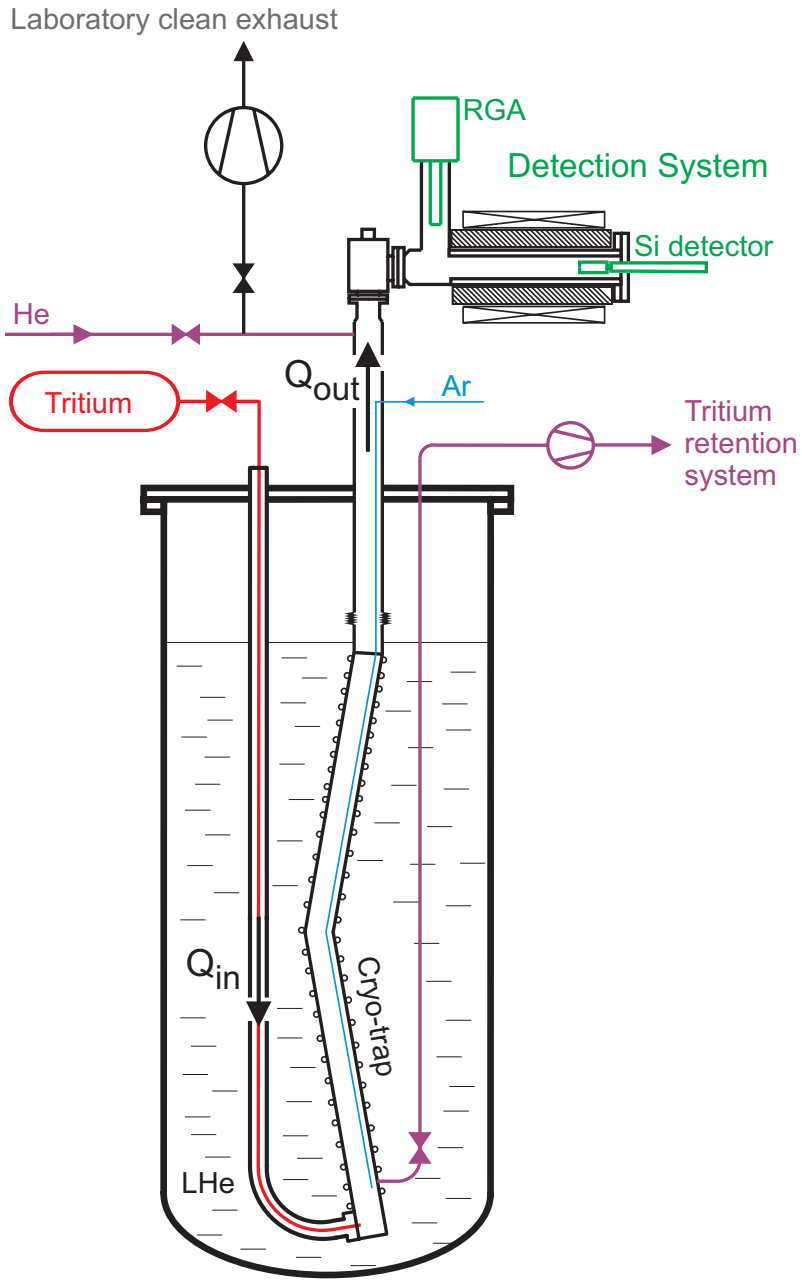

Figure 4.2: Schematic of the TRAP experiment. After evacuation of the system and cool-down with LHe, argon is injected via a perforated capillary and distributed approximately homogeneously over the Cryo-trap to form the adsorbent. Tritium injection is performed from a calibrated buffer vessel via a low-conductance capillary at the bottom of the Cryo-trap. Tritium which has migrated along the Cryo-trap can be detected at the top with a residual gas analyzer (RGA) or a silicon detector. In order to remove the tritium after a measurement phase, the LHe in the cryostat is evaporated and the Cryo-trap is being heated with a built-in heater. The Cryo-trap is simultaneously purged with gaseous helium from top to bottom to keep the the tritium contamination at the upper end of the Cryo-trap low.

4.3 Experimental setup of TRAP

This section covers the experimental setup of the TRAP test experiment. Figure 4.3 shows a simplified flow diagram of the system which consists of seven subsystems: The *Cryo-system*, the *Cryo-trap*, the *Argon Inlet System*, the *Tritium Inlet System*, the *Helium Purging System*, the *Pumping System* and finally the *Detection System*. These subsystems are shortly described in the following. More detailed descriptions, especially for the first four subsystems, can be found in [Eic04]. Appendix A summarizes the changes to the experimental rig that were necessary for operation with tritium.

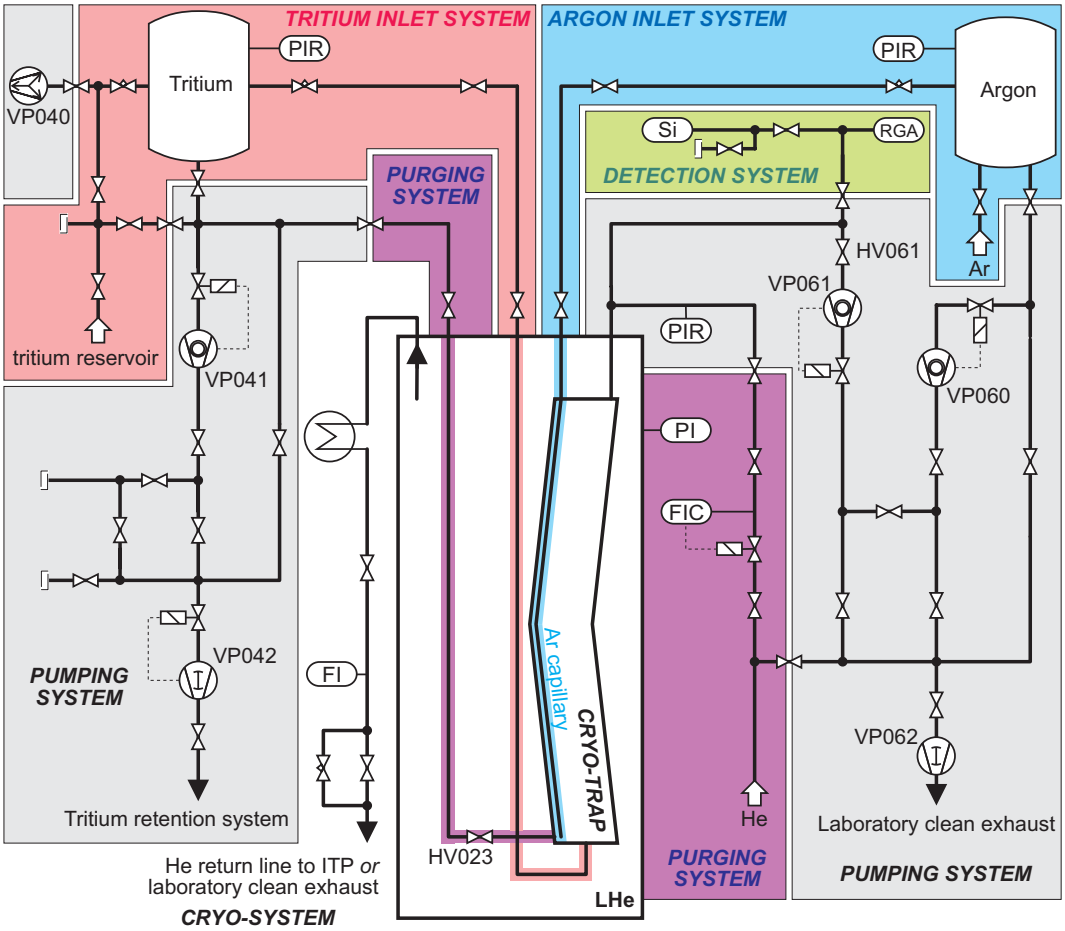

Figure 4.3: Simplified process and instrumentation diagram (PID) of TRAP. A detailed flow diagram is available in appendix D

4.3.1 The Cryo-system

The Cryo-system provides the temperature of 4.2 K for the Cryo-trap (see sec. 4.3.2):

- A standard vertical LHe bath cryostat of 500 mm diameter and 1500 mm height is used as a container for the Cryo-trap.

- A heater mat at the bottom of the cryostat allows to increase the LHe evaporation rate if necessary.

- The Cryo-trap and additional equipment shown in fig. 4.4 are fixed on the cryostat flange. TVO[3] temperature sensors [Sue95] on the base of carbon resistors allow for the temperature measurement of the Cryo-trap during cooling down. Superconducting LHe level meters ascertain the LHe fill height in the cryostat.

- The He pressure in the cryostat is monitored by an absolute pressure sensor of membrane type.

- The exhaust He from the cryostat is warmed up in a water bath heater, counted by a gas counter (FI on fig. 4.3) and transferred either

  – through a $\sim$ 300 m subterranean line to the helium liquefier at the Institute for Technical Physics (ITP) during cooldown of the cryostat and measurements with deuterium or

  – to the laboratory exhaust channel during tritium measurements which ensures that no tritium is transferred to ITP in case of a leakage in the Cryo-trap.

  The LHe consumption rate in steady state is about 3 l/h [Eic04].

4.3.2 The Cryo-trap

The Cryo-trap (or cryo-surface) consists of a stainless steel tube (DIN standard 1.4571, ASTM 316Ti) of 50 mm diameter and 1 m length with two straight parts and an angle of 20° in-between them to prevent the beaming effect of molecular flow. It is closed at the bottom and connected to the Detection System via the connecting tube (see fig. 4.4). The Ar coverage of the Cryo-trap is done by the Argon Inlet System (see sec. 4.3.3), the tritium inlet by the Tritium Inlet System (see sec. 4.3.4) through the tritium inlet tube at the bottom (see fig. 4.4).

The gas conductance of the Cryo-trap can be estimated using the formula of a straight tube of diameter $D = 5$ cm and length $L = 100$ cm in the molecular flow regime [Rot90]:

$$C = 3.81 \left[\frac{\mathrm{l}}{\mathrm{s\ cm^2}} \sqrt{\frac{\mathrm{g/mol}}{\mathrm{K}}} \right] \cdot \frac{D^3}{L} \cdot \sqrt{\frac{T}{M}}\,. \tag{4.4}$$

For molecular tritium ($M = 6$ g/mol) and $T = 4.2$ K, the conductance is ~ 4 l/s.

The Cryo-trap can be heated by a heater wrapped and brazed around the tube. This is needed for the regeneration procedure as well as for baking out.

[3] Translation of "TBO" from Russian: thermally resistant, moisture resistant, compacted

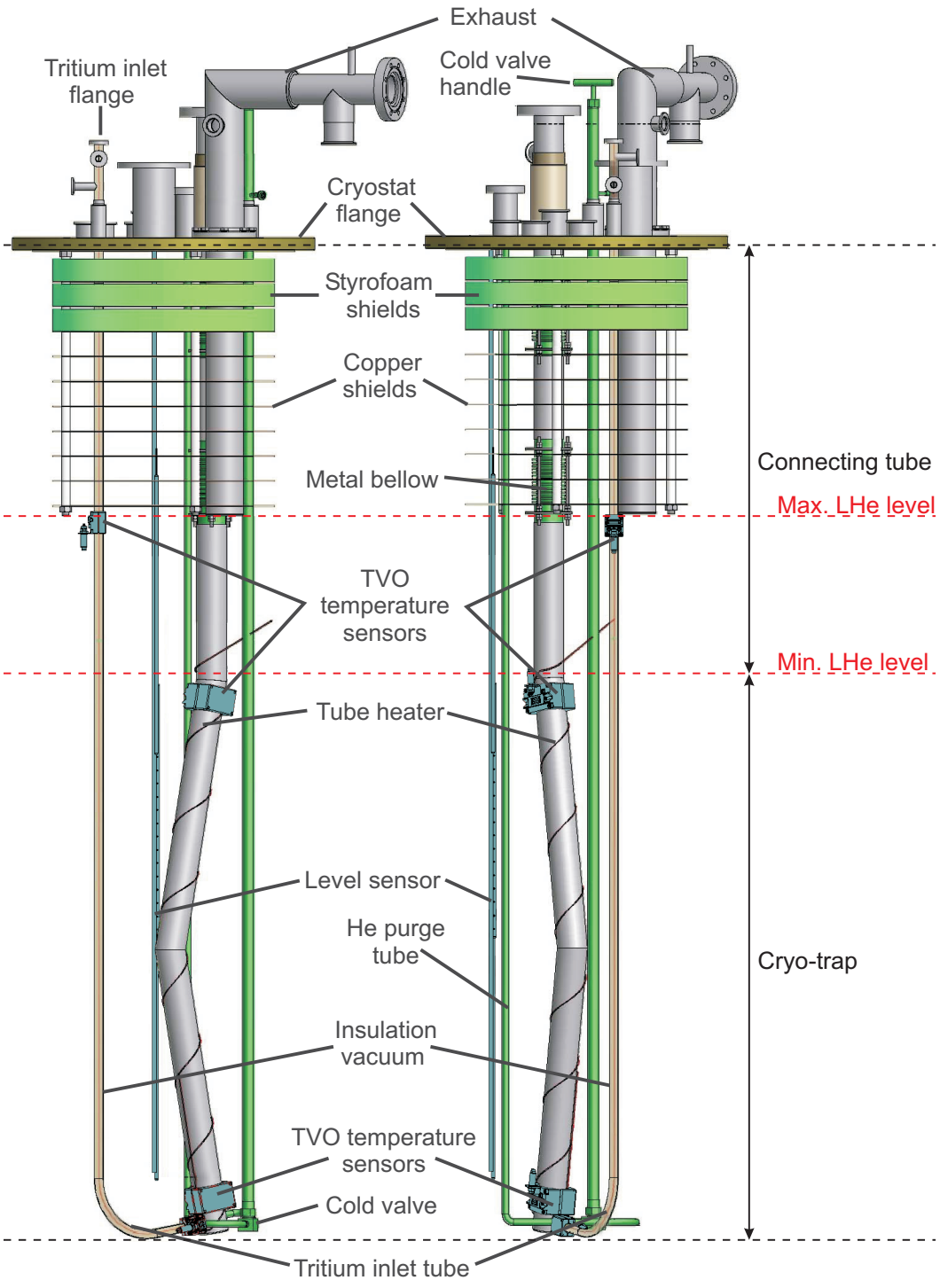

Figure 4.4: The cryostat internals. (based on [Bra03])

4.3.3 The Argon Inlet System

Argon is injected from a calibrated buffer (volume 1.3 l) by adjusting a needle valve to the desired inlet flow rate. The latter can be determined from the pressure drop in the buffer measured with an absolute pressure gauge (MKS Baratron 390HA, range 0-1000 Torr). The argon cryo-deposit is prepared on the cryo-surface through a perforated capillary, which runs along the Cryo-trap to the bottom and is heated above ~ 80 K to prevent freezing of argon inside and on the outside of this capillary. The diameter of the capillary is 2 mm, the hole spacing along its length 5 cm and the diameter of each hole 0.2 mm providing a homogeneous distribution of the argon adsorbent on the cryo-surface.

4.3.4 The Tritium Inlet System

Tritium is injected from a calibrated buffer (volume 1.3 l) through a needle valve and a low-conductance capillary ($C \approx 10^{-5}$ l/s) which allows for setting inlet flow rates in the 10^{-7} mbar l/s regime. The pressure drop in the buffer during inlet is measured with an absolute pressure gauge (MKS Baratron 690A, range 0-10 Torr, accuracy 0.12%). Tritium enters the Cryo-trap at the bottom via the capillary mentioned before and the tritium inlet tube (see fig. 4.4). The latter is located inside an insulation vacuum and in addition heated above ~ 30 K to prevent adsorption of tritium on its inner surface. Furthermore, TVO temperature sensors attached to the tritium inlet tube are used to monitor its temperature.

4.3.5 The Helium Purging System

About 150 mCi of tritium is supposed to be collected on the Cryo-trap during a measurement run. Afterwards, the cryo-surface will be regenerated which means the removal of the argon cryo-deposit together with any adsorbed tritium. During the regeneration procedure, the Cryo-trap is heated and purged with helium gas in order to preserve the tritium surface contamination gradient from high contamination at the injection point (bottom part of the Cryo-trap) to low contamination at the top.

The helium gas flow, which is controlled by a flow controller, enters the Cryo-trap from the top and leaves it at the bottom through a cold valve (HV023) and the helium purge tube (see fig. 4.4). The argon/helium/tritium mixture is hereupon transferred through a transport pump (VP042) to the tritium retention system of the laboratory. The roots pump VP042 is part of the Pumping System (see sec. 4.3.6).

4.3.6 The Pumping System

In the Pumping System several pumps can be used for evacuation. They are subdivided into two groups:

- Pumps with negligible amount of tritium, exhaust to the laboratory clean exhaust:
  - VP060: Turbomolecular pump, Pfeiffer TPU170
  - VP061: Turbomolecular pump, Pfeiffer TMU200MP
  - VP062: Roots pump, Alcatel ACP28
- Pumps carrying tritium, their exhaust is transferred to the main stage of TLK's central tritium retention system, where the atmosphere of all glove boxes is being detritiated (average tritium activity ~ 1 MBq/m^3):
  - VP040: Ion getter pump, Leybold IZ12 (no exhaust, never used in the experiments)
  - VP041: Turbomolecular pump, Pfeiffer TPU170
  - VP042: Roots pump, Alcatel ACP15

This subdivision is imperative for the experiment since the Detection System (refer to sec. 4.3.7) could be contaminated with tritium, if any connection existed from the pumps VP061 and VP062 to TLK's tritium infrastructure.

The roots pump VP042 is also used as a transport pump during the regeneration procedure (see sec. 4.3.5). Furthermore, a cold cathode pressure sensors allows for measuring the total pressure in the system.

4.3.7 The Detection System

Tritium migrating through the Cryo-trap can be detected in the Detection System directly with a residual gas analyzer[4] and via its β decay electrons with a silicon solid state detector. Figure 4.5 shows a schematic of the TRAP Detection System viewed from above with the following main features:

- The Si detector is located inside a solenoid manufactured at ITP [Geh06]. It generates a magnetic field of 0.1 T maximum strength. β electrons are guided onto the detector surface on cyclotron tracks.
- The Si detector is cooled via a liquid nitrogen (LN_2) bath in order to decrease electronic noise.
- A gate valve allows for the separation of the Detection System from the rest of the experimental setup during regeneration. This prevents strong contamination of the Detection System.
- A second gate valve allows for the separation of the RGA and detector chambers.

[4]Type 1: mass range $1-100$ amu (atomic mass unit); type 2: $1-6$ amu; details in appendix F.

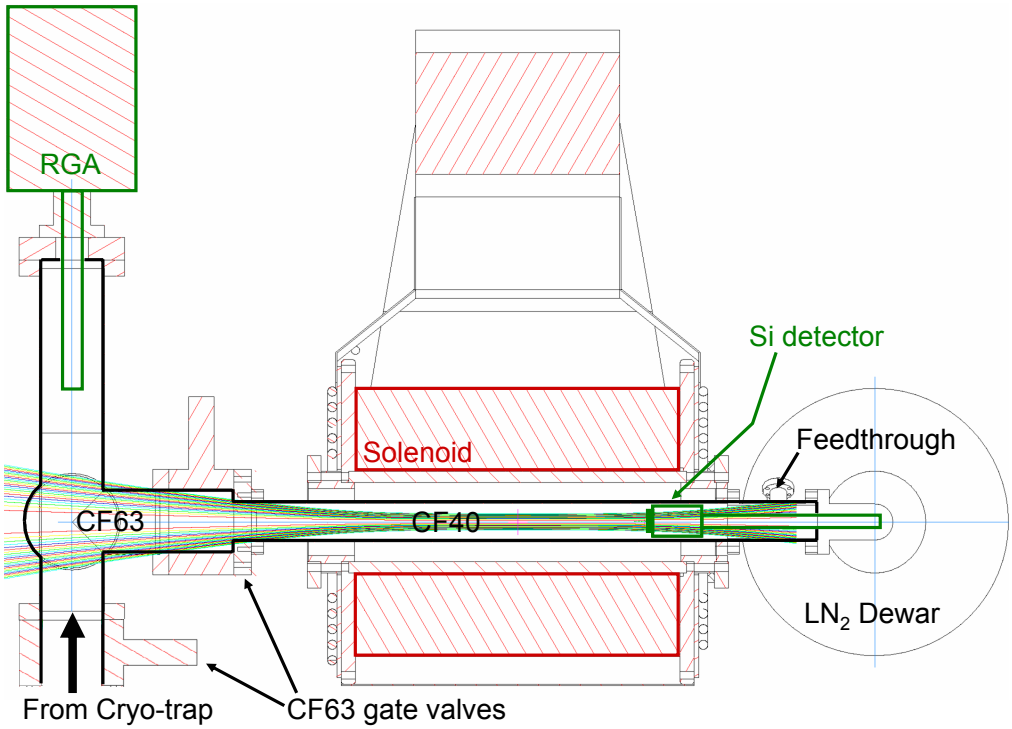

Figure 4.5: The Detection System of TRAP. The Detection System features a residual gas analyzer (RGA) for detection of tritium in the gas phase and a silicon detector for detection of tritium via its decay electrons. (based on [Mel06, Geh06])

The strong support structure that has been built for the detector, the LN_2 dewar and the solenoid is visible in fig. 4.6. The solenoid alone weighs $\sim$ 150 kg and is placed 2 m above ground.

The following sections will introduce the detector components in detail, which is necessary for the discussion of the experimental results. For further information see [Stu07].

4.3.7.1 Requirements for the Si detector and its electronics

In the following, the requirements for the semiconductor detector and its associated electronics are given:

- All components must be vacuum compatible and cavities as well as closed volumes are to be avoided since the total pressure in the Detection System will be as low as 10^{-9} mbar during measurements.
- The measured spectrum is always superimposed by the electronic noise of the detector and its electronics (refer to fig. 4.7). The noise contribution to the detector's signal should therefore be as low as possible.

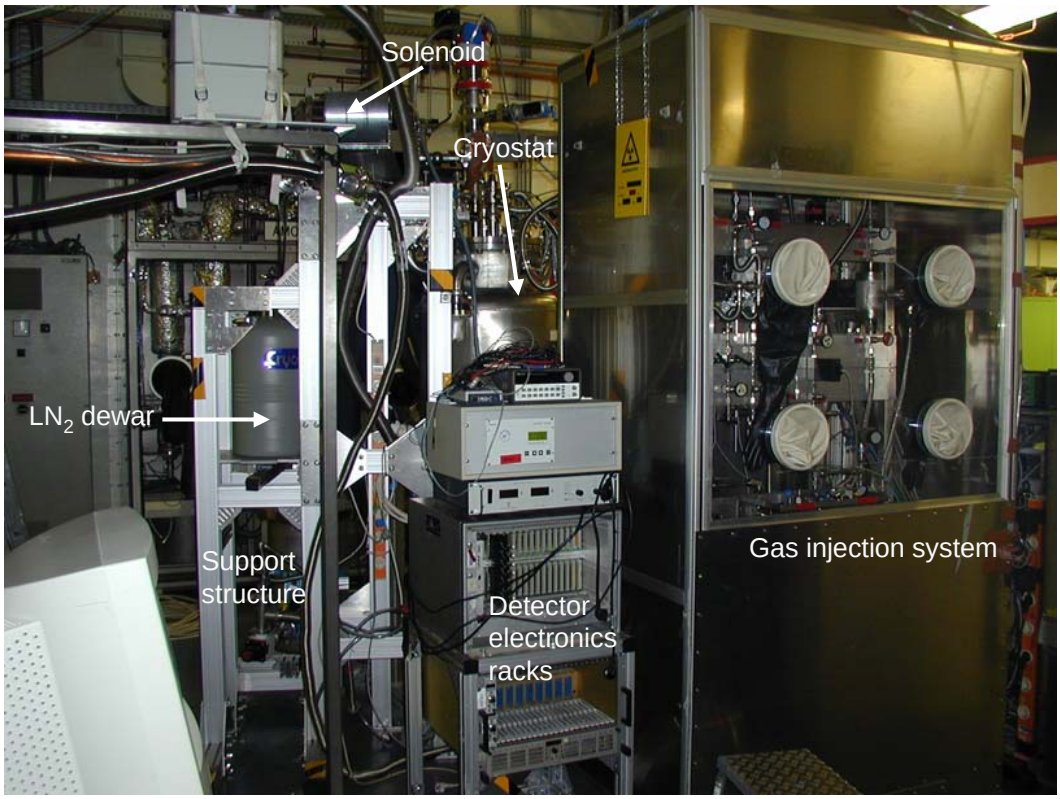

Figure 4.6: Front view of the TRAP experiment.

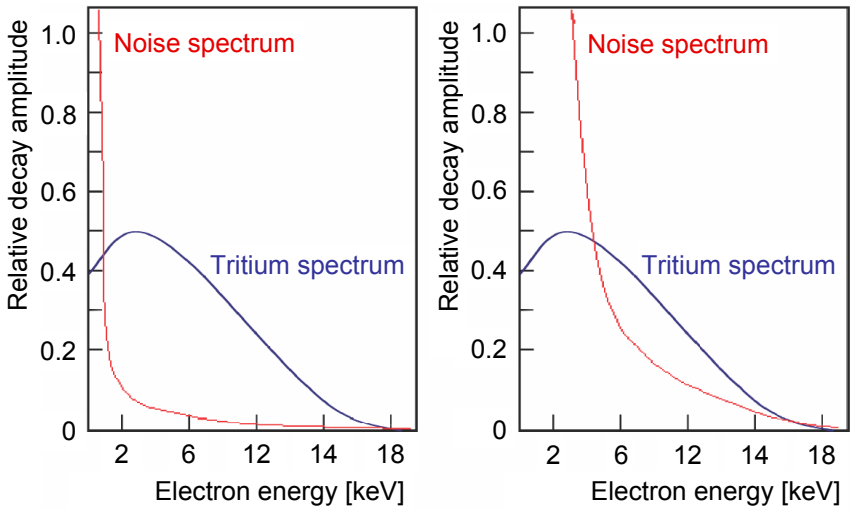

Figure 4.7: Influence of electronic noise on the measured beta spectrum. Left: low electronic noise threshold, the tritium β spectrum will be clearly discernible above the noise; right: high electronic noise, the threshold will overlay the tritium β spectrum. (based on [Stu07])

- The detector should be rather large for a large accepted solid angle. However, this increases its depletion layer capacitance and electronic noise.
- The main noise contribution stems from the first amplification stage, where the signal's strength is still very low (μV). Therefore, it has to be conceived preferably noiseless, cooled like the detector chip itself and positioned near the detector to avoid capacitive disturbances in the connections between the two.
- *Microphonics* has to be avoided with a proper carrier for the detector chip. These acoustic signals excite lattice oscillations in the detector material that superimpose the electric signal.
- For every recorded signal, the time information should be saved, too. Microphonics can then be discriminated by the characteristic fast succession of signals.
- Electrons continuously lose energy while traversing the detector. The amount of energy stored in this way in the so-called *deadlayer* is not visible to the readout electronics. The deadlayer is the detector's top layer that is insensitive to radiation. It consists of SiO_2 in the case of the TRAP detector. Depending on this layer's thickness, the measured spectrum is shifted to lower energies and thus into regions with higher electronic noise contribution. In addition, the detector's energy resolution is decreased. From this follows that the deadlayer must be as thin as possible.

The technically best solution for these issues would be a segmented detector that features a large overall surface with small individual pin sizes. However, such a design requires amplification electronics for each single detector pin which considerably increases costs. For TRAP, the cheaper solution of a standard silicon PIN diode with 300 mm^2 surface area and an in-house produced first amplification stage was chosen.

4.3.7.2 Detector chip

The semiconductor detector from ORTEC is a reverse-biased silicon PIN diode (ORTEC BU-014-300-500, bias voltage 40 V), where the "P" layer is doted with boron and the "N" layer with arsenic. The intermediate layer "I" is of intrinsic silicon material. The diode has an active surface of 300 mm^2 and a depletion layer of 500 μm thickness with a deadlayer of only 50 nm.

Since the original detector housing from ORTEC suffered from very strong microphonics in the energy region of interest up to 20 keV, the Si chip has been removed from its standard shell and glued onto an aluminum-oxide (Al_2O_3) substrate using *Epotek H20E*, a silver epoxy manufactured by *Epoxy Technology*. Figure 4.8 shows the disassembled ORTEC detector and fig. 4.9 the finished TRAP detector. Al_2O_3 was chosen for being an electrical insulator with a high heat conductance value of

$18 - 28$ W$(\mathrm{m} \cdot \mathrm{K})^{-1}$ [ITK06] which is necessary for the detector cooling concept applied in the experiment (refer to sec. 4.3.7.3).

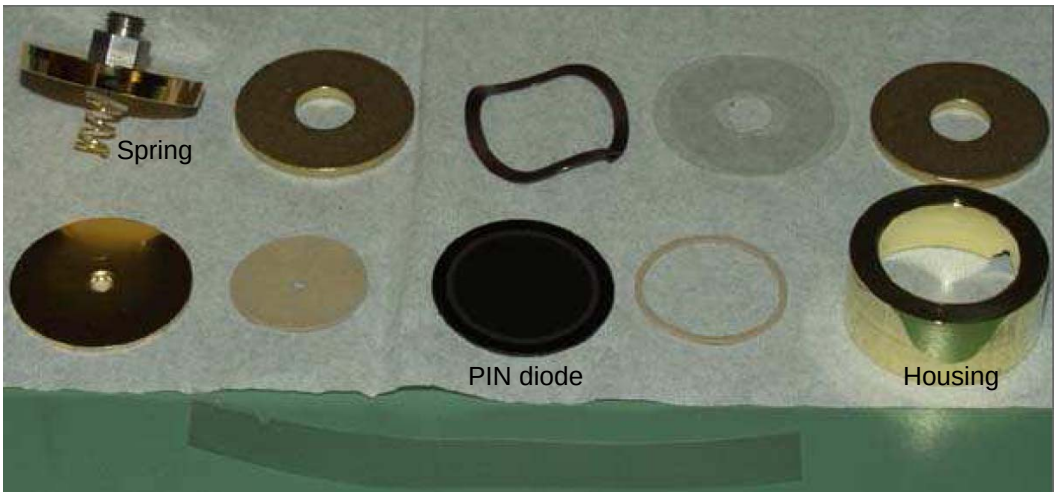

Figure 4.8: Disassembled ORTEC detector BU-014-300-500. The PIN diode was pressed against the housing by the spring visible in the top left. This attachment probably caused vibrational motion which led to the strong microphonics observed with this setup. [Wue04]

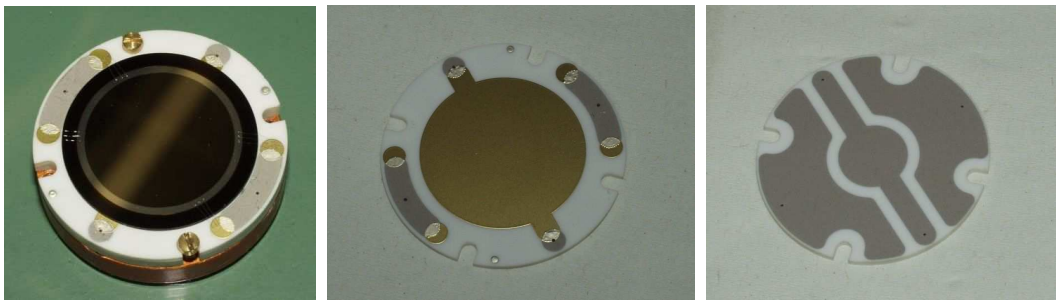

Figure 4.9: The TRAP detector. Left: the Si chip is glued on Al_2O_3 and screwed on a copper ring; center: front side of the Al_2O_3 plate with electric contacts; right: back side. [Wue04]

4.3.7.3 Cooling concept

In order to significantly reduce electronic noise, the detector chip and the first amplification stage (*JFET hybrid*, fig. 4.12) are cooled during operation to approximately $-100°$C by a copper cold finger dipping into liquid nitrogen (refer to fig. 4.10). The silicon detector chip on its Al_2O_3 substrate is screwed onto the hollow ending of the cold finger (fig. 4.11) with the JFET hybrid sticking inside. The electric signals are led out of the vacuum chamber via a feedthrough.

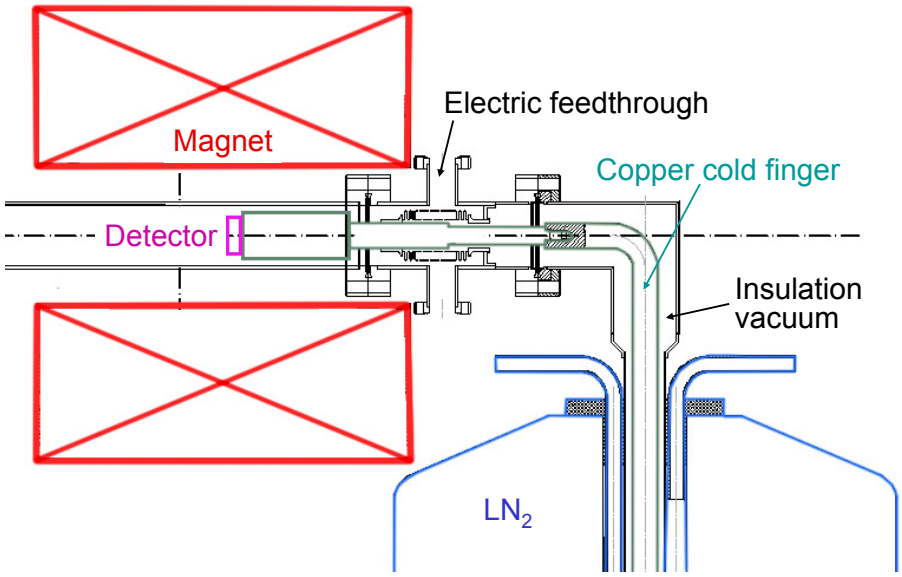

Figure 4.10: Detector cooling concept. The detector and the first amplification stage are cooled via a copper cold finger submerged in liquid nitrogen. (based on [Kaz04])

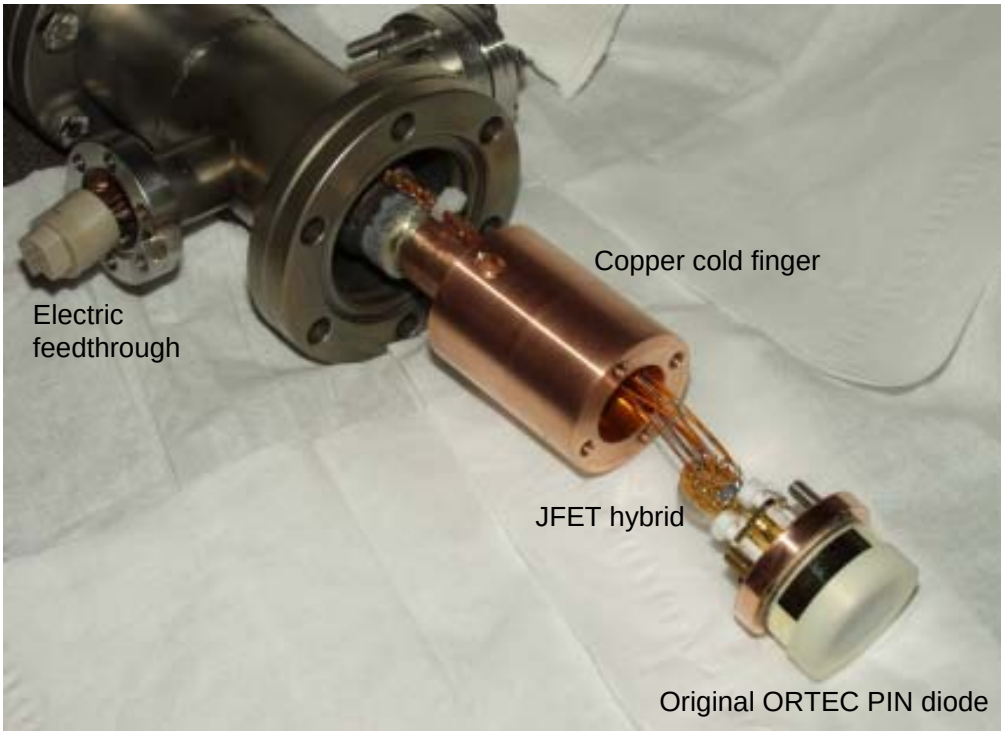

Figure 4.11: Detector bearing. During operation, the copper carrier of the detector is screwed onto the cold finger (the JFET hybrid being enclosed inside). The photo shows the original ORTEC detector that suffered from strong microphonics. It was later exchanged for the one depicted in fig. 4.9.

4.3.7.4 Detector electronics and data acquisition system

An incident β electron creates electron-hole pairs in the detector's semiconductor material, each requiring an energy of 3.7 eV in silicon at $-100°C$. An average tritium β electron of ~ 6 keV will therefore produce around 1621 electron-hole pairs [Stu07]. The bias voltage (40 V) separates these charges so that a current flows.

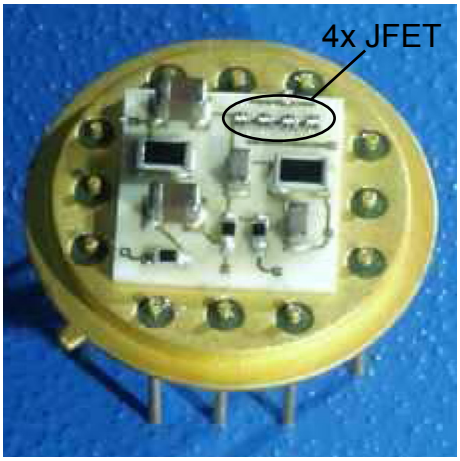

Figure 4.12: Hybrid chip of the first amplification stage. [Wue04]

The electronics connected to the Si detector (refer to fig. 4.13) needs to convert this charge burst into a voltage signal which can then be amplified and recorded with the data acquisition system. Therefore, a resistor is connected in series to the PIN diode and the voltage drop at the resistor due to the electric current is fed into a JFET (Junction Field Effect Transistor). For TRAP four JFETs (Type: IPE-316/4/6 [Wue04]) are operated in parallel as the first amplification stage right behind the Si detector. They are located on the JFET hybrid depicted in fig. 4.11 and in more detail in fig. 4.12. A circuit diagram of the JFET hybrid is available in appendix E.

The voltage signal from the JFET hybrid is led out of the vacuum chamber via an electric feedthrough. Additionally, the pins on the feedthrough are used for the bias voltage, the test pulser input and connections for temperature measurement and heating of the JFET hybrid. The actual pre-amplifier, a reassembled CANBERRA MOD.2001, where the first amplification stage was removed, is located just outside of the vacuum chamber near the feedthrough. Here, the signal is being shaped and amplified. The following main amplifier, built by the University of Washington in Seattle (USA), amplifies the signal further, digitalizes and passes the signal to the data acquisition system ORCA [ORC04] together with a time stamp generated by a trigger card.

The reassembling of the detector chip, the manufacturing of the JFET hybrid and the modification of the pre-amplifier was performed by an expert in the IPE (Institut

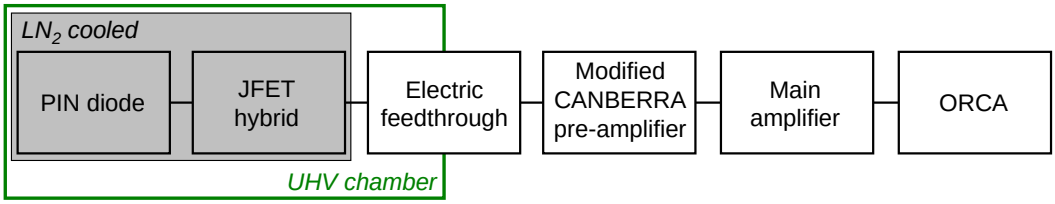

Figure 4.13: Principle of the data acquisition system. (based on [Stu07])

für Prozessdatenverarbeitung und Elektronik) [Wue04].

ORCA, the Object oriented Realtime Control and Acquisition software system, was originally developed for the SNO experiment [SNO00] but will also be used in KATRIN. It allows to set the threshold value of the Analog-to-Digital Converter (ADC) and the gain of the main amplifier. For each event, the energy information as well as the time stamp are saved. For analyzing the spectral data with ROOT [ROO06] various utilities were developed [Stu07].

4.3.7.5 Energy calibration and detector background

It is imperative to check the energy calibration of the detector electronics regularly during the tritium measurements with TRAP. Usually, this is done by using the photopeak in the energy spectrum of γ emitters of specific energy (see fig. 4.14, for example). The sharpness of this peak is defined by the detector's energy resolution at the given energy.

However, this method cannot be applied in TLK, since a handling license exists only for ^{3}H, depleted uranium and, since 2007, ^{83m}Kr and ^{83}Rb for calibration of the KATRIN experiment. The calibration of the detector electronics during the measurements is therefore conducted with a highly accurate pulse generator, that

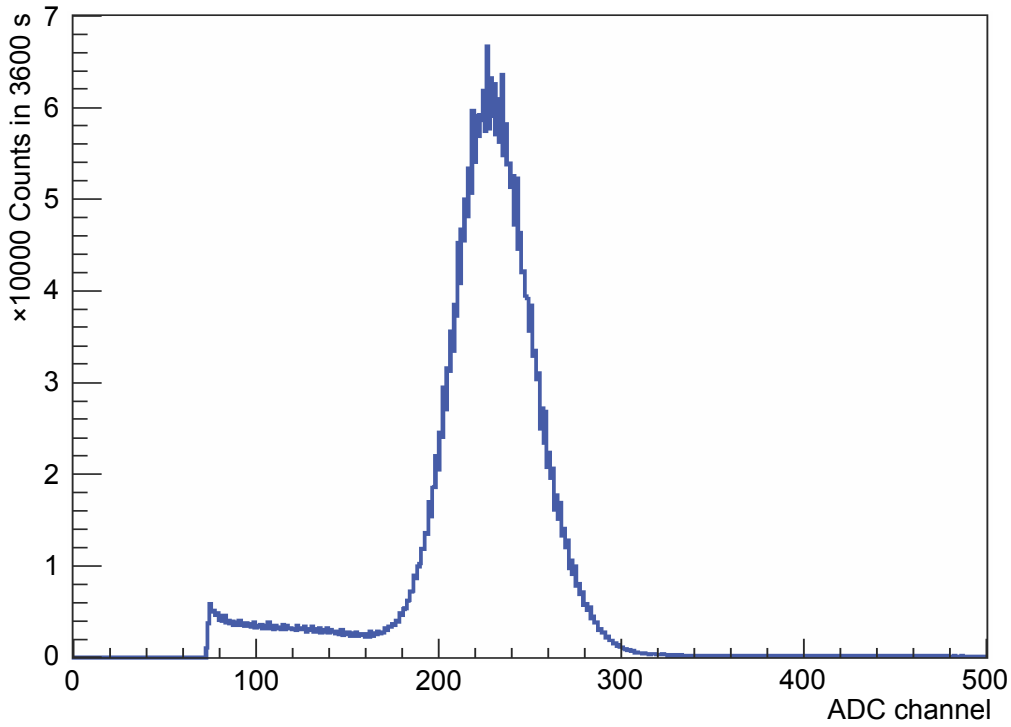

Figure 4.14: Molybdenum spectrum measured with the Si detector. Depicted is the detector response on the K_α line of molybdenum at 17.479 keV. Electronic noise, which dominates the low energy regime, was cut off. (based on [Stu07])

was itself calibrated against nuclear standards in the following way:

1. Before bringing the detector and its electronics to TLK, an ^{241}Am source with different exit windows was used for calibration in a licensed laboratory. The americium emits γ quanta of 59.9 keV which excite characteristic X-ray fluorescence in the window foil. Table 4.1 contains the available windows and their characteristic γ energies. The spectrum was recorded with the detector for each window in order to get the dependence between incident energy and ADC channel.

2. A pulse generator (type *Hewlett Packard 33120A 15MHz Function / Arbitrary Waveform Generator*) was connected to the test input of the JFET hybrid and a voltage signal of $200 - 1000$ mV was applied. From this, the dependence between voltage and ADC channel was obtained.

3. The two results are combined for the dependence between voltage and energy.

Assuming that the energy calibration of the PIN diode is sufficiently stable, the detector electronics can be calibrated without the need for a γ emitter. More information on the calibration of the test pulser is available in [Stu07].

The detector's energy resolution was determined with the ^{241}Am source and the Ba window:

$$\Delta E(\text{FWHM}) = 2.1 \text{ keV} \qquad \text{at} \qquad E \approx 30 \text{ keV}\,. \tag{4.5}$$

As mentioned earlier (sec. 4.3.7.1), a low background threshold is imperative for tritium detection with the Si detector. Before starting any tritium measurements, the background in the energy window $6 - 20$ keV was determined to be as low as 0.07 counts/s, which is sufficient for the TRAP experiment (see sec. 5.3.2).

Table 4.1: X-ray fluorescence energies for various materials. [XRD01]

	Cu	Rb	Mo	Ag	Ba	Tb
E_γ [keV]	8.048	13.37	17.479	22.162	32.193	44.481

Chapter 5

Measurements with TRAP

All runs conducted at the TRAP experiment are summarized in table 5.1. This chapter presents the results from the TRAP runs#3-#6. The last three runs had to be aborted due to an increased tritium contamination in the system in case of runs#7 and #8 and due to mechanical damage in case of run#9. Nevertheless, decontamination methods as described in chapter 6 were developed and tested during these three runs.

This chapter is structured in the following way: The common procedures for all runs are introduced in sec. 5.1. Section 5.2 presents the results obtained in the last deuterium run (TRAP run#3). Before the tritium runs (run#4-#6) are presented in sec. 5.4, the method of tritium detection is explained in sec. 5.3.

Table 5.1: TRAP runs. In the framework of this thesis, runs#3-#9 were conducted. The abbreviations stand for: SS - Stainless Steel, RGA - Residual Gas Analyzer, Si - Silicon detector.

Run	Time [d]	Inj. gas	Detection device	Material in Detection System	Remarks
#1	11	D_2	RGA	as-received SS	commissioning [Eic04]
#2	7	D_2	RGA	as-received SS	commissioning [Eic04]
#3	11	D_2	RGA	electropolished SS	D_2 run (sec. 5.2)
Changes of the experimental rig for tritium operation (appendix A)					
#4	18	tritium	RGA	electropolished SS	tritium runs (sec. 5.4)
#5	32	tritium	RGA/Si	electropolished SS	
#6	39	tritium	RGA/Si	as-received SS	
#7	9	tritium	Si	gold plated SS	aborted: increased tritium contamination
#8	21	tritium	Si	gold plated SS	
Detritiation of the complete TRAP setup, (sec. 6.5)					
#9	56	tritium	Si	gold plated SS	aborted: mech. damage

5.1 Common procedures for all TRAP runs

5.1.1 Cooling of the cryo-surface

All runs with the TRAP experiment start with evacuation of the Cryo-trap and cool-down of the cryostat with liquid helium. In order to maintain a constant cryo-surface temperature of ~ 4.2 K over the whole runtime period, the cryostat needs to be refilled with liquid helium, which is delivered from the liquefier in the ITP to the TRAP experiment in 268 l transport vessels. The refilling is necessary at least every 12 h, the refilling itself taking approximately 1 h. The cryostat is slightly pressurized during operation:

- If the helium exhaust from the cryostat is transferred to ITP through the helium return line (refer to the simplified PID in fig. 4.3), the overpressure in the cryostat is ~ 100 mbar due to the gas conductance of the ~ 300 m long tube to ITP and the pressure in the helium reservoir at ITP. During refillings with liquid helium, the overpressure increases to ~ 200 mbar. The helium return line to ITP is only used when no tritium is injected into the Cryo-trap, that is in deuterium measurements (refer to sec. 5.2) and in tritium measurements during cooldown of the cryostat and preparation of argon condensate.
- During and after tritium injection, the helium from the cryostat is transferred to the laboratory exhaust channel for safety reasons in case of a leak in the Cryo-trap. The cryostat is deliberately pressurized to ≤ 50 mbar overpressure in order to prevent condensation of air inside the cold helium volume. This is done by redirecting the helium exhaust of the cryostat through a regulating valve. Yet, during the refillings with liquid helium, when large helium amounts are to be conducted, the helium is transferred to the laboratory exhaust channel through tubes of high gas conductance. The overpressure in the cryostat then drops to zero.

5.1.2 Preparation of the argon condensate

Before preparation of the argon cryo-deposit, the Cryo-trap is evacuated and cooled down with LHe leading to a total pressure of $\sim 10^{-7}$ mbar in the Cryo-trap. The argon condensate is then prepared during $2-3$ h with an average argon injection rate of $9 \cdot 10^{-3}$ mbar l/s at low liquid helium fill height in the cryostat as explained in sec. 5.2.2.2. The rate of deposition was chosen rather high to obtain a small average crystallite size (refer to sec. 3.3.1). The injection capillary was heated with a heating power of about 20 mW during deposition to prevent freezing of argon inside or on the outside of the capillary. With an argon amount between 75 mbar l (run#6) and 96 mbar l (run#4), a condensate layer thickness of about $1-2$ μm is reached, which corresponds to ~ 1500 monolayers. After condensation of argon on the cryo-surface, the turbomolecular pump VP061 (see simplified PID in fig. 4.3) was used to pump

down any surplus of argon. The argon pressure in the Cryo-trap is higher than the argon saturation pressure at 4.2 K, since surfaces with temperatures above the preparation temperature are also accessible to argon during preparation (e.g. parts above the Cryo-trap).

Morphology studies predict a smaller average crystallite size and hence a higher monolayer capacitance of the argon condensate for preparation temperatures around 5 K compared to those at 4.2 K [Nep05]. In order to reach a higher temperature during argon condensate preparation, the helium pressure in the cryostat was increased to ~ 2 bar absolute pressure during argon deposition in run#6.

5.1.3 Regeneration of the cryo-surface

At the end of each run, the argon cryo-deposit along with any adsorbed tritium needs to be removed from the Cryo-trap. This so-called *regeneration* of the Cryo-trap is achieved by warming up and purging with gaseous helium from top to bottom. A detailed description of the procedure is available in appendix G.

During regeneration, the helium purge gas flow rate needs to exceed the tritium diffusion rate in helium in order to conserve the tritium contamination gradient from high contamination at the injection point (bottom) to low contamination at the exit point (top). The diffusion rate can be estimated as follows:

Einstein's equation [Ott98]

$$\overline{X^2} = 2Dt \tag{5.1}$$

yields the mean squared diffusion length $\overline{X^2}$ within time t. D, being the diffusion coefficient for tritium in helium, should be slightly smaller than the helium self-diffusion coefficient

$$D_{\mathrm{He}} = \frac{\eta}{\rho} \tag{5.2}$$

due to the higher average mass of the tritium isotopomers HT, DT and T_2 (see eqs. 5.2 and 5.3). η is the gas viscosity and ρ the mass density given by

$$\rho = \frac{P}{k_B\,T} \cdot \frac{M_{\mathrm{He}}}{N_A} \tag{5.3}$$

at pressure P and gas temperature T. Herein, $M_{\mathrm{He}} = 4$ g/mol is the atomic weight of helium and N_A the Avogadro constant.

Since an upper limit for $\overline{X^2}$ is sufficient, D_{He} is used in place of D. Assuming $T = 30$ K, $\eta \approx 4 \cdot 10^{-5}$ g cm^{-1}s^{-1} [Lid92] and $P = 1$ bar during helium purging, the mean squared diffusion length is

$$\sqrt{\overline{X^2}} = 0.22 \text{ cm} \tag{5.4}$$

within 1 s.

On the other hand, a purging flow rate of 4 l/min yields an average displacement of

$$\overline{v} = 3.4 \text{ cm/s} \tag{5.5}$$

in the Cryo-trap of tube diameter 5 cm. This helium purging flow rate should superpose any tritium diffusion along the Cryo-trap and is therefore used during the regeneration procedure.

5.2 Deuterium run (TRAP run#3)

Before starting measurements with tritium, three complete runs with deuterium were performed. These runs allowed to test boundary conditions of the TRAP cryo-pump like the maximum pumping speed and capacitance. Since high gas flow rates and amounts are needed for the determination of these parameters, they cannot be measured with tritium due to safety reasons. Results from the commissioning runs#1 and #2 can be found in [Eic04]. In the following, run#3 will be presented. While measuring with deuterium, only the RGA is available for detection in the Detection System.

5.2.1 Description of the deuterium run

At the beginning of run#3 the Cryo-trap was evacuated using the turbomolecular pump VP061 (see fig. 4.3). After cooldown of the cryostat with liquid helium, three experimental phases were conducted during which the cryostat was kept at 4.2 K for nine consecutive days:

- In **phase I**, the gate valve HV061 was closed and deuterium was injected into the Cryo-trap and adsorbed onto the blank stainless steel cryo-surface. The aim was to be able to compare the capacitance and equilibrium pressure of adsorption on stainless steel with those of adsorption on argon condensate as conducted in phase II. When the capacitance limit of the stainless steel surface was reached, the deuterium injection was stopped and the surplus of deuterium gas was pumped with the turbomolecular pump VP061 (refer to sec. 5.2.2.1).
- In **phase II**, argon condensate was prepared as described in sec. 5.1.2 over the layer of previously adsorbed deuterium. Afterwards, the deuterium injection was resumed and deuterium was adsorbed on argon condensate for six days (sec. 5.2.2.2 and 5.2.2.3).
- In **phase III**, the deuterium injection was continued, but the valve HV061 to the turbomolecular pump VP061 was opened to obtain the deuterium flow rate suppression factor of the TRAP cryo-pump (sec. 5.2.2.4).

Finally the Cryo-trap was regenerated by warming up and purging with gaseous helium (refer to sec. 5.1.3).

5.2.2 Results

The results of run#3 are presented as partial pressure data obtained with the residual gas analyzer of $1 - 100$ amu mass range which was calibrated before measurements as described in sec. 5.3.1. The detection limit of the RGA for deuterium is $\sim 5 \cdot 10^{-14}$ mbar (see appendix F). Beyond, the pressure reading is dominated by the RGA's electronic noise superimposed on the ionization current, which can lead to negative pressure readings, too. The silicon semiconductor detector is not available for measurement with non-radioactive deuterium.

5.2.2.1 Deuterium adsorption on stainless steel

TRAP type pumps used for differential pumping in vacuum systems are usually characterized by three parameters: the trapping coefficient $\Gamma = n_{trapped}/n_{in}$, the transmission coefficient $W = n_{trans}/n_{in}$ and the reflection coefficient $R = n_{ref}/n_{in}$, where n stands for the number of gas molecules in each case. These coefficients are related to each other by $\Gamma + W + R = 1$ [Sak88] and were calculated for the TRAP like case of cylindrical tubes with tube length to radius ratio $L/r = 40$ and sticking coefficient $\alpha = 0.6$. The results given in [Smi66] are $\Gamma \approx 0.88$ and $W < 0.001$.

In the first phase of the measurement, deuterium was injected into the Cryo-trap at flow rates of 10^{-6} and 10^{-5} mbar l/s (10 and 100 times higher than expected for KATRIN). As can be seen from fig. 5.1, the pressure in the RGA chamber was of the order of 10^{-13} mbar which is 10 times lower than the vapor saturation pressure of deuterium at 4.2 K [Sou86]. Since R must be very close to zero due to the small diameter of the tritium inlet tube compared to the diameter of the Cryo-trap, $\Gamma \approx 1$ and $\alpha \approx 1$ can be assumed. The beaming effect in TRAP is compensated by the bent in the tube. Taking into account that these parameters are equal for both injection flow rates, the pumping speed limit of the blank stainless steel cryo-surface was not yet reached.

Nonetheless, the capacitance limit was reached with an inlet amount of 1.4 mbar l, which corresponds approximately to one monolayer of deuterium on the cryo-surface taking into account that the physical surface is approximately ten times the geometrical one. The capacitance limit is visible in fig. 5.1 as the strong increase of the partial pressure after approximately 30 h of deuterium injection. Such behavior of the outlet pressure can be explained by a change of the adsorption mechanism from physisorption on stainless steel to pure condensation.

Furthermore, periodic fluctuations of the deuterium partial pressure are apparent corresponding to the 12 h refill periods of the cryostat. During cryostat refills and for approximately two hours afterwards, the overpressure in the cryostat is increased from ~ 100 mbar to ~ 200 mbar (refer to sec. 5.1.1) which, in turn, increases the helium temperature by ~ 0.1 K [Mal73] and therefore the deuterium partial pressure.

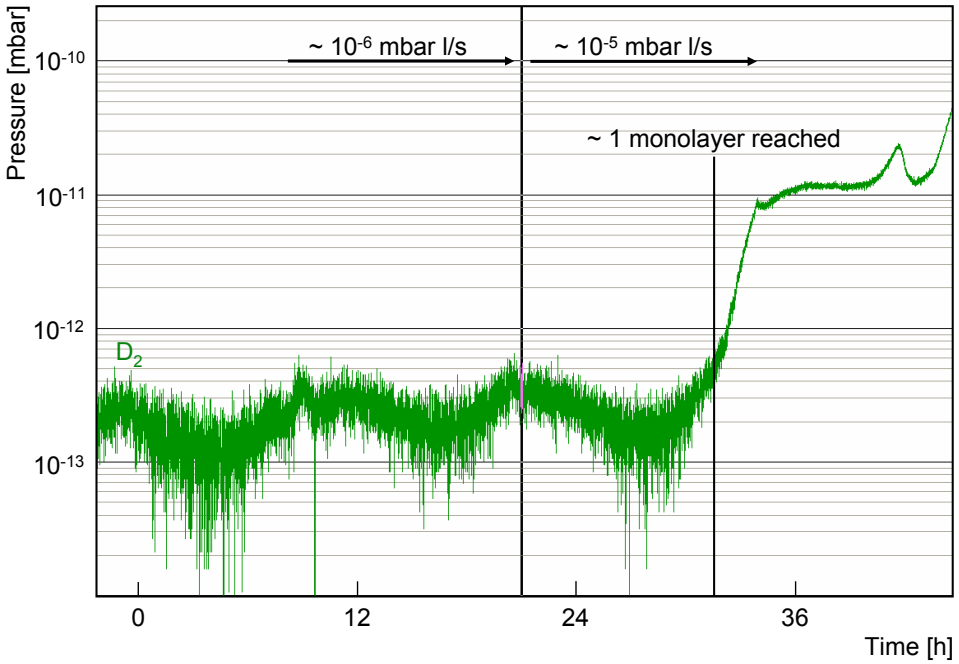

Figure 5.1: Run#3: Deuterium adsorption on stainless steel. Displayed is the time development of the deuterium partial pressure reading of the $1 - 100$ amu RGA. Two different deuterium injection rates (10^{-6} mbar l/s and 10^{-5} mbar l/s) were used. The capacitance limit is visible as the pressure increase after approximately one monolayer of deuterium on stainless steel is reached.

5.2.2.2 Argon pressure variation in time

After reaching the capacity limit of the pure stainless steel substrate, the argon condensate ($\sim$ 91.7 mbar l) was prepared on the previously adsorbed deuterium at $\sim$ 4.2 K as described in sec. 5.1.2

The time evolution of the argon partial pressure after preparation is shown in fig. 5.2. One again observes a 12 h periodical rise of the partial pressure as it was the case with the deuterium pressure (sec. 5.2.2.1). The argon pressure then exceeds the limit of 10^{-11} mbar expected from the diagram in fig. 3.4. The explanation for this behavior is the following: When the cryostat refilling is started and the LHe in the cryostat starts to boil, the parts of the *connecting tube* (fig. 4.4) inside the cryostat which are above LHe level are cooled to lower temperatures thus adsorbing more argon and decreasing the equilibrium pressure; the argon pressure drops instantaneously. When the liquid helium level decreases with time, these parts of the tube emerge from the LHe and are warmed up again, releasing argon. During these adsorption-desorption cycles, argon is gradually transferred to parts of the tube which are always below the LHe level and at $\sim$ 4.2 K: the argon partial pressure diminishes with time which is visible in fig. 5.2, too. Therefore, surfaces with a temperature above the cryo-surface temperature should be avoided during argon preparation. This has to be considered in the design of the CPS, too.

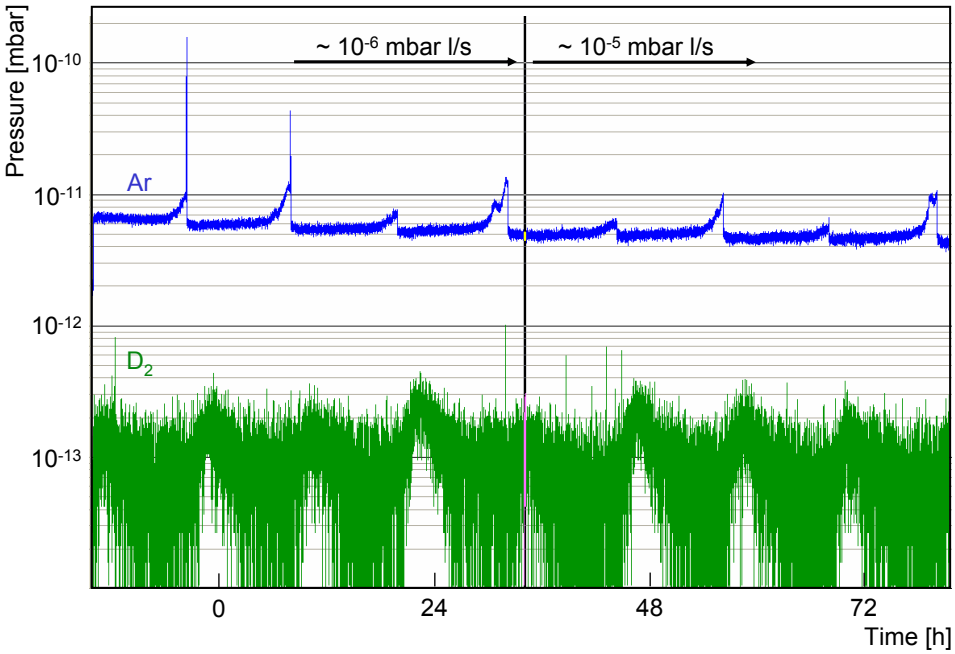

Figure 5.2: Run#3: D_2 adsorption on argon. Displayed is the time development of the argon and deuterium partial pressure readings of the $1 - 100$ amu RGA. Two different deuterium injection rates (10^{-6} mbar l/s and 10^{-5} mbar l/s) were used.

Since we were already aware of this fact from the previous commissioning runs#1 and #2, where the argon peaks even reached 10^{-8} mbar, the argon condensate was prepared at a LHe fill height below the minimum fill height of standard operation depicted in fig. 4.4.

5.2.2.3 Deuterium adsorption on argon cryo-deposit

In phase II of the measurement run, deuterium was injected and adsorbed on argon cryo-deposit. The time evolution of the deuterium partial pressure is shown in fig. 5.2. The injection rate was at first set again to 10^{-6} and 10^{-5} mbar l/s. Again the periodic 12 h fluctuations are visible, yet the capacity of the argon cryo-deposit for deuterium is much higher than that of the pure stainless steel cryo-surface. The injection rate was even further increased to 10^{-4} mbar l/s leading to a D_2 partial pressure above the detection limit (see fig. 5.3).

The binding energy per mole adsorbate E_B can be estimated assuming steady state conditions in the Cryo-trap: In this case the injection flow rate equals both the total adsorption rate on the cryo-surface as well as the total desorption rate everywhere along the cryo-surface. The desorption rate dn_D/dt is given by eq. 3.8. With $dn_D/dt \approx 2.75 \cdot 10^{-4}$ mbar l/s and $n \approx 3 \cdot 10^{20}$ molecules, one obtains a binding energy around 1400 J/mole, which is comparable to available literature data [Hae81]. On the other hand, calculating the equilibrium pressure according to eq. 3.9 yields $P_{eq} \approx 10^{-9}$ mbar for $\alpha \approx 0.7$ in the case of deuterium adsorption

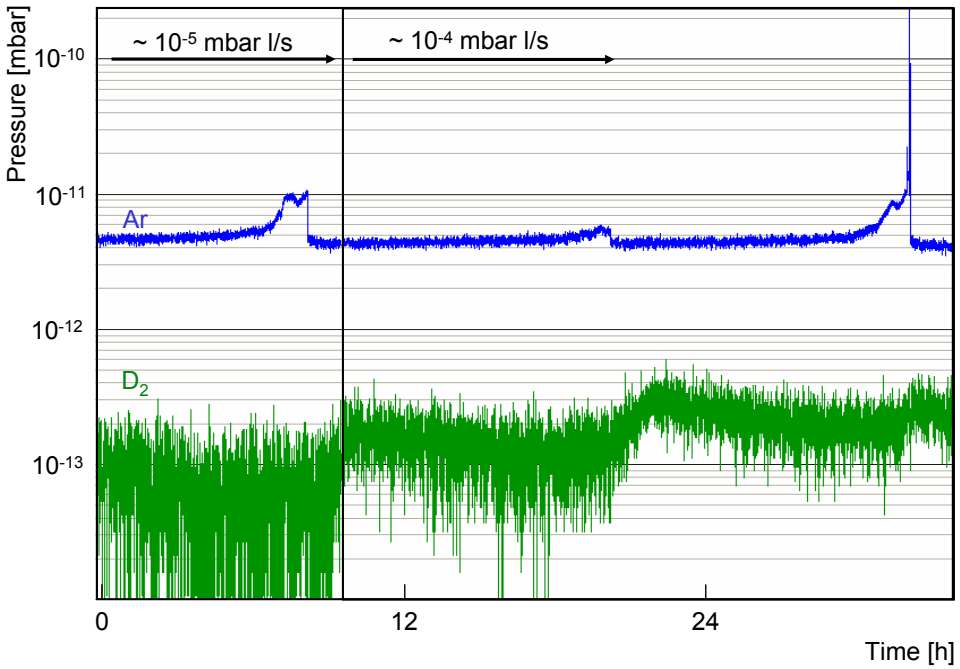

Figure 5.3: Run#3: Deuterium adsorption on argon at high injection rate. Displayed is the time development of the argon and deuterium partial pressure readings of the $1 - 100$ amu RGA. Two different deuterium injection rates (10^{-5} mbar l/s and 10^{-4} mbar l/s) were used. For the higher injection rate, an equilibrium pressure above the RGA's detection limit of $\sim 5 \cdot 10^{-14}$ mbar is reached.

on argon condensate [Hae81]. Since the RGA shows a deuterium partial pressure between $10^{-13} - 10^{-12}$ mbar (fig. 5.2) this can be seen as a clue that the assumption of steady state along the cryo-surface is not valid. Rather, the adsorption and desorption rates will be higher at the deuterium injection point and lower towards the upper end of the Cryo-trap.

5.2.2.4 Deuterium flow rate suppression factor

In the last phase of the experiment (phase III), the deuterium flow rate suppression factor

$$F = \frac{Q_{in}}{Q_{out}} \tag{5.6}$$

of the Cryo-trap was estimated.

The incoming deuterium flow rate Q_{in} equals the injection rate which can be calculated from the pressure drop in the inlet buffer vessel. It was set to

$$Q_{in} \approx 10^{-3} \text{ mbar l/s}\,. \tag{5.7}$$

The outgoing deuterium flow rate Q_{out} was determined by continuous pumping of the Cryo-trap with the turbomolecular pump (TMP) VP061 during deuterium injection (refer to fig. 5.4):

The pumping speed of the pump is known for helium from the technical specifications ($S = 150$ l/s) and the vacuum conductance C of the channel connecting this pump to the Cryo-trap can be calculated using eq. 4.4. With

$$S_{eff}^{-1} = S^{-1} + C^{-1} \tag{5.8}$$

and $M = 4$ g/mol, $T \approx 296$ K, $D = 6$ cm and $L \approx 30$ cm, one obtains:

$$Q_{out} = S_{eff} \cdot p \approx 5 \cdot 10^{-12} \text{ mbar l/s}\,. \tag{5.9}$$

Herein $p \approx 5 \cdot 10^{-14}$ mbar is the deuterium partial pressure measured with the residual gas analyzer. Since the deuterium pressure is at the detection limit of the mass filter in this mode of operation, one can only give an upper limit for the deuterium pressure resulting in an upper limit for the outgoing flow rate Q_{out} and a lower limit for the flow rate reduction factor

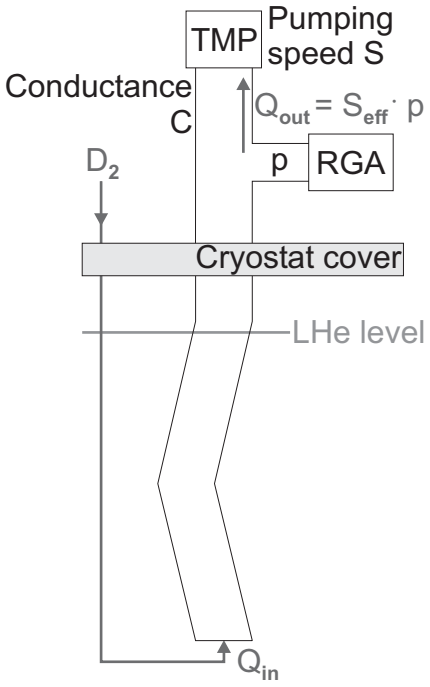

Figure 5.4: Run#3: Deuterium flow rate suppression factor. Schematic for calculation (see text).

$$F = \frac{Q_{in}}{Q_{out}} > \frac{10^{-3} \text{ mbar l/s}}{5 \cdot 10^{-12} \text{ mbar l/s}} = 2 \cdot 10^{8}\,. \tag{5.10}$$

The scheme of this approximation is quite realistic for the given KATRIN geometry where the Pre-spectrometer functions just like a turbomolecular pump with a high pumping speed for hydrogen isotopes.

5.2.3 Conclusions

During this test measurement with deuterium, the flow rate suppression factor was determined. Compared to the design value of $F > 10^7$ for the CPS [KAT04], the result for deuterium looks very promising. Although TRAP itself is shorter than the complete CPS, it can still manage to provide a higher suppression factor than demanded. On the other hand one should not forget that this value is only valid for deuterium, where no radioactivity is present. The influence of radioactivity on the pumping properties can only be investigated by using tritium instead (see sec. 5.4).

Special care needs to be taken when specifying the CPS to prevent a high argon gas load to the Pre-spectrometer. Therefore a cold valve separating the cold ($3 - 4.5$ K) from the warm ($77 - 300$ K) part of the CPS is suggested to be introduced into the design (see sec. 7.2).

5.3 Tritium detection and surface effects in TRAP

Before presenting the results obtained during the tritium runs, the method of tritium detection shall be introduced first. Figure 5.5 shows the Detection System where the outgoing tritium flow rate Q_{out} from the Cryo-trap, which equals the incoming flow rate into the Detection System, is marked along with several components it can be subdivided into:

Q_G: accumulation rate of tritium in the gas phase increasing the tritium pressure
Q_W: accumulation rate of tritium on the walls of the Detection System
Q_D: adsorption rate of tritium on the detector surface
Q_C: adsorption rate of tritium on the copper cold finger shown in fig. 4.11
Q_B: permeation rate of tritium into the walls' bulk material[1]

$$Q_{out} = Q_G + Q_W + Q_D + Q_C + Q_B \,. \tag{5.11}$$

The first constituent Q_G can be determined by the RGA, the second two Q_W and Q_D are accessible with the Si detector. However, the last two are not directly accessible and will be estimated or in case of Q_B addressed by employing gold plated tubes for future measurements (refer to sec. 5.3.5).

[1]The adsorption rate of tritium on the walls of the Detection System is the sum of the accumulation rate Q_W and the permeation rate Q_B. Only in case of negligible Q_B, the tritium adsorption rate on the walls is represented by Q_W alone.

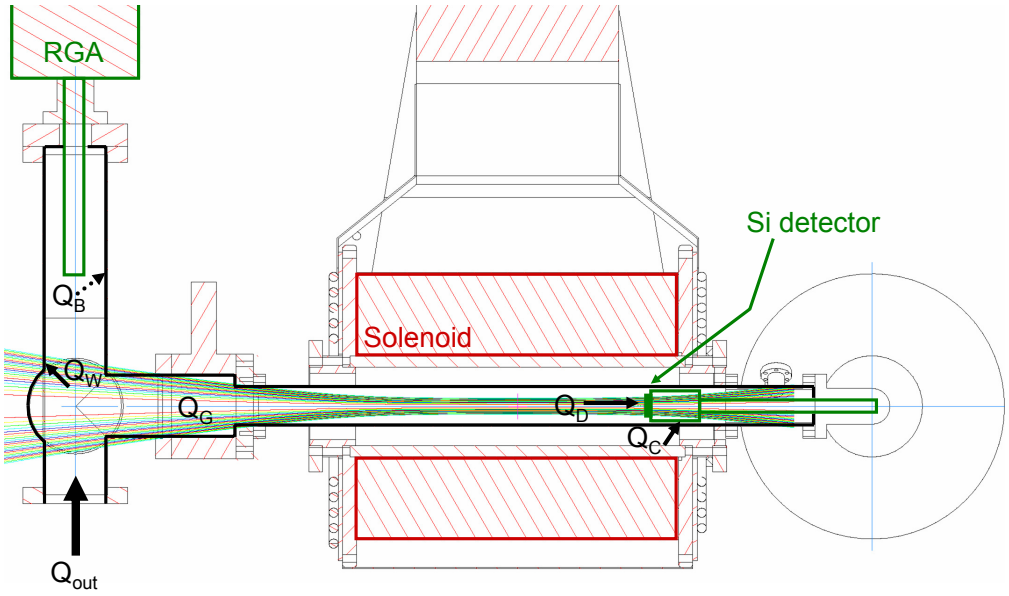

Figure 5.5: Constituents of the outgoing flow rate. Tritium entering the Detection System is either accumulated in the gas volume increasing the pressure (accumulation rate Q_G), accumulated on the walls of the Detection System (accumulation rate Q_W), adsorption on the cold detector surface (adsorption rate Q_D), adsorbed on the copper cold finger (adsorption rate Q_C) or diffuses into the bulk material of the Detection System's walls (diffusion rate Q_B). (based on [Mel06, Geh06])

5.3.1 Tritium detection with the RGA

A residual gas analyzer directly detects tritium in the gas phase and can therefore be used to obtain the accumulation rate in the gas phase Q_G (refer to fig. 5.5). Two different RGAs are available, albeit not simultaneously: a $1-100$ amu and a high resolution $1-6$ amu RGA from MKS (technical specifications in appendix F).

During the tritium runs, DT (atomic mass 5) was used for observation for the following reasons:

- DT is the most abundant isotopomer in the inlet mixture. Not pure tritium but a hydrogen mixture containing tritium atoms is injected in the experiments (refer to sec. 5.4.1).
- Mass 5 showed the lowest background reading of the tritium isotopomers HT, DT and T_2 prior to tritium injection.
- DT is pumped worse on Ar frost than T_2, since the saturated vapor pressure of condensation is lower for T_2 than for DT [Sou86]. The DT pressure will thus give an upper limit for the T_2 pressure.
- HT, although being the worst of the tritium isotopomers to be pumped (see sec. 3.4.2), could not be used for observation, since mass 4 could be HT, D_2 and He. It was impossible, even with the high resolution $1-6$ amu RGA, to separate D_2 from HT. Yet, D_2 and He could be separated (masses calculated using data from [Lid92]: He 4.0026 g/mol, HT 4.0239 g/mol, D_2 4.0282 g/mol).

Prior to the tritium measurements, both RGAs were calibrated against a cold cathode total pressure gauge using the appropriate correction coefficients for the gases in question [Ley02]: The $1-100$ amu RGA using both He and Ar at $\sim 10^{-5}$ mbar, the $1-6$ amu RGA with He at $\sim 10^{-6}$ mbar.

5.3.2 Tritium detection with the Si detector

The Si detector is used to detect tritium nuclei via their beta decay electrons, which hit the detector creating an energy signal between 0 and 18.6 keV. Unlike the RGA, the Si detector is primarily sensitive to tritium located on the walls of the Detection System and on the detector surface itself, which makes the contributions Q_W and Q_D in eq. 5.11 accessible. The total contribution to the detector's count rate from tritium in the gas phase is negligible, as the following calculation demonstrates:

As we shall later see (sec. 5.4.2.1), the DT partial pressure in the Detection System ($V \approx 2.5$ l) never exceeds 10^{-13} mbar. Therefore, the maximum tritium decay rate in the gas phase amounts to $dN/dt \approx 0.011$ s^{-1} at room temperature[2], which is also

[2]The ideal gas law $PV = Nk_BT$ and the decay equation $-dN/dt = \lambda N$ with the tritium decay constant $\lambda = 1.78 \cdot 10^{-9}$ s^{-1} were used in the calculation.

the maximum count rate possibly observed on the detector. The real count rate will be much lower due to the geometry, the detection probability and the region of interest chosen (see sec. 5.3.2.1). For comparison: The count rates one obtains during the measurements in the energy window $6 - 20$ keV are between 0.2 s^{-1} and 2 s^{-1} (sec. 5.4.2.2). The contribution of tritium in the gas phase to the count rate measured with the detector is therefore negligible.

Furthermore, the Si detector is sensitive to all other radiations from any source which might hit its surface. Since the RGA's filament casts light on the detector, the Si detector and the RGA cannot measure simultaneously.

5.3.2.1 Spectral shape

Figure 5.6 shows the integral tritium spectrum measured with the Si detector during run#6 (see sec. 5.4) together with a simulated one. Both fit well above ~ 5.5 keV. Below this value the measured spectrum is dominated by electronic noise. Therefore, the energy window for tritium detection in TRAP has been set to $6 - 20$ keV: The lower cut suppresses electronic noise, the upper one marks approximately the endpoint of the tritium β spectrum taking the ~ 2.1 keV detector energy resolution at

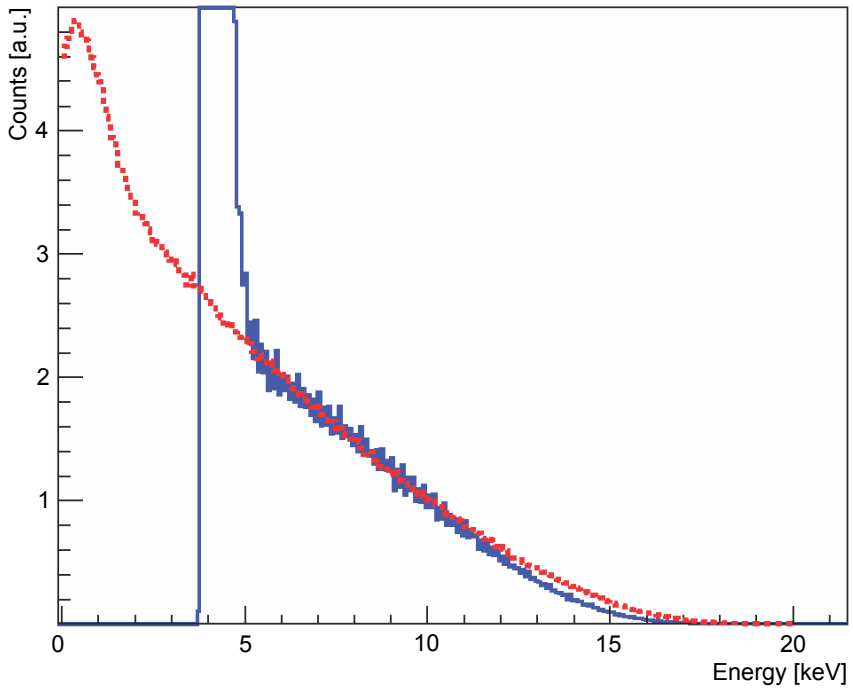

Figure 5.6: Tritium spectrum measured with the Si detector during run#6. Scaled to the experimental spectrum is a simulated one of a Si detector with 2.1 keV energy resolution and 50 nm dead layer. Deviations between the two are based on inaccuracies in the detector response models and on electronic noise which is not considered in the simulation. (based on [Stu07])

30 keV into account. Prior to any tritium measurement, the background count rate (electronic noise) in the energy window amounted to ~ 70 counts/1000 s (70 mHz).

Since radioactive decay is a random process following Poisson statistics, an exponential dependence of the time difference distribution of two consecutive events is to be expected as shown exemplarily in fig. 5.7 for the detector run 4442 during TRAP run#6. In particular background events originating from vibrational microphonics would lead to distortions in the time difference distribution and, indeed, some detector runs are affected by such noise. As it turns out, microphonics at the TRAP detector induces signals, which are quite similar to the tritium β spectrum. If a discrimination between real β signals and noise signals is not unambiguously possible, it is advantageous to process data including this vibrational noise, as this will lead to an over-estimation of tritium in the Detection System.

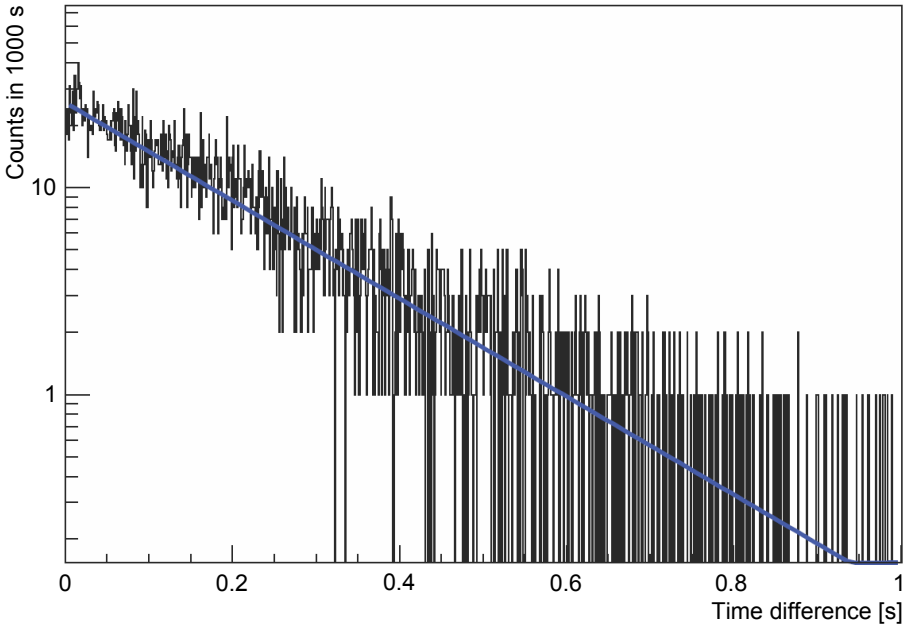

Figure 5.7: Time difference distribution of detector run 4442. The time difference between two successive events shows an exponential behavior. (based on [Stu07])

5.3.2.2 Detector count rate and magnetic field

The Si detector is used to detect tritium nuclei via their radioactive decay. The tritium β electrons hit the Si detector creating N events in the energy window $6-20$ keV during a detector run period $\Delta t = 1000$ s. If the detector run was started at time t, the average count rate is given by

$$A(t) = \frac{N}{\Delta t}\,. \tag{5.12}$$

The TRAP experiment has two operational modes when measuring with the Si detector, which lead to two different count rates:

- **Magnetic field off:** The count rate at the detector is $A_{off}(t)$, originating from β electrons hitting the detector surface by chance. A_{off} is primarily generated by tritium adsorbed on the cold detector surface.

- **Magnetic field on:** The count rate at the detector is $A_{on}(t)$. Three different mechanisms are involved in generating the count rate:

  1. β electrons from tritium adsorbed on the detector hit the detector directly.
  2. β electrons from tritium adsorbed on the detector travel away from the detector and are reflected back at the magnetic pinch in the middle of the solenoid. They are then guided along the magnetic field lines onto the detector surface (also see fig. 5.5).
  3. β electrons from tritium located on the stainless steel walls of the Detection System are guided magnetically to the detector surface (fig. 5.5).

Generally $A_{on} > A_{off}$ holds true.

5.3.2.3 From count rate to surface contamination

The tritium adsorption rate on the detector surface Q_D and the accumulation rate on the walls of the Detection System Q_W can be determined from the count rates $A_{off}(t)$ and $A_{on}(t)$. In order to achieve this, we first need to calculate the time-dependence of the tritium surface contamination on the detector $C_D(t)$ and on the walls of the Detection System $C_W(t)$ (both in Bq). These contaminations transfer to the count rates with and without magnetic field in the following way:

$$A_{off} = c \cdot C_D + a \cdot C_W \tag{5.13}$$

$$A_{on} = r \cdot c \cdot C_D + b \cdot C_W \tag{5.14}$$

with constants a, b, c and r:

a: fraction of the wall contamination detected by the detector with magnet off
b: fraction of the wall contamination detected by the detector with magnet on
c: fraction of the detector contamination detected by the detector with magnet off
r: reflection coefficient due to the reflection of decay electrons in the magnetic field

Using eq. 5.13 and 5.14, one can calculate the surface contaminations in terms of the measured count rates A_{off} and A_{on}:

$$C_W = \frac{r \cdot A_{off} - A_{on}}{r \cdot a - b}\,, \tag{5.15}$$

$$C_D = \frac{A_{off}}{c} - \frac{a}{c} \cdot \frac{r \cdot A_{off} - A_{on}}{r \cdot a - b} \tag{5.16}$$

$$\approx \frac{A_{off}}{c} \qquad (a \ll c)\,. \tag{5.17}$$

The parameters a, b, c and r are specific to the TRAP geometry and its magnetic field. Since the cyclotron radii[3] [Ott98]

$$r = \frac{\sqrt{2Em_e}}{Be} \tag{5.18}$$

of tritium decay electrons in the Detection System's magnetic field are similar to the tube dimensions, it is difficult and questionable to estimate the parameters a, b, c and r from purely geometrical considerations. Instead, an electron tracking Monte Carlo (MC) simulation was implemented in a diploma thesis [Stu07] supervised during this work.

5.3.2.4 Monte Carlo electron tracking simulation

The above parameters a, b, c and r were determined via an electron tracking MC Simulation using electron tracking code also employed for electromagnetic field calculations for the KATRIN spectrometers [Glü06]. The simulation of tritium decay in the TRAP Detection System works in the following way [Stu07]:

1. Homogeneous distribution of DT molecules on the detector surface and the walls of the Detection System. This assumption is quite realistic taking into account that the hydrogen surface diffusion coefficient will be high at 300 K.

2. Simulation of tritium decay: randomized heading of outgoing β electrons and their energy using a discrete tritium β spectrum

3. Stepwise tracking of electrons in the magnetic field, collision check with walls or the detector after each step

4. If the walls are hit: The electron is lost, no implementation of backscattering from the walls since the contribution is negligible [Stu07].

5. If the detector is being hit:

   - Simulate the backscattering probability of electrons on the detector surface along with the energy loss while passing the detector dead layer. A new electron tracking loop is started for the backscattered electron, which might again hit the detector due to reflection in the magnetic field.
   - Simulate the detector response along with the energy loss in the detector dead layer and the detector's energy resolution.

[3] Non-relativistic approximation with radius r, kinetic energy of electrons E, electron mass m_e, magnetic field B and elementary charge e

Improvements[4] with regard to the originally published result in [Stu07] yield the following constants:

$$a = (6.51 \pm 0.07) \cdot 10^{-4}\,, \tag{5.19}$$
$$b = (1.58 \pm 0.01) \cdot 10^{-3}\,, \tag{5.20}$$
$$c = (7.12 \pm 0.03) \cdot 10^{-2} \text{ and} \tag{5.21}$$
$$r = 1.21 \pm 0.01\,. \tag{5.22}$$

The errors are statistical errors of the MC simulation [Stu07].

Not considered in the simulation are the production of secondary electrons and collisions of the decay electrons with residual gas molecules. In the first process electrons with energies < 50 eV are produced [Rei77], which is far below the relevant energy window $6 - 20$ keV. Collisions with molecules of the residual gas can be neglected at the standard operation pressure of $< 10^{-8}$ mbar.

Yet, other issues exist which are not included in the simulation. First and foremost is the assumption that tritium is decaying on the surface of the stainless steel wall, which is a simplification in view of surface roughness and the existence of surface water (refer to sec. 5.3.4): It is probable that decay electrons lose energy while traversing from cavities to the stainless steel surface or deposit energy in the surface water layer. Thus, a systematic error of 100% was assumed on C_W. The systematic error on C_D was assumed to be 100%, too, if C_D was calculated with the exact relation in eq. 5.16. A smaller systematic error of 30% was applied on C_D for the calculation according to the approximation in eq. 5.17 since this equation depends on c alone.

Figures 5.8 and 5.9 show the regions of the Detection System's walls from where decay electrons are guided to the Si detector with magnet off and on, respectively. Only a small fraction of the decay electrons starting from the walls of the Detection System at a certain location Z actually reach the detector. Furthermore, the results of the MC simulation are reasonable concerning the regions of the Detection System from where decay electrons can reach the detector:

- The fraction of decay electrons, that start at a certain distance Z from the detector and reach the detector surface, is very low without magnetic field ($< 2.4\%$). The fraction drops rapidly with increasing Z (see fig. 5.8).
- A small fraction of decay electrons starting from the spherical wall of the T-piece facing the detector reach the detector by chance (see fig. 5.8).
- The detector is shielded from some wall regions; none of the decay electrons starting from these walls reach the detector (see fig. 5.9).
- The fraction of decay electrons which are guided onto the detector along the magnetic field lines is highest for the spherical wall of the T-piece facing the detector (see fig. 5.9).

[4] The internal surfaces of the gate valves in the Detection System were not considered before.

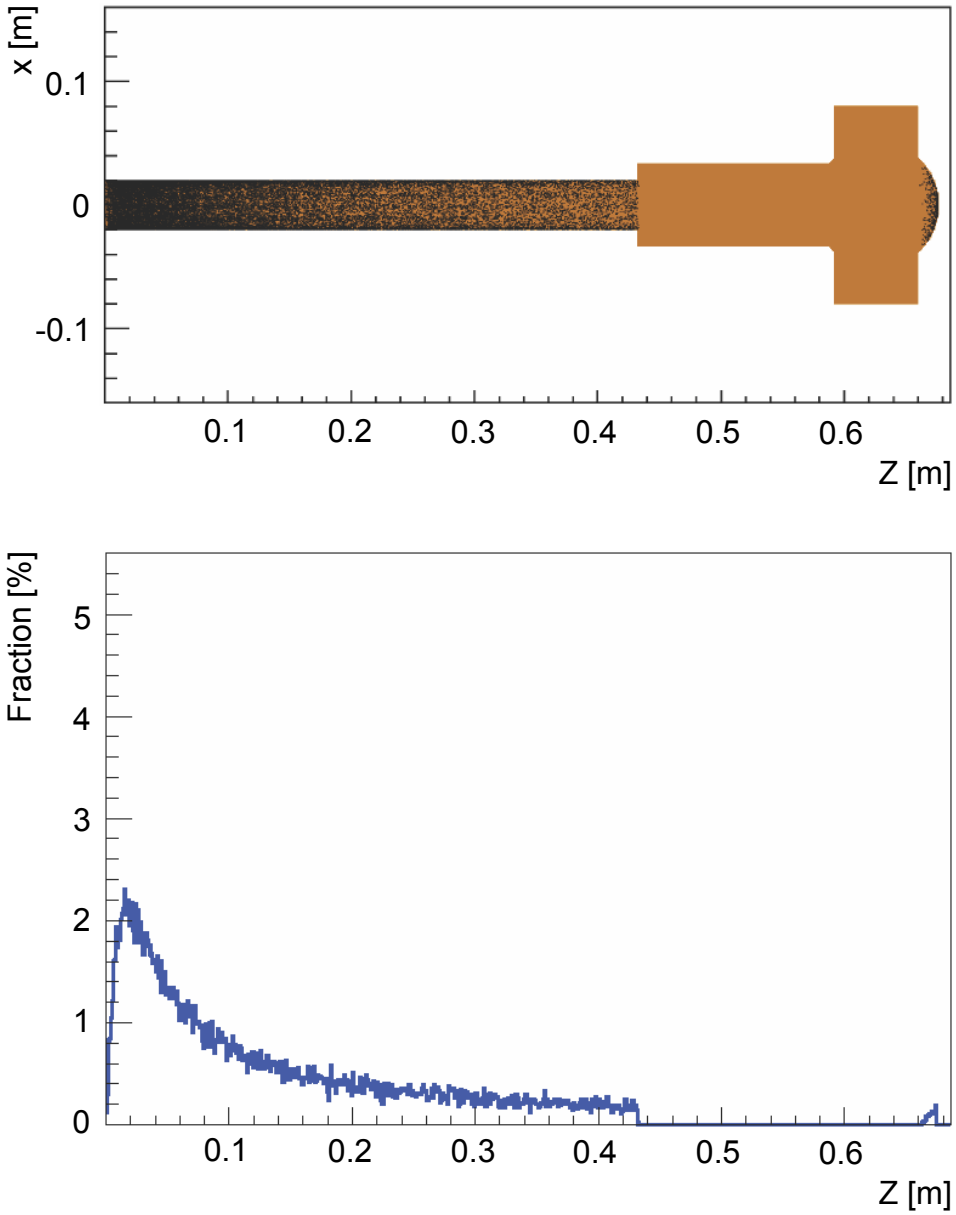

Figure 5.8: Results of MC simulation: magnet off. The Monte Carlo simulation allows for the identification of the Detection System's walls from where decay electrons can reach the detector. These wall regions are shown in black in the upper picture, the detector being at $Z = 0$. The lower picture shows the portion of electrons starting at respective Z positions that actually hit the detector. As expected, the portion of decay electrons reaching the detector drops with Z. (based on [Stu07])

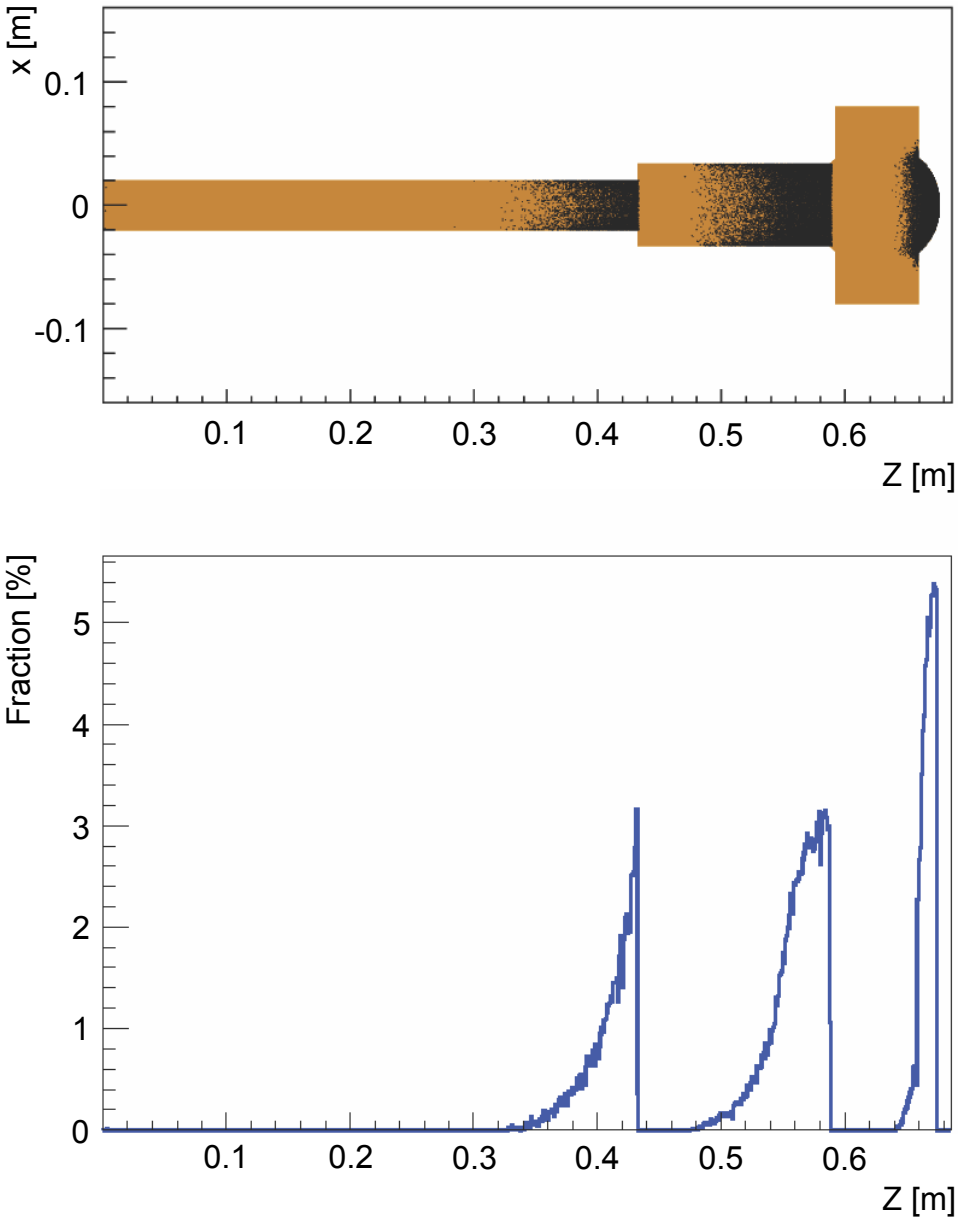

Figure 5.9: Results of MC simulation: magnet on. The Monte Carlo simulation allows for the identification of the Detection System's walls from where decay electrons are guided along the magnetic field lines to the detector. These wall regions are shown in black in the upper picture, the detector being at $Z = 0$. The lower picture shows the portion of electrons starting at respective Z positions that actually hit the detector. Only a few percent of all the decay electrons in the Detection System are detected. (based on [Stu07])

5.3.3 Tritium adsorption on the silicon detector

Tritium is being adsorbed on the detector surface since the detector contamination C_D increases with time as we shall see in sec. 5.4.2.3. The removal of this contamination from the detector can be achieved by heating the detector to $\sim 75°C$ for half a day which causes the detector count rate to drop back to the background rate of about 70 mHz in the energy window $6 - 20$ keV. Therefore, it is reasonable to assume pure physisorption of tritium on the cold detector which consists of SiO_2 and pre-condensed H_2O. The latter is still present in the Detection System since baking of the detector and the first amplification stage is not available above 80°C.

If steady state is not yet reached, the effective adsorption rate of hydrogen molecules Q_2 (Q=H,D,T) on the detector surface is given by

$$\frac{dn}{dt} = \frac{dn_A}{dt} - \frac{dn_D}{dt}\,, \tag{5.23}$$

where n is the number of Q_2 molecules adsorbed on the detector. The adsorption rate dn_A/dt and the desorption rate dn_D/dt are given by eq. 3.7 and eq. 3.8, respectively. Under the assumption of constant pressure P, one obtains a linear differential equation for the time dependence of the detector contamination $n(t)$, which is solved by

$$n(t) = 2.63 \cdot 10^{22} \left[\frac{\sqrt{\text{g/mol K}}}{\text{s mbar cm}^2}\right] \cdot \frac{P\alpha S}{\sqrt{MT}} \cdot t_s \cdot \left(1 - e^{-t/t_s}\right) + n_0 \cdot e^{-t/t_s} \tag{5.24}$$

as described in detail in appendix B. The number of hydrogen molecules n on the detector surface and the tritium surface activity C_D are linked by the decay law

$$C_D(t) = 2\lambda r \cdot n(t)\,, \tag{5.25}$$

where r is the tritium purity and $\lambda = 1.78 \cdot 10^{-9}$ s^{-1} the tritium decay constant. The time development of the total tritium surface contamination is obtained by combining eqs. 5.24 and 5.25:

$$C_D(t) = 5.26 \cdot 10^{22} \left[\frac{\sqrt{\text{g/mol K}}}{\text{s mbar cm}^2}\right] \cdot \frac{P\alpha S\lambda r}{\sqrt{MT}} \cdot t_s \cdot \left(1 - e^{-t/t_s}\right) + C_0 \cdot e^{-t/t_s} \tag{5.26}$$

with starting values n_0 and $C_0 = 2\lambda r \cdot n_0$. This means that the number of tritium molecules on the detector increases until the adsorption and desorption rates are equal. Equation 5.26 is later used to fit the data for the tritium contamination of the Si detector (see sec. 5.4.2.3).

5.3.4 Tritium adsorption on the stainless steel walls

Tritium is being adsorbed on the stainless steel walls of the Detection System, too (see sec. 5.4.2.6). Using the notation from eq. 5.11, the adsorption rate can be

represented as the sum of the accumulation rate on the surface Q_W and the permeation rate into the surface Q_B. The tritium adsorption capability of stainless steel is strongly connected to the amount of surface water where tritium is being trapped by isotopic exchange reactions or by physisorption [Shm03]. Nishikawa et al. [Nis00] identified three different kinds of such water:

- **Physically adsorbed water**, whose amount is correlated to the water vapor pressure by Langmuir isotherms. Thus, physically adsorbed water can be removed by purging with dry gas and vacuum treatment.
- **Chemically adsorbed water**, which cannot be removed by purging with dry gas alone, but which requires additional heating above $\sim 100°C$.
- **Structural water**, which includes -OH bases, that is strongly bound to the metal surface via hydrogen bonds and cannot be removed in reasonable time even with heating.

The tritium trapping mechanism on the surface can be split into three different sub-reactions, where the first two are connected to the surface water:

- **Physisorption:** Tritium is bound to the surface water via van der Waals forces. The adsorption and desorption rates are given by eq. 3.7 and 3.8, respectively.
- **Isotopic exchange:** Tritium is isotopically exchanged with hydrogen present in the surface water. The reaction is in principle reversible, but the amount of hydrogen in the Detection System exceeds the amount of tritium by far: The H_2 pressure is at least three orders of magnitude higher than the DT pressure (see sec. 5.4.2.1). Therefore, the isotopic exchange reaction can be regarded as non-reversible in TRAP.
- **Chemisorption:** Tritium is bound covalently to the metal surface. Hydrogen molecules are dissociated when chemically bound to the surface of metals. The adsorption rate is proportional to the square root of the hydrogen pressure in the Detection System [Lae89]. With the conditions present in the Detection System during measurements, this process is not reversible: The walls of the Detection System are at room temperature, yet for the removal of chemisorbed hydrogen, higher temperatures are required.

All three reactions are *heterogeneous reactions*[5] with constant reaction rates k that follow the *Arrhenius equation*

$$k = k_0 \cdot \exp\left[-\frac{E_A}{RT}\right] . \tag{5.27}$$

[5] Heterogeneous reactions have reactants in two or more phases.

Herein, E_A is the activation energy per mole for the reaction in question, T is the temperature and k_0 and $R = 8.314$ J/(mol K) are constants.

For physisorption, the behavior described in sec. 5.3.3 evolves as follows: The effective adsorption rate decreases with time since the desorption rate from the surface increases with the amount of tritium molecules adsorbed. E_A from eq. 5.27 is negative in this case and the reaction rate increases with decreasing temperature. With the conditions present during the TRAP measurements, the amount of tritium bound to the stainless steel walls of the Detection System by isotopic exchange reactions and chemisorption increase with time without reaching saturation (see sec. 5.4.2.6).

The tritium contamination on the stainless steel walls of the Detection System cannot be described as well as the tritium contamination on the Si detector, where only physisorption needs to be discussed. It is unknown to what degree physisorption, chemisorption and isotopic exchange reactions are involved in the process of collecting tritium on the stainless steel: This strongly depends on the history of the stainless steel in question [Lae89]. Therefore, a linear fit, which corresponds to a constant pumping speed of the stainless steel walls, was used for determination of the tritium adsorption rate.

5.3.5 Tritium diffusion through the stainless steel bulk

As we shall see later in sec. 5.4.2, the constituents of the outgoing flow rate (eq. 5.11) Q_G, Q_W and Q_D are very low. Therefore, the tritium adsorption rate on the stainless steel walls of the Detection System is not equal to the accumulation rate Q_W alone, but the tritium permeation rate into the stainless steel bulk material Q_B needs to be taken into account, too. Tritium dissolved in the stainless steel bulk can neither be detected by the residual gas analyzer nor by the silicon detector since beta electrons lose all their energy while traversing to the surface.

After adsorption and dissociation of hydrogen molecules on the stainless steel surface, atomic hydrogen is dissolved and chemically bound in the stainless steel bulk. The dependence of the concentration of atomic hydrogen in the bulk c_Q from the pressure of molecular hydrogen above the stainless steel surface P_{Q2} is given for ideal gas conditions by *Sievert's Law* [Lae89]:

$$c_Q = K \cdot \sqrt{P_{Q2}}\,. \tag{5.28}$$

The *Sievert constant* K, also called *Solubility*, depends from temperature T according to

$$K = K_0 \cdot \exp\left(\frac{-\Delta H}{RT}\right) \tag{5.29}$$

with the heat of solution ΔH and the parameter K_0, which is connected to the standard molar entropy change involved in the solution process. Literature values for the Sievert constant show a strong variation that is mostly due to oxide layers on the metal surface and defects in the lattice. Conservative values for ΔH and K_0,

which yield a high solubility K, are given for H_2 and 300-series ASTM stainless steel in [San05]:

$$\Delta H = 5.9 \text{ kJ mol}^{-1} \tag{5.30}$$

$$K_0 = 135 \text{ (mol } H_2\text{) m}^{-3} \text{ MPa}^{-1/2}\,. \tag{5.31}$$

Assuming that isotope effects are negligible with regard to solubility, which is supported by [San05], the average permeation rate into the stainless steel bulk material Q_B can be determined from this data by inserting the partial pressure of DT, the most abundant tritium isotopomer in TRAP, in eq. 5.28 and dividing by the injection time.

The result obtained in this way should be handled with care, though. Sievert's Law (eq. 5.28) is only valid for pure materials with a perfect lattice. Any occurrence of trapping sites for hydrogen in the metal lattice, like grain boundaries, phase boundaries and dislocations, leads to different experimental results. The fact that the DT pressure expected in the TRAP Detection System is very low ($< 10^{-13}$ mbar) raises further questions concerning the application of eq. 5.28. At very low pressures hydrogen trapping in defects and on surface water becomes predominant over pure solution in the lattice [San05]. Zarchy et al. [Zar79] report on low pressure tritium permeation through stainless steel ASTM 304. The permeation rate dominated by diffusion along grain boundaries reported in this work is lower than the permeation rate expected from lattice dominated diffusion. Furthermore, it is known [San05, Swa79], that oxide layers on the metal surface concludes the square root dependence from pressure, as the dissociation of hydrogen on the metal surface is suppressed. Taking into account that the stainless steel surfaces in the TRAP Detection System are certainly oxidized, the data for ΔH and K_0 given above, which were obtained from thoroughly purified samples, will yield an upper limit for the amount of tritium in the bulk.

The uncertainties in estimating the amount of dissolved tritium in the stainless steel bulk material of the Detection System at such a low pressure are huge; the errors are easily 100%. In order to rule out or at least minimize these uncertainties, the use of a different material with much lower solubility for hydrogen at room temperature is advised, for example gold [McL73]. Therefore, gold plated tubes in the Detection System of TRAP are considered for further measurements with tritium.

5.3.6 Tritium adsorption on the copper cold finger

Tritium adsorbed on the copper cold finger (see fig. 4.11) can neither be detected by the RGA nor by the Si detector: Due to the geometry, decay electrons from tritium adsorbed on the copper cold finger cannot reach the sensitive detector surface. Yet, the tritium adsorption rate on the copper cold finger Q_C can be neglected compared to the other contributions Q_D, Q_W and Q_B for the following reasons:

- The probability for tritium molecules to reach the copper cold finger is rela-

tively small as indicated by the schematic in fig. 5.10:

$$P = \frac{A_{ring}}{A_{tube}} \approx 20\% \,, \tag{5.32}$$

where A_{ring} is the frontal surface area of the ringlike cavity and A_{tube} the cross section of the detection chamber. Therefore, more tritium will be adsorbed per unit time on the Si detector and the Al_2O_3 bearing than on the copper cold finger.

- The surface area of stainless steel is much larger than that of copper in the Detection System. The surface area ratio is

$$\frac{A_{copper}}{A_{stainless\ steel}} \approx 2\% \,. \tag{5.33}$$

Furthermore, the tritium trapping capacity, which is strongly influenced by surface water (see sec. 5.3.4), is higher for stainless steel at room temperature than for copper at ~ 173 K [Nis00].

- The solubility of hydrogen in copper is smaller than the one of hydrogen in stainless steel at room temperature [McL73]. The difference in solubility is further increased by the temperature difference between the stainless steel walls and the copper cold finger. Therefore, hydrogen solution in copper is not an issue in TRAP.

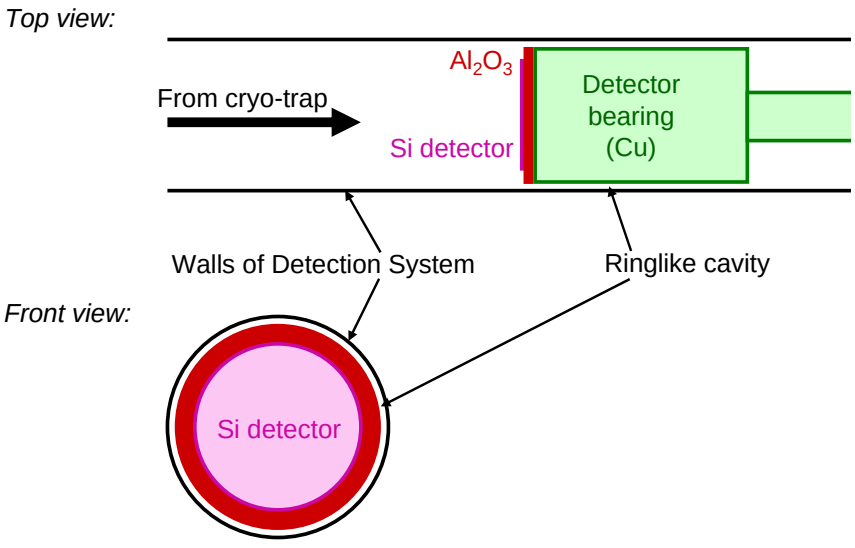

Figure 5.10: Schematic of the detector surroundings. Shown are the top and front views of the Si detector surroundings with the narrow ringlike cavity between the detector bearing and the walls of the Detection System.

5.4 Tritium runs (TRAP runs#4-#6)

After the last deuterium run (run#3, see sec. 5.2) the experimental setup was changed for tritium operation (refer to appendix A). Thereupon, six runs with tritium were conducted, the major objective being the determination of the tritium flow rate suppression factor

$$F = \frac{Q_{in}}{Q_{out}} = \frac{\text{incoming tritium flow rate}}{\text{outgoing tritium flow rate}} \,. \tag{5.34}$$

The experimental procedures and the results of runs#4-#6 with tritium are presented in this section. The last three TRAP runs had to be aborted due to a high tritium contamination in the system (run#7 and #8) and due to mechanical damage (run#9).

5.4.1 Description of tritium runs

The main experimental parameters of the TRAP runs#4-#6 are summarized in table 5.2 and explained in the following:

- **Ar amount:** The argon gas amount used for preparing the argon condensate of $1-2$ μm thickness
- **Ar preparation pressure:** The absolute pressure in the liquid helium cryostat during preparation of the argon adsorbent. In run#6, the cryostat was pressurized in order to obtain a temperature around 5 K.

Table 5.2: TRAP tritium runs#4-#6: parameter summary. The abbreviations stand for: SS - Stainless Steel, RGA - Residual Gas Analyzer, Si - Silicon detector.

	Run#4	Run#5	Run#6
Ar amount [mbar l]	96	94	75
Ar preparation pressure [bar]	~ 1	~ 1	~ 2
Hydrogen amount [mbar l]	0.096	0.096	0.13
Activity [GBq]	4	5.6	5.6
Average injection rate [mbar l/s]	$\sim 10^{-6}$	$\sim 10^{-6}$	$\sim 10^{-7}$
Injection duration [d]	1	1.5	10
Steady state duration [d]	13	25	18
Material in Detection System	SS (electropolished)		SS
RGA type [amu]	$1-100$	$1-6$	$1-6$
Detection method	100% RGA	~ 80% RGA	~ 90% Si

- **Hydrogen amount:** Not pure tritium, but a hydrogen mixture of 43% DT, 19% T_2, 7% HT and 31% non-tritiated hydrogen molecules was injected. The gas composition, determined by gas chromatography, is known with an uncertainty of $\sim 10\%$.
- **Activity:** The tritium activity in the tritium inlet mixture (44% tritium)
- **Average injection rate:** The average tritium injection rate measured from the pressure drop in the tritium inlet buffer vessel (see for example fig. 5.11)
- **Injection duration:** The duration of tritium injection
- **Steady state duration:** Time spent with cold cryostat after stopping tritium injection
- **Material in Detection System:** The surface material of the tubes in the Detection System.
- **RGA type** used in the run: $1-100$ amu or $1-6$ amu
- **Detection method:** Detection device and approximate percentage of measurement time

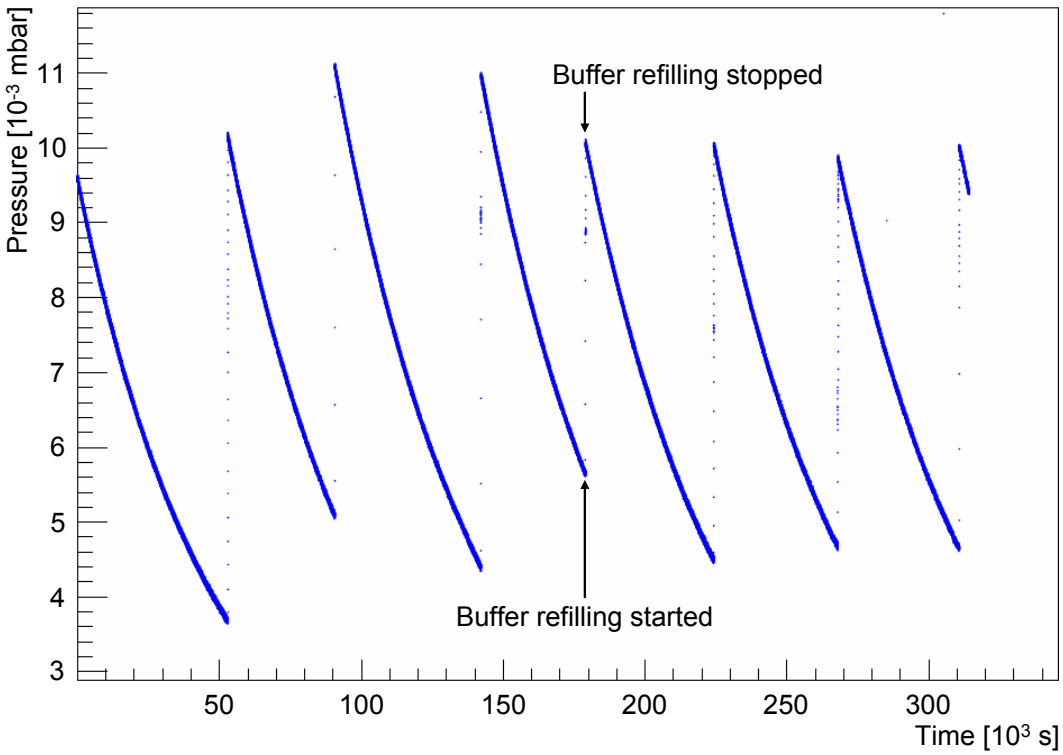

Figure 5.11: Pressure in the tritium inlet buffer BD002 during run#6. The tritium inlet buffer needs to be refilled regularly. With decreasing pressure in the buffer, the tritium injection rate decreases, too. The average injection rate is calculated by dividing the total injection amount through the total injection time.

Generally, each run consists of two main phases:

- The **Injection phase**: During the injection phase tritium is continuously injected into the Cryo-trap. It allows for the determination of the tritium flow rate suppression factor as described in sec. 5.4.2.7.
- The **steady state phase**: During the steady state phase no tritium injection occurs. The Cryo-trap is left standing with tritium adsorbed on the argon cryo-deposit. It allows for the investigation of tritium migration as described in sec. 5.4.2.3.

It can be seen from table 5.2 that runs#4 and #5 had relatively high tritium injection rates and short injection durations compared to run#6. They were used to investigate tritium migration. Run#6, on the other hand, with its long tritium injection duration was used to calculate the tritium flow rate suppression factor.

Run#4 was the first tritium run with the TRAP experiment. For tritium detection, the $1-100$ amu RGA was used observing mass 5 (refer to sec. 5.3.1). In order to be more sensitive to tritium in the gas phase and to cross check the results obtained before, a different high resolution RGA of mass range $1-6$ amu was employed during run#5. Additionally, the Si detector was tested. When stable operation of the Si detector could be guaranteed, it became the main instrument for tritium detection in run#6. The $1-6$ amu RGA was then used exclusively during the liquid helium refillings of the cryostat where strong microphonics on the detector rendered measurements with the detector impossible. During the measurements with the Si detector, its energy calibration was regularly checked with an accurate test pulser.

For the walls of the Detection System electropolished stainless steel was chosen initially for vacuum reasons. Later, when the diminutiveness of the contributions Q_G, Q_W and Q_D became apparent (refer to sec. 5.4.2), the issue of tritium permeation through the stainless steel bulk material was raised. Normally, such permeation is negligible at room temperature, yet compared to the other small contributions it might become predominant. Furthermore, the electropolishing of stainless steel saturates its surface a few microns deep with hydrogen, which promotes tritium permeation into the bulk by isotopic exchange reactions [Glu05]. The tubes in the Detection System were changed hereupon temporarily to "as-received" (non-electropolished) stainless steel tubes for run#6. At the same time, the possibility for non-galvanic plating of these tubes for future runs was investigated [Stu07] and finally put into effect by magnetron sputtering. The gold layer thickness achieved in this way was 250 nm. Galvanic plating was rejected since this method would saturate the surface with hydrogen, leading to isotopic exchange reactions with tritium gas.

The following runs with a gold plated Detection System (runs#7-#9) had to be aborted due to reasons mentioned before.

5.4.2 Results

The experimental results of TRAP are presented in a combined way for the tritium runs#4-#6: the RGA data is given in sec. 5.4.2.1 and the data from the Si detector in sec. 5.4.2.2. Sections 5.4.2.3 and 5.4.2.6 discuss the tritium surface contamination on the Si detector and on the walls of the Detection System, respectively. The determination of the tritium pressure as well as an estimate for the amount of tritium dissolved in the bulk material of the Detection System's walls can be found in secs. 5.4.2.4 and 5.4.2.5. Finally, the tritium flow rate suppression factor of the Cryo-trap is derived in sec. 5.4.2.7.

5.4.2.1 RGA data

Figures 5.12 and 5.14 show the DT partial pressure over time for run#4 and #5, respectively, along with a linear fit applied to the data points. The values presented are not only data obtained during tritium injection but also afterwards. The corresponding diagrams for run#6 can be found in appendix C.1.

It is obvious from the slopes of the fit functions that no change in the DT partial pressure with time is observable in all runs. In fact, the DT partial pressure is always below the RGAs' detection limits of $\sim 5 \cdot 10^{-14}$ mbar which is visible in figs. 5.13 and 5.15, where the frequency of pressure readings are plotted against the pressure readings: The distributions are Gaussian centered around zero, the RGAs' electronic noise exceeds the ionization current produced by the residual DT. Slight deviations from the Gaussian shape are visible in the data sets from the $1-6$ amu RGA. These can be attributed to the sharp drops of the partial pressure existing in figs. 5.14 and C.1, where instabilities in the RGA's very sensitive electronics seem to occur.

An upper limit for the accumulation rate in the gas phase Q_G (see sec. 5.3) can be estimated by assuming that the DT pressure gradually increased during the 10 d tritium injection period in run#6 until the RGA's detection limit of $5 \cdot 10^{-14}$ mbar was just reached upon stopping the injection:

$$Q_G < \frac{\Delta P \cdot V}{\Delta t} = \frac{5 \cdot 10^{-14}\ \text{mbar} \cdot 2.5\ \text{l}}{10\ \text{d}} < 60\ \text{T atoms/s}\,, \tag{5.35}$$

where $V = 2.5$ l is the volume of the Detection System.

A small amount ($\sim 10^{-4}$ mbar l) of helium at room temperature was injected into the Cryo-trap during the regeneration of the cryo-surface in run#4. This immediately led to desorption of both argon and DT from the cryo-surface as indicated in fig. 5.16. The DT pressure increased more than three orders of magnitude from $< 5 \cdot 10^{-14}$ mbar to $> 10^{-10}$ mbar. Therefore, any gas entering the Cryogenic Pumping Section of KATRIN should be pre-cooled before reaching the argon adsorbent in order to prevent such desorption.

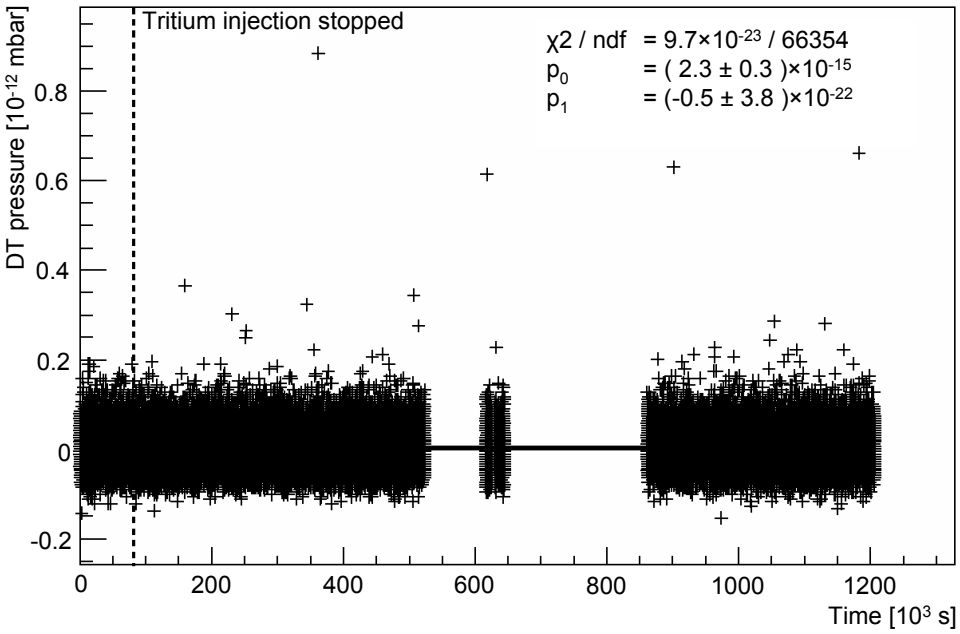

Figure 5.12: Run#4: RGA data. Data for DT with the $1-100$ amu RGA: the dotted line marks the end of the injection phase, a linear fit $f(x) = p_0 + p_1 x$ was applied.

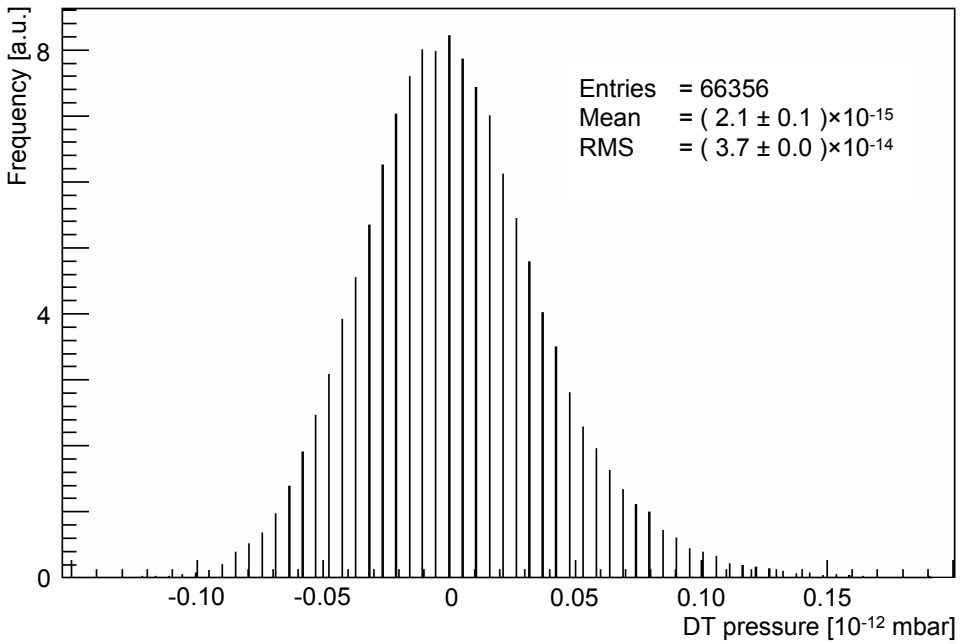

Figure 5.13: Run#4: RGA data projection. Frequency of DT partial pressure readings on the $1-100$ amu RGA during injection and steady state phase (RMS: Root Mean Square).

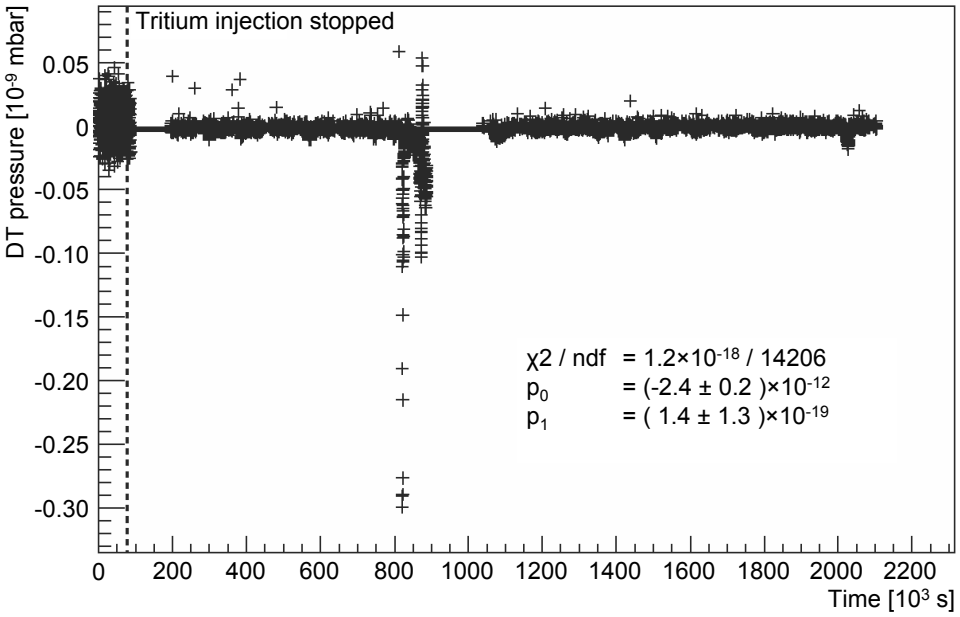

Figure 5.14: Run#5: RGA data. Data for DT with the $1-6$ amu RGA: the dotted line marks the end of the injection phase where a different gain was used on the RGA. A linear fit $f(x) = p_0 + p_1 x$ was applied.

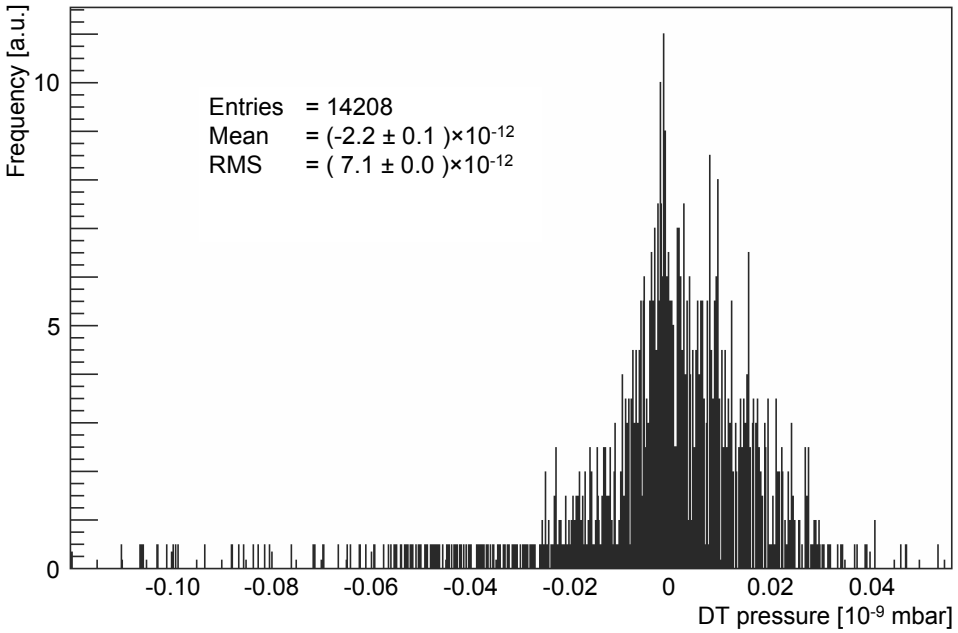

Figure 5.15: Run#5: RGA data projection. Frequency of DT partial pressure readings on the $1-6$ amu RGA during injection and steady state phase (RMS: Root Mean Square).

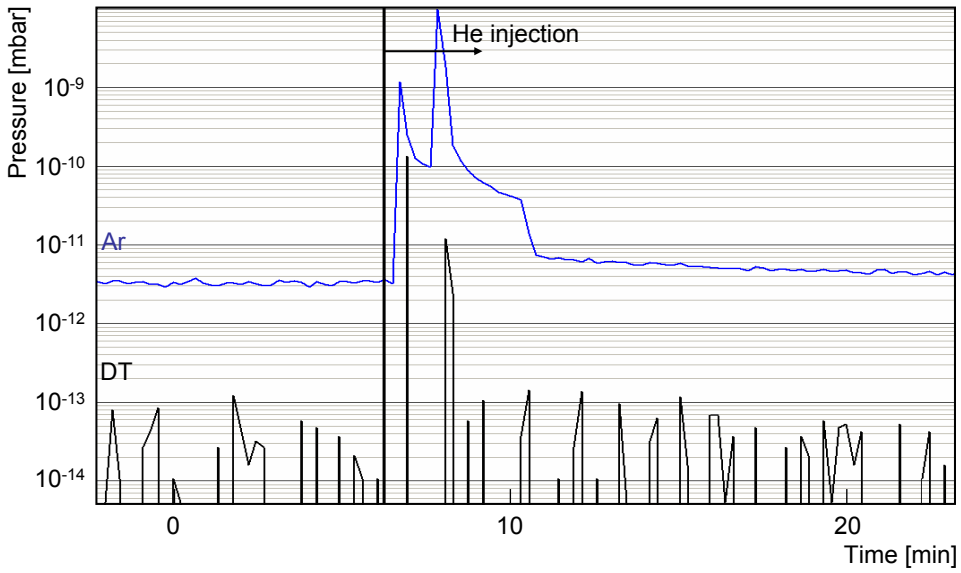

Figure 5.16: Run#4: Injection of warm He. The injection directly led to strong desorption of DT from the cryo-surface. The partial pressure increased to $\sim 10^{-10}$ mbar.

5.4.2.2 Si detector data

The detector count rates $A_{off}(t)$ and $A_{on}(t)$ for magnetic field off and on, respectively, are determined in the following way: During a detector run period of 1000 s that started at time t, the spectral data from the Si detector are recorded with the ORCA system and converted to ROOT files [Stu07]. These are then used in a probability analysis for suppression of electronic noise and microphonics:

The time difference between two independent events that happen at a constant rate, which is exactly the case in radioactive decays, is described by the exponential distribution [Sta08]

$$P_\lambda(t) = \lambda \cdot e^{-\lambda t} \tag{5.36}$$

with the probability density $P_\lambda(t)$ and the rate factor λ.

$$dP = P_\lambda(t)\, dt \tag{5.37}$$

is the probability, that the first event arrives in the time interval $[t, t + dt]$. The probability for a time difference $< dt$ between two consecutive events is then

$$P = P_\lambda(0)\, dt = \lambda\, dt\,. \tag{5.38}$$

The rate factor λ is calculated by dividing the total number of events in the energy window $6 - 20$ keV through the detector run duration of 1000 s.

In the data analysis, only those events in the energy window $6 - 20$ keV are considered, for which the probability P for the time difference to the predecessor event in the same energy window is higher than 0.1%. The number of valid events is determined and divided by 1000 s in order to obtain the count rates A_{off} or A_{on}. If more

than 30% of the events in the detector run are omitted due to a low probability P, the detector run is considered to be noise dominated and discarded. This method was tested on different, more or less noisy, detector runs and proved to be reliable.

Figure 5.17 shows the data obtained in this way plotted against time for run#6 during the injection phase. Figures 5.18 and 5.19 show the analogous data for run#5 and #6 during the steady state phase. The error bars indicated in the diagrams are pure statistical errors. All count rates increase with time, so tritium is being collected in the Detection System. Furthermore, $A_{on}(t_1) > A_{off}(t_2)$ with $t_1 \approx t_2$ is true[6].

During run#6 the Si detector was heated to $\sim 75°$C at the end of the injection phase in order to remove any tritium adsorbed on its surface. The measured count rate with magnetic field off A_{off} dropped from ~ 1200 counts/1000 s at the end of the injection phase to ~ 70 counts/1000 s at the beginning of the steady state phase.

In order to further evaluate the data, the total tritium contamination on the walls of the Detection System C_W and on the detector C_D needs to be calculated according to eqs. 5.15, 5.16 and 5.17.

[6] In fact, it is impossible to determine A_{on} and A_{off} simultaneously for the same time t, since one cannot measure with and without magnetic field at the same time. Therefore, neighboring detector runs with $|t_1 - t_2| = 1000$ s are used in eq. 5.15 and 5.16.

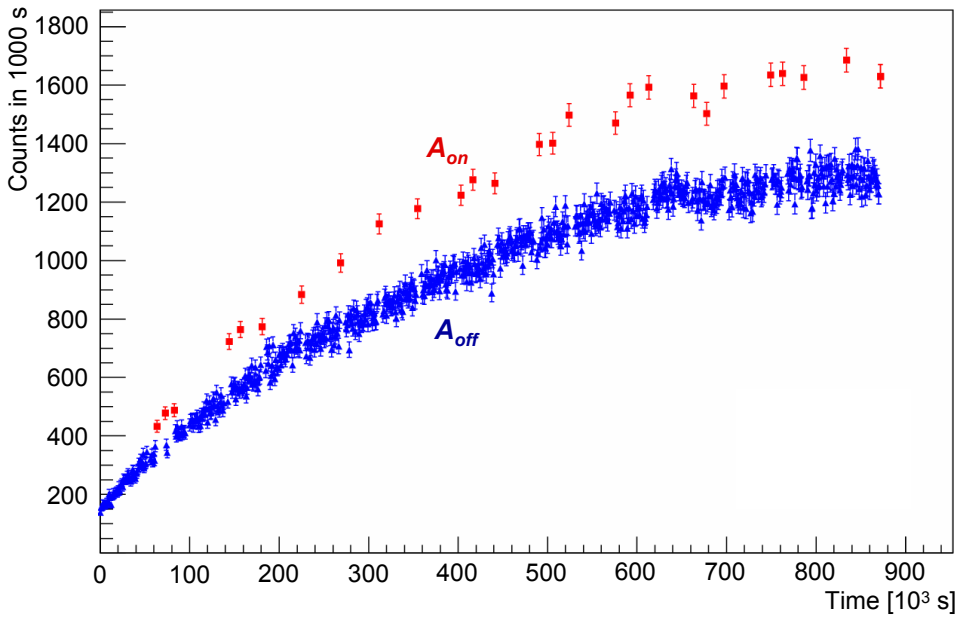

Figure 5.17: Run#6: Si detector data during injection phase. Shown is the count rate measured with the Si detector in the energy range $6 - 20$ keV over time. For explanations see text.

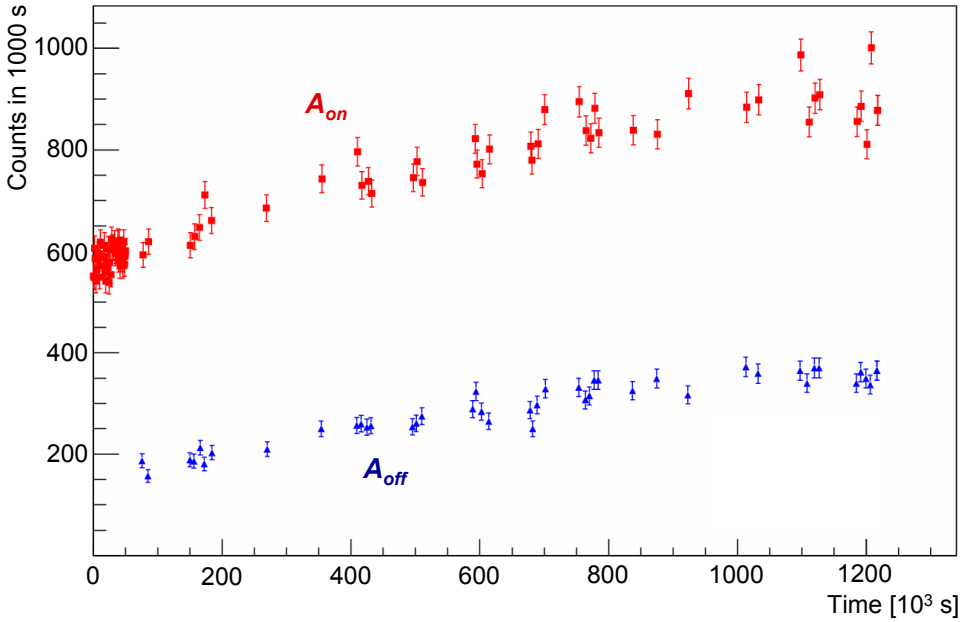

Figure 5.18: Run#5: Si detector data during steady state phase. Shown is the count rate measured with the Si detector in the energy range $6-20$ keV over time. For explanations see text.

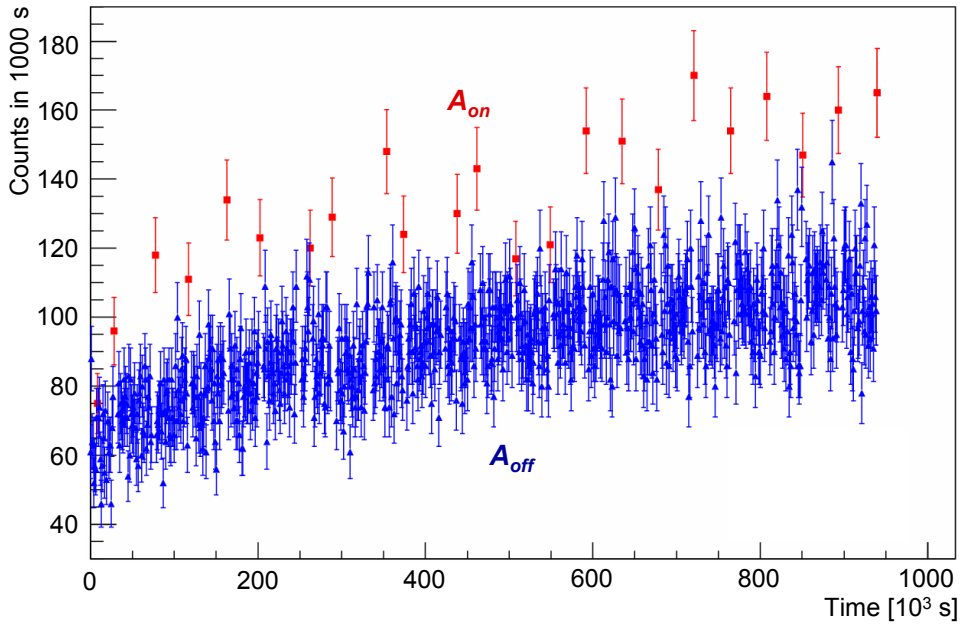

Figure 5.19: Run#6: Si detector data during steady state phase. Shown is the count rate measured with the Si detector in the energy range $6-20$ keV over time. For explanations see text.

5.4.2.3 Tritium on the silicon detector

The time development of the total detector contaminations $C_D(t)$ was calculated with the approximation (eq. 5.17) in order to minimize systematic uncertainties: The data calculated from eq. 5.16 includes a systematic uncertainty of 100% whereas the calculation according to the approximation eq. 5.17 only 30% (see sec. 5.3.2.4). The error introduced by using the approximation is negligible compared to that from the MC simulation.

Figure 5.20 presents the time development of the detector contamination C_D for the 10 d tritium injection phase in run#6. Figures 5.21 and 5.22 show the appropriate data for the steady state phases of run#5 and #6, respectively. The diagrams calculated according to the exact equation (eq. 5.16) are available in appendix C.2. The error bars indicated are pure statistical errors calculated by Gaussian error propagation from the statistical errors on A_{off} and on the MC parameter c.

The time dependence of the detector contamination shows the expected behavior: Its increase rate is large at the beginning and the contamination approaches saturation when the adsorption and desorption rates of tritium are equal. Therefore, tritium migration along the Cryo-trap can be excluded for the $\sim$ 10 d measurement intervals during the steady state periods of runs#5 and #6 (see figs. 5.21 and 5.22). Otherwise, the adsorption rate on the detector should suddenly increase together with the pressure in the Detection System according to eq. 3.7; the result would be a kink in the curves.

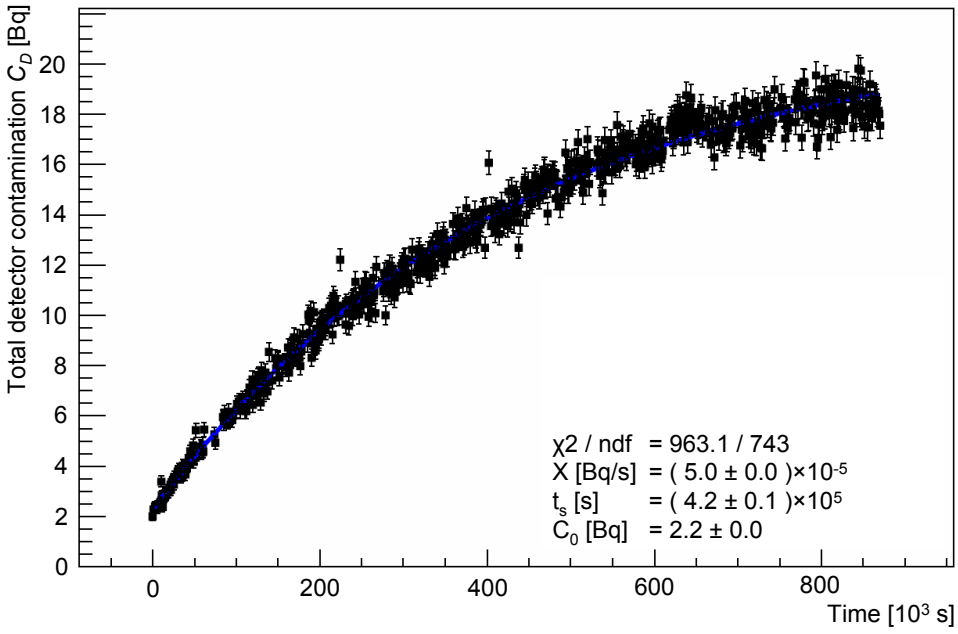

Figure 5.20: Run#6: Approximate detector contamination C_D during injection phase. Shown is the total tritium contamination on the Si detector over time. For explanations see text.

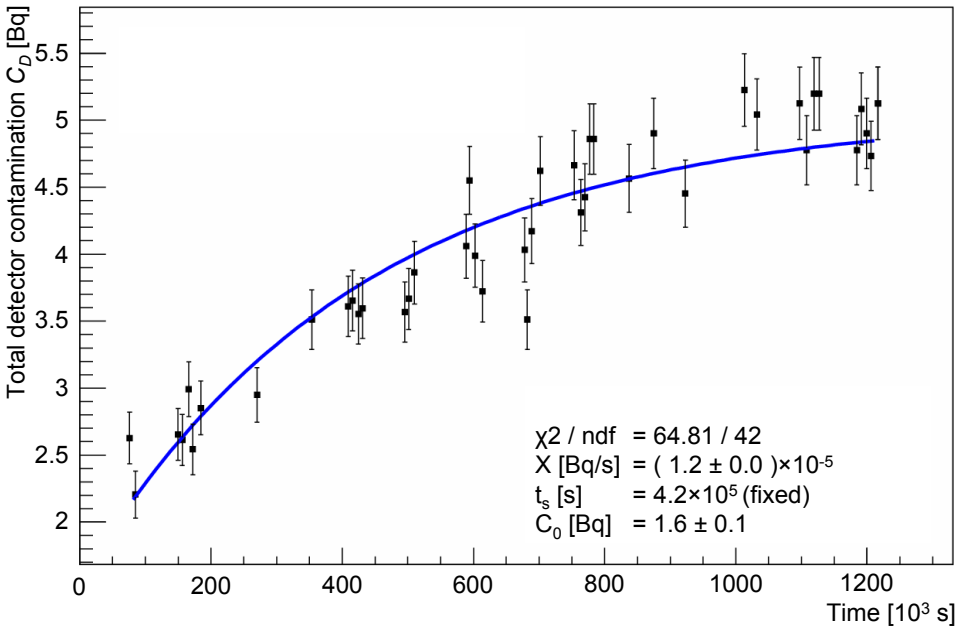

Figure 5.21: Run#5: Approximate detector contamination C_D during steady state phase. Shown is the total tritium contamination on the Si detector over time. For explanations see text.

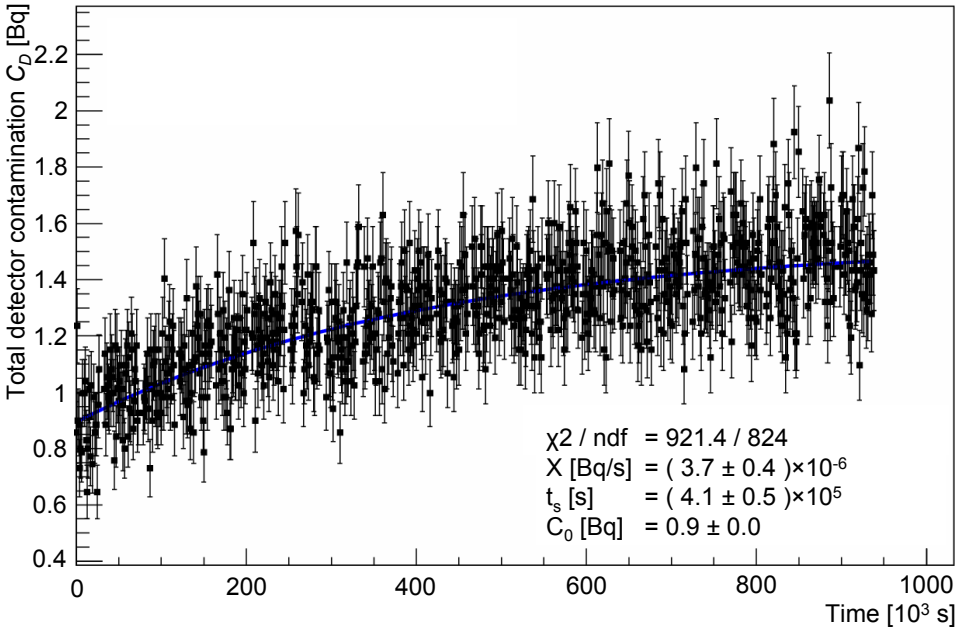

Figure 5.22: Run#6: Approximate detector contamination C_D during steady state phase. Shown is the total tritium contamination on the Si detector over time. For explanations see text.

The data for the detector contamination C_D in the diagrams was fitted to

$$C_D(t) = X \cdot t_s \cdot \left(1 - e^{-t/t_s}\right) + C_0 \cdot e^{-t/t_s} \tag{5.39}$$

allowing for the determination of the sojourn time t_s and the product of pressure and sticking coefficient ($P\alpha$) by comparison with eq. 5.26. In the latter case, one gets

$$P\alpha = 1.9 \cdot 10^{-23} \left[\frac{\text{s mbar cm}^2}{\sqrt{\text{g/mol K}}}\right] \cdot \frac{X\sqrt{MT}}{S\lambda r} \tag{5.40}$$

from which the tritium pressure in the Detection System can be derived. A detailed discussion follows in sec. 5.4.2.4.

The sojourn time t_s was determined from the run#6 data during the injection phase (fig. 5.20) that offers the lowest statistical error:

$$t_s = (424300 \pm 5018_{\text{stat}})\ \text{s}\,. \tag{5.41}$$

The systematic error on t_s, which is introduced by the 30% systematic error on C_D, is negligible compared to the statistical error. The sojourn time t_s obtained from the injection phase of run#6 is equal to that obtained from the steady state phase in run#6 (fig. 5.22). For the fit of the run#5 data (fig. 5.21), t_s was fixed for the fit routine to converge.

Using eq. 3.1, the average binding energy of tritium molecules on the detector surface can be estimated from the sojourn time t_s and the detector surface temperature $T_C = (173 \pm 10_{\text{sys}})$ K:

$$E_B = RT_c \cdot \ln\left[\frac{t_s}{t_0}\right] = (61.7 \pm 0.0_{\text{stat}} \pm 3.6_{\text{sys}})\ \text{kJ/mol}\,. \tag{5.42}$$

The relatively high binding energy and the easy removal of the tritium contamination on the detector at $\sim 75°$C suggest that the trapping mechanism of tritium on the surface involves both, adsorption on pre-condensed water and isotopic exchange.

An upper limit for the tritium adsorption rate on the detector surface Q_D can be obtained from the highest slope of $C_D(t)$ at $t = 0$. Differentiation of eq. 5.39 and dividing by the tritium decay constant λ leads to

$$Q_D < \frac{1}{\lambda}\frac{dC_D}{dt}_{(t=0)} = \frac{X}{\lambda} - \frac{C_0}{\lambda\, t_s}\,, \tag{5.43}$$

assuming that one tritium atom exists per tritium molecule (DT being the most abundant isotopomer in the inlet mixture).

The limits for the adsorption rates are then

$$Q_D < (25188 \pm 211_{\text{stat}} \pm 9341_{\text{sys}})\ \text{T atoms/s} \tag{5.44}$$

for the injection phase in run#6 (fig. 5.20),

$$Q_D < (4622 \pm 156_{\text{stat}} \pm 2625_{\text{sys}})\ \text{T atoms/s} \tag{5.45}$$

for the steady state phase in run#5 (fig. 5.21) and

$$Q_D < (866 \pm 247_{\text{stat}} \pm 991_{\text{sys}}) \text{ T atoms/s} \tag{5.46}$$

for the steady state phase in run#6 (fig. 5.22). The systematic errors were calculated by error propagation from the systematic errors on X and C_0 using eq. 5.43. The systematic errors of X and C_0 itself were determined by deviating C_D by 30% and checking the influence on the two in eq. 5.39.

The variation in the adsorption rates are directly connected to the different DT partial pressures in the Detection System as discussed in the next section.

5.4.2.4 DT partial pressure in the Detection System

Since DT is the most abundant tritium isotopomer in the hydrogen injection mixture, P in eq. 5.26 can be regarded as the DT partial pressure. The product of P and the sticking coefficient α can be estimated using eq. 5.40 with the complete detector surface (including not sensitive parts) $S = 5.43$ cm^2, the gas temperature $T \approx 300$ K, the DT molar mass $M \approx 5$ g/mol and the tritium purity of the inlet mixture $r = 44\%$. Including the fit results for X from sec. 5.4.2.3, one obtains

$$P\alpha = (8.67 \pm 0.06_{\text{stat}} \pm 2.60_{\text{sys}}) \cdot 10^{-18} \text{ mbar} \tag{5.47}$$

for the injection phase in run#6 (fig. 5.20),

$$P\alpha = (2.06 \pm 0.02_{\text{stat}} \pm 0.62_{\text{sys}}) \cdot 10^{-18} \text{ mbar} \tag{5.48}$$

for the steady state phase in run#5 (fig. 5.21) and

$$P\alpha = (0.64 \pm 0.06_{\text{stat}} \pm 0.19_{\text{sys}}) \cdot 10^{-18} \text{ mbar} \tag{5.49}$$

for the steady state phase in run#6 (fig. 5.22). The systematic errors on $(P\alpha)$ and later P (see below) were determined by error propagation from the systematic error on X using eq. 5.40.

In order to calculate P, the sticking coefficient α for hydrogen physisorption on the 173 K detector surface is required. Yet, the surface condition of the Si detector, e.g. amount of pre-adsorbed water, can only be estimated which makes adopting α from literature questionable. A lower limit for the sticking coefficient, however, will result in an upper limit for the DT pressure in the Detection System: The sticking coefficient for hydrogen chemisorption on metallic nonevaporable Zr-V-Fe alloy getter at room temperature is ~ 0.03, for example [Day07]. The one for hydrogen physisorption on the detector surface at 173 K should be in the same order, at least. Using $\alpha = 0.01$ will thus yield an upper limit for the DT pressure in the Detection System:

$$P < (8.67 \pm 0.06_{\text{stat}} \pm 2.60_{\text{sys}}) \cdot 10^{-16} \text{ mbar} \tag{5.50}$$

for the injection phase in run#6,

$$P < (2.06 \pm 0.02_{\text{stat}} \pm 0.62_{\text{sys}}) \cdot 10^{-16} \text{ mbar} \tag{5.51}$$

for the steady state phase in run#5 and

$$P < (0.64 \pm 0.06_{\text{stat}} \pm 0.19_{\text{sys}}) \cdot 10^{-16} \text{ mbar} \tag{5.52}$$

for the steady state phase in run#6.

The DT partial pressure is highest during tritium injection in run#6 as expected: When assuming a constant pumping speed of the cryo-surface, the pressure in the system increases when additional gas is constantly offered. The DT pressure in steady state, that is after tritium injection, is lower in case of run#6 than in run#5. Several explanations are possible for this phenomenon:

- The argon cryo-deposit was prepared differently. In run#6 the pressure in the cryostat was increased for a higher preparation temperature in order to approach the optimum preparation temperature of 6 K. This leads to a smaller average crystallite size and more trapping sites with a high binding energy were available. Therefore, the equilibrium pressure is lowered (refer to sec. 3.3.1).
- The tritium injection rate was higher in run#5 than in run#6. Therefore, the average adsorption site of tritium molecules on the cryo-surface is shifted downstream toward the Detection System. The probability of tritium molecules to reach the detector is hence higher in case of run#5.
- The tubes of the Detection System were treated differently in the two runs: run#5 employed electropolished stainless steel tubes, whereas standard ("as-received") components were used in run#6.

5.4.2.5 Tritium atoms dissolved in the stainless steel bulk

With the pressures calculated above, an estimate for the concentration of atomic tritium in the stainless steel bulk material of the Detection System's walls can be obtained from Sievert's law (eq. 5.28) with the solubility

$$K = 12.7 \text{ mol m}^{-3} \text{ MPa}^{-1/2} \tag{5.53}$$

calculated from the data in [San05]. For the tritium injection period in run#6, one obtains

$$c_Q < (1.63 \pm 0.01_{\text{stat}} \pm 0.49_{\text{sys}}) \cdot 10^{-15} \text{ mol cm}^{-3}\,. \tag{5.54}$$

This result needs to be handled with care, though. The indicated systematic error stems from the uncertainty of the calculated DT pressure alone. Yet, as described in sec. 5.3.5, the notion of hydrogen solubility in the stainless steel lattice is no more valid for the very low pressure regime of TRAP which renders the application of Sievert's law (eq. 5.28) questionable. Therefore, the result in eq. 5.54 should be

regarded rather as a very rough estimate for the tritium concentration in the walls of the Detection System.

The permeation rate of tritium into the walls of the Detection System Q_B (refer to sec. 5.3) can be estimated for the tritium injection period of run#6: Assuming that the whole volume of the stainless steel bulk is saturated with DT up to the concentration given in eq. 5.54 during the 10 d injection,

$$Q_B < (425681 \pm 0_{\text{stat}} \pm 127704_{\text{sys}}) \text{ T atoms/s} \tag{5.55}$$

is obtained as an upper limit. Again, the value for Q_B should be takes as a very rough estimate only.

5.4.2.6 Tritium on the walls of the Detection System

The total tritium contamination on the walls of the Detection System $C_W(t)$ was calculated from the count rates $A_{off}(t_1)$ and $A_{on}(t_2)$ with $|t_1 - t_2| < 1000$ s and $t = \max(t_1, t_2)$ using eq. 5.15. Figure 5.23 shows the time development of C_W for the injection phase in run#6. Figures 5.24 and 5.25 show the appropriate diagrams for the steady state phases in run#5 and #6. In all data sets the $\sim 100\%$ systematic uncertainty of the MC simulation on C_W needs to be taken into account in addition to the statistical errors shown in the diagrams. The statistical errors were calculated by Gaussian error propagation from the statistical errors on A_{off} and A_{on} and on the MC parameters a, b, c and r.

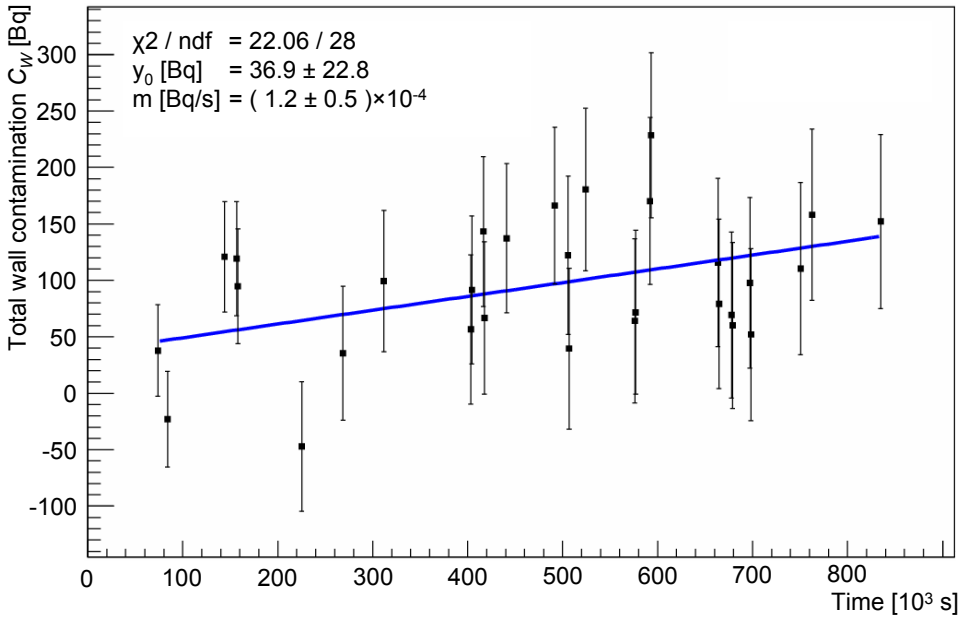

Figure 5.23: Run#6: Wall contamination C_W during injection phase. Shown is the total tritium contamination on the walls of the Detection System over time. For explanations see text.

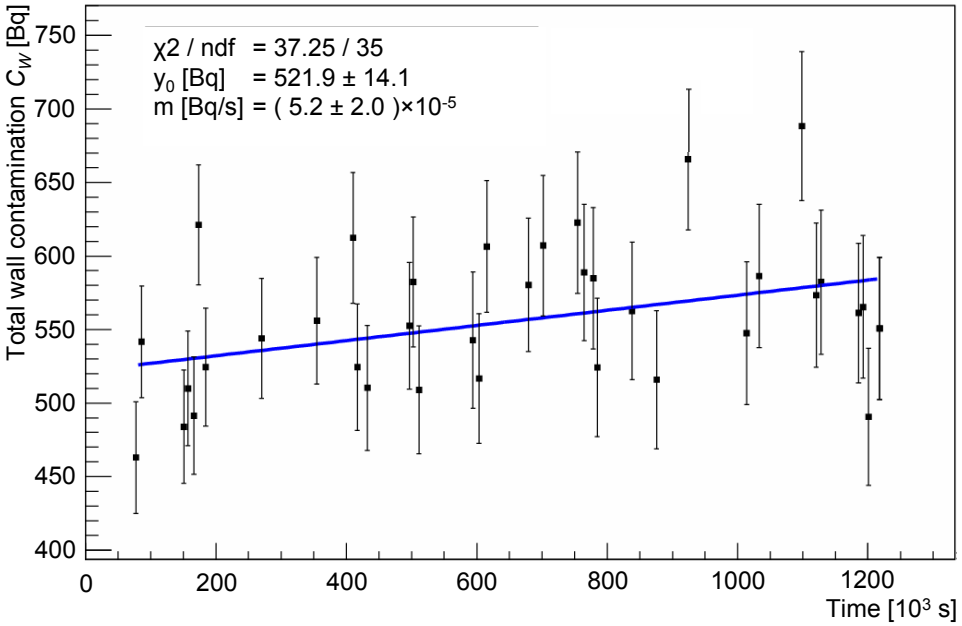

Figure 5.24: Run#5: Wall contamination C_W during steady state phase. Shown is the total tritium contamination on the walls of the Detection System over time. For explanations see text.

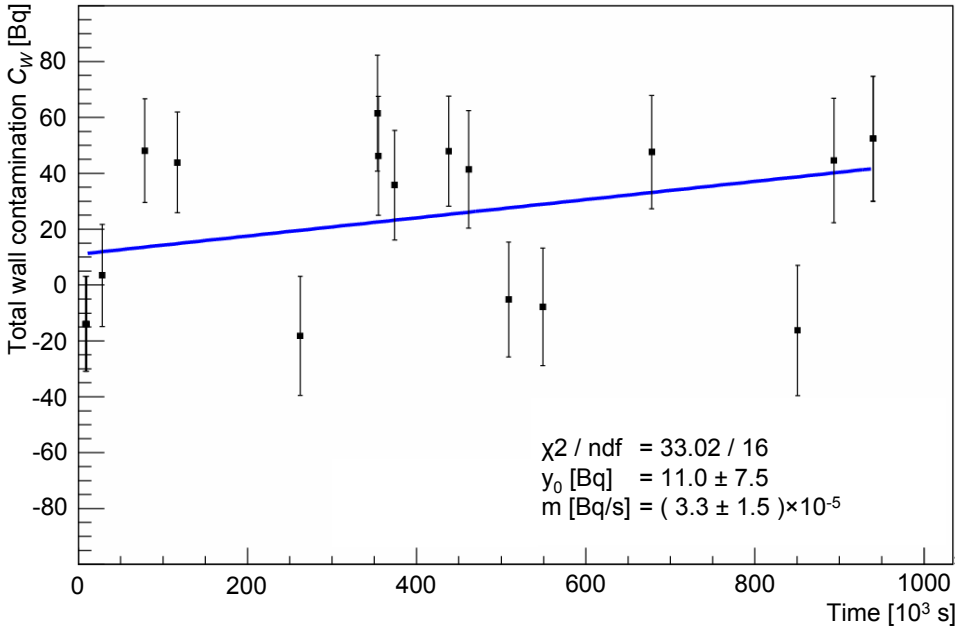

Figure 5.25: Run#6: Wall contamination C_W during steady state phase. Shown is the total tritium contamination on the walls of the Detection System over time. For explanations see text.

It is conspicuous, that the starting tritium contamination C_W is much higher for run#5 (fig. 5.24) than for run#6 (figs. 5.23 and 5.25). The walls of the Detection System were already slightly contaminated with tritium in run#5 from the previous run: As described in sec. 5.4.2.1, a small amount of warm helium was injected into the system during run#4 leading to an immediate desorption of tritium from the cryo-surface. A larger difference in the count rates A_{on} and A_{off} for run#5 (fig. 5.18) compared to run#6 (figs. 5.17 and 5.19) is the result.

The phenomenon of negative contamination values in the run#6 data can be attributed to the very low tritium contamination on the walls of the Detection System. After run#5, the electropolished stainless steel tubes in the Detection System were exchanged for new "as-received" tubes which were never used in any tritium environment before. Therefore, the count rates measured with the detector with magnetic field switched on (A_{on}) are much lower in run#6 than in run#5. The wall contamination C_W is calculated according to eq. 5.15, where the denominator $(ra-b)$ is negative. Negative values of C_W will occur, if the numerator $(rA_{off}-A_{on})$ is positive, that is if $A_{on} < rA_{off}$. This means that when applying the magnetic field, the increase of count rate $(A_{on} - A_{off})$ is dominated by decay electrons from tritium on the detector that travel away from the detector and are reflected back in the magnetic field and not by the tritium contamination on the walls.

As discussed in sec. 5.3.4, a linear fit

$$C_W(t) = m \cdot t + y_0 \tag{5.56}$$

was applied to the data points of $C_W(t)$ in order to describe the tritium accumulation rate on the walls of the Detection System. This corresponds to a constant tritium pumping speed of the walls of the Detection System which is realistic regarding the large adsorption surface and the small pumping speed.

The accumulation rate on the walls of the Detection System is then

$$Q_W = \frac{m}{\lambda} \approx (68652 \pm 27921_{\text{stat}} \pm 68652_{\text{sys}}) \text{ T atoms/s} \tag{5.57}$$

for the injection phase in run#6 (fig. 5.23),

$$Q_W \approx (28938 \pm 11079_{\text{stat}} \pm 28938_{\text{sys}}) \text{ T atoms/s} \tag{5.58}$$

for the steady state phase in run#5 (fig. 5.24) and

$$Q_W \approx (18309 \pm 8506_{\text{stat}} \pm 18309_{\text{sys}}) \text{ T atoms/s} \tag{5.59}$$

for the steady state phase in run#6 (fig. 5.25) assuming that one tritium atom exists per tritium molecule (DT being the most abundant isotopomer in the inlet mixture).

The accumulation rates on the walls of the Detection System are all equal within the error bars. The uncertainties involved in the MC simulation are too large to really distinguish any differences. Yet, taking the DT pressures into account (see sec. 5.4.2.4), the adsorption rate, which is equal to the sum of Q_W and Q_B, shows the expected behavior: It is highest for run#6 during tritium injection and lowest for run#6 after the injection of tritium.

5.4.2.7 Tritium flow rate suppression factor

In this section the tritium flow rate suppression factor

$$F = \frac{Q_{in}}{Q_{out}} \tag{5.60}$$

of the TRAP cryo-pump is finally calculated. This factor can be used as a lower limit for the tritium flow rate suppression factor of the Cryogenic Pumping Section of KATRIN which will be, in fact, an improved and optimized TRAP-like cryo-pump.

In order to determine F, the tritium injection rate Q_{in} and the outgoing tritium flow rate

$$Q_{out} = Q_G + Q_W + Q_D + Q_C + Q_B \tag{5.61}$$

must be measured simultaneously. Run#6 is the only TRAP run so far where the tritium injection flow-rate was chosen low enough for a 10 day non-stop injection without exceeding the maximum allowed tritium inventory of 5.6 GBq in the Cryo-trap.

The injection rate Q_{in} is calculated from the pressure drop in the tritium inlet buffer vessel (see fig. 5.11):

$$Q_{in} = (3.6 \pm 0.2_{\text{stat}} \pm 0.2_{\text{sys}}) \cdot 10^{12} \text{ T atoms/s} \tag{5.62}$$

Q_{out} is determined from the data given in the previous sections for the tritium injection period of run#6:

- **Accumulation rate in the gas phase:**

  $$Q_G < 60 \text{ T atoms/s}\,. \tag{5.63}$$

  This value, being extremely low compared to the other contributions, can be neglected in the calculation of the tritium flow rate suppression factor (see below).

- **Accumulation rate on the walls of the Detection System:**

  $$Q_W \approx (68652 \pm 27921_{\text{stat}} \pm 68652_{\text{sys}}) \text{ T atoms/s}\,. \tag{5.64}$$

- **Adsorption rate on the Si detector:**

  $$Q_D < (25188 \pm 211_{\text{stat}} \pm 9341_{\text{sys}}) \text{ T atoms/s}\,. \tag{5.65}$$

- **Adsorption rate on the copper cold finger:**

  Q_C is negligible as discussed in sec. 5.3.6.

- **Permeation rate into the bulk[7]:**

  $$Q_B < (425681 \pm 0_{\text{stat}} \pm 127704_{\text{sys}}) \text{ T atoms/s}\,. \tag{5.66}$$

[7]The statistical error is smaller than 0.5 T atoms/s.

Putting all together, the tritium flow rate suppression factor of the TRAP cryo-pump is

$$F = \frac{Q_{in}}{Q_{out}} > (6.9 \pm 0.5_{\text{stat}} \pm 3.1_{\text{sys}}) \cdot 10^6 \tag{5.67}$$

determined from the data of the injection phase in run#6 with the outgoing flow rate

$$\begin{aligned} Q_{out} \approx Q_W + Q_D + Q_B &< (519521 \pm 27922_{\text{stat}} \pm 205697_{\text{sys}}) \text{ T atoms/s} \\ &= (2.0 \pm 0.1_{\text{stat}} \pm 0.8_{\text{sys}}) \cdot 10^{-14} \text{ mbar l/s}\,. \end{aligned} \tag{5.68}$$

It is assumed herein that one tritium atom exists per tritium molecule (DT being the most abundant isotopomer in the inlet mixture).

5.4.3 Conclusions

The TRAP measurements with tritium demonstrated that a reduction of the tritium flow rate in the order of $\sim 10^7$ is feasible. The overall tritium flow rate suppression factor for TRAP was determined to be

$$F = \frac{Q_{in}}{Q_{out}} > (6.9 \pm 0.5_{\text{stat}} \pm 3.1_{\text{sys}}) \cdot 10^6\,. \tag{5.69}$$

Nevertheless, one should keep in mind that the flow rate suppression factor determined in the TRAP experiments is that for the specific isotopic mixture which was injected into the Cryo-trap with DT as the most abundant isotopomer. For a different mixture, the flow rate suppression factor will be different. If HT is the dominating hydrogen species, for example, F will be lower due to the higher equilibrium pressure of HT (see discussion in sec. 3.4.2). This could well be the case in the CPS of KATRIN due to isotopic exchange reactions of T_2 with residual H_2 on the walls of the beamline and due to the higher pumping speed in DPS2-F for the heavier DT and T_2 molecules. The CPS should therefore be conceived in a way to greatly improve its tritium retention performance compared to TRAP. The most important measures are

- to lower the operating temperature to ~ 3 K,
- to decrease the coverage by increasing the cryo-surface area,
- to integrate a fin structure in the beamline and
- to make the CPS longer than the Cryo-trap in TRAP.

Furthermore, a large safety margin for the tritium flow rate suppression factor should be introduced in CPS also due to the large uncertainties existing in the estimate of the tritium permeation rate into the bulk material of the stainless steel walls of the Detection System (Q_B). An upper limit for Q_B was estimated from the solubility of tritium in stainless steel using available literature data. However, published

values for the Sievert constant show a strong variations which is connected to the history of the steel sample used in such measurements, e.q. the existence of an oxide layer, electropolishing and cold working. Therefore, further runs with TRAP are recommended with gold plated stainless steel tubes in the Detection System. This should strongly suppress Q_B and allow for a comparison of the experimental results obtained with stainless steel and gold plated tubes.

Taking the *Knudsen effect* into account, the DT pressure in the Cryo-trap is lower than the partial pressure in the Detection System (eq. 5.50) due to the temperature difference: In the molecular flow regime, the pressures P_1 and P_2 in two chambers separated by an orifice depend from the gas temperatures in the chambers T_1 and T_2 according to [Hae81]

$$\frac{P_1}{P_2} = \sqrt{\frac{T_1}{T_2}}\,. \tag{5.70}$$

If the connection is a tube instead of an orifice, the dependence is

$$\frac{P_1}{P_2} < \sqrt{\frac{T_1}{T_2}} \quad \text{for} \quad T_1 > T_2\,. \tag{5.71}$$

The deviation from the exact equation increases with the length of the connecting tube. In case of TRAP, eq. 5.70 is a good approximation. Therefore, the DT pressure in the Cryo-trap is in the order of 10^{-16} mbar and in agreement with the requirements for the CPS. However, the HT pressure will be higher as mentioned earlier.

Concluding, one can say that the tritium flow rate suppression factor F lies within the order of magnitude specified for the Cryogenic Pumping Section of KATRIN [KAT04]. A summary of all recommendations from TRAP which led to the specification of the CPS are given in sec. 7.2.

Chapter 6

Detritiation of TRAP

After an increased tritium contamination was observed in TRAP, various detritiation procedures were investigated. The detritiation procedure that was developed is of major interest for the CPS, too. It was shown that an in-situ detritiation of the CPS and the Pre-spectrometer is feasible in case of an unforeseen tritium contamination during the runtime of KATRIN.

This chapter presents the detritiation campaigns conducted at the TRAP experiment. The first section (sec. 6.1) gives an introduction and explains how the increased tritium background affects the detector signal. Furthermore, a benchmark parameter for evaluation of the detritiation success is defined. Section 6.2 reviews current knowledge on tritium contamination of stainless steel and the detritiation thereof. Sections 6.3, 6.4 and 6.5 cover the methods and results of the detritiation campaigns performed at TRAP. The possibility of detritiation of the CPS or even the Pre-spectrometer is deduced in the final section (sec. 6.6).

6.1 Increased tritium contamination at TRAP

After three successful TRAP measurements with tritium, run#7 had to be aborted due to a very high tritium count rate in the energy window $6 - 20$ keV even before tritium injection was started. As it turned out, the tritium contamination level of the upper parts of the rig above the cryostat (refer to fig. 4.2) had increased beyond an acceptable limit for the experiment. The source of this contamination was unknown, yet the following possibilities have been discussed:

- After TRAP runs#4 and #5, purging of the Cryo-trap with gaseous helium was continued for $\sim$ 11 d at a flow rate of 1 l/min even after finishing the regeneration procedure described in appendix G. After run#6, however, the purging was continued for $\sim$ 3 d only. Maybe residual tritium in the system was therefore relocated towards the Detection System.

- The gas injection system of TRAP as well as the hood had to be relocated by $\sim$ 3 m to make room for the infrastructure facility AMOR (Anlage zur Molsieb Regenerierung). Therefore, TRAP was left without any pumping for four months before all connections were rebuilt and leak checked. As no tritium could be removed from the system during this time period, the probability for tritium relocation towards the Detection System is increased compared to the constantly evacuated system.

- AMOR extracts tritiated water from molecular sieves for waste processing and disposal [Hut96]. The tritium background level in the laboratory exhaust channels in the vicinity of this facility is $\sim$ 4 times higher than in the rest of the laboratory [Bes08] which might have caused an increased tritium contamination due to a backflow of tritium through the laboratory exhaust channel. This topic is addressed in more detail in sec. 6.5.

In order to enable further tritium measurements, TRAP had to be detritiated by a factor of 1000. The experience obtained thereby is of utmost importance for the CPS and maybe even for the Pre-spectrometer, too. Keeping in mind the fact that TRAP was contaminated with tritium, a method for in-situ detritiation of the KATRIN components CPS and Pre-spectrometer is desirable.

This expands the experimental objectives of TRAP introduced earlier in sec. 4.1 by the following objective:

Develop and test an in-situ detritiation procedure for decontamination of the CPS and the Pre-spectrometer.

6.1.1 Detritiation benchmark parameter

A benchmark parameter is needed in order to quantify the tritium contamination in TRAP and to compare different levels of contamination. It is already known from sec. 5.4.2.2 that tritium adsorbs on the cold Si detector surface, which leads to a gradual increase of the count rate on the detector. This also happens without any tritium injection, since the system is already slightly contaminated with tritium from previous runs.

Without tritium injection, the tritium pressure in the Detection System is dominated by desorption of HT from the walls of the Detection System. HT is created by isotopic exchange reactions with H which is still the most abundant hydrogen isotope in the system. The adsorption rate of tritium molecules on the Si detector surface, given by eq. 3.7 for pure physisorption, exceeds the desorption rate from the detector surface (eq. 3.8)

- if the tritium contamination in the vicinity of the Si detector is high compared to that on the detector and

- if the time window of measurement is smaller than the sojourn time t_s (eq. 3.1).

The increase rate m [Hz/s] of the detector count rate A_{off} in the energy window $6-20$ keV for magnetic field off is then solely defined by the adsorption rate of HT molecules on the detector surface:

$$m = 2.63 \cdot 10^{22} \left[\frac{\sqrt{\text{g/mol K}}}{\text{s mbar cm}^2} \right] \frac{P\,\alpha\,S\,c\,\lambda}{\sqrt{MT}} \tag{6.1}$$

with HT pressure P, sticking coefficient α, detector surface $S = 5.43$ cm^2 (including non-sensitive parts), MC parameter $c = 7.12 \cdot 10^{-2}$ (see sec. 5.3.2.4), tritium decay constant $\lambda = 1.78 \cdot 10^{-9}$ 1/s, atomic mass $M = 4$ g/mol and gas temperature $T \approx 300$ K. Integration leads to the time dependence of the detector count rate

$$A_{off}(t) = m \cdot t + A_0 \tag{6.2}$$

as shown in figs. 6.1 and 6.2 at the beginning of run#6 and #7, respectively. The linear dependence from time t as described by eq. 6.2 is well fulfilled. However, the considered time window in fig. 6.2 is already comparable to t_s; the curve of the graph is slightly visible since the desorption rate from the detector surface increases.

The slope m is three orders of magnitude higher for the data at the beginning of run#7 compared to the corresponding data for run#6, making further measurements with tritium impossible. For comparison: During tritium injection in run#6 the count rate on the detector without magnetic field increased from ~ 200 to ~ 1300

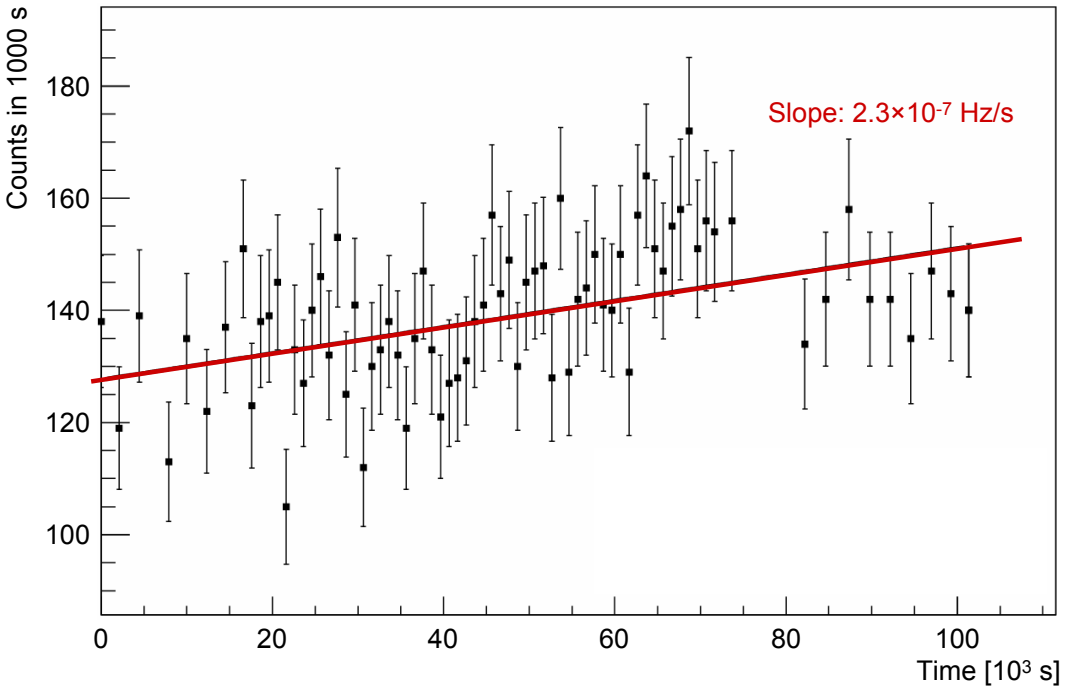

Figure 6.1: Detector background before run#6. Shown are the counts in the energy window $6-20$ keV measured with the Si detector during 1000 s over time. The magnetic field is off. The line represents a linear fit with a slope of $2.3 \cdot 10^{-7}$ Hz/s.

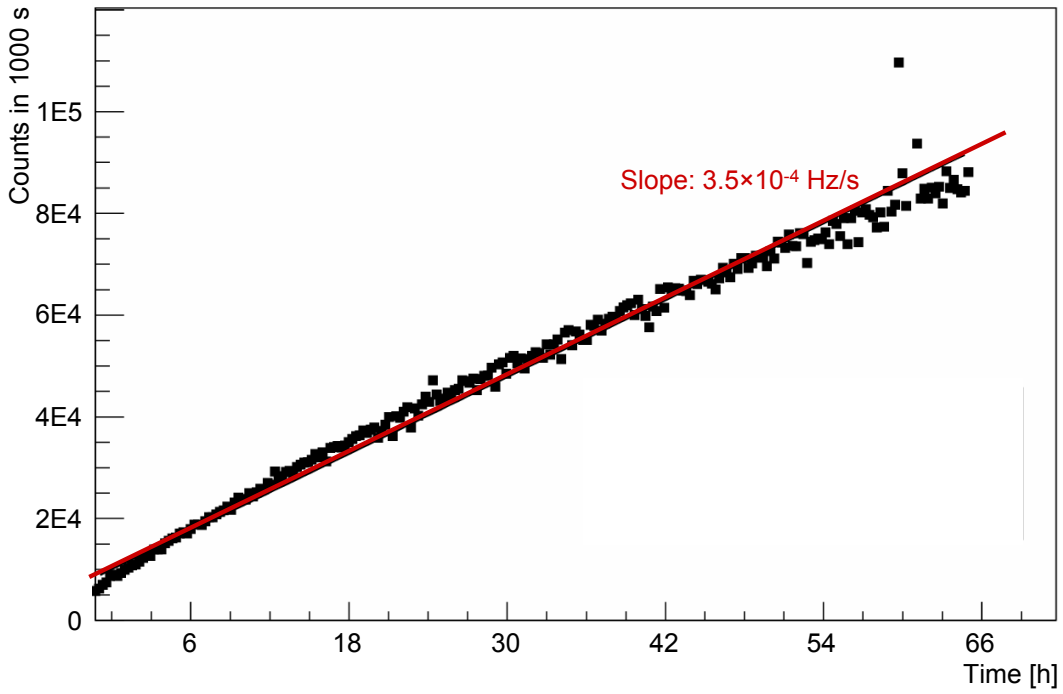

Figure 6.2: Detector background before run#7. Shown are the counts in the energy window $6-20$ keV measured with the Si detector during 1000 s over time. The magnetic field is off. The line represents a linear fit with a slope of $3.5 \cdot 10^{-4}$ Hz/s.

counts per 1000 s in 10 days (fig. 5.17). The parameter m, being directly proportional to the HT pressure in the Detection System, constitutes a suitable benchmark parameter for evaluation of the tritium contamination in the system.

Using eq. 6.1 with $0.01 < \alpha < 1$ as in sec. 5.4.2.4, the HT pressure in terms of m is restricted to the interval

$$1.9 \cdot 10^{-12} \left[\text{mbar s}^2\right] \cdot m < P < 1.9 \cdot 10^{-10} \left[\text{mbar s}^2\right] \cdot m \,. \tag{6.3}$$

For the slopes in the two figures above, one obtains

$$4.4 \cdot 10^{-19} \text{ mbar} < P < 4.4 \cdot 10^{-17} \text{ mbar} \quad \text{for run\#6 and} \tag{6.4}$$
$$6.7 \cdot 10^{-16} \text{ mbar} < P < 6.7 \cdot 10^{-14} \text{ mbar} \quad \text{for run\#7.} \tag{6.5}$$

Both values and also the surface contamination of the walls of the Detection System, which was measured by smear tests, are much lower than the permitted limits (concentration in air: $3 \cdot 10^5$ Bq/m^3 $\approx 7 \cdot 10^{-9}$ mbar; on surfaces: 100 Bq/cm^2). Therefore, "contaminated" at TRAP means that the tritium contamination is too high for measurements but still no concern for safety.

6.1.2 Tritium in the Si detector bulk material

During operation of the (LN_2-cooled) Si detector, tritium is adsorbed on its SiO_2 surface. The detector count rate in the energy windows $6-20$ keV is thus increased according to eq. 6.2. The accumulated tritium contamination on the surface can be easily removed by warming up the chip to $\sim 75°C$. After half a day of heating, the detector count rate in the energy interval $6-20$ keV drops back to the background rate A_0. Over the course of time, that is from run#4 to run#7, A_0 has increased from its initial value of ~ 70 counts per 1000 s (refer to sec. 4.3.7.5) to ~ 300 counts in 1000 s.

Experience shows that this contamination cannot be removed via heating at such a moderate temperature, which leads to the conclusion that atomic tritium is solved in the Si bulk material. The number of tritium atoms bound in this way amounts to

$$\frac{(300-70)/(1000\text{ s})}{\lambda} = 1.3 \cdot 10^8 \tag{6.6}$$

in the active detector volume of 150 mm^3.

The SiO_2 surface layer impedes the penetration of hydrogen isotopes into the Si bulk as reported for deuterium in [Nic95]. The data for deuterium concentration in polycrystalline Si published there is many orders of magnitude higher than in case of TRAP. This is barely a surprise considering the fact that they measured the deuterium permeation rate at a much higher deuterium pressure than the relevant HT pressure in TRAP. Furthermore, atomic deuterium was used in their experiments. In TRAP, however, dissociation of HT is required prior to the solution of tritium in the bulk material.

6.1.3 Contaminated components of TRAP

The tritium contaminated components of TRAP include:

- vacuum components (tubes, valves, vacuum gauges) of stainless steel type ASTM 304 and 316 (including the Cryo-trap),
- gold plated stainless steel tubes in the Detection System,
- copper components in the vicinity of the detector (fig. 4.11) that are kept at 173 K during measurements and
- the Si detector with Al_2O_3 substrate and SiO_2 surface.

All these components had to be detritiated, yet the stainless steel surfaces constitute the major challenge in reducing its tritium contamination to an acceptable level for the following reasons:

- Detritiation of gold surfaces is much easier than detritiation of stainless steel, since hydrogen molecules are weakly bound to the surface compared to stainless steel. At first, hydrogen molecules do not dissociate upon contact with the surface due to the high activation energy for this reaction [Sto93]. Secondly, physisorption of molecular hydrogen is observed only below 15 K [Ebe82], whereas chemisorption of molecular hydrogen takes place on unsintered gold films[1]. Yet, the binding energy is low (25 to 40 kJ/mol) and desorption already occurs above 150 K [Sto96]. As we shall see in sec. 6.4, the gold plated tubes of the Detection System could indeed be detritiated quite easily.

- According to sec. 5.3.6, the tritium contamination on the copper components can be neglected compared to the one on stainless steel.

- Al_2O_3 and SiO_2 at the detector constitute small surfaces compared to the gold and stainless steel ones.

In the following section, detritiation of stainless steel is addressed in more detail.

6.2 Tritium on stainless steel and its detritiation

In sec. 5.3.4 tritium adsorption on the stainless steel walls of the Detection System was discussed in detail. The same argumentation can be adopted for the contaminated system at the beginning of run#7, where the pressure is still in the order of 10^{-13} mbar (refer to eq. 6.5): The tritium contamination on the stainless steel surfaces in TRAP is strongly influenced by the amount of surface water which can be categorized into physically and chemically adsorbed water as well as structural water (see sec. 5.3.4). If tritium atoms are present in the structural water, e.g. after isotopic exchange reactions with gaseous tritium, they are strongly bound to the surface making detritiation of stainless steel so difficult compared to gold and copper where the amount of surface water is much lower [Nis00].

Depth profiles obtained by chemical etching of tritium loaded stainless steel samples followed by Liquid Scintillation Counting (LSC) of the acid solution revealed a subsurface layer of $15 - 20$ μm thickness highly enriched with tritium [Tor04, Per02]. Its specific activity was approximately two orders of magnitude higher than the one in the stainless steel bulk [Per02].

Due to the surface water layer, tritium release from stainless steel is mostly in form of tritiated water [Sur88, Hir84, Won91]. The ratio of desorbed HT to desorbed HTO, for example, was reported to be $1/8 - 1/6$ for heat treated stainless steel samples and $\sim 1/230$ for "as-received" stainless steel [Cor92]. Since TRAP could not be properly heat treated, the latter ratio is more realistic for the contaminated stainless steel components of TRAP.

[1] The components of the Detection System were not yet sintered. For this procedure, a temperature of > 700 K is required.

Due to the high mobility of hydrogen atoms in metals, a time-delayed re-growth effect of surface tritium after detritiation of the surface is observed even at room temperature [Per02, Cor05].

The most commonly considered methods for detritiation of stainless steel are:

- **Thermal desorption:** Thermal desorption, often in an inert gas stream, is used for evaporation of the physically and chemically adsorbed tritiated surface water from stainless steel. The method gains considerably in efficiency for temperatures above 150°C [Cor92]. However, temperatures above ~ 350°C will strongly increase the solubility of tritium in stainless steel (see eq. 5.29) and thus increase the tritium inventory in the stainless steel bulk. An ideal temperature for thermal desorption was reported around ~ 300°C [Per02].
- **Isotopic exchange reactions with protium/deuterium:** By offering hydrogen/deuterium, the isotopic equilibrium of the three hydrogen isotopes in the system is disturbed leading to isotopic exchange reactions that remove tritium from the metal surface. This is one method for removing the strongly bound structural water. Various investigations for detritiation with this methods have been conducted, among them were, for example, purging with Ar-NH_3 and Ar-H_2 mixtures [Per02] as well as purging with humid air [Cor92, Tor04].
- **Washing/leaching:** Surface tritium and tritiated water is removed from stainless steel by washing with or submersion in liquids. To some extent isotopic exchange reactions might contribute as well. Examples of this method are given in [Pen06].
- **Chemical or electrochemical etching:** Stainless steel surfaces are decontaminated by removal of a very thin surface layer, in particular the oxide layer where tritium is chemically bound [Won91]. This method is also used for determination of tritium contamination depth profiles by first etching the metal sample followed by LSC of the solution [Tor04].
- **Glow discharge:** The stainless steel walls are bombarded with ions in a plasma and thereby eroded. The so called *sputtering* of the surface is not only driven by direct ion bombardment, but also by bombardment with neutral atoms, which in turn were accelerated via collisions with ions. This method was used for detritiation, for example, in He or H_2 [Nak04] and He-O_2 glow discharges [Hop07].
- **Open flame heating:** The metal surface is detritiated by heating with an open flame. For example, detritiation of stainless steel ASTM standard 316 with methane-air flame is described in [Per02].
- **Melting:** During this destructive method stainless steel components are melted (at ~ 1600°C) in order to remove tritium from the bulk material for later waste disposal [Ros00].

Only the first three methods are feasible in TRAP. These are covered in the following.

6.3 First in-situ detritiation campaign

In the following section (6.3.1), various procedures are described which were employed in the first in-situ detritiation campaign of TRAP. The results are provided in sec. 6.3.2.

6.3.1 Methods of detritiation

- **Heating of components:** The components of TRAP were heated during all the following procedures in order to increase the reaction rates of desorption and isotopic exchange. Different temperatures were applied following the schematic in fig. 6.3. The heating temperature inside the cryostat was limited to 120°C to prevent the styrofoam convection shields below the cryostat cover from melting (see fig. 4.4). The temperature on the components above the cryostat were limited to $160 - 180$°C. The maximum heating temperature of the detector is 80°C. Above, the glue fixing the detector chip on its Al_2O_3 substrate softens.
- **He-H_2 purging:** A mixture of He and 5% H_2 was purged through the system at ~ 1 bar with a flow rate of 30 l/h according to the schematic in fig. 6.3 for ~ 2 d. The gas stream entered the system behind the Si detector and left the Cryo-trap through the cold valve at the bottom of the cryostat. Detritiation was expected by isotopic exchange of wall tritium with molecular hydrogen from the gas stream.
- **Methanol flooding:** A buffer vessel containing liquid methanol was connected to the system near the Si detector (refer to fig. 6.4). Afterwards, TRAP was evacuated together with the methanol vessel. Due to the low freezing point of methanol at ~ 10 mbar, the methanol freezes inside the buffer vessel and can be evaporated by warming up the vessel with a hot air blower. The system was filled with this method with 100 mbar methanol vapors and left standing for 10 minutes. The vapors were then pumped down and the procedure was repeated 12 times. Detritiation was expected by isotopic exchange reactions with the hydrogen atoms in methanol (CH_3OH). After methanol flooding, heating of the system for several days was required to evaporate all methanol from the system. Since water is bound to methanol via hydrogen bonds, tritiated water from the metal surfaces was removed by this process, too.
- **N_2-H_2O purging:** N_2 was purged through a water bath at 10°C. The humidified N_2 stream was injected behind the Si detector and transferred through the cold valve as depicted in fig. 6.3. For ~ 4 d the system was purged at ~ 1 bar with a gas flow rate of 60 l/h and for ~ 3 d purging was performed at ~ 74 mbar and 240 l/h. Detritiation was expected due to isotopic exchange reactions with the hydrogen in water molecules. Furthermore, reactions exchanging tritiated water on the surface with pure (non-tritiated) water from the gas stream contribute to the detritiation.

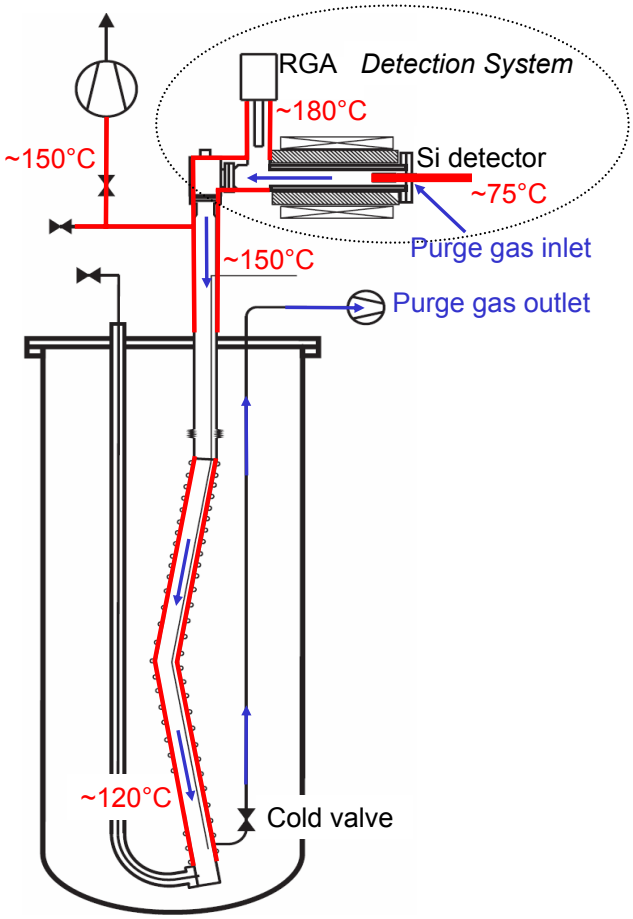

Figure 6.3: First in-situ detritiation with gas purging. The gas stream enters the system behind the Si detector and is transferred from areas of lower tritium contamination above the cryostat to areas of higher tritium contamination at the bottom of the cryostat. There, the gas stream exits the Cryo-trap through the cold valve.

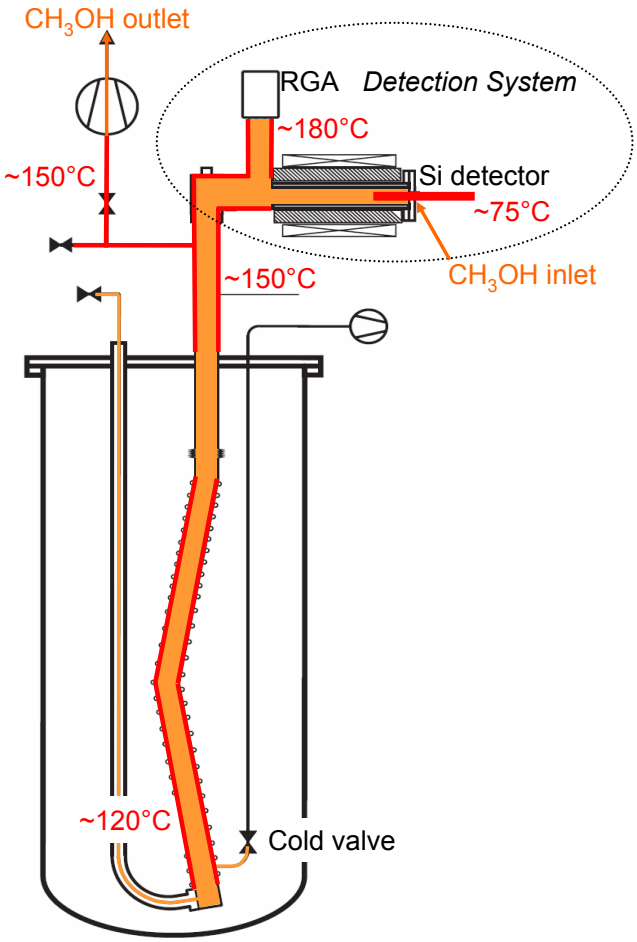

Figure 6.4: First in-situ detritiation with methanol flooding. The methanol is injected into the system just behind the Si detector.

6.3.2 Results and discussion

Regularly after the detritiation steps, the heaters were stopped and the system was thoroughly evacuated. The Si detector was then cooled and the background increase rate without magnetic field (benchmark parameter m) was determined for the whole system (for PID see fig. D.1):

- The Cryo-trap KY001 was at room temperature.
- Valves HV005 and HV006 between Cryo-trap and Si detector were opened.
- HV004, HV007, HV022 and HV023 were closed.
- HV061 was opened and the TMP VP061 was running.

The results of the first in-situ detritiation campaign are presented in fig. 6.5 as the time development of the benchmark parameter m. It is obvious, that the contami-

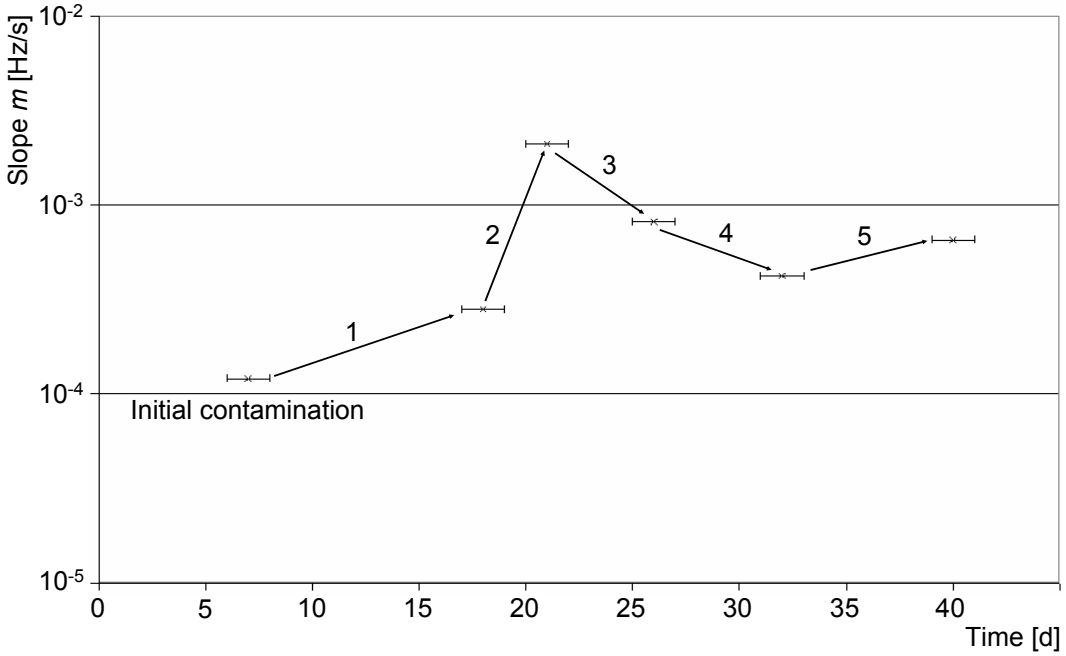

Figure 6.5: Results of first in-situ decontamination campaign. Initial contamination with cold cryostat; components baked according to fig. 6.4; (1) He-H_2 (5%): Purging at $\sim$ 1 bar with $\sim$ 30 l/h for $\sim$ 2 d; (2) CH_3OH: 12$\times$ flooding for $\sim$ 10 min with 100 mbar; (3) Baking only; (4) Baking only; (5) N_2-H_2O (10°C): Purging at $\sim$ 1 bar with 60 l/h for $\sim$ 4 d.

nation inside the system could not be lowered. Worse still, the contamination in the vicinity of the Si detector was increased. It seems, as if tritium was relocated from the stronger contaminated Cryo-trap to the lower contaminated Detection System, especially during flooding with methanol vapors. But also during purging with He-H_2 and humid N_2, tritium back diffusion against the general flow direction exists.

An additional gate valve just above the cryostat is recommended and was introduced during the ultrasonic bath cleaning campaign (sec. 6.4) in order to separate areas of higher tritium contamination (Cryo-trap) from those of very low tritium contamination (components above the cryostat).

6.4 Cleaning in ultrasonic bath

After the limited success of the first in-situ detritiation campaign (sec. 6.3), the components of TRAP above the cryostat were disassembled for cleaning in an ultrasonic bath. Furthermore, a CF63 gate valve was introduced just above the cryostat to separate the higher contaminated Cryo-trap form the low contaminated upper parts of the setup (refer to fig. 6.7).

6.4.1 Cleaning procedure

The surface contamination of the disassembled components (see fig. 6.6) was first determined by smear tests[2]. The components listed in table 6.1 were then cleaned in a large ultrasonic bath with deionized water at 70°C for several hours. The water in the bath was measured for tritium contamination with LSC (LSC analyzer: *PerkinElmer Tri-Cab 2800TR*) before and after cleaning. Treatment of the gold plated tubes of the Detection System in the ultrasonic bath was impossible, since the gold layer would have been removed during this process. Therefore, they were only rinsed with deionized water. After cleaning, all components were bathed in ethanol and heated with a hot air blower to remove any residual water.

[2] A defined surface area is smeared with a piece of styrofoam which is then dissolved in a liquid scintillator (*PerkinElmer Insta-Gel Plus*). The tritium content of the solution is determined via LSC. The errors of such measurements are easily 100% since the force applied during smearing and the surface area smeared have a strong impact on the amount of tritium removed from the surface.

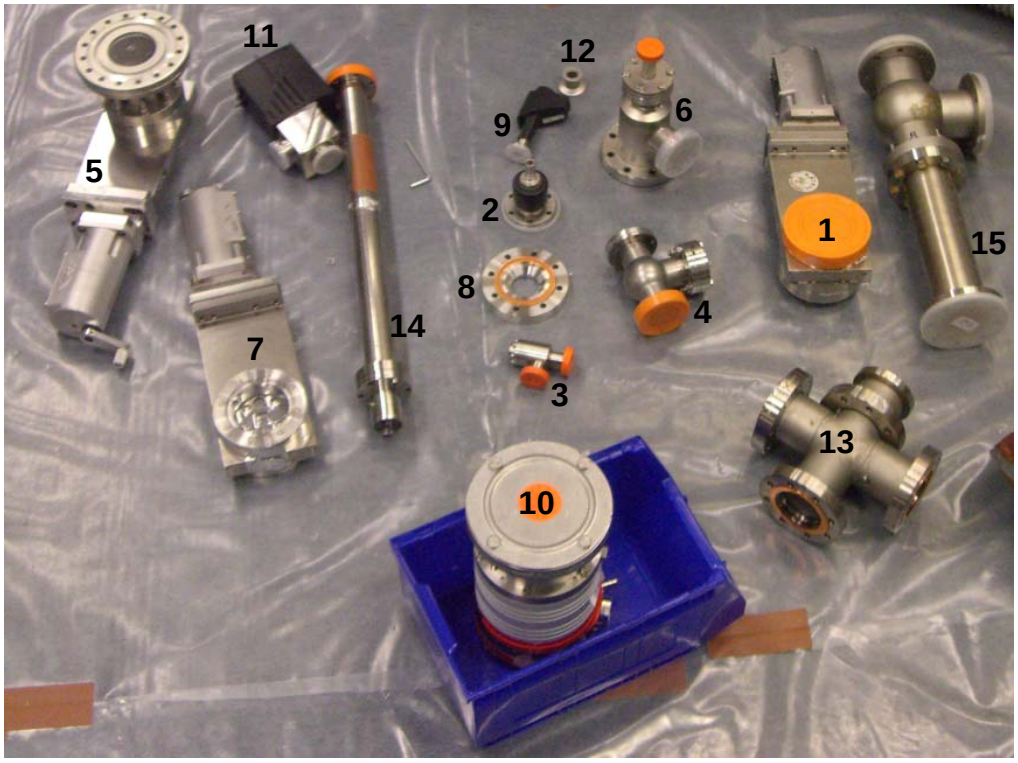

Figure 6.6: Disassembled components. Items: (1) VAT CF63 gate valve (HV006); (2) cold cathode pressure gauge (RP002); (3) VAT CF16 angle valve (HV022); (4) CF40 T-piece (connection to item no. 2); (5) VAT CF63 gate valve (HV061); (6) CF63-CF40 T-piece; (7) VAT CF63 gate valve (HV005); (8) CF60-40 transition flange; (9) Pirani pressure gauge (RP003); (10) turbomolecular pump (VP061); (11) KF25 automatic valve (AV061); (12) KF16-KF25 transition flange; (13) CF63 cross piece; (14) gold plated detector chamber; (15) gold plated RGA chamber and T-piece of the Detection System. A PID is available in appendix D.

6.4.2 Results and discussion

Table 6.1 shows the results of the ultrasonic bath detritiation campaign for the components cleaned in the bath. The columns indicate:

- **Item no.:** The item number according to fig. 6.6. The number in brackets states, whether it is the 1st, 2nd or 3rd cleaning of the given component.
- **Smear test [Bq/cm^2]:** The surface contamination determined by smear tests, errors are easily in the order of 100%
- **Leaching time [h]:** The treatment time in the ultrasonic bath
- **Water contamination [Bq/ml]:** The specific water contamination in the bath before and after detritiation, errors are about 5%

Table 6.1: Results of detritiation in ultrasonic bath. The item numbers correspond to those in fig. 6.6. Some items very cleaned more than once (indicated in brackets). The second column presents the surface contamination determined by smear tests. The third column gives the cleaning time in the ultrasonic bath and columns four and five the specific water contamination before and after cleaning, respectively, measured by liquid scintillation counting. With the volume of water in the bath (column six), the released tritium activity can be calculated (column seven).

Item no.	Smear test [Bq/cm^2]	Leaching time [h]	Water contamination before [Bq/ml]	Water contamination after [Bq/ml]	Water amount [l]	Total removed [kBq]
1 (1st)	1.2 ± 1.2	3.6	0.3 ± 0.02	2.9 ± 0.15	6.0 ± 0.3	15.6 ± 1.2
1 (2nd)	-	3.9	0.3 ± 0.02	2.3 ± 0.12	4.0 ± 0.2	8.0 ± 0.6
1 (3rd)	-	3.0	0.2 ± 0.01	1.3 ± 0.07	10.0 ± 0.5	11.0 ± 0.8
2 (1st)	94 ± 94	3.0	0.2 ± 0.01	12.3 ± 0.7	1.5 ± 0.1	18.2 ± 1.3
2 (2nd)	-	4.1	0.3 ± 0.02	12.9 ± 0.7	0.7 ± 0.0	8.8 ± 0.6
2 (3rd)	-	1.4	0.3 ± 0.02	12.6 ± 0.7	0.6 ± 0.0	7.4 ± 0.5
3 (1st)	30 ± 30	3.0	0.2 ± 0.01	6.2 ± 0.31	0.5 ± 0.0	3.0 ± 0.2
3 (2nd)	-	3.2	0.3 ± 0.02	0.5 ± 0.03	0.4 ± 0.0	0.1 ± 0.0
3 (3rd)	-	2.4	0.3 ± 0.02	0.5 ± 0.03	0.6 ± 0.0	0.1 ± 0.0
4 (1st)	5.8 ± 5.8	1.7	0.1 ± 0.01	17.1 ± 0.9	2.5 ± 0.1	42.6 ± 3.0
4 (2nd)	-	1.4	0.1 ± 0.01	3.1 ± 0.16	2.0 ± 0.1	6.0 ± 0.4
5 (1st)	4.2 ± 4.2	5.1	0.1 ± 0.01	3.5 ± 0.18	1.7 ± 0.1	5.8 ± 0.4
5 (2nd)	-	3.3	0.2 ± 0.01	0.4 ± 0.02	2.0 ± 0.1	0.4 ± 0.0
6 (1st)	4.5 ± 4.5	3.5	0.1 ± 0.01	4.5 ± 0.23	4.0 ± 0.2	17.6 ± 1.3
7 (1st)	1.6 ± 1.6	4.6	0.3 ± 0.02	52.0 ± 2.6	5.0 ± 0.3	258.5 ± 18.3
8 (1st)	0.2 ± 0.2	3.0	0.2 ± 0.01	1.3 ± 0.07	0.5 ± 0.0	0.6 ± 0.0

- **Water amount [l]:** The total amount of water, measurement errors are about 5%. Actually, the ultrasonic bath was completely filled with water ($\sim$ 75 l) and the components to be cleaned were put inside plastic bags which were then filled with deionized water, too. Thereby, not all of the water was contaminated after treatment, but only the water inside the bag ($<$ 10 l). The water outside was regularly checked for contamination in case of tritium penetration through the plastic bags.
- **Total removed [kBq]:** The total activity which was removed from the component in question taking the water background before treatment into account

The tritium surface contamination was determined to be < 100 Bq/cm^2 for all samples which is below the permitted contamination limit outside the laboratory. The highest surface contamination was found on the cold cathode pressure gauge (item 2 in fig. 6.6) which is no surprise taking into account that such devices work just like ion-getter pumps. The gauge was cleaned 3 times, the removed tritium contamination only decreasing slowly. It is also conspicuous, that tritium is removed quite early in the cleaning process, since the removed activity is almost the same for treatment during 4.1 and 1.4 h.

One of the three VAT CF63 gate valves, that is item 7 in fig. 6.6, showed the highest contamination release of 258.5 kBq. The other two gate valves (items 1 and 5 in fig. 6.6) showed moderate to low tritium releases and were cleaned several times.

After detritiation, subassemblies of the components were individually checked for contamination with the Si detector. Thereby it was found, that rinsing of the gold plated tubes with deionized water was enough to decrease their tritium contamination to an acceptable level: The components were rinsed with water 3 times; the removed tritium contamination was 6 kBq, 0.8 kBq and 0.5 kBq (equal to the water background). However, many stainless steel components were not sufficiently detritiated even after repeated cleaning in the ultrasonic bath.

The following components were therefore exchanged for new ones (PID in fig. D.1):

- Two pressure gauges: RP002 of Pirani type (item 9), RP003 of cold cathode type (item 2 in fig. 6.6)
- Three vacuum valves: HV022 (item 3), AV061 (item 11), HV005 (item 7 in fig. 6.6)
- Various vacuum components: the CF63 cross (item 13), two T-pieces (items 6 and 14), transitions (items 8 and 12 in fig. 6.6)
- The turbomolecular pump VP061 (item 10 in fig. 6.6), which could not be cleaned in the ultrasonic bath at all.

The only parts which were actually cleaned and reused are the gold plated tubes of the Detection System and two VAT CF63 gate valves. One of those was introduced

just above the cryostat as HV008 in order to be able to separate the Cryo-trap from the components above the cryostat (see fig. 6.7). The other was used as HV005. Since no new experimental insights were expected from the RGA (refer to sec. 5.4.2.1), it was removed together with HV006, which became obsolete after removing the RGA.

At the end of the detritiation campaign with the ultrasonic bath, the benchmark parameter for the components above HV008 was low enough for further measurements with tritium:

$$m = 7.1 \cdot 10^{-8} \text{ Hz/s}\,. \tag{6.7}$$

6.5 Second in-situ detritiation campaign

Shortly after the ultrasonic bath cleaning campaign was finished successfully, TRAP was again contaminated and the next tritium run (run#8) had to be aborted, too:

The infrastructure facility AMOR released traces of tritiated water vapors into the laboratory's exhaust channels. The tritium activity in the exhaust channel increased from the background reading of $\sim$ 0.5 MBq/m^3 to 7 MBq/m^3. The exhaust of TRAP's roughing pump VP062 (refer to appendix D for PID) was connected to the same channel and tritium penetrated against the air flow direction in the exhaust channel backwards through the roughing pump VP062 and the turbomolecular pump VP061 into the interior of the TRAP experiment. Since the Si detector is so sensitive to tritium, the benchmark parameter m increased for the components above HV008 from the initial $7.1 \cdot 10^{-8}$ Hz/s to $2.7 \cdot 10^{-5}$ Hz/s.

Thereupon, it was decided to retry some in-situ detritiation methods from sec. 6.3.1, after having introduced HV008 for separation of the Cryo-trap from the low contaminated parts above the cryostat. The specific procedures performed in the second in-situ detritiation campaign are described in sec. 6.5.1. Section. 6.5.2 discusses the results achieved.

6.5.1 Method of detritiation

The newly introduced valve HV008 allows for a separate detritiation of the upper and lower parts of the system (refer to fig. 6.7). The gas inlet and outlet for the components above HV008 are both just behind the Si detector as was the case during the first in-situ detritiation campaign (sec. 6.3.1). The gas injection into the Cryo-trap below HV008 is conducted through the argon injection capillary of the Argon Inlet System (refer to sec. 4.3.3); the evacuation is done through the cold valve at the bottom of the cryostat. Heating of the components as indicated in fig. 6.7 was maintained throughout the procedures described in the following.

- **Methanol flooding:** The components above HV008 were flooded for 10 min with $\sim$ 4 mbar methanol and then evacuated as described in sec. 6.3.1. This procedure was repeated ten times. Afterwards, the system was baked for 1 d.

- **D_2 flooding:** Both, the components above and below HV008 were repeatedly flooded with D_2 at various pressures and evacuated after some time (ranging from hours to days). The exact numbers are summarized in fig. 6.8 where the results are presented, too. Since the residual gas pressure in TRAP is still dominated by H_2 and the amount of D_2 and T_2 in the system is very similar, flooding with D_2 leads to a stronger disturbance of the steady state condition compared to H_2. A stronger increase in the isotopic exchange rate is therefore expected when offering D_2. This is different in strongly contaminated systems, where tritium atoms are the dominating hydrogen species.

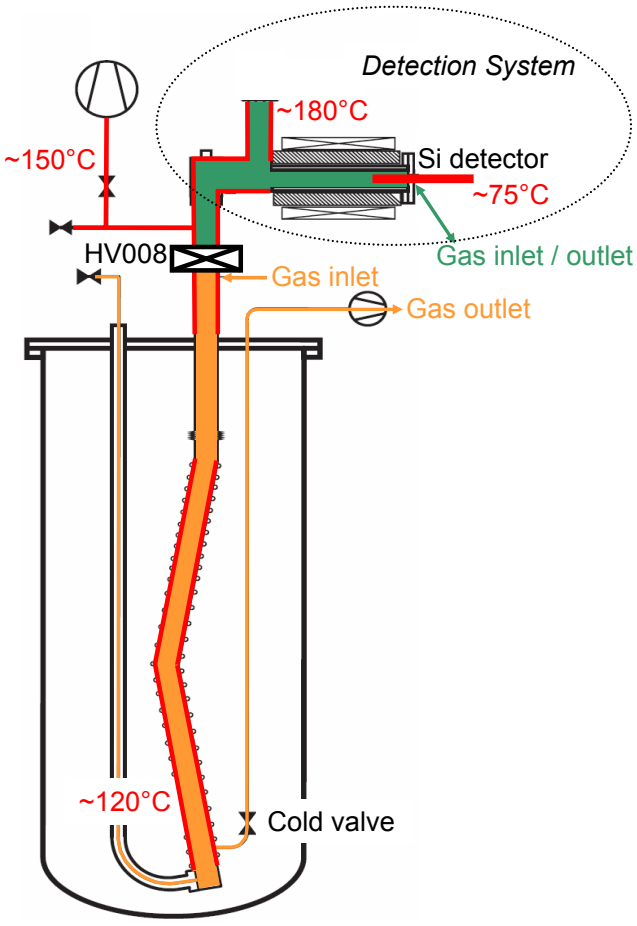

Figure 6.7: Second in-situ detritiation with deuterium flooding. The newly introduced gate valve HV008 allows for the separation of the higher contaminated Cryo-trap from the much lower contaminated parts above HV008 during detritiation.

6.5.2 Results and discussion

After the detritiation steps, the benchmark parameter m was checked with the Si detector (for PID see fig. D.1):

- Valves HV007 and HV008 were closed. Therefore, only the components above the cryostat were checked for contamination.
- HV005 was opened (HV006 was already removed after cleaning in the ultrasonic bath, see sec. 6.4.).
- HV061 was opened and the TMP VP061 was running.

The results of the second in-situ detritiation campaign are presented in fig. 6.8 along with a detailed description of the detritiation parameters. m was decreased by approximately two orders of magnitude to $\sim 3 \cdot 10^{-7}$ Hz/s which seems to be the detritiation limit. The time needed was ~ 2 months.

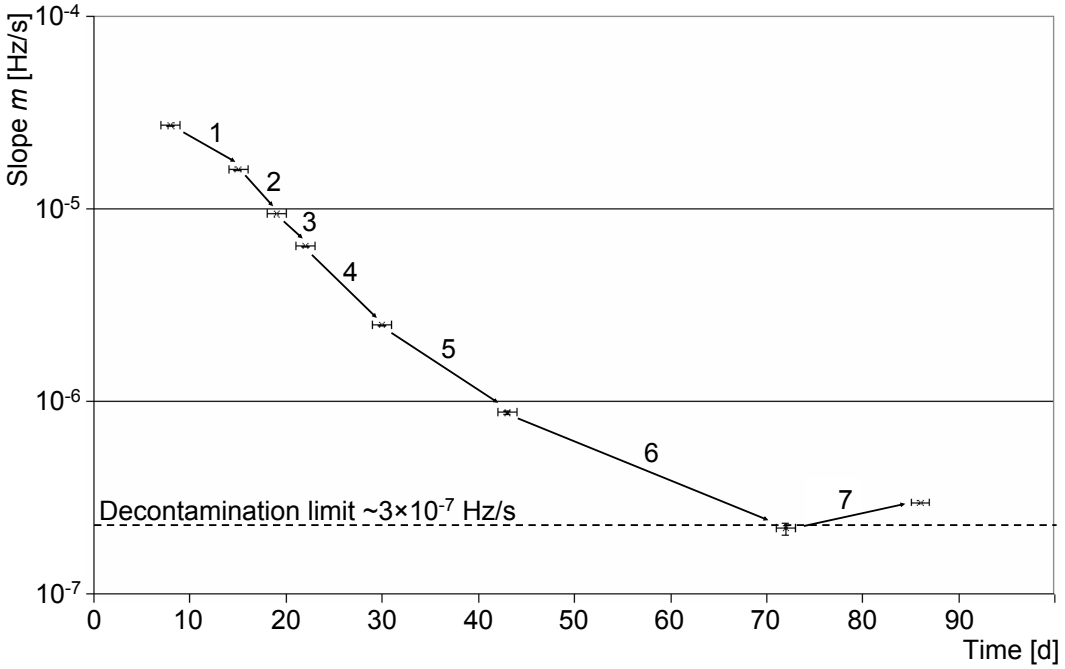

Figure 6.8: Results of second in-situ decontamination campaign. Shown in this picture are results for the upper parts above HV008 only. Components were always baked according to fig. 6.7; (1) CH_3OH: $10\times \sim 10$ min at 4 mbar, afterwards baking for 1 d; (2) D_2: $\sim 1/2$ d at ~ 300 mbar; (3) D_2: $7\times\ 30-60$ min at $10-20$ mbar, $1\times$ ~ 16 h at $10-20$ mbar; (4) CH_3OH-D_2: ~ 1 d at ~ 120 mbar CH_3OH and ~ 800 mbar D_2, D_2: 17 h at 16 mbar, 6 h at 85 mbar, 40 h at 65 mbar; (5) D_2: $7\times\ 20-26$ h, $1\times$ 5 h, $1\times$ 6 h, $1\times$ 67 h, $1\times$ 48 h at $50-90$ mbar; (6) D_2: $19\times \sim 1$ d at $10-20$ mbar, evacuation with TMP over weekends; (7) D_2: $8\times \sim 1$ d at $10-20$ mbar, evacuation with TMP over weekends

The following procedure was determined to be most effective for TRAP in view of detritiation performance and workload:

1. continuous baking of components ($120 - 160°C$) and evacuation
2. flooding with D_2 up to ~ 10 mbar
3. wait for $\sim 1/2$ d
4. evacuate
5. start again at 2)

The Cryo-trap below HV008 was also detritiated with this method. At the beginning of run#9 when the cryostat was cooled with LHe and argon condensate was prepared on the cryo-surface, the benchmark parameter m was determined for the complete system with HV008 opened. The time development of the detector count rate in $6 - 20$ keV for magnetic field off is given in fig. 6.9 along with the slope m. Using eq. 6.3, the HT partial pressure is restricted to

$$5.9 \cdot 10^{-19} \text{ mbar} < P < 5.9 \cdot 10^{-17} \text{ mbar}\,. \tag{6.8}$$

The second in-situ detritiation campaign was successful and enabled further tritium measurements with TRAP. The detritiation was only possible due to the gate valve

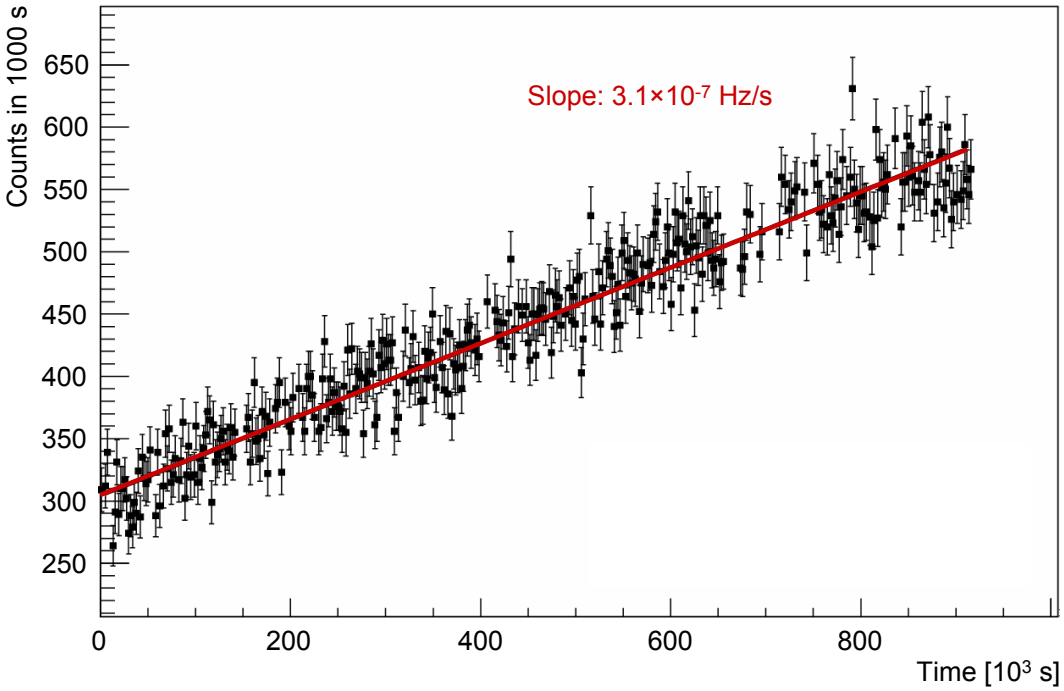

Figure 6.9: Detector background before run#9. Shown are the counts in the energy window $6 - 20$ keV measured with the Si detector during 1000 s over time. The magnetic field is off. The line represents a linear fit with a slope of $3.1 \cdot 10^{-7}$ Hz/s.

HV008 which was introduced into the experimental setup in order to separate the stronger contaminated Cryo-trap from the much lower contaminated components above the cryostat.

6.6 Conclusions for CPS and the Pre-spectrometer

Figure 6.10 shows the background count rate in $6-20$ keV at the beginning of run#9 with cold cryostat and argon cryo-deposit prepared for magnetic field on and off. This data set can be compared to the one presented in fig. 5.17 which was obtained during tritium injection in run#6. In the latter case, the outgoing tritium flow rate Q_{out} was determined to be in the order of 10^{-14} mbar l/s (refer to sec. 5.4.2.7). The conclusion is that the outgoing tritium flow rate Q_{out} achieved after the second in-situ detritiation campaign (sec. 6.5) is at least of the same order, too. Although the surface material was different for the two data sets, this is still valid because of the higher binding energy and solubility of tritium in stainless steel compared to gold (refer to sec. 6.1.3).

The detritiation method described in sec. 6.5.2 allows to decontaminate the CPS

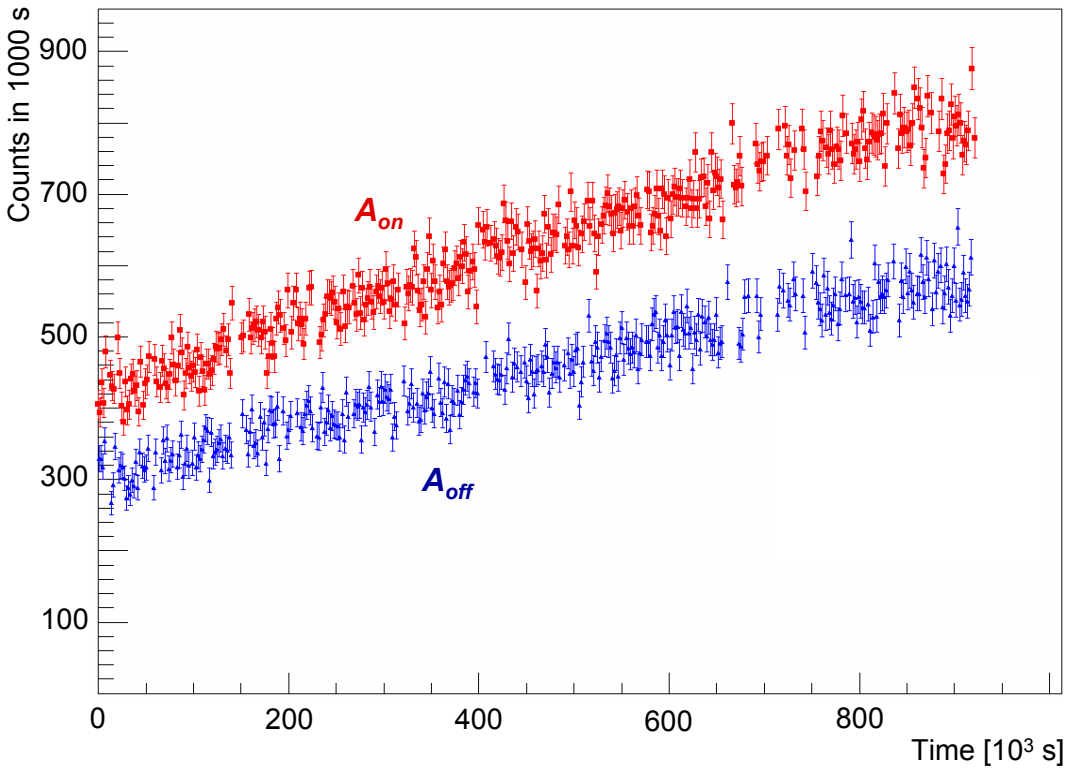

Figure 6.10: Detector background before run#9, both rates. Shown are the counts in the energy window $6-20$ keV measured with the Si detector during 1000 s over time for both, magnetic field on and off.

to an acceptable level leading to an acceptable tritium flow rate towards the Pre-spectrometer. Furthermore, the HT pressure in the Detection System (eq. 6.8) is approximately of the same order of magnitude which is required for the Pre-spectrometer. The efficiency of the detritiation will be even higher in case of the CPS and the Pre-spectrometer due to the higher temperatures available during bake out. This will strongly increase the tritium desorption and isotopic exchange rates.

Considering the work of Roland et al. [Rol06], it should be possible to further optimize the detritiation procedure obtained at TRAP. They determined the equilibrium constants for isotopic exchange reactions between D_2 and H_2O on the surface of stainless steel 304 vessels using a very similar method to the one employed during detritiation of TRAP: A stainless steel vessel of type 304, whose surface was purposely covered with a layer of H_2O, was flooded with $\sim$ 1 mbar D_2 and left standing for different reaction time periods, ranging from 40 s to 10 h. The relative concentrations[3] on the stainless steel surface was then determined by outgassing measurements. It was found that the relative concentration of HDO strongly increases with reaction time until $\sim$ 1 h, where saturation is reached. The relative concentration of D_2O reaches saturation later, after $\sim$ 4 h. Yet, its relative concentration is approximately one order of magnitude lower than that of HDO. Assuming that most of the tritium on the stainless steel surfaces is in form of tritiated water (HTO and T_2O), a reaction time of $\sim$ 1 h together with more frequent exchanges of D_2 might yield a better detritiation performance. However, automation of the process is required in this case.

For the CPS setup, the following recommendations can be derived from the experience obtained during detritiation of the TRAP components:

- The beamline of the CPS should be gold plated to allow for an easier detritiation compared to stainless steel.
- The CPS should be subdivided into two parts which are separated by a valve. This allows for an independent detritiation of the higher contaminated upstream from the lower contaminated downstream part.
- The CPS should feature a tritium monitoring detector to make sure that the tritium background is low enough before opening the valve to the Pre-spectrometer.

All recommendations from TRAP which led to the specification of the CPS are summarized in chapter 7.

[3] Ratio HDO/(H_2O+HDO+D_2O) and D_2O/(H_2O+HDO+D_2O) of HDO and D_2O, respectively

Chapter 7

Summary and Impact on the CPS

This chapter summarizes the results and experiences obtained with the TRAP experiment (sec. 7.1) and presents their impact on the design of the CPS (sec. 7.2). The final section (sec. 7.3) gives an outlook on the future of the TRAP experiment.

7.1 Summary

In the framework of this work, the last experimental run with deuterium was finished (sec. 5.2) and the setup was changed for tritium operation (appendix A). Three measurements with tritium followed with increasing importance of the semiconductor detector as the main tritium detection device in the Detection System (sec. 5.4). In order to derive the tritium adsorption rates on the detector and on the walls of the Detection System, a MC electron tracking simulation was implemented in a diploma thesis (sec. 5.3.2.4). Since the permeation rate through the bulk material of the stainless steel walls of the Detection System can be estimated only roughly, the relevant tubes were coated with gold for future measurements. After the occurrence of a strong contamination in the Detection System, the components in question were successfully decontaminated (chapter 6).

Summarizing, the TRAP experiment has fulfilled its main objectives given earlier in sec. 4.1:

- It has proven that the concept of tritium retention by a cryo-pump with precondensed argon is working. This issue was imperative for the licensing of the KATRIN experiment by the regulating authority: Since the controlled area of TLK ends just downstream of the CPS, an experiment was required to demonstrate that the amount of tritium released to the environment through the Pre-spectrometer is below the allowed limit.

- The tritium flow rate suppression factor was determined to be

$$F = \frac{Q_{in}}{Q_{out}} > (6.9 \pm 0.5_{\text{stat}} \pm 3.1_{\text{sys}}) \cdot 10^6 \,. \tag{7.1}$$

  As discussed in sec. 5.4.3, the tritium flow rate suppression factor given here is that for the specific hydrogen mixture used in the TRAP runs.

  The remaining uncertainties in the determination of F can be ruled out by future measurements with gold plated tubes in the Detection System.

- The setup and operation of TRAP has provided tremendous input data and experience for the specification of the CPS. The findings and the resulting implications for the CPS are given in sec. 7.2.

- A regeneration procedure for the cryo-surface was developed and successfully employed during three measurements with tritium (see appendix G).

- In this work only argon was tested as cryo-deposit. However, no additional changes in the experimental rig are necessary for operation with krypton, for example. This could be done in future measurements.

Furthermore, the additional objective given in sec. 6.1 was fulfilled:

- An in-situ detritiation procedure for decontamination of the CPS and the Pre-spectrometer was developed and successfully tested in TRAP.

In conclusion it can be stated that the TRAP experiment, the first experiment specially built for KATRIN that operates with tritium, was a success. It managed to determine the tritium flow rate leaving the Cryo-trap on the extremely low level of $\sim 10^{-14}$ mbar l/s. Furthermore, it provided essential experience and input data for the specification of the CPS. Especially the setbacks connected to the increased tritium contamination in the system proved to be valuable afterwards: They revealed possible contamination sources for the CPS and the Pre-spectrometer. In addition, decontamination procedures were developed which allow to decontaminate both components to an acceptably low residual tritium contamination.

7.2 Specification of the CPS

In the following, aspects of the specification of the CPS [CPS08a] are summarized, where results and experiences from TRAP decisively determined the CPS design.

The major impact from TRAP is visible in fig. 7.1: The original design of the CPS foresaw two independent cryostats that were separated by a warm gate valve. Both parts, the CPS1-F and the CPS2-F, were to be operated as cryo-sorption pumps at

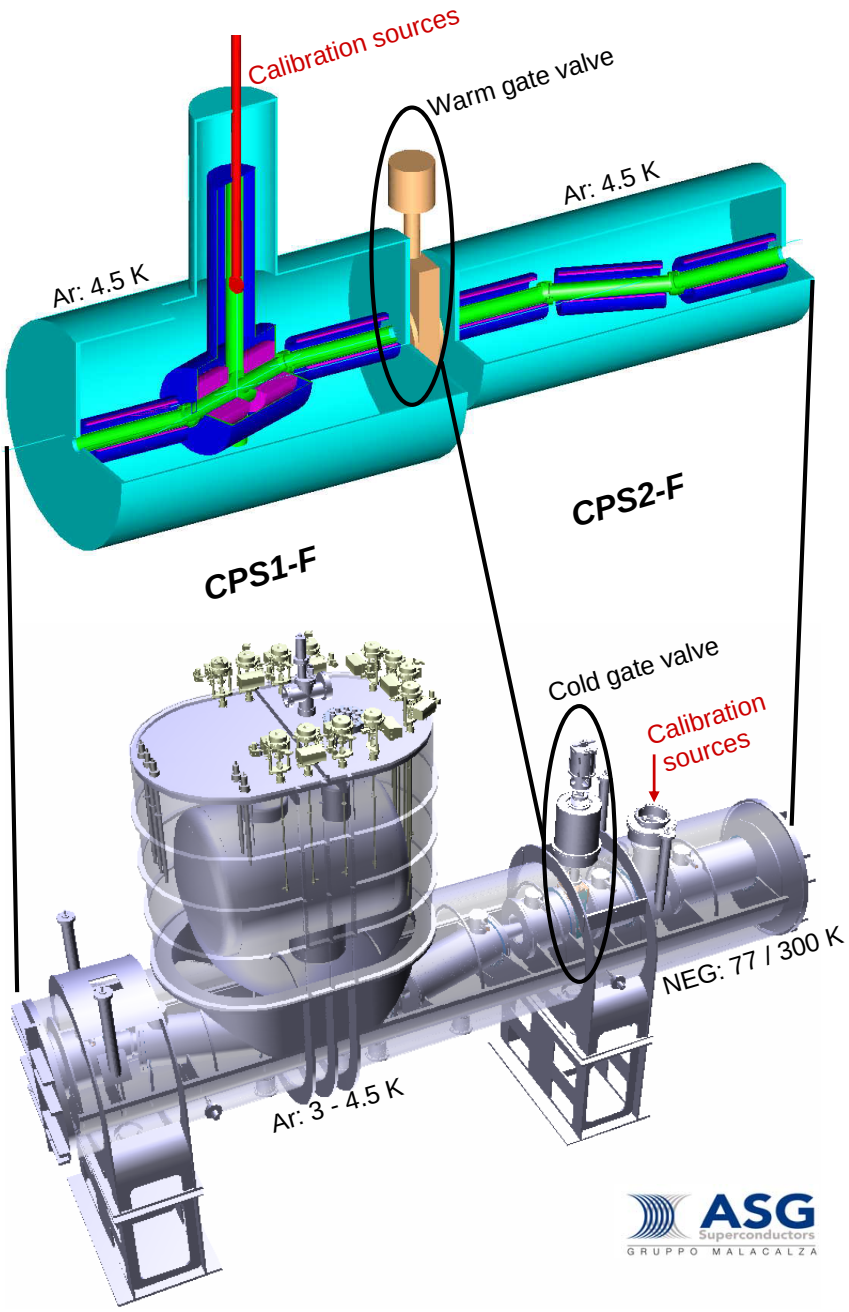

Figure 7.1: Comparison of old/new CPS design. Earlier in the design of the experiment it was planned to operate both parts of the CPS as cryo-sorption pumps with pre-condensed argon as adsorbent at $\sim$ 4.5 K. The two parts of the CPS were separated by a warm gate valve [KAT04]. The results of TRAP showed that the cryo-surface temperature should be lowered and that a cold gate valve should be introduced for separation of the CPS1-F and CPS2-F. The design was changed thereupon in favor of a single cryostat. Furthermore, it was decided to operate the CPS2-F with non-evaporable getter (NEG) strips at 77/300 K in order to guarantee sufficient pumping speed in the CPS2-F in case of a failure in the cooling system. (based on [CPS08b])

$\sim$ 4.5 K with pre-condensed argon as adsorbent. However, the results which were obtained during the measurements with TRAP as described in chapter 5 made the following changes necessary compared to the original design in [KAT04]:

- The temperature of the cryo-sorption surface should be lowered in order to achieve a higher tritium flow rate suppression factor as discussed in sec. 5.4.3. Especially HT, having the highest equilibrium pressure, poses the major challenge. Lowering the temperature from 4.5 K to 3 K will decrease the HT vapor pressure by $\sim$ 5 orders of magnitude according to fig. 3.5. In case of HT adsorption on pre-condensed argon, the decrease of equilibrium pressure should be similar. Thus, the new design of the CPS1-F allows for the operation in the temperature range $3 - 4.5$ K.
- Surfaces which are warmer than the cryo-surface have to be avoided during preparation of the argon condensate. Otherwise, the argon background pressure will be too high for the Pre-spectrometer (see sec. 5.2.2.2). A cold gate vale at $\sim$ 4.5 K instead of a warm one is therefore foreseen between the CPS1-F and CPS2-F. This valve will be closed during preparation of the cryo-deposit.
- Any injection of warm gas leads to an immediate desorption of adsorbent and tritium (see sec. 5.4.2.1). The tritium entering the CPS1-F should therefore be thermally accommodated. In the new design this is achieved by a tube section of an intermediate temperature of 77 K at the entrance to the CPS1-F. A schematic overview of the CPS beamline is given in fig. 7.2.

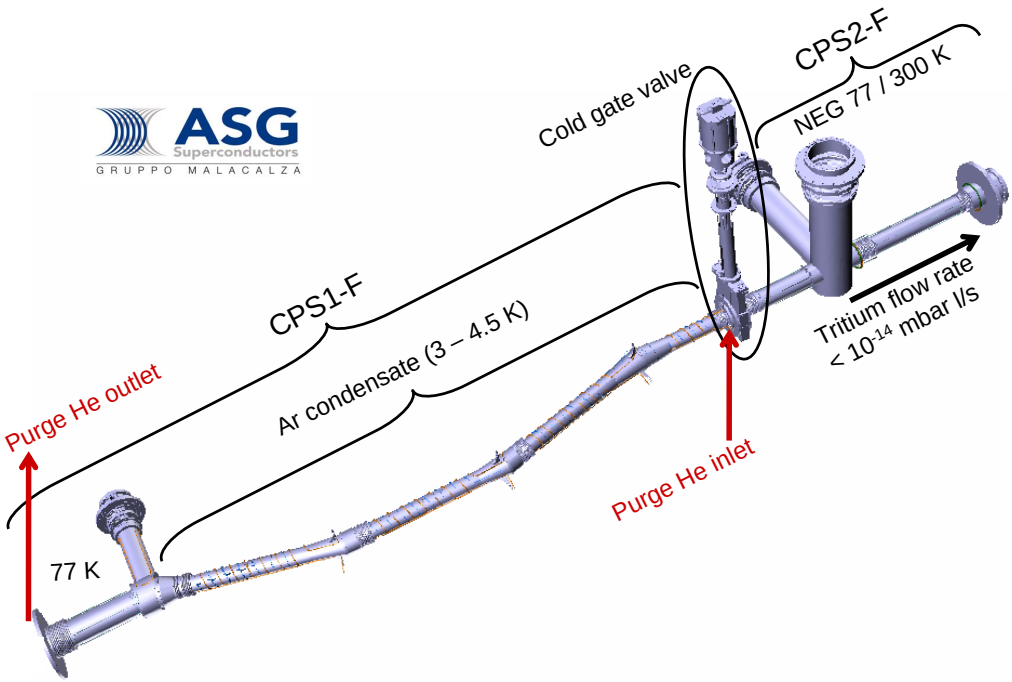

Figure 7.2: Schematic of the CPS beamline. (based on [CPS08b])

- TRAP showed that the amount of tritium leaving the Cryo-trap and entering the Detection System is in the order of 10^{-14} mbar l/s. Since the CPS1-F will have a higher tritium flow rate suppression factor than TRAP due to its more than 10 times larger cryo-surface, the amount of tritium entering the CPS2-F will be even lower than that entering the Detection System of TRAP. Therefore, it was decided to operate the CPS2-F with non-evaporable getter (NEG) strips at 77/300 K instead of pre-condensed argon at $\sim$ 4.5 K. This will guarantee a sufficient pumping speed in the CPS2-F in case of a failure in the cooling system and allow to close the gate valve in front of the Pre-spectrometer without contaminating the latter.

- The specification of the CPS should allow for the operation with krypton as cryo-deposit in the CPS1-F, which may further increase its tritium retention capability. The difference in operation with argon or krypton is mainly the different heating power required for heating the injection capillaries. The heating is necessary to prevent premature condensation of the gases inside the capillaries. For comparison, the boiling points are 87.3 K for argon and 119.9 K for krypton [Lid92].

Other recommendations for the design of the CPS are connected to the investigations regarding the tritium contamination in TRAP as described in chapter 6:

- The inner surface of the CPS should be gold plated in order to enable a much easier detritiation of the surface in case of an unforeseen tritium contamination (refer to sec. 6.4.2).

- Special care should be taken on how to connect the CPS to the laboratory exhaust channels of TLK. The connection should be conceived in a way that it is located as far away from the stack as possible. Otherwise, a tritium contamination of the CPS could occur through back diffusion of tritium through these channels as discussed in sec. 6.5.

- A tritium monitor should be foreseen in the CPS1-F that monitors the tritium contamination level before opening the cold valve. Such a monitor could be a solid state detector similar to the one employed in TRAP mounted in the pump port of the CPS1-F.

- The two-barrier safety concept of TLK requires the cooling fluid helium and the beamline of the CPS to be separated by two barriers. Otherwise, with only one single barrier, any leakage in this barrier could lead to a tritium contamination of the refrigerator that is located outside of TLK.

- The experience obtained during operation and decontamination of TRAP calls for a valve between the CPS1-F and CPS2-F in order to separate areas of high tritium contamination from those of low contamination if an in-situ detritiation of the CPS is required. The cold gate valve mentioned above exactly fulfills this requirement.

- The cold gate valve should be inserted with the sealed plate facing upstream where the tritium contamination will be higher. Thereby, the surface accessible to tritium is smaller in case of closed valve.

The theory of cryo-sorption, whose most important aspects are summarized in chapter 3, recommends the following optimizations to the design of the CPS:

- The thickness of the prepared argon layer should not exceed ~ 5 μm in order to keep its surface temperature low (refer to sec. 3.3.1).
- The operation temperature of the cryo-surface must be kept lower than the preparation temperature of the argon cryo-deposit at all times in order to prevent recrystallization in the argon condensate (see sec. 3.3.2). Therefore, the CPS cryostat cannot be a simple bath cryostat like the TRAP cryostat, but needs the possibility to set more than one temperature (operating temperature: $3 - 4.5$ K, argon preparation temperature ~ 6 K). This is achieved by tubes filled with LHe that are connected to the outside of the CPS1-F beamline. The higher temperature during argon preparation is achieved by an electric heater.
- The coverage of the argon frost pump CPS1-F should be kept low. Since the maximum amount of tritium gathered on the argon during the 60 day run time is fixed with ~ 1 Ci [KAT04], the coverage can only be decreased by increasing the cryo-surface area, for example by introducing baffles in the CPS1-F as shown in fig. 2.13. One should keep in mind that residual hydrogen coming from the Pre-spectrometer also increases the coverage in the CPS1-F. Therefore, the hydrogen from the Pre-spectrometer should be suppressed in the CPS2-F by non-evaporable getters (NEG).
- The baffles in the CPS1-F also prevent desorbed tritium from traveling far along the beamline since the neighboring baffle stopping the particle motion is only ~ 1 cm away. Thus, this measure will greatly hinder the tritium migration towards the Pre-spectrometer.
- In order to minimize desorption of tritium due to thermal irradiation from the DPS2-F, the first tube section is coated black resulting in a high thermal absorption coefficient (> 0.9).

An important objective of TRAP was the development and test of a regeneration procedure for the cryo-surface. Such a procedure was successfully developed and can be found in appendix G. A similar procedure is foreseen for the CPS1-F:

- The regeneration of the CPS1-F will be performed by heating and simultaneous purging with gaseous helium from the closed cold gate valve to the upstream end which is connected to the DPS2-F (see fig. 7.2). The purge gas enters the CPS1-F through a small flange at the upstream end of the cold gate valve and exits the CPS1-F through another small flange at the downstream end of the warm gate valve which connects the CPS to the DPS2-F.

- While regenerating the CPS1-F with purging, the mixture of helium/argon/tritium can be transferred to the ring manifold of the the main stage of the central tritium retention system of TLK. The valve to the ring manifold must not be opened without an ample helium flow rate, otherwise a strong tritium contamination of the CPS1-F will occur.

Summarizing, it can be stated that the results and experiences from TRAP decisively defined the specification of the CPS [CPS08a].

7.3 Future of the TRAP experiment

After repairing the mechanical damage inside the cryostat, the main focus of future measurements of TRAP is the elimination of uncertainties connected to the permeation rate of tritium through the walls of the Detection System. Therefore, gold plated tubes, for which the permeation rate is much smaller [McL73], will be employed instead of stainless steel ones. This will allow for the determination of the flow rate suppression factor with a much higher confidence.

Furthermore, measurements with krypton as cryo-deposit instead of argon are considered. Due to its higher atomic number, it features stronger van der Waals forces between adsorbate and adsorbent particles. This results in a lower tritium partial pressures in the Cryo-trap and thus to a higher tritium suppression factor at the same temperature compared to argon. Such a measurement could answer the question, whether it is possible to employ krypton at 4.5 K instead of argon at $\sim$ 3 K and still have a comparable tritium retention.

Apart from measurements directly connected to the CPS, TRAP allows to investigate tritium pumping properties of cryo-pumps with pre-condensed gases as adsorbent which are of interest in other scientific fields, too. In the nuclear fusion reactor ITER [ITE01], for example, cryo-pumps with activated charcoal are employed for pumping of the exhaust gas from the tokamak [Glu06]. As mentioned above in sec. 3.1.2, charcoal has some disadvantages with regard to operation with tritium, one of them being possible dust formation.

TRAP is a working experimental rig licensed for operation with tritium and could, for example, measure adsorption isotherms of tritium adsorption on different gas condensates: At constant temperature (4.2 K), the tritium content in the Cryo-trap, that is the coverage, is increased stepwise. The silicon detector could then be used to determine the tritium equilibrium pressure during the steady state phase.

Appendix A

Changes in the Experimental Setup

For operation with tritium, parts of the experimental setup had to be changed compared to the status described in [Eic04]. Appendix A.1 summarizes the requirements for safe tritium operation; their implementation is described in appendix A.2. Furthermore, changes were also made in order to improve the experiment (see appendix A.3).

A.1 Requirements for safe tritium operation

For the safe operation of the TRAP experiment with tritium, certain requirements had to be fulfilled. First of all, a complete safety description for licensing of the experiment was prepared. The general guidelines are summarized in the following:

1. It is necessary for TRAP to fulfill TLK's so-called *Technical Terms of Delivery and Acceptance* which describe tritium compatible components like buffer vessels and pipework. The most important features for TRAP are:
   - the utilization of certified (tritium compatible) materials and metal sealings,
   - the X-raying of 50% of all weldings,
   - to prevent cavities, where tritium inventories could be collected,
   - to keep volumes as small as possible and
   - to smoothen inner surfaces.
2. The (primary) tritium containment should be enclosed within a secondary containment (two barrier concept).
3. Tritium monitors should be used to detect any accidental tritium releases.

4. The TRAP experiment needs connections to the TLK infrastructure for contaminated exhaust gases.

Item 1 was already considered while building the cryostat internals (fig. 4.4) and the gas injection system [Eic04]. Yet, some of the above requirements could be officially relaxed by a concession request since the total tritium inventory in TRAP is relatively small (< 4 Ci $\approx 1.5 \cdot 10^{11}$ Bq) and the experiment operates at low tritium pressures: The highest tritium pressure of ~ 100 mbar exists in the tritium reservoir of 25 cm^3 volume; in the rest of the experiment, the tritium pressure is well below 0.1 mbar.

For the last three items additional construction work was necessary as described in the next section.

A.2 Changes of the setup for safe tritium operation

- In order to enforce the two barrier concept, the gas injection system is enclosed in a hood (see fig. 4.6) that is connected to the laboratory's clean exhaust. The cryostat itself constitutes a secondary hull for the cryostat internals (fig. 4.4).
- Ionization chambers below the hood and above the cryostat are used for tritium monitoring.
- During tritium runs, the helium return line to ITP is not used since tritium might penetrate into the LHe of the cryostat in case of a leak. The exhaust helium is instead transferred to the laboratory's clean exhaust and wasted through the stack. The maximum inventory in the Cryo-trap, which would be released to the environment in accidental case, is 1 Ci = 37 GBq. The TLK's license allows for a weekly tritium release of $2 \cdot 10^{12}$ Bq through the stack.

  Due to the length of the return line to ITP, a considerable overpressure of ~ 100 mbar in the cryostat is necessary for helium transportation. The tube to the laboratory's exhaust, on the other hand, is very short with the ventilation system creating a slight underpressure in the exhaust channels. Therefore, needle valves were introduced in the piping to the laboratory's clean exhaust channel to ensure a slight overpressure in the cryostat in order to prevent any leakage of air into the cryostat.
- The Pumping System of TRAP (sec. 4.3.6) is separated into two parts: Pumps that carry a negligible amount of tritium in terms of safety considerations (VP060, VP061 and VP062), whose exhaust is transferred to the laboratory's clean exhaust, and pumps for evacuation of the Tritium Inlet System (VP040, VP041 and VP042). The exhaust of the latter pumps is transferred to the main stage of TLK's central tritium retention system.

  Unlike described in [Eic04], no getter pumps are used for pumping tritium. The ion getter pump VP040 was never commissioned, too.

A.3 Improvements to the experimental setup

The following changes were made compared to [Eic04] in order to improve the setup:

- The vacuum conductance from the Cryo-trap toward the Detection System was increased by exchanging the DN40 CF components of the Detection and the Pumping System to DN63 CF components. Furthermore, the DN40 CF angle valves used in the system previously were exchanged to DN63 CF gate valves.
- The RGA chamber was enlarged to DN63 CF components in order to prevent increased outgassing due to heating of the walls by the RGAs' filaments.
- The Detection System was enhanced with the Si detector as described in detail in sec. 4.3.7.

Appendix B

Deduction of $C_D(t)$

In the following, eq. 5.24 is deduced from the effective adsorption rate of hydrogen[1] on the Si detector surface

$$\frac{dn}{dt} = \frac{dn_A}{dt} - \frac{dn_D}{dt}\,. \tag{B.1}$$

The adsorption rate dn_A/dt and the desorption rate dn_D/dt are given by eq. 3.7 and 3.8, respectively. Putting all together, one obtains an inhomogeneous linear differential equation for the number n of hydrogen molecules on the detector:

$$\frac{dn(t)}{dt} + A \cdot n(t) = B \tag{B.2}$$

with

$$A = \frac{1}{t_s} \qquad \text{and} \qquad B = 2.63 \cdot 10^{22} \left[\frac{\sqrt{\text{g/mol K}}}{\text{s mbar cm}^2}\right] \frac{P\ \alpha\ S}{\sqrt{MT}}\,. \tag{B.3}$$

The parameters are:

- t_s: Sojourn time (see eq. 3.1)
- P: Hydrogen pressure in the Detection System. Since a mixture of hydrogen molecules is injected, "hydrogen pressure" should be understood as an effective value. In the following, P is assumed to be constant.
- α: Sticking coefficient for hydrogen on the Si detector
- S: Si detector surface area, including non-sensitive parts
- M: Molar weight of hydrogen. Since a mixture of hydrogen molecules is injected, it should be regarded as an effective value, too.
- T: Gas temperature, ~ 300 K

The general solution of an inhomogeneous linear differential equation is obtained by the sum of the general solution of the associated homogeneous and a specific solution of the inhomogeneous differential equation [Mer06].

[1] Q_2, all six hydrogen isotopomers are considered

Homogeneous differential equation: The associated homogeneous equation

$$\frac{dn(t)}{dt} + A \cdot n(t) = 0 \tag{B.4}$$

is solved by

$$n_H(t) = C \cdot e^{-At} \tag{B.5}$$

with constant C.

Inhomogeneous differential equation: According to [Mer06] a specific solution for the inhomogeneous equation can be derived from the general solution of the associated homogeneous equation by the method of *Variation of the Constant*, where the constant C is regarded as a function of t:

$$n_I(t) = C(t) \cdot e^{-At}\,. \tag{B.6}$$

Putting eq. B.6 in eq. B.2, one obtains

$$\left(\frac{dC(t)}{dt} \cdot e^{-At} - A \cdot C(t) \cdot e^{-At}\right) + A \cdot \left(C(t) \cdot e^{-At}\right) = B\,, \tag{B.7}$$

which is solved by

$$C(t) = \frac{B}{A} \cdot e^{At}\,. \tag{B.8}$$

Thus, a specific solution of the inhomogeneous differential equation is

$$n_I(t) = \frac{B}{A}\,. \tag{B.9}$$

The general solution of the inhomogeneous differential equation is the sum of eqs. B.5 and B.9:

$$n(t) = n_H(t) + n_I(t) = C \cdot e^{-At} + \frac{B}{A}\,. \tag{B.10}$$

The constant C is constrained by the boundary condition

$$n(0) = n_0\,, \tag{B.11}$$

which means that at $t = 0$ already n_0 hydrogen molecules stick to the Si detector. It then follows that the constant C is

$$C = n_0 - \frac{B}{A}\,. \tag{B.12}$$

Putting eqs. B.3, B.10 and B.12 together together, eq. 5.24 is finally obtained.

Appendix C

Additional diagrams

Diagrams that were excluded from chapter 5 in favor of readability can be found here.

C.1 RGA data from run#6

The RGA data from run#6 do not yield any new insights and are quite comparable to those from run#5 (refer to sec. 5.4.2.1). Nevertheless, they are included for completeness.

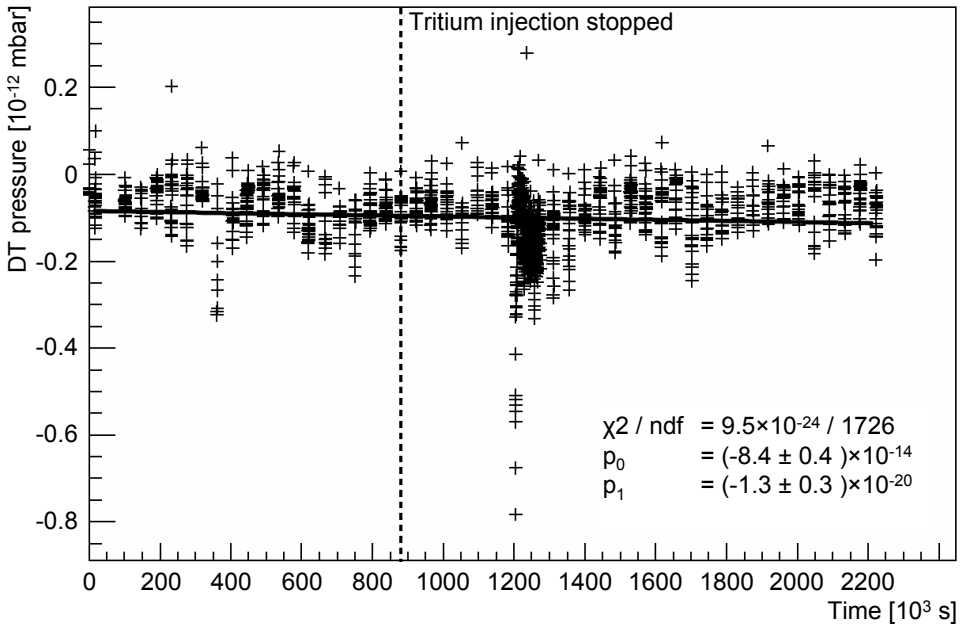

Figure C.1: Run#6: RGA data. Data for DT with the $1-6$ amu RGA: the dotted line marks the end of the injection phase, a linear fit $f(x) = p_0 + p_1 x$ was applied.

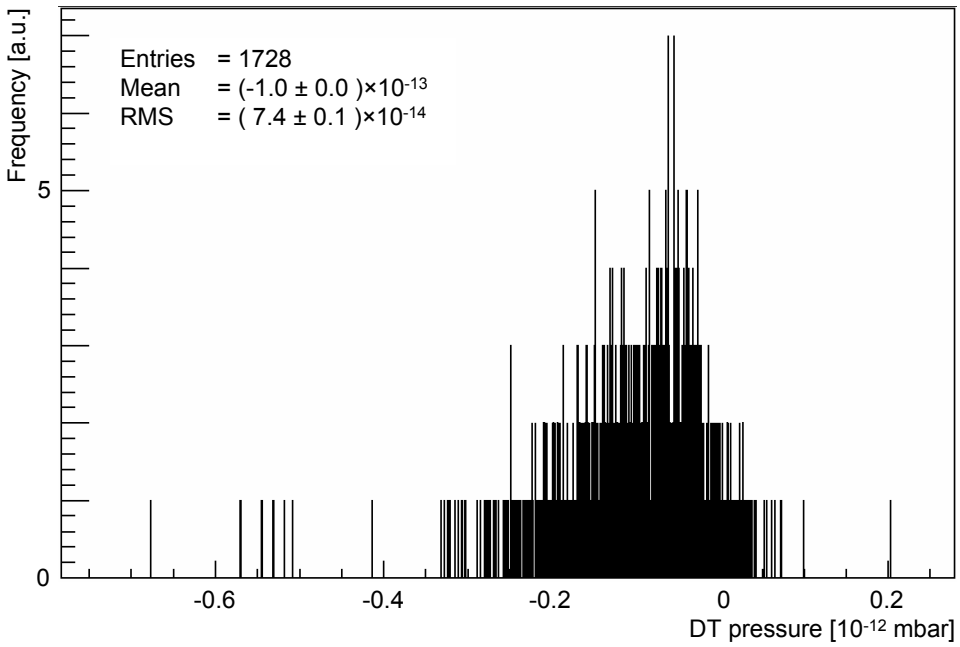

Figure C.2: Run#6: RGA data projection. Frequency of DT partial pressure readings on the $1-6$ amu RGA during injection and steady state phase (RMS: Root Mean Square).

C.2 Detector contamination - exact calculation

The tritium contamination on the detector C_D can be calculated in two different ways:

- In sec. 5.4.2.3, the approximation from eq. 5.17 was used. The uncertainties of the MC simulation introduce a systematic error of 30% on C_D (refer to sec. 5.3.2.4).
- In this section, the exact formula from eq. 5.16 is used. This yields a higher systematic uncertainty of 100% on C_D (refer to sec. 5.3.2.4).

The data for the detector contamination C_D calculated in the latter way is shown in figs. C.3, C.4 and C.5. The data points $C_D(t)$ were calculated from the count rates $A_{off}(t_1)$ and $A_{on}(t_2)$ with $|t_1 - t_2| < 1000$ s and $t = \max(t_1, t_2)$ using eq. 5.16. The error bars are statistical errors calculated by Gaussian error propagation from the statistical errors on A_{off} and A_{on} and on the MC parameters a, b, c and r.

The data was fitted to eq. 5.39. The adsorption rate on the detector Q_D and the DT partial pressure in the Detection System P are calculated in the same manner as described in sec. 5.4.2.3 and sec. 5.4.2.4, respectively. The results are:

$$Q_D < (17788 \pm 3816_{\text{stat}} \pm 29920_{\text{sys}}) \text{ T atoms/s and} \quad \text{(C.1)}$$
$$P < (7.3 \pm 1.1_{\text{stat}} \pm 7.3_{\text{sys}}) \cdot 10^{-16} \text{ mbar} \quad \text{(C.2)}$$

for the injection phase in run#6 (fig. C.3),

$$Q_D < (3690 \pm 410_{\text{stat}} \pm 4235_{\text{sys}}) \text{ T atoms/s and} \quad \text{(C.3)}$$
$$P < (-8.4 \pm 6.5_{\text{stat}} \pm 8.4_{\text{sys}}) \cdot 10^{-18} \text{ mbar} \quad \text{(C.4)}$$

for the steady state phase in run#5 (fig. C.4) and

$$Q_D < (297 \pm 244_{\text{stat}} \pm 2595_{\text{sys}}) \text{ T atoms/s and} \quad \text{(C.5)}$$
$$P < (4.5 \pm 0.5_{\text{stat}} \pm 4.5_{\text{sys}}) \cdot 10^{-17} \text{ mbar} \quad \text{(C.6)}$$

for the steady state phase in run#6 (fig. C.5).

As a consistency check, these results are compared to the results obtained earlier in secs. 5.4.2.3 and 5.4.2.4, where the approximation from eq. 5.17 was used: All values for Q_D and those of run#6 for P are comparable. Yet, the systematic errors are much higher. The DT partial pressure value for run#5, on the other hand, shows a difference of ~ 2 orders of magnitude. This can be attributed to the high starting contamination on the walls of the Detection System in run#5 (refer to sec. 5.4.2.6):

Equation 5.16 can be written as

$$C_D = C'_D - \frac{a}{c} C_W \,, \quad \text{(C.7)}$$

where C'_D is the approximated detector contamination (eq. 5.17). If C_W is at least $c/a \approx 109$ times higher than C'_D, C_D will be very small or even negative as is the case for run#5.

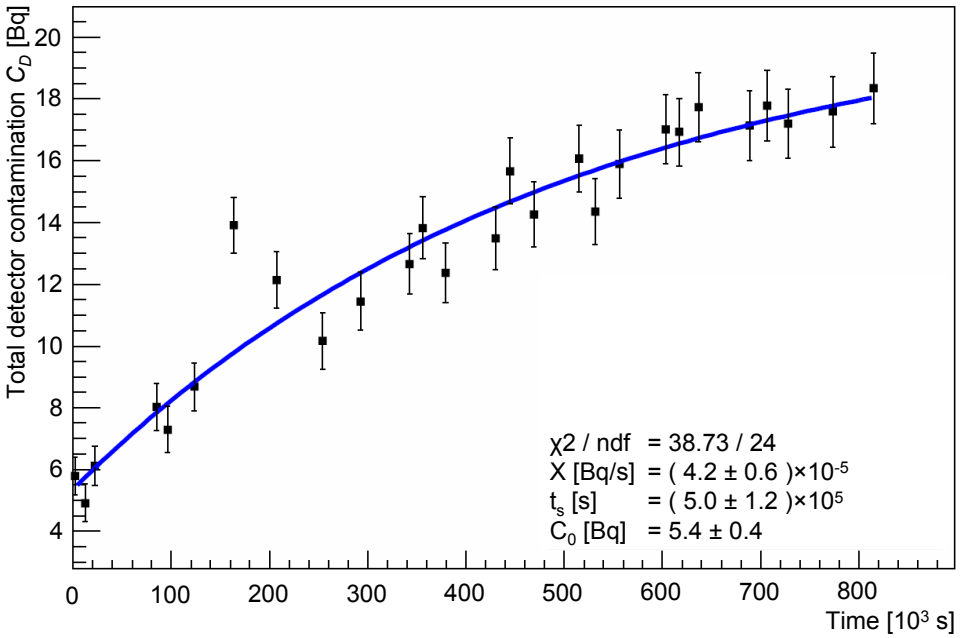

Figure C.3: Run#6: Detector contamination C_D during injection phase. Sown is the total tritium contamination on the Si detector over time. For explanations see text.

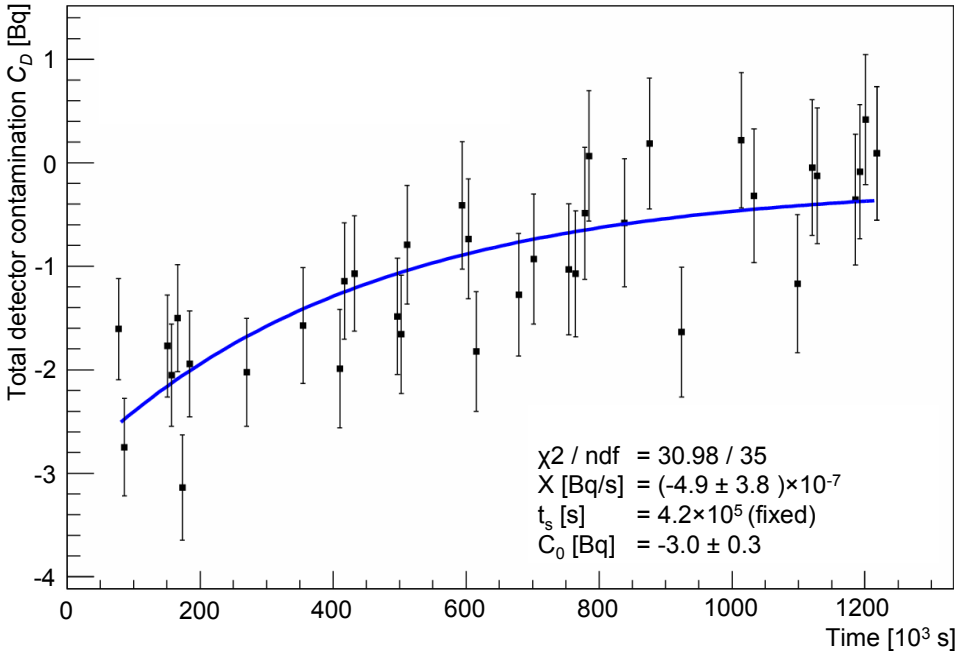

Figure C.4: Run#5: Detector contamination C_D during steady state phase. Sown is the total tritium contamination on the Si detector over time. For explanations see text.

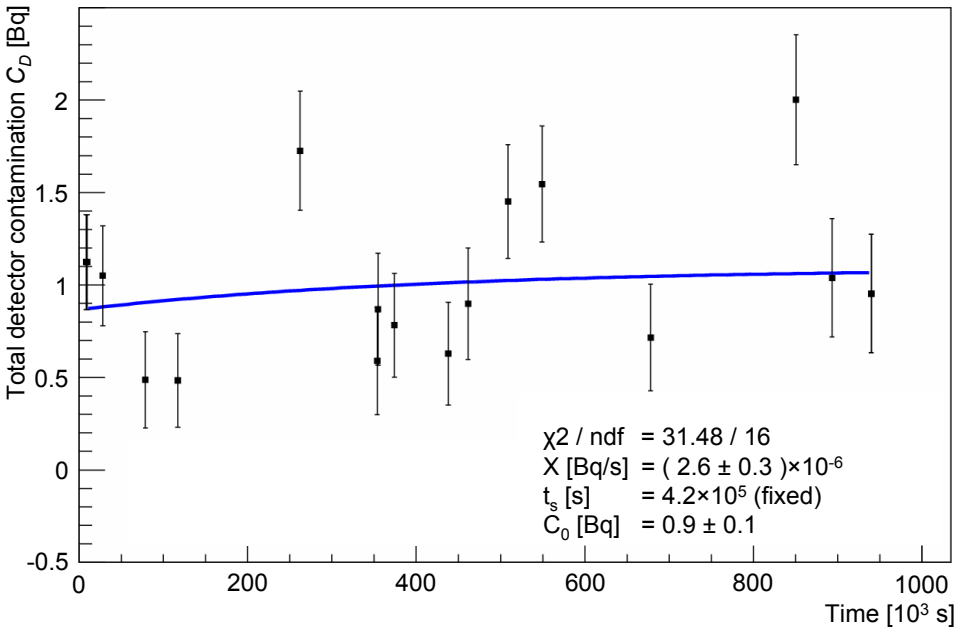

Figure C.5: Run#6: Detector contamination C_D during steady state phase. Sown is the total tritium contamination on the Si detector over time. For explanations see text.

Appendix D

Process and Instrumentation Diagram and List of Components

In the following, the list of components as well as the process and instrumentation diagram (PID) of TRAP are given. The PID in fig. D.1 shows all components which were ever part of the experimental rig. For comments refer to table D.1.

Table D.1: List of components.

Name	Description
AV001	Part of flow controller TYLAN FC730, VCR 1/4 in.
AV044	Balzers EVCF40, ISO CF40 (controlled by VP041)
AV052	Leybold EV25 EM VA, ISO KF 25 (controlled by VP042)
AV061	Leybold EV25 EM VA, ISO KF 25 (controlled by VP061)
AV062	Balzers EVCF40, ISO CF40 (controlled by VP060)
BD002	Tritium inlet buffer vessel: 1.3 l
BD030	Argon inlet buffer vessel: 1.3 l
HV001	Valve on tritium storage vessel, VCR 1/4 in.
HV002	Swagelok SS-4BG-V51, VCR 1/4 in.
HV003	Swagelok SS-4BG-V51, VCR 1/4 in.
HV004	VAT UHV16 angle valve, ISO CF16
HV005	VAT UHV63 gate valve, ISO CF63
HV006	VAT UHV63 gate valve, ISO CF63 (removed during ultrasonic bath cleaning, see sec. 6.4)
HV007	Pink angle valve, ISO CF16

Name	Description
HV008	VAT UHV63 gate valve, ISO CF63 (introduced after ultrasonic bath cleaning, see sec. 6.4)
HV020	Swagelok SS-4BG-V51, VCR 1/4 in.
HV021	Swagelok SS-4BG-V51, VCR 1/4 in.
HV022	Swagelok SS-4BG-V51, VCR 1/4 in.
HV023	Swagelok SS-8UW-TW (cold valve, handle extended)
HV024	Leybold angle valve, ISO CF40
HV025	Swagelok SS-8BG-VCR, VCR 1/2 in.
HV030	Swagelok SS-4BRG-V51, VCR 1/4 in.
HV032	Swagelok SS-4BG-V51, VCR 1/4 in.
HV033	Leybold angle valve, ISO KF16
HV040	Swagelok SS-4BG-V51, VCR 1/4 in.
HV041	VAT UHV16 angle valve, ISO CF16
HV042	Swagelok SS-4BG-V51, VCR 1/4 in.
HV043	Swagelok SS-4BG-VCR, VCR 1/4 in.
HV044	Leybold angle valve, ISO KF25
HV045	Swagelok SS-8BG-VCR, VCR 1/2 in.
HV046	Swagelok SS-8BG-VCR, VCR 1/2 in.
HV047	Swagelok SS-8BG-VCR, VCR 1/2 in.
HV048	Swagelok SS-8BG-VCR, VCR 1/2 in.
HV049	Swagelok SS-8BG-VCR, VCR 1/2 in.
HV050	Balzers angle valve, ISO KF25
HV051	Pink angle valve, ISO KF50 (part of TLK infrastructure)
HV060	VAT UHV16 angle valve, ISO CF16
HV061	VAT UHV63 gate valve, ISO CF63 (exchanged later to VAT UHV63 angle valve, ISO CF63, see sec. 6.4)
HV062	Pink angle valve, KF25
HV063	Swagelok SS-8BG-VCR, VCR 1/2 in.
HV064	Swagelok SS-8BG-VCR, VCR 1/2 in.
HV065	Swagelok SS-8BG-VCR, VCR 1/2 in.
HV066	Swagelok SS-8BG-VCR, VCR 1/2 in.
HV068	Swagelok SS-4BG-V51, VCR 1/4 in.
HV081	Leybold butterfly valve, ISO KF40
HV082	Leybold angle valve, ISO KF16
HV090	Swagelok SS-4BRG-V51, VCR 1/4 in.
HV091	Leybold angle valve, ISO KF25
KY001	Cryo-trap (see sec. 4.3.2)
RF020	Part of TYLAN FC730 flow controller, VCR 1/4 in.

Name	Description
RF080	Gas flow meter, Elster Experimentiergaszähler
RGA	MKS residual gas analyzer (see appendix F)
RP001	MKS Baratron 690A (0-10 Torr)
RP002	Leybold Thermovac (Pirani)
RP003	Leybold Penningvac (cold cathode)
RP031	MKS Baratron 390HA (0-1000 Torr)
RP080	Membrane pressure gauge (0-10 bar), ISO KF16
RP081	Membrane pressure gauge (0-1.6 bar), ISO KF16
RV002	MKS flow controller (adjusted electronically)
RV003	Swagelok SS-4BMG-VCR, VCR 1/4 in.
RV031	Swagelok SS-4BMG-V51, VCR 1/4 in.
RX080	Ionization chamber, Berthold Multi-Logger LB5310 (below hood)
RX081	Ionization chamber, Berthold Multi-Logger LB5310 (above cryostat)
Si	Si detector (see sec. 4.3.7)
VP040	Leybold IZ12
VP041	Pfeiffer TPU170, turbomolecular pump
VP042	Alcatel ACP15, roots pump
VP060	Pfeiffer TPU170, turbomolecular pump
VP061	Pfeiffer TMU200MP, turbomolecular pump
VP062	Alcatel ACP28, roots pump
VP090	Pfeiffer DCU, pumping trolley
WT080	Water heat exchanger

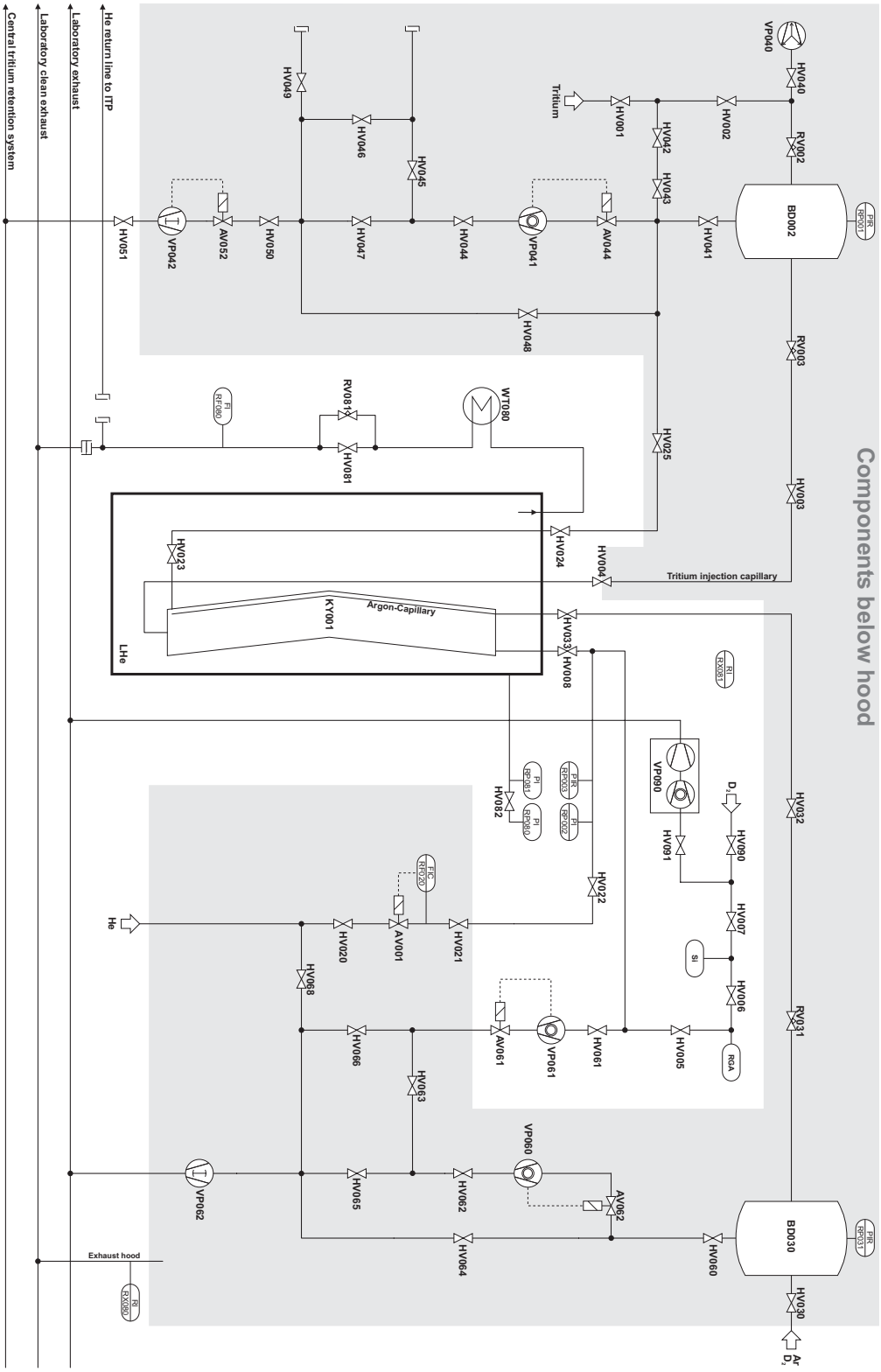

Figure D.1: PID of TRAP.

Appendix E

JFET Hybrid Circuit Diagram

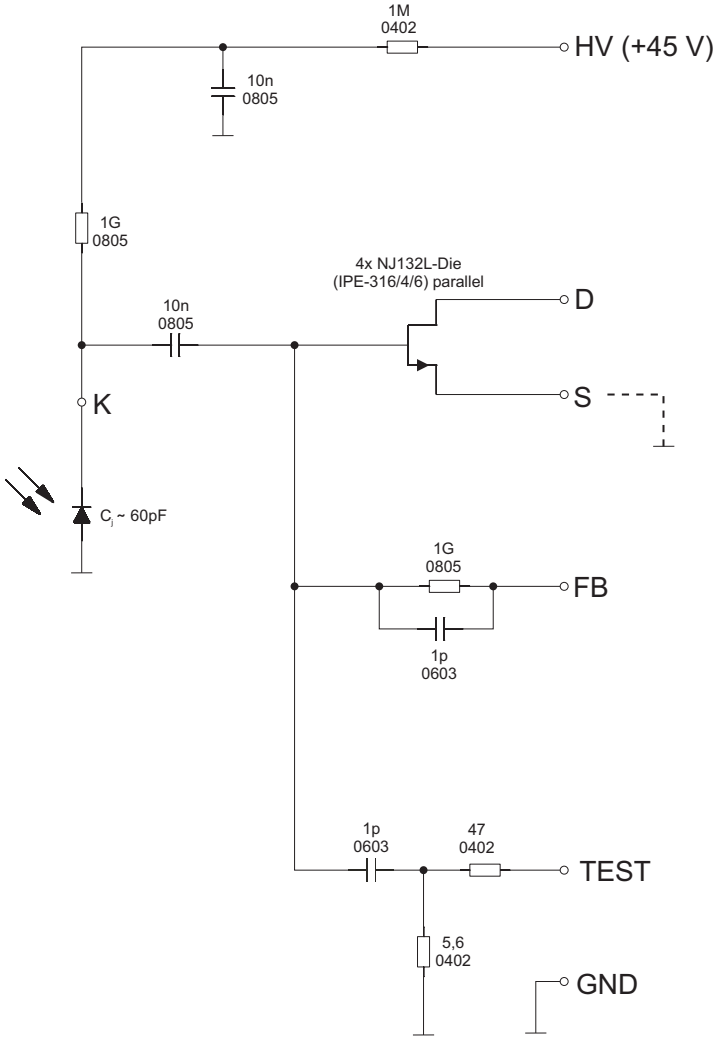

Figure E.1: Circuit diagram of the JFET hybrid. The JFET hybrid is depicted in fig. 4.12 and introduced in sec. 4.3.7.4. (based on [Wue04])

Appendix F

Residual Gas Analyzers

Two residual gas analyzers from MKS, both of type *Spectra Microvision Plus Smart Head*, with different mass ranges ($1-100$ amu and $1-6$ amu) are used in TRAP. The most important data of the residual gas analyzers are summarized in table F.1.

Table F.1: RGA specifications. Exert from [MKS04]

Mass range	$1-100$ amu ($1-6$ amu)
Maximum operational pressure	10^{-4} mbar
Detection limit	Faraday: $2 \cdot 10^{-11}$ mbar
	Channelplate SEM: $5 \cdot 10^{-14}$ mbar
	Single channel SEM: $2 \cdot 10^{-14}$ mbar
Mass stability with $T = const$	Better than $\pm$0,1 amu during 8 h
Resolution	$< 10\%$ between two peaks of same height
Maximum baking temperature	250°C (electronic unit disconnected)
Maximum operational temperature	200°C (faraday mode)
Vacuum connection	ISO CF40
Ion source options	Open, UHV, closed, cross-beam
Ion source stability	$2 \cdot 10^{-4}$ A/mbar
Ion source parameters	Electron energy: $20-100$ eV
	Emission current: $0-5$ mA
	Ion energy: $0-10$ V
	Ion acceleration potential: 0 bis -130 V
Specified outgassing rate	$< 10^{-9}$ mbar l/s
Filaments	Twin tungsten

Appendix G

Regeneration of the Cryo-trap

After each run, the Cryo-trap needs to be regenerated. The procedure is presented in the following. Refer to fig. 4.4 for an illustration and fig. D.1 for a PID.

1. Start evaporation of the LHe with the heater mat that is situated at the bottom of the cryostat.
2. When temperature increase measured by the TVO sensors gets visible on the Cryo-trap (temperature rises above 4.2 K), start purging with GHe. Set the volume flow rate to $\sim$ 4 l/min and purge through HV020, HV021, HV022, (HV008)[1], HV023, HV024, HV025, HV048, HV050, AV052, VP042 and HV051 into the tritium retention system of TLK.
3. When all the LHe is evaporated from the cryostat, switch on the tube heater to warm up the cryo-surface (heating power $\sim$ 60 W).
4. Flood the cryostat with warm GHe to get rid of the cold GHe.
5. When the cryo-surface reaches $\sim$ 100 K after $\sim$ 3 h, decrease the purge flow rate to $\sim$ 1 l/min and continue heating and purging for several days.
6. Stop purging when the system reaches $\sim$ 300 K after $\sim$ 3 d.
7. Evacuate, using first VP040 and VP042 and then VP061 and VP062.

[1] Inserted after detritiation with ultrasonic bath, refer to sec. 6.4

Bibliography

[Aal02] C. E. AALSETH et al., *arXiv:hep-ex*/0201021v1 (2002)

[Abd94] J. N. ABDURASHITOV et al., *Phys. Lett. B* **328** (1994) 234
`http://pdg.lbl.gov/`

[Alu94] E. ALUI et al., *Phys. Rev. Lett.* **94** (1994) 081802

[Ans92] P. ANSELMANN et al., *Phys. Lett. B* **285** 386

[Ara04] T. ARAKI et al., *arXiv:hep-ex*/0406035 (2004)

[Arn03] C. ARNABOLDI et al., *arXiv:hep-ex*/0302006v1 (2003)

[Arp08] C. ARPESELLA et al., *Phys. Lett. B* **658** (2008) 101

[Bac88] H. BACKE et al., *Phys. Scr. T* **22** (1988) 98

[Bae62] W. BÄCHLER et al., *Trans. Nat. Vac. Symp.* **9** (1962) 216

[Bah06] J. N. BAHCALL et al., *Astrophys. J. Supp. Series* **165** (2006) 400

[Bel95] A. I. BELESEV et al., *Phys. Lett. B* **350** (1995) 263

[Ben76] C. BENVENUTI et al., *J. Vac. Sci. Technol.* **13** (1976) 1172

[Ben83] C. BENVENUTI, *Nucl. Inst. Meth.* **205** (1983) 391

[Bes08] U. BESSERER, private communication, Tritiumlabor (ITP-TLK), Forschungszentrum Karlsruhe (2008)

[Bon99] J. BONN et al., *Nucl. Inst. Meth. A* **421** (1999) 256

[Bor60] E. S. BOROWIK et al., *Zhur. Tekhn. Fiz.* **30** (1960) 506

[Bra03] J. BRAND, R. MÜLLER, drawings of the cryostat internals, Hochmuth & Partner, Reinhold-Schneider-Str. 73d, 76199 Karlsruhe (2003)

[Cle95] B.T. CLEVELAND et al., *Nucl. Phys. B* (Proc. Suppl.) **38** (1995) 47

[Cor92] V. J. CORCORAN et al., *Fus. Technol.* **21** (1992) 727

[Cor05] D. CORNELI et al., *Fus. Sci. Technol.* **48** (2005) 55

[CPS08a] KATRIN COLLABORATION, *Technical Specification Cryogenic Pumping Section (CPS)*, Annex_TA_10-DSP-4210-1, internal document (2008)

[CPS08b] ASG SUPERCONDUCTORS, *KATRIN CPS - Technical Design Report Part 1*, internal document (2008)

[Dan00] M. DANILOV et al., *Phys. Lett. B* **480** (2000) 12

[Dav94] R. DAVIS, *Prog. Part. Nucl. Phys.* **32** (1994) 13

[Dav96] R. DAVIS, *Nucl. Phys. B* **48** (1996) 284

[Day03] C. DAY et al., *Fus. Eng. and Des.* **69** (2003) 97
C. DAY, *Handbook of Surfaces and Interfaces of Materials* **5** (2001) 265

[Day04] C. DAY, *Kryovakuumtechnik und Kryopumpen*, VDI-Seminar Kryotechnik, Karlsruhe, March 17-19 (2004)

[Day07] C. DAY et al., *J. Vac. Sci. Tech. A* **25** (2007) 824

[Doe08] P. DOE, *Status of the focal plane detector (FPD)*, presentation at the 15th KATRIN Collaboration Meeting, Karlsruhe, September 29-30 (2008)

[Dre05] G. DREXLIN, *Nucl. Phys. B (Proc. Suppl.)* **138** (2005) 282

[Ebe82] W. EBERHARDT et al., *Sol. St. Comm.* **42** (1982) 799

[Eic04] F. EICHELHARDT, *Diploma Thesis*, Universität Karlsruhe (2004)

[Emm37] P. H. EMMETT, S. BRUNAUER, *J. Am. Chem. Soc.* **59** (1937) 1553
`http://www.iter.org/pdfs/Summary_FDR.pdf`

[Fuk98] Y. FUKUDA et al., *Phys. Rev. Lett.* **81** (1998) 1562

[Fuk06] M. FUKUGITA et al., *arXiv:astro-ph*/0605362v1 (2006)

[Geh06] R. GEHRING, magnetic field calculations, Institut für Technische Physik (ITP), Forschungszentrum Karlsruhe (2006)

[Glü06] F. GLÜCK, Institut für Experimentelle Kernphysik (IEKP), Universität Karlsruhe (2006)

[Glu05] M. GLUGLA, private communication, Central Engineering and Plant Support Department, ITER Organization, Cadarache (2005)

[Glu06] M. GLUGLA et al., *Fus. Eng. Des.* **81** 733

[Gol58] M. GOLDHABER et al., *Phys. Rev.* **109** (1958) 1015

[Gri87] D. GRIFFITHS, *Introduction to Elementary Particles*, John Wiley & Sons, Inc. (1987)

[Hab09] F. HABERMEHL, *PhD Thesis*, Universität Karlsruhe, in preparation (2009)

[Hae81] R. A. HAEFER, *Kryo-Vakuumtechnik*, Springer Verlag (1981)
R. A. HAEFER, *Cryopumping*, Clarendon Press, Oxford (1989)

[Hak06] H. HAKEN, H. C. WOLF, *Molekülphysik und Quantenchemie*, 5. Auflage, Springer Verlag (2006)

[Han06] S. HANNESTAD, *arXiv:astro-ph*/0607101v1 (2006)

[Hin08] G. HINSHAW et al., *arXiv:astro-ph*/08030732v2 (2008)

[Hir84] T. HIRABAYASHI, M. SAEKI, *J. Nucl. Mater.* **120** (1984) 309

[Hir89] K.S. HIRATA et al., *Phys. Rev. Lett.* **63** (1989) 16

[Hon60] R. E. HONIG et al., *RCA Rev.* **21** (1960) 360

[Hop07] C. HOPF et al., *J. Nucl. Mater.* **363** (2007) 882

[Hos06] J. HOSKA et al., *Phys. Rev. D* **73** (2006) 112001

[Hun63] A. L. HUNT et al., *Adv. Cryog. Eng.* **8** (1963) 100

[Hut96] E. HUTTER et al., *Fus. Technol.* **29** (1996) 1189

[Iba99] H. IBACH, H. LÜTH, *Festkörperphysik*, fifth edition, Springer (1999)

[ITE01] ITER, *Summary of the ITER Final Design Report* (2001)

[ITK06] INFORMATIONSZENTRUM TECHNISCHE KERAMIK
`http://www.keramverband.de/`

[Jac99] J. D. JACKSON, *Classical Electrodynamics*, third edition, John Wiley & Sons (1999)

[KAT04] KATRIN COLLABORATION, *FZKA Scientific Reports* **7090** (2004)

[Kaz04] O. KAZACKENKO, drawing of the TRAP detector bearing, Tritiumlabor (ITP-TLK), Forschungszentrum Karlsruhe (2004)

[Kaz08] O. KAZACHENKO et al., *Fus. Sci. Technol.* **54** (2008) 67

[Kla01] H. V. KLAPDOR-KLEINGROTHAUS et al., *Eur. Phys. J. A* **12** (2001) 147

[Kla04] H. V. KLAPDOR-KLEINGROTHAUS et al., *Phys. Lett. B* **586** (2004) 198

[Kra05] C. KRAUS et al., *Eur. Phys. J. C* **40** (2005) 447

[Lae89] R. LAESSER, *Tritium and Helium-3 in Metals*, Springer (1989)

[Lee72] T. J. LEE, *J. Vac. Sci. Technol.* **9** (1972) 257

[Leu07] J. LEUNIG, schematic drawings of KATRIN, Institut für Kernphysik (IK), Forschungszentrum Karlsruhe (2007)

[Lew07] R. LEWIS, *PhD Thesis*, Swansea University (2007)

[Ley02] LEYBOLD, *Grundlagen der Vakuumtechnik* (2002)

[LHC] LHC COLLABORATION, *LHC Homepage* `http://lhc.web.cern.ch/lhc/`

[Lid92] D. R. LIDE (Editor-in-Chief), *Handbook of Chemistry and Physics*, 72nd Edition, CRC Press, Boston (1992)

[Lob85] V. M. LOBASHEV et al., *Nucl. Inst. Meth. A* **240** (1985) 305

[Lob99] V. M. LOBASHEV et al., *Phys. Lett. B* **460** (1999) 227

[Lob03] V. M. LOBASHEV, *Proc. 17. Int. Conf. on Nuclear Physics in Astrophysics*, Debrecen, Hungary, 2002, *Nucl. Phys. A***719** (2003) 153

[LoI01] KATRIN COLLABORATION, *arXiv:hep-ex/*0109033 (2001)

[Luo04] X. LUO et al., *KATRIN DPS2-F Vacuum Monte Carlo Simulation (Version 2)*, 10-ME-4101-1, internal document (2004)

[Luo05] X. LUO, C. DAY, *Estimation of the vacuum performance of the KATRIN DPS1-F by Monte Carlo simulation*, 10-ME-2104-0, internal document (2005)

[Mai99] L. MAIANI , *Fus. Eng. Des.* **46** (1999) 433

[Mal73] M. P. Malkov et al., *Handbook on Physical and Technical Basis of Cryogenics*, Energiya, Moskwa (1973)

[McL73] R. B. McLELLAN, *J. Phys. Chem. Solids* **34** (1973) 1137

[Mel06] M. MELONI, D. STERN, drawings of the Detection System of TRAP, Institut für Kernphysik (IK), Forschungszentrum Karlsruhe (2006)

[Mer06] G. MERZIGER, T. WIRTH, *Repetitorium der Höheren Mathematik*, 5. Auflage, Binomi Verlag (2006)

[Mik85] S. P. MIKHEYEV, A. Y. SMIRNOV, *Sov. J. Nucl. Phys.* **42** (1985) 1441

[MKS04] MKS, *Data Sheet MKS Microvision PLUS SmartHead* (2004) `http://www.mksinst.com/docs/UR/microv.pdf`

[Mon06] A. MONFARDINI et al., *Nucl. Inst. Meth. A* **559** 346

[Nak04] H. NAKAMURA, *Fus. Eng. Des.* **70** (2004) 163

[Nep05] S. A. NEPIJKO et al., *Chem. Phys. Chem.* **6** (2005) 235

[Nic95] N. H. NICKEL et al., *Phys. Rev. B* **52** (1995) 7791

[Nis00] M. NISHIKAWA, *J. Nucl. Mater.* **277** (2000) 99

[ORC04] M. A. HOWE et al., *IEEE Transactions on Nucl. Sci.* **51** (2004) 878

[Ott98] E. OTTEN, *Repetitorium Experimentalphysik*, Springer (1998)

[Ott08] E. OTTEN, C. WEINHEIMER, *Rep. Prog. Phys.* **71** (2008) 086201

[PDG08] C. AMSLER et al. (Particle Data Group), *Phys. Lett. B* **667** (2008) 1

[Pen06] R. D. PENZHORN et al., *J. Nucl. Mater.* **353** (2006) 66

[Per02] A. N. PEREVEZENTSEV et al., *Removal of Tritium from Stainless Steel Type 316 (I)*, Annual Report of Hydrogen Isotope Research Center, Toyama University (2002)

[Pic92] A. PICARD et al., *Nucl. Inst. Meth. B* **63** (1992) 345

[Rei77] L. REIMER, *Raster-Elektronenmikroskopie*, Springer (1977)

[Rin05] A. RINGWALD, *arXiv:hep-ph*/0505024v1 (2005)

[Rob88] R. G. H. ROBERTSON, D. A. KNAPP, *Ann. Rev. Nucl. Sci.* **38** (1988) 185

[Rol06] T. F. ROLAND et al., *J. Nucl. Mater.* **353** (2006) 193

[ROO06] CERN, *ROOT, An Object-Oriented Data Analysis Framework* (2006) `http://root.cern.ch/`

[Ros00] S. ROSANVALLON et al., *Fus. Eng. Des.* **51** (2000) 605

[Rot90] A. ROTH, *Vacuum Technology*, third, updated and enlarged edition, North Holland (1990)

[Sae00] A. SAENZ et al., *Phys. Rev. Lett.* **84** (2000) 242

[Sak88] G. L. SAKSAGANSKIJ, *Molecular flow in complex vacuum systems*, Gordon and Breach (1988)

[San05] C. SAN MARCHI, *Permeability, Solubility and Diffusivity of Hydrogen Isotopes in Stainless Steels at High Gas Pressures*, WSRC-STI-2007-00579 (2005)

[Sch97] N. SCHMITZ, *Neutrinophysik*, Teubner Verlag (1997)

[Sch05] S. SCHÖNERT et al., *Nucl. Phys. B* **145** (2005) 242

[Sch08] P. SCHNEIDER, *Einführung in die Extragalaktische Astronomie und Kosmologie*, Springer Verlag (2008)

[Sch09] M. SCHLÖSSER, *Diploma Thesis*, Universität Karlsruhe, in preparation (2009)

[Shm03] W. T. SHMAYDA, *Decontamination of Tritiated Metals*, presentation at the Workshop on the Experience in the Management of Wastes from Fusion Facilities, EFDA-JET, Culham Science Center, Abingdon, UK (2003)

[Sis04] M. SISTI et al., *Nucl. Inst. Meth. A* **520** 125

[Smi66] C. C. SMITH, G. LEWIN, *Vac. Sci. Tech.* **3** (1966) 92

[SNO00] SNO COLLABORATION, *Nucl. Inst. Meth. A* **449** (2000) 172

[SNO01] SNO COLLABORATION, *arXiv:nucl-ex*/0106015v2 (2001)

[SNO02] SNO COLLABORATION, *arXiv:nucl-ex*/0204008v2 (2002)

[Sou86] P. C. SOUERS, *Hydrogen Properties for Fusion Energy*, University of California press, Berkeley (1986)

[Sta04] S. STAHL, *Feasibility Study: Implementation of Intra-beam-line Penning Traps for Online Monitoring of Ion Density at the KATRIN Experiment*, Elektronik-Beratung, Sonderanfertigungen, Kellerweg 23, 67582 Mettenheim (2004)

[Sta08] W. A. STAHEL, *Statistische Datenanalyse: eine Einführung für Naturwissenschaftler*, Vieweg (2008)

[Sto93] L. STOBINSKI, R. DUS, *Czech. J. Phys.* **43** (1993) 1035

[Sto96] L. STOBINSKI, *App. Sur. Sci.* **103** (1996) 503

[Stu07] M. STURM, *Diploma Thesis*, Universität Karlsruhe (2007)

[Stu10] M. STURM, *PhD Thesis*, Universität Karlsruhe, in preparation (2010)

[Sue95] M. SÜSSER, *ICEC Proc.* **17** (1995)

[Sur88] R. A. SURETTE, R. G. C. MCELROY, *Fus. Technol.* **14** (1988) 1141

[Swa79] W. A. SWANSIGER, R. BASTASZ, *J. Nuc. Mater.* **85** (1979) 335

[Tem71] K. E. TEMPELMEYER, *J. Vac. Sci. Technol.* **8** (1971) 612

[TLK05] L. DÖRR et al., *Fus. Sci. Technol.* **48** (2005) 262

[TLK08] L. DÖRR et al., *Fus. Sci. Technol.* **54** (2008) 143

[Tor04] Y. TORIKAI et al., *J. Nucl. Mater.* **329** (2004) 1624

[Val09] K. VALERIUS, *PhD Thesis*, Westfälische Wilhelms-Universität Münster, in preparation (2009)

[Wei93] C. WEINHEIMER et al., *Phys. Lett. B* **300** (1993) 210

[Wei03] C. WEINHEIMER, in *Neutrino Mass*, pp25-52, G. ALTARELLI and K. WINTER, Ed., Springer (2003)

[Wol78] L. WOLFENSTEIN, *Phys. Rev. D* **17** (1978) 2369

[Won91] K. Y. WONG, *Fus. Eng. Des.* **16** (1991) 159

[Wue04] S. WÜSTLING, development of the TRAP detector and its electronics, Institut für Prozessdatenverarbeitung und Elektronik (IPE), Forschungszentrum Karlsruhe (2004)

[XRD01] X-RAY DATA BOOKLET, Center for X-ray Optics and Advanced Light Source, Lawrence Berkeley, National Laboratory (2001)
`http://xdb.lbl.gov/`

[Yuf67] V. B. YUFEROV, F. E. BUSOL, *Sov. J. Tech. Phys.* **11** (1967) 1518

[Yuf70] V. B. YUFEROV, R. M. KOBEZ, *Sov. J. Tech. Phys.* **14** (1970) 1261

[Zar79] A. S. ZARCHY, R. C. AXTMANN, *J. Nucl. Mater.* **79** (1979) 110

Acknowledgments

First of all, I would like to express my gratitude to my consultants Prof. Dr. G. Drexlin from Karlsruhe and Prof. Dr. C. Weinheimer from Münster.

Furthermore, my thanks go to Dr. B. Bornschein and Dr. O. Kazachenko for all the fruitful discussions and their continuous support. N. Kernert and M. Sturm were irreplaceable assistants during all laboratory work. I thank H. Frenzel, J. Leunig, K. Mehret, M. Meloni, R. Neeb, and D. Stern for their commitment in the design and setup of the extractor hood and the detector support structure.

I would like to thank Dr. M. Steidl, K. Valerius and Dr. F. Glueck for their support in creating the electron tracking MC simulation and S. Wüstling for the planning and assembly of the detector electronics. F. Fränkle, F. Habermehl and P. Renschler were very helpful in getting and keeping ORCA running.

I gratefully acknowledge the support from the personnel at TLK, H. D. Adami, Dr. U. Besserer, Dr. C. Caldwell-Nichols, Dr. I. Cristescu, Dr. D. Demange, H. Dittrich, Dr. L. Dörr, E. Fanghänel, M. Göckel, A. Gotsova, K. Günther, G. Hellriegel, H. Kissel, B. Kloppe, F. Kramer, S. Krieger, T. L. Le, C. Melzer, R. Michling, L. Pfeiffer, E. Porter, F. Rehlinghaus, P. Schäfer, P. Schuster, K. H. Simon, M. Sirch, R. Wagner, S. Welte, Dr. J. Wendel, W. Wurster and those who left TLK, Dr. S. Beloglazov, Dr. I. R. Cristescu, Dr. M. Glugla and F. Scheel.

During the TRAP measurement many people were involved in keeping the cryostat filled with LHe. Apart from those already mentioned above, one should not forget L. Anselment, J. Bohn, Dr. L. Bornschein, W. S. Gil, H. Gutzeit, S. Horn, H. Krause, M. Kuhl, M. Mark, H. Rapp, M. Riegel, E. Ternig and H. Zimmermann.

Last but not least, I would like to thank Z. Balci, H. Stober and P. Tuchscherer from the MHC company for the mechanical assembly and welding work they performed at TRAP.

The support from the German Federal Ministry of Education and Research under contracts 05CK1VK1/7, 05CK1UM1/5 and 05CK2PD1/5 is gratefully acknowledged.